Factors Influencing the Thermal Properties of Nanofluids and Phase Change Materials

By

S. ANBUMOZHI ANGAYARKANNI

Enrolment No: PHYS0220104011

Indira Gandhi Centre for Atomic Research, Kalpakkam,
Tamil Nadu, India 603 102

A Thesis submitted to the
Board of Studies in Physical Sciences
In partial fulfillment of requirements
For the degree of

DOCTOR OF PHILOSOPHY

of

HOMI BHABHA NATIONAL INSTITUTE

May, 2015

Recommendations of the Viva Voce Board

As members of the Viva Voce Board, we certify that we have read the dissertation prepared by **S. Anbumozhi Angayarkanni** entitled "**Factors Influencing the Thermal Properties of Nanofluids and Phase Change Materials**" and recommend that it may be accepted as fulfilling the dissertation requirement for the Degree of Doctor of Philosophy.

____**Date:**

Chairman-**Dr. T. Jayakumar**

____**Date:**

Convener-**Dr. John Philip**

____**Date:**

Member 1-Examiner

____**Date:**

Member 2-**Dr. B. V. R. Tata**

____**Date:**

Member 3- **Dr. T. R. Ravindran**

Final approval and acceptance of this dissertation is contingent upon the candidate's submission of the final copies of the dissertation to HBNI.

I hereby certify that I have read this thesis prepared under my direction and recommend that it may be accepted as fulfilling the thesis requirement.

Date: **Dr. John Philip**

Place: (Guide)

CERTIFICATE

I hereby certify that I have read this thesis prepared under my direction and recommend that it may be accepted as fulfilling the thesis requirement.

Date:	**Dr. John Philip**
Place:	(Guide)

STATEMENT BY AUTHOR

This dissertation has been submitted in partial fulfillment of requirements for an advanced degree at Homi Bhabha National Institute (HBNI) and is deposited in the Library to be made available to borrowers under rules of the HBNI.

Brief quotations from this dissertation are allowable without special permission, provided that accurate acknowledgement of source is made. Requests for permission for extended quotation from or reproduction of this manuscript in whole or in part may be granted by the Competent Authority of HBNI when in his or her judgment the proposed use of the material is in the interests of scholarship. In all other instances, however, permission must be obtained from the author.

Kalpakkam (**S. ANBUMOZHI ANGAYARKANNI**)
May, 2015

DECLARATION

I, hereby declare that the investigation presented in the thesis has been carried out by me. The work is original and has not been submitted earlier as a whole or in part for a degree/diploma at this or any other Institution/University.

Kalpakkam **(S. ANBUMOZHI ANGAYARKANNI)**

May, 2015

List of Publications arising from the thesis

1. "Effect of Nanoparticle Size, Morphology and Concentration on Specific Heat Capacity of Nanofluids", **S. A. Angayarkanni**, Vijutha sunny and John Philip, *J. Nanofluids***,** **2015**, 4, 1-8.
2. "Tunable thermal transport in phase change materials using inverse micellar templating and nanofillers", **S. A. Angayarkanni** and John Philip, *J. Phys. Chem C,* 2014, 118, 13972-13980.
3. "Effect of nanoparticles aggregation on thermal and electrical conductivities of nanofluids", **S. A. Angayarkanni** and John Philip, *J. Nanofluids*, **2014**, 3, 17-25.
4. "Role of adsorbing moieties on thermal conductivity and associated properties of nanofluids", **S. A. Angayarkanni** and John Philip, *J. Phys. Chem C,* **2013**, 117, 9009-9019.
5. "Role of surface charge, morphology and adsorbed moieties on thermal conductivity enhancement of nanofluids", **S. Anbumozhi Angayarkanni** and John Philip, *Appl. Phys. Lett.*, **2012**, 101, 173113

Communicated/in preparation

6. **S. A. Angayarkanni** and John Philip, "Effect of Concentration, Bulk thermal conductivity and Morphologies of Nanoinclusions on Thermal Conductivity Enhancement in Phase Change Materials under Freezing".
7. **S. A. Angayarkanni** and John Philip, "Thermal conductivity of polymer nanocomposite".
8. **S. A. Angayarkanni** and John Philip, "Thermal conductivity and associated properties of pH induced Silica gel".

Conferences

1. **S. Anbumozhi Angayarkanni** and John Philip, "*Role of surface charge, morphology, and adsorbed moieties on thermal conductivity enhancement of nanofluids.*" ***5th Bangalore Nano*** at The Lalit Ashok, Bangalore during December 5 – 7, 2012.

2. **S. Anbumozhi Angayarkanni** and John Philip, "Studies on Thermal properties of Nanofluids." ***International Conference on Nanoscience and Technology*** **(ICONSAT-2014)** organized by Institute of Nano Science and Technology, Chandigarh, India during March 3– 5, 2014.

Kalpakkam **(S. ANBUMOZHI ANGAYARKANNI)**

May, 2015

DEDICATIONS

To my Aunty,

R. Padmasini

ACKNOWLEDGEMENTS

First of all I would like to thank God, the Almighty, for having made everything possible by giving me strength and courage to do this work.

With great privilege I would like to thank former centre directors, **Dr. Baldev Raj** and **Shri. C. Chetal** and the present Director, **Dr. P. R. Vasudeva Rao** for allowing me carry out research work in Indira Gandhi Centre for Atomic Research.

I would like to express my sincere gratitude and deepest appreciation to my advisor **Dr. John Philip**, whose expertise, understanding, and patience, added considerably to my graduate experience. I have learned a great deal from his unique perspective on research, his sharp insight on almost any issue, and his personal integrity and expectations of excellence. I thank him for the systematic guidance and great effort he put into training me in the scientific field. I shall do my best to return all this investment and solicitude by means of a passionate and dedicated work.

I am thankful to my doctoral committee chairman **Dr. T Jayakumar** and members **Dr. B. V. R. Tata**, **Dr. T. R. Ravindran** and **Dr. V. P. Venugopalan** for their valuable comments and support. I am grateful for the financial assistance from **DAE-BRNS** through a perspective research grant (2009/38/01/BRNS). I am grateful to **Dr. Sai Baba** for the wonderful hospitality during my stay at JRF Enclave. I owe a big thanks to SMARTS and RTS family for the encouragement and support. A special thanks to all IGCAR research scholars for making my daily routine more pleasant.

Some people go to priests, others to poetry, I to my friends. I take this opportunity to thank my friends **Mr. M. Kalyan Phani, Ms. Leona J Felicia, Mr. E. Rajarajan** and **Dr. Prasad Rao** for helping me getting through the difficult times, and for all the emotional support, comraderie, entertainment, and caring they provided during my Ph.D period. I would like to thank my seniors **Dr. Sudhanshu** and **Dr. Joy** for their constant support in helping me learn instruments and for the tea time discussions. I would also like to thank all my Friends and Research Scholars at JRF Enclave for their support.

Lastly, and most importantly, I wish to thank my Aunty, **Ms. Padmasini**. She bore me, raised me, supported me, taught me, and loved me. Her support has been unconditional all these years; she has given up many things for me to be at IGCAR; she has cherished with me every great moment and supported me whenever I needed it. To her I dedicate this thesis. I am indebted to my father **R. Somasundaram** and my sisters **Dr. Anbuselvi** and **Dr. Anbuanjugum** for their constant support, love and encouragement.

CONTENTS

Chapter I

Introduction

Chapter II

Materials and Experimental Techniques

Chapter III

Role of Adsorbing Moieties on Thermal Conductivity and Associated Properties of Nanofluids

Chapter IV

Effect of Nanoparticles Aggregation on Thermal and Electrical Conductivities of Nanofluids

Chapter V

Effect of Nanoparticle Size, Morphology and Concentration on Specific Heat Capacity of Nanofluids

Chapter VI

Tunable Thermal Transport in Phase Change Materials Using Inverse Micellar Templating and Nanofillers

Chapter VII

Role of Nanoinclusions on Thermal Conductivity enhancement in Phase Change Materials under Freezing.

Chapter VIII

Conclusions and Recommendations for Future Work

SYNOPSIS

The quest for efficient cooling and energy storage materials led to the emergence of a new research field of called nanofluid. Nanofluids have been a topic of great interest during the last one decade primarily due to the initial reports of anomalous thermal conductivity enhancement in nanofluids with a small percentage of nanoparticles. This field has been quite controversial, with multiple reports of anomalous enhancement in thermal conductivity. Also, there is lack of consensus on the exact mechanisms responsible for the observed enhancement in thermal conductivity. One of the grey areas in the understanding of thermal property variations in nanofluids is the role of interfacial resistance and morphology of suspended nanoparticles on k enhancement. Therefore, a systematic study to understand the effect of interfacial resistance, aggregation and other physico-chemical properties such as viscosity, specific heat capacity and density on thermal conductivity of nanofluid is important. Though the thermal properties of nanofluids are investigated intensely, the studies on heat capacity of nanofluids are scarce. From the initial focus on thermophysical properties of nanofluids, the attention is now shifted to tailoring of novel nanofluids with large thermal conductivities and their applications. To overcome the limitations of traditional heat transfer media, phase change materials are being considered as effective media for thermal energy storage. Though there are some studies on thermal conductivity of PCM with nanoinclusion in the recent years, there are no reports on the effect of aggregation of such nanoinclusions on the thermal conductivity of PCMs.

The main objectives of the thesis are (a) to study the role of particle size, volume fraction and morphology, interfacial resistance, density and viscosity on the thermal properties of nanofluids (b) to study the effect of aggregation of dispersed nanomaterials on the thermal properties of stable and unstable nanofluid (c) to probe the role of size, morphology and concentrations of nanoinclusion on specific heat capacity of nanofluids (d) to develop new methodologies to achieve extremely large tunable thermal conductivity in phase change alkane and (e) to study the role of aggregation of dispersed nanomaterials on thermal conductivity of phase change alkanes.

This thesis consists of 8 chapters. **Chapter 1** gives a brief introduction about the nanofluids and their applications. Literature survey on classical theories, experimental findings in various nanofluids, motivation and the objectives of the present work are also presented. **Chapter 2** describes the details of sample preparation methods, the experimental tools used to study thermal conductivity, rheology, hydrodynamic size and associated properties. **Chapter 3** describes the effect of adsorbing moieties on thermal conductivity, rheology, density, contact angle and refractive index of 'soft' and 'hard' nanofluids. **Chapter 4** describes the thermal conductivity, electrical conductivity, viscosity and refractive index of two non-aggregating nanofluids and two aggregating nanofluids. **Chapter 5** describes the effect of particle size, particle morphology and volume fraction of nanoparticles on the temperature dependent specific heat capacity of metal oxide nanofluids. **Chapter 6** describes a new approach to achieve large tunable thermal conductivity in phase change alkane using inverse micellar templating. **Chapter 7** presents the thermal conductivity changes in phase change alkane incorporated with copper nanowire, multiwalled carbon nanotube, graphite nanofibers and graphene nanoplatelets. **Chapter 8** summarizes the results obtained, conclusions drawn and the scope of future work.

The key findings of this thesis work are as follows: The thermal conductivity of soft micellar systems of different sizes, surface charges, and morphologies follow the effective medium theory of poor thermal conductors. The adsorption of surface active moieties on nanoparticles does not lower the enhanced thermal conductivity of nanofluids but significantly enhances the stability and dispersibility of nanomaterials.

For stable nanofluids, the experimental thermal conductivity data fitted well with the Effective Medium Theory (EMT) at lower concentration but deviated at higher concentration. In the case of aggregating nanofluids, thermal conductivity values are found to be more than the EMT predictions. In stable nanofluid, the thermal conductivity is found to be time independent whereas it is time dependent in the case of stable nanofluid. The temperature dependent specific heat capacity of metal oxide show that the specific heat capacity decreases with increase in volume fraction and particle size in kerosene based Fe_3O_4 nanofluids but enhances in the case of PAO based Al_2O_3 nanofluids.

Thermal properties of n-hexadecane basefluids containing inverse micelles of different volume fractions have been studied using two ionic and non-ionic surfactants. The thermal conductivity enhancements of micelle templated alkanes were perfectly reversible under repeated thermal cycling because of their monodispersity and non-aggregation behaviour. These results suggest that during the first order phase transition, the inverse micelles are pushed to the grain boundaries of alkane crystals thereby reducing the interfacial thermal resistance. In addition to this, the internal stress generated during freezing also improves the heat conduction through crystallites. The effect of concentration, bulk thermal conductivity and morphologies of nanoinclusions on thermal conductivity enhancement in phase change materials under freezing studies show that an optimal nanoparticle loading where the space filling agglomerates in a phase change alkane can provide extremely large tunable thermal conductivity.

LIST OF FIGURES

LIST OF TABLES

LIST OF ABBREVIATIONS

AOT	Dioctyl sodium sulfosuccinate
CMC	Critical Micellar Concentration
CNT	Carbon Nanotube
CTAB	Cetyltrimethylammonium bromide
CuNW	Copper Nanowire
DLS	Dynamic Light Scattering
DSC	Differential Scanning Calorimetry
EC	Electrically Commutated
EM	Electro Magnetic
EMT	Effective medium Theory
FTIR	Fourier Transform Infrared
GNF	Graphite Nanofibers
GNP	Graphene Nanoplatelets
IPS	Inter-micellar Spacing
IR	Infra Red
KD	Krieger-Dougherty
MCR	Modular Compact Rheometer
MWCNT	Multi-walled Carbon Nanotube
ND	Number Density
NP 9/NP 10	Nonylphenol ethoxylate
NR	Nanorods

NS	Nanospheres
OA	Oleic Acid
PAO	Polyalphaolefin
PCM	Phase Change Material
PMT	Photomultiper Tube
QELS	Quasi-Elastic Light Scattering
SAXS	Small angle X-ray Scattering
SDS	Sodium dodecyl sulfate
SEM	Scanning Electron Microscope
Span 80	Sorbitan Oleate
TCA	Thermal Constant Analyzer
TEM	Transmission Electron Microscopy
TGA	Thermogravimetric Analyzer
THW	Transient Hot Wire

LIST OF SYMBOLS

D	Thermal diffusivity
D'	Diffusive constant
k_B	Boltzmann Constant
E_i	Exponential Integral
β	Euler’s Constant
δ_T	Liquid layer thickness
$R_p(\tau)$	Probe Resistance
$D(\tau)$	Geometric function
T	Temperature
ΔT	Temperature difference
$\Delta T(\tau)$	Temperature rise of the probe
q	Scattering wave vector
n	Shape factor

γ^{sl}	Solid-liquid interfacial tension
γ^{sv}	Solid-vapor interfacial tension
γ^{lv}	Liquid-vapor interfacial tension
θ	Contact angle
$I(q)$	Scattering intensity
k	Thermal conductivity
k_{nf}	Thermal conductivity of nanofluid
k_p	Thermal conductivity of Nanoparticle
k_f	Thermal conductivity of basefluid
k/k_f	Effective thermal conductivity
k_{cl}	Thermal conductivity of clusters
σ	Electrical conductivity
η	Viscosity
η/η_0	Reduced Viscosity
φ	Volume fraction
R_0	Resistance offered by water
R_H	Resistance offered by Head
R_T	Resistance offered by Tail
R_{BD}	Phonon boundary resistance
R_k	Kapitza resistance
a_k	Kapitza radius
C_p	Specific heat capacity
$C_{p,nf}$	Specific heat capacity of nanofluid
$C_{p,bf}$	Specific heat capacity of basefluid
$C_{p,nf} / C_{p,bf}$	Normalized Specific heat capacity
ρ	Density
ρ_n	Density of the nanoparticle
ρ_f	Density of the base fluid
ρ_{nf}	Density of nanofluid
λ	Wavelength of X- ray source

d	Diameter of the particle
β	Full width at half maximum
θ	Contact angle
θ′	Half of the diffraction angle
Na	Avagadro’s Number
m_{nf}	Mass of the nanofluid
V_{nf}	Volume of the nanofluid
υ	Group velocity
Λ_{eff}	Effective mean free path
l	Phonon mean free path
C_k, C_n, A, m, c	Constant
Re	Reynolds number
T_m	Melting point
a	Lattice constant

Chapter I Introduction

1.1 Introduction

The term nano originated from the Greek word 'nanos' which means 'dwarf'. When the size of a material is on the nanoscale (1 -100 nanometers), in at least one of dimension, it is called nanomaterial. Examples for materials with one, two and three dimension in the nanoscale are layers, nanowires and particles, respectively. Nanotechnology deals with the production and application of materials at nanoscale and the integration of the resulting nanostructures into larger systems. Trends indicate that nanotechnology is likely to impact our daily life in a big way in the coming decades.[1] Nanotechnology may find applications in areas such as materials and manufacturing, nanoelectronics, medicine, healthcare, energy, biotechnology, information technology, and national security. Two principal factors affecting the properties of materials at nanoscales are increased relative surface area, and quantum effects, which can dramatically change or enhance properties such as optical, electrical, magnetic behaviour of materials, reactivity and strength. As the size of a particle decreases, a greater proportion of atoms are found at the surface compared to those inside. The unique, chemical, physical, and mechanical properties of nanomaterials are exploited in a wide variety of applications such as sunscreens, cosmetics, paints, displays, batteries, catalysis, medicine, sensors, energy, agriculture, coolant, plastic packaging, stain resistant textiles etc.

The quest for efficient cooling materials led to the emergence of a new field of research called nanofluid.[2-40] Nanofluids are dispersions of nanomaterials (nanoparticles, nanofibers, nanotubes, nanowires, nanorods, nanosheet, or droplets) in base fluids.

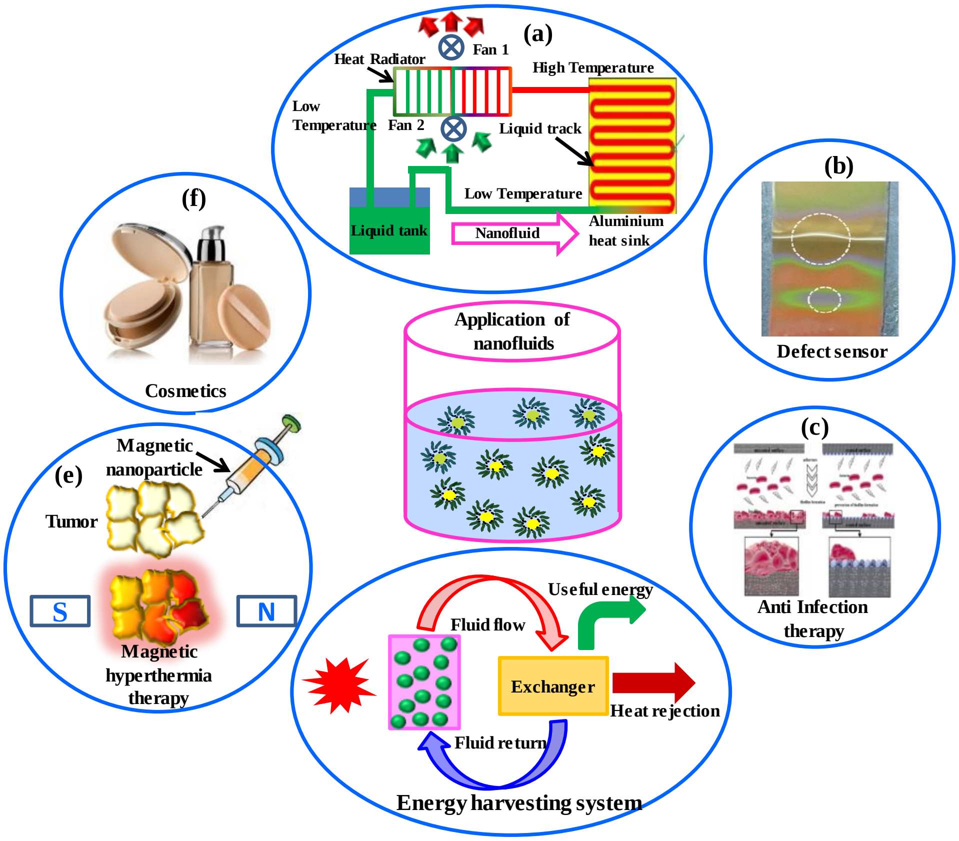

Figure 1.1 Schematic representation of some of the applications of nanofluids in (a) Heat transfer,[41] (b) Defect sensors,[42] (c) Anti infection theraphy,[43] (d) Energy harvesting system,[44] (e) Hyperthermia[45] and (e) Cosmetics.

Nanofluids have some unique features which are quite different from dispersions of mm or µm sized particles. Compared to conventional cooling liquids such as water, kerosene, ethylene glycol and microfluids, nanofluids have been shown to exhibit higher thermal conductivities. Further, nanofluids do not block flow channels and induces a very small pressure drop during flow, which is beneficial for heat transfer applications. Traditionally, this field falls in the realm of colloidal science and hence abundant knowledge on preparation, characterization and stabilization of nanofluids exist. The vigorous Brownian motion of suspended nanoparticles in base fluids makes nanofluids more stable compared to microfluids,[46] which is one of the attractions of nanofluids for heat transfer applications. Three properties that are making nanofluids a promising coolant are the increased thermal conductivity, the increased heat transfer, and the increased critical heat flux. Studies showed that relatively small amounts of nanoparticles can enhance thermal conductivity of base fluids to a large extent. Two features that are very important for heat transfer systems are extreme stability, and high thermal conductivity. Different types of nanofluids have been used in a broad range of engineering applications such as in automobiles, as coolants,[47] in brake fluids,[48] in domestic refrigerators,[49] in solar devices,[50, 51] cosmetics, drug delivery,[52] defect sensors,[42] optical filters,[45] hyperthermia,[53] sealant[54] etc. A schematic representation of the applications of nanofluids is shown in **Fig.1.1**.

1.2 Preparation of Nanofluids

The following are the two methods widely used for the preparation of nanofluids.

1.2.1 Two Step Method

In a two step method, the nanomaterials are first produced as dry powders either by physical or chemical process. The prepared nanoparticles are then dispersed into a fluid with the aid of intensive magnetic force agitation, ultrasonic agitation, high-shear mixing, homogenizing, or ball milling. The most widely used method for preparing nanofluids is the two step method due to large scalability and cost effectiveness. Nanoparticles are prepared by transition metal salt reduction,[55] ligand reduction and displacement from organometallics,[56] microwave synthesis[57] and coprecipitation.[58]

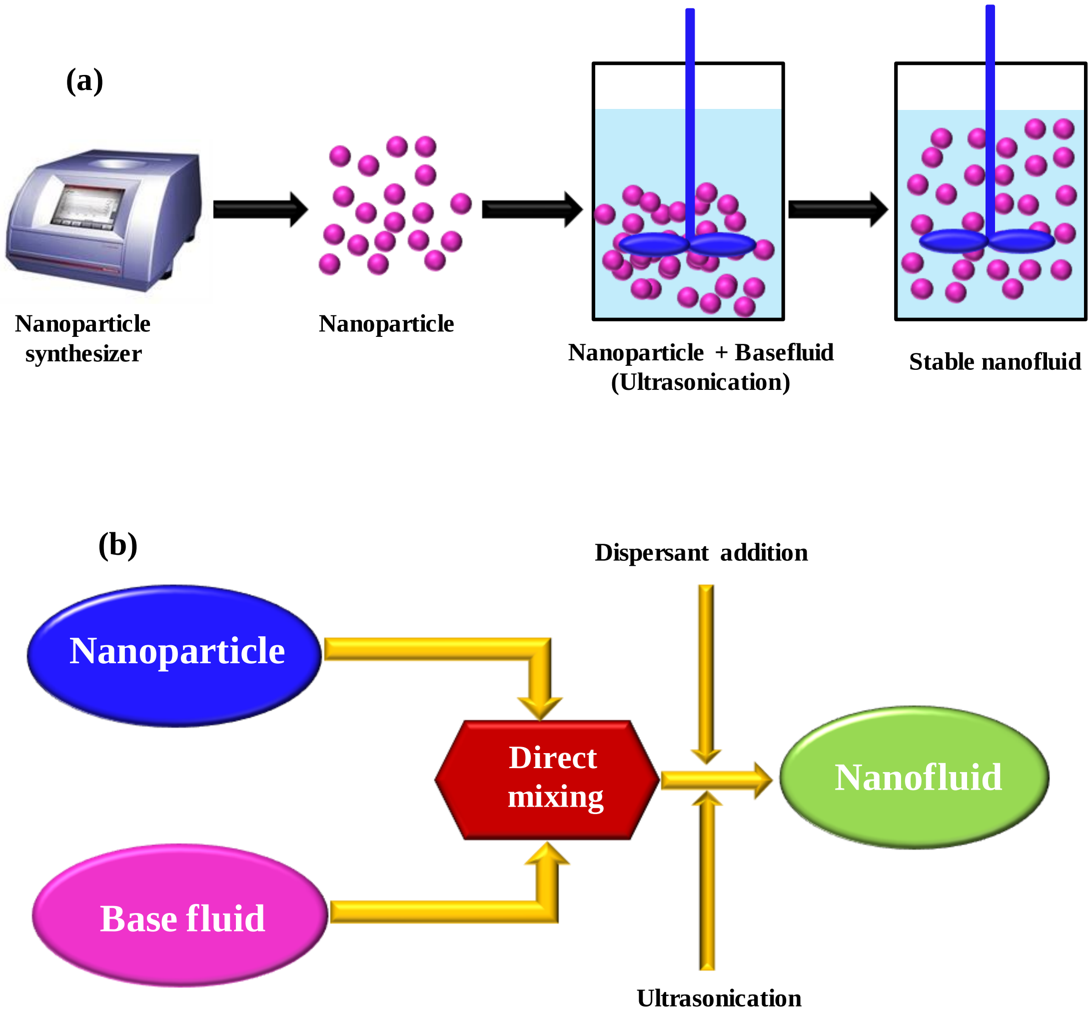

Figure 1.2 Two step preparation process of nanofluids. (a) Naparticles prepared by microwave synthesizer and particles are dispersed in base fluid by mechanical stirrer. (b) Direct mixing of nanoparticles followed by addition of dispersant and ultrasonication.

Due to the high surface area and surface activity, nanoparticles have a tendency to aggregate. Therefore, the nanoparticles are to be stabilized to prevent from agglomeration.[59] Bonnemann et al.[60] developed a method for the production of palladium (Pd) particles of size 2.2 nm via chemical reduction pathways. Copper (Cu) nanofluids are prepared by dispersing commercially obtained Cu nanoparticles in both water and transformer oil by sonication in the presence of stabilizers.[61] Murshed et al.[27] prepared water based titanium dioxide (TiO_2) nanofluid using ultrasonic dispersion. Kim et al.[62] prepared copper oxide (CuO) nanofluids by directly dispersing the commercially obtained CuO nanoparticles in ethylene glycol by sonication, without stabilizers. They found that the optimum duration of sonication was 9 hours for 60 nm diameter nanoparticle. Nanofluids containing single-wall carbon nanotubes (SWCNTs) and multi-walled carbon nanotubes (MWCNTs) are usually prepared by the two-step method.[28, 35, 63] The carbon nanotubes are first synthesized by pyrolysis method and then suspended in a base fluid with or without the use of a surfactant.[28, 35, 64, 65] Lee et al.[66] prepared metal oxide nanoparticles (Al_2O_3, CuO) using sol gel method and then dispersed the obtained nanoparticles in water using a sonicator. Suresh et al.[67] prepared alumina–copper hybrid powder by a thermo chemical synthesis method followed by dispersing of nanopowder in deionized water with sodium lauryl sulphate (SLS) as a dispersant by using an ultrasonic vibrator. Water based silver (Ag) nanofluid is prepared by the two-step technique.[68] In the first step Ag nanoparticles are prepared by chemical reduction of silver nitrate in the presence of an organic surfactant. The obtained Ag nanoparticles are then dispersed in the deionized water by ultrasonic vibration. Hwang et al.[69] prepared carbon black in water and Ag in silicon oil nanofluids by two step method and high-pressure homogenizer methods in order to achieve small particle size, and a good dispersion. Ethylene glycol (EG) based zinc oxide (ZnO) nanofluids are prepared by two step technique using a magnetic stirrer.[70] Ammonium citrate is added as a dispersant, to enhance the stability of suspension. Choi et al.[71] used zirconium dioxide (ZrO_2) bead milling in a vertical, super-fine grinding mill, for the preparation of transformer oil based aluminium oxide (Al_2O_3) and aluminium nitride (AlN) nanofluid with n-hexane as a dispersant. Water based TiO_2

nanofluids were prepared by the two step method using a high shear homogenizer to prevent agglomeration.[72] A schematic representation of two different the two step methods involving microwave assisted synthesis and direct mixing technique is shown in **Fig. 1.2**.

1.2.2 One Step Method

In one-step method, nanoparticle preparation and dispersing in a base fluid are done simultaneously.[73] The one-step process can prepare uniformly dispersed nanoparticles stably in a base fluid. In this method, the processes of drying, storage, transportation, and dispersion of nanoparticles are not required. Therefore, the agglomeration of nanoparticles can be minimized, and the stability of fluids can be increased.[74] The disadvantage in the one-step method is that the residual reactants (impurities) are left in the nanofluids due to the incomplete reaction, which are difficult to remove. The methods used to prepare nanofluids through a one step process include the thermal decomposition of an organometallic precursor in the presence of a stabilizer,[75] physical vapor condensation,[38] chemical reduction[76-78] and polyol synthesis.[79]

Direct evaporation Technique: Akoh et al.[80] reported a single step direct evaporation method for the preparation of nanofluids. In this method, the direct evaporation and condensation of the nanoparticulate materials in base liquid are obtained to produce stable nanofluids.[81] Choi[82] developed a ‘direct-evaporation’ technique which consists of a cylinder containing a fluid which is rotated and a source material is vaporized in the middle of the cylinder. The vapour condenses after it comes into contact with the cooled liquid **(Fig. 1.3)**. The drawbacks of this technique however, are the requirement of low vapour pressure liquids and lower yield.

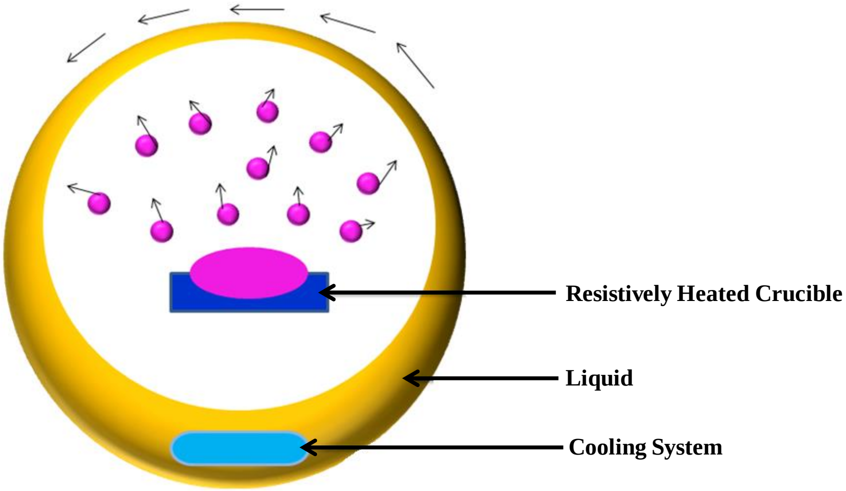

Figure 1.3 Schematic of the one-step nanofluid production system, which simultaneously produces and dispersed nanoparticles into a low vapour-pressure liquid.[82]

Chemical reduction: Metallic nanoparticles are prepared in various solvents by reducing metal salts into nanofluids.[83] The cuprous oxide nanofluids were prepared by the chemical reduction of copper acetate by glucose in the presence of sodium lauryl sulfate.[77] Kumar et al.[78] prepared copper (Cu) nanofluids by chemical reduction of copper sulphate pentahydrate in the presence of SLS in water.

Submerged Arc Nanoparticle Synthesis System: A stable CuO nanofluid is prepared by submerged arc nanoparticle synthesis system (SANSS),[84] where a pure copper rod is submerged in a dielectric liquid in vacuum chamber. A suitable electric power source is used to produce with a temperature ranging 6000 - 12000 °C, which melts and vaporizes the metal rod in the region along with vapor of the deionized water. The vaporized metal undergoes nucleation, growth and condensation resulting in nanoparticles dispersed in deionized water. Using this approach nanofluids containing CuO particles of size 49.1 ± 38.9 nm were obtained.[84] Ethylene glycol based nanofluid containing silver nanoparticle of size 12.5 nm were synthesized using SANSS.[85] A schematic representation of submerged arc nanoparticle synthesis system is shown in **Fig. 1.4**

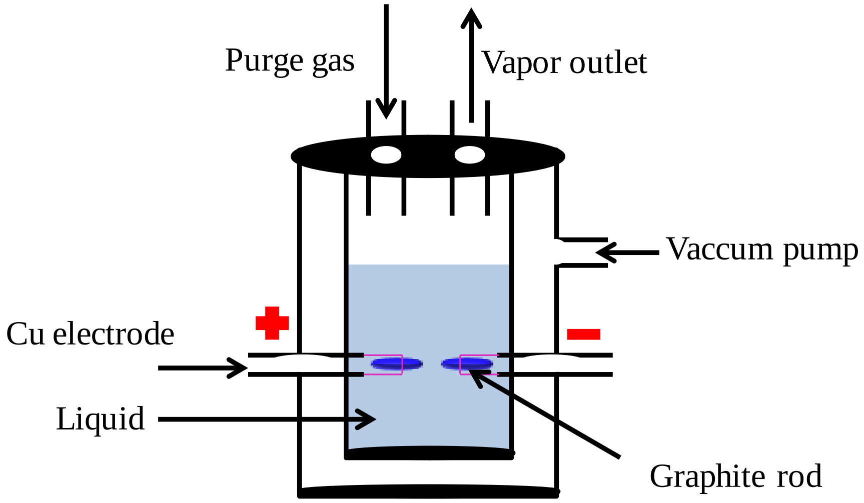

Figure 1.4 Schematic representation of submerged arc nanoparticle synthesis system.

Laser ablation: Laser ablation is another single-step technique to produce and disperse nanoparticles directly in the base fluids. Various nanofluids have been prepared by laser ablation method[86-88] by ablating solid metals such as Cu, Ag, gold (Au), which are submerged in the base fluid (e.g. water, lubrication oils, etc). This method produces stable nanofluids without addition of dispersant.[87] Kim et al.[86] prepared bare Au-water nanofluids by pulsed laser ablation in liquids. A gold-tablet was placed at the bottom of a glass-beaker filled with pure water. A Q-switched Nd:YAG laser was used to produce Au/water nanofluids by varying the irradiation time from 1 to 18 h. The pulsed laser beam was focused using a biconvex lens, onto a Au-tablet placed in pure water. The schematic representation of pulsed laser ablation in liquids is shown in **Fig. 1.5**. Lee et al.[87] prepared water based Cu nanofluid at a concentration of 0.001 vol% by PLAL method with Cu pellets. A schematic representation of laser ablation is shown in **Fig. 1.5.**

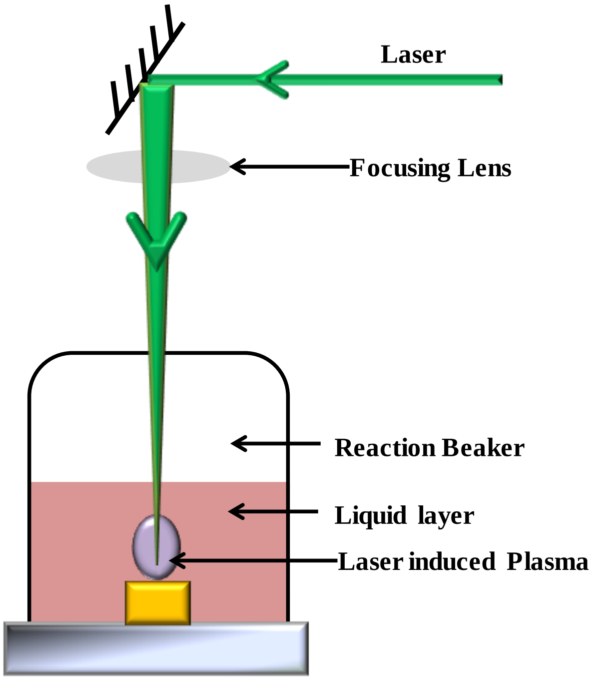

Figure 1.5 Schematic illustration of the experimental apparatus for Laser ablation.

Microwave Irradiation: Another one step approach adopted for nanofluids synthesis is based on microwave irradiation.[89] Copper nanofluids is prepared by reducing $CuSO_4 \cdot 5H_2O$ with $NaH_2PO_2 \cdot H_2O$ in ethylene glycol (EG) under microwave irradiation.[90] Mineral oil (MO) based silver nanofluids were also prepared using this method.[91] Ethanol-based silver nanofluids were prepared by microwave-assisted one-step method.[92] Polyvinylpyrrolidone (PVP) was used as a stabilizer and reducing agent for colloidal silver in solution.[92]

Polyol Process: In the polyol process,[93, 94] a metal precursor is dissolved in a liquid polyol (usually ethylene glycol) and the experimental conditions are adjusted to reduce the metallic precursor, followed by nucleation and growth.[93] Water based nanoparticles are prepared using this method by coating hydrophilic polyol over the nanoparticles. Other one step techniques used for nanofluid preparation are step physical vapor condensation method[38] and plasma discharging technique.[95]

Phase-Transfer Method: In phase transfer method, the reactant migrates from one phase into another phase where the reaction occurs. This method has the advantage of overcoming the problems associated with the insolubility of precursor materials in base fluids during the preparation of nanofluids.[96] A general protocol was developed, by Yang et al.[97], to transfer metal ions from an aqueous solution to an organic medium. Combining phase transfer technology with wet chemistry method for the synthesis of nanoparticles is an effective way for the preparation of nanofluids.[96] A simple process based on amine chemistry for the phase transfer of platinum nanoparticles from an aqueous to an organic solution was reported by Kumar et al.[98] By vigorous shaking of a biphasic mixture of platinum nanoparticles in an aqueous medium and octadecylamine (ODA) in hexane, the aqueous platinum nanoparticles complex with the ODA molecules present in the organic phase. This process renders hydrophobicity to the nanoparticles, which enables their dispersion in an organic phase.[98] In a similar way, gold and silver nanoparticles are transferred from aqueous to organic phase with alkylamine as surfactant.[99] Graphene oxide nanosheets (GONs) were successfully transferred from water to n-octane after modification by oleylamine.[100] The schematic illustration of the phase transfer process is shown in **Fig. 1.6**

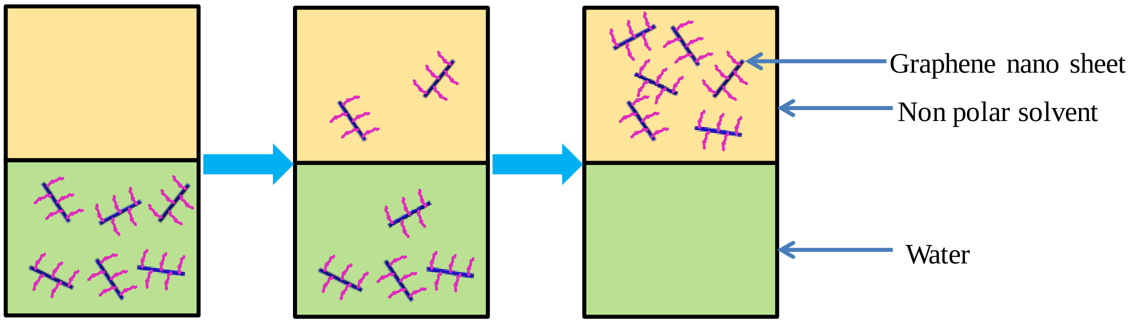

Figure 1.6 Schematic illustration of the phase transfer process for preparation of graphene oxide nanosheets. [100]

Due to the high reactivity of nanoparticles, they have a tendency to agglomerate, which limits its benefits of having the high surface area to volume ratio, resulting in the settling of nanoparticles in base fluid. To prepare stable nanofluids, surfactants are often used as stabilizing agents which provide electrostatic or steric repulsion or the combination of these two between nanoparticles and prevent particle agglomeration due to van der Waals attractive force. Apart from surfactants and polymers,[101] surface treatment[102] is also used to produce stable nanofluids. But the addition of additives can modify the surface properties of the particles, which may have a synergistic or antagonistic effect on thermal properties.

1.3 Thermal Properties of Nanofluid

1.3.1 Theoretical Studies on Thermal Conductivity of Nanofluids

Maxwell[103] derived an expression for the thermal conductivity of composite mixtures using Effective Medium Theory (EMT) by considering a spatially homogeneous electromagnetic response.[104] The basic assumption for theoretical models describing effective thermal conductivity of two component systems is that the systems constitute a continuous matrix in which particles (discontinuous component) are embedded. EMT assumed mixtures under static condition and a low volume fraction of inclusions within the matrix without considering clustering of dispersed materials.[104] Using this approach, the thermal conductivity of the nanofluid (k_{nf}) at low volume fractions of non-interactive spherical particles is determined by considering the thermal conductivities of base fluid (k_f), nanoparticles (k_p) and volume fraction of nanoparticle (φ).[122] According to Maxwell's theory,[103,122] for a dilute suspension of spherical particles, the effective thermal conductivity (k/k_f) is given as $\frac{k}{k_f} = \frac{1+2\beta\phi}{1-\beta\phi}$, where, $\beta = \frac{(k_p - k_f)}{(k_p + 2k_f)}$. To account for the interfacial thermal resistance R_b, k_f is modified as, $k_f \rightarrow k_f + \alpha k_p$,where $\alpha = \frac{2R_b k_f}{d}$ and d is the average particle diameter. At high volume fractions, Maxwell model (lower bounds) fails to explain the k_{nf} enhancement because of the interaction between the particles becomes prominent at higher φ. By considering the interparticle interaction at higher volume fraction, Bruggeman[105] modified the Maxwell's **Equ 1.1** . According to Bruggeman model,

$$\frac{k}{k_f} = k_f \frac{\left[(3\varphi - 1)\frac{k_p}{k_f} + (2 - 3\varphi) + \sqrt{\Delta} \right]}{4} \tag{1. 1}$$

where $\Delta = (3\varphi - 1)^2 \left(\frac{k_p}{k_f} \right)^2 + (2 - 3\varphi)^2 + 2\left(2 + 9\varphi - 9\varphi^2\right)\left(\frac{k_p}{k_f} \right)$

In a nanofluid, series and parallel modes of thermal conduction through the base fluid and the nanoparticles can be visualized. The parallel mode has a geometric configuration that allows the most efficient means of heat propagation.[14] Hashin and Shtrikman (HS) bounds for thermal conductivity of a nanofluid, on the basis of volume fraction alone is given by[106]

$$k_f \left[1 + \frac{3\varphi\left(k_p - k_f\right)}{3k_f + (1 - \varphi)k} \right] \le k \le \left[1 - \frac{3(1 - \varphi)\left(k_p - k_f\right)}{3k_p - \varphi\left(k_p - k_f\right)} \right] k_p \tag{1. 2}$$

In the lower HS limit, nanoparticles are well suspended and the conduction is through series mode whereas in the upper HS limit, the conduction path is through dispersed particles. In the limit $\left(\varphi k_p / k_f\right)$ >>1, the predicted values of k/k_f for the upper HS and parallel modes are $(2\varphi/3)\ k_p/k_f$ and $(\varphi k_p/k_f)$, respectively. The upper and lower bounds reverse when $k_p < k_f$.

Hamilton and Crosser[107] (H-C) developed a modified Maxwell's theory for two-component systems containing different particle shapes and particle sizes ranging between millimeters to micrometers. According to H-C model, k/k_f is given by,

$$\frac{k}{k_f} = k_f \left[\frac{k_p + (n-1)k_f - (n-1)(k_f - k_p)\varphi}{k_p + (n-1)k_f + (k_f - k_p)\varphi} \right] \tag{1. 3}$$

where n is the shape factor, $n = \frac{3}{\psi}$, where ψ is the particle sphericity, which is equal to 1, for spherical particle. For prolate ellipsoids ψ is equal to 0.5. Yu et al.[108] modified the H-C model by including the particle-liquid interfacial layer for the prediction of the thermal conductivity of nanofluids having ellipsoidal particles.

$$\frac{k}{k_f} = \left(1 + \frac{n\varphi A}{1 - \varphi A} \right) k_1 \tag{1. 4}$$

where $A = \frac{1}{3} \sum_{j=a,b,c} \frac{k_{pj} - k_f}{k_{pj} + (n-1)k_f}$

A modified Maxwell's model was proposed by Xuan et al.[109] by considering Brownian motion of the particle in the base fluid for the thermal conductivity enhancement. It is given as

$$\frac{k}{k_f} = \frac{k_p + 2k_f - 2(k_f - k_p)\varphi}{k_p + 2k_f + (k_f - k_p)\varphi} k_f + \frac{\rho_p \varphi c_p}{2} \sqrt{\frac{k_B T}{3\pi r_c \mu}} \tag{1. 5}$$

where k_B is the Boltzmann constant, and r_c is the apparent radius of the cluster, which in turns depends on the dimensions of the cluster structure. Kumar et al.[110] modified the Maxwell's model in order to account viscosity of the base fluid and the temperature dependence. The expression thermal conductivity taking into account the Brownian motion and temperature is as follows[110]

$$\frac{k}{k_f} = k_b + c\frac{2k_B T}{\pi \eta d^2}\frac{\varphi r_b}{k_b(1-\varphi)r_b}k_b \tag{1. 6}$$

Where *c* is the constant, η is the dynamic viscosity of the base fluid. But this model fails at higher concentrations, due to prominent interparticle interaction. Prasher et al.[26] modified the Maxwell's model by including the convection caused by Brownian motion of the nanoparticle and is given as

$$\frac{k}{k_f} = \left(1 + A\mathrm{Re}^m \,\mathrm{Pr}^{0.333}\varphi\right)\left[\frac{k_p + 2k_f + 2\left(k_p - k_f\right)\varphi}{k_p + 2k_f - \left(k_p - k_f\right)\varphi}\right]k_p \ , \tag{1. 7}$$

where $h = \dfrac{k_p}{a\left(1 + A\mathrm{Re}^m \,\mathrm{Pr}^{0.333}\varphi\right)}$,

the Reynolds number $\mathrm{Re} = \dfrac{1}{v}\sqrt{\dfrac{18k_f T}{\pi \rho_p d_p}}$, *Pr* is the Prandtl number and *A* and *m* are constants.

A unit cell model for the effective thermal conductivity of nanofluid containing carbon nanofibers was proposed by Yamada et al.,[111] and it is given as

$$\frac{k}{k_f} = \frac{\dfrac{k_p}{k_f} + K - K\varphi\left(1 - k_p / k_f\right)}{\dfrac{k_p}{k_f} + K + \varphi\left(1 - k_p / k_f\right)}k_f \tag{1. 8}$$

where *K* is the shape factor and $K = 2\varphi^{0.2}(l_p/d_p)$ for the cylindrical particle with length (l_p) and diameter (d_p) are the length and diameter of the cylindrical particle. Hesselman et al.[112] proposed a new model for thermal conductivity of dilute nanofluids, by considering the thermal barrier resistance at the interface between the materials for spherical, cylindrical and flat plate particle, which is given as

$$\frac{k}{k_f}=\frac{[\alpha(1+2\beta+2)]+2\varphi[\alpha(1-\beta)-1]}{[\alpha(1+2\beta+2)]-\varphi[\alpha(1-\beta)-1]} \tag{1. 9}$$

where $\beta = R_k k_f / k_p$ and R_k is the Kapitza resistance. By considering the thickness liquid layer and Brownian motion of the dispersed particle Jang et al.[32] derived the expression for k/k_f, which is given as

$$\frac{k}{k_f}=k_f+(1-\varphi)+k_p\varphi+\varphi h\delta_T \tag{1. 10}$$

where h is the coefficient of heat transfer and δ_T is the liquid layer thickness. By considering the effect of clusters and their distribution, Wang et al.[113] modified the Maxwell model as

$$\frac{k}{k_f}=\frac{(1-\varphi)+3\varphi\displaystyle\int_0^{\infty}\frac{k_{cl}(r)n(r)}{k_{cl}(r)+2k_f}\,dr}{(1-\varphi)+3\varphi\displaystyle\int_0^{\infty}\frac{k_f n(r)}{k_{cl}(r)+2k_f}\,dr} \tag{1. 11}$$

where $k_{cl}(r)$ is the effective thermal conductivity of clusters and $n(r)$ is the radius distribution function. Meibodi et al.[114] used the thermal resistance approach in one-dimensional Cartesian coordinate for estimating thermal conductivity of suspension including micro and nano particles. According to their model,

$$\frac{k}{k_f}=\frac{\alpha^{'}(1+\frac{\Delta}{d})}{1+\frac{\alpha^{'}\Delta}{d}} \tag{1. 12}$$

where $\alpha' = k_p/k_f$.

By considering the freezing point of the base fluid Corcione[115] developed a the following empirical correlation

$$\frac{k}{k_f} = 1 + 4.4\,\mathrm{Re}^{0.4}\,\mathrm{Pr}^{0.66}\left(\frac{T}{T_{fr}}\right)^{10}\left(\frac{k_p}{k_f}\right)^{0.03}\varphi^{0.66} \qquad (1.\ 13)$$

T is the nanofluid temperature, T_{fr} is the freezing point of the base liquid.

Several mechanisms have been proposed for explaining the anomalous increase in thermal conductivity of nanofluids.[2] They are briefly discussed below.

a) Brownian motion of the Nanoparticles

Brownian motion enables direct solid-solid transport of heat from one particle to another, resulting in an increase in thermal conductivity. It is characterized by the particle diffusion constant D′, given by the Stokes-Einstein formula, $D' = \frac{k_B T}{3\pi\eta d}$.

By comparing the time scale of particle motion with the heat diffusion in the liquids, the effect of Brownian motion on thermal conductivity can be determined. The time (τ_D) required for the particle of diameter d to move by the distance equal to its size, $\tau_D = \frac{3\pi\eta d^3}{6k_B T}$. The time ($\tau_H$) required for heat to move in the liquid by the same distance, $\tau_H = \frac{d^2 c_p \rho}{6k_f}$, where C_p is the specific heat capacity of the nanofluid, ρ density. For water (η = 0.001 Pa.s, k_f = 0.4 W/m K, ρ = 1 g/cm^3, C_p = 4.2 J/ g.°C) based Cu nanofluid containing particles of diameter 10 nm at room temperature, τ_D and τ_H are 2×10^{-7} and 4×10^{-10}, respectively, the ratio of τ_D/τ_H ~ 500. It decreases to ~25 when the particle size equals to the atomic size. Hence the Brownian motion of the nanoparticle is slow to transport significant amount of heat through a nanofluid. However, Brownian motion of particles may influence particle clustering, which can influence thermal conductivity enhancement.

b) Liquid Layering at the Liquid/Particle Interface

In particle-fluid mixtures, the liquid molecules close to a particle surface are known to form layered structures and behave much like a solid.[116] Though the thickness of this liquid layer is of the order of nanometer, this nanolayer is thought to play an important role in heat transport from solid to adjacent liquid.[2, 66, 108] As the specific surface area (SSA) of micron-sized particle is less, the effect of interfacial nanolayer is negligible.

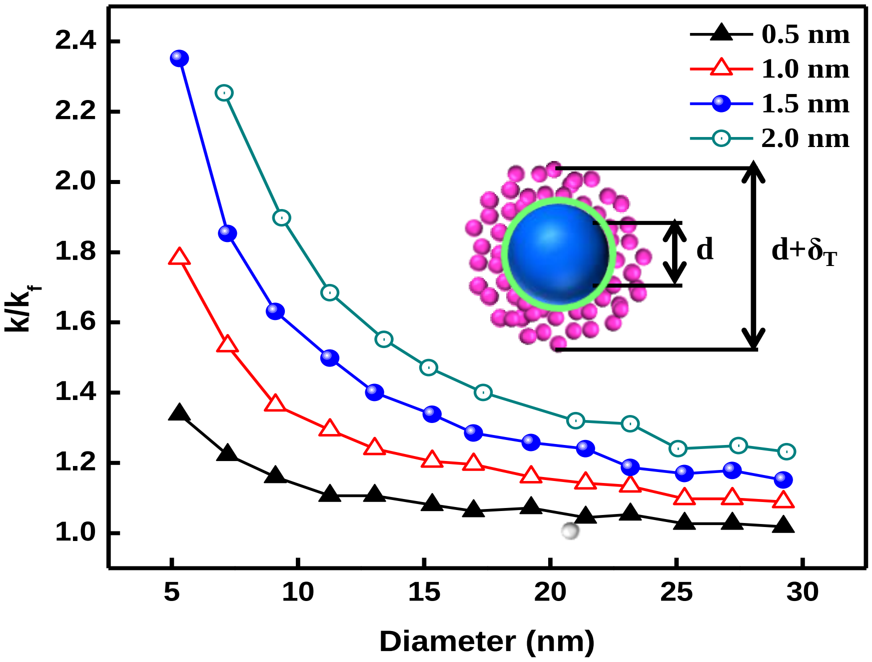

Figure 1.7 Effective thermal conductivity enhancement due to liquid layering at liquid/particle interface.[2]

Due to very large SSA of nanoparticles, the liquid layering become important and has a role in the heat transfer across the interface. The upper limit for the particle layered liquid structure is estimated by considering, the thermal conductivity of the interfacial liquid layer as the same as that of the solid. The enhanced thermal conductivity due to the effective volume of different particle-layered-liquid structure is shown in **Fig 1.7**. For example, a layered liquid thickness of δ_T ~ 2.5 nm is required to double the effective volume of the particle with diameter of 10 nm. A typical interfacial layer thickness is of the order of 1 nm.[117, 118] These studies show that although the presence of the interfacial layer may play a role in heat transport, it is not a dominating factor for the anomalous increase in thermal conductivity. This is evident in ethylene glycol based Cu nanofluid where an increase in thermal conductivity more than an order of magnitude larger than that predicted by HC theory is reported.[38]

c) Nature of the Heat Transport in the Nanoparticles

In crystalline solids, heat is carried by the propagation of lattice vibrations i.e., phonons, which are created at random, propagate in random directions, and are scattered by each other or by defects.[2] Mean free path of the phonon is given by, $l = \frac{10aT_m}{\gamma T}$, where T_m is the melting point, a is the lattice constant and γ is the Gruneisen parameter. For Al_2O_3, at room temperature T_m/T ~ 7 and l ~ 35 nm. Therefore, phonon cannot diffuse in a particle with diameter 10 nm but must move ballistically across the particles.[2] Hence the assumption of diffusive heat transport in nanoparticle is not valid and therefore theoretical model based on ballistic phonon is considered.[119]

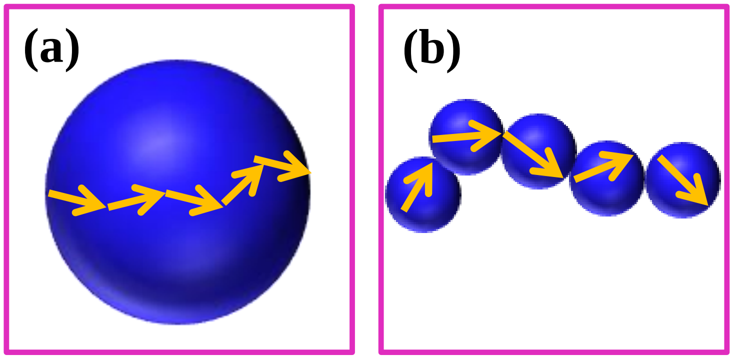

Figure 1.8: Schematic diagram of (a) diffusive and (b) ballistic phonon transport mechanism in a solid particle.[2]

As the interparticle distance in nanofluid is small, even at low φ, the ballistic phonons can persist in the liquid and reach a nearby particle, resulting in a larger thermal conductivity, though the phonon mean free path in liquid is very short (~1-2 nm).[2] For example, 10 nm sized particle are separated by ~5 nm at a volume fraction of 5 %. Due to the Brownian motion, the particle can be much closer and thus enhance the heat flow among the particle. Hence, ballistic heat transport process was proposed to be the possible mechanism for the observed *k* enhancement in nanofluid. The experiment on sound propagation in colloidal system shows an analogous phenomenon that the acoustic excitations propagated coherently between neighboring particles when the diameter of particles was comparable to the wavelength of the sound.[120] **Fig. 1.8** shows a schematic diagram of (a) diffusive and (b) ballistic phonon transport mechanism in a solid particle.

d) Nanoparticle Clustering

Clustering of nanoparticle can create paths of lower thermal resistance and enhance the thermal conductivity (*k*) significantly.[2] But, larger clusters settle down in the basefluids with elapsed time, resulting in a physical volume of particle much smaller than the effective volume of the cluster. Heat can move very rapidly within such clusters, and increase in thermal conductivity effectively. The effect of clustering is illustrated in **Fig. 1.9**, which shows the *k* enhancement originating from the increased effective volume of the highly conducting clusters, as a function of the volume fraction of the cluster.

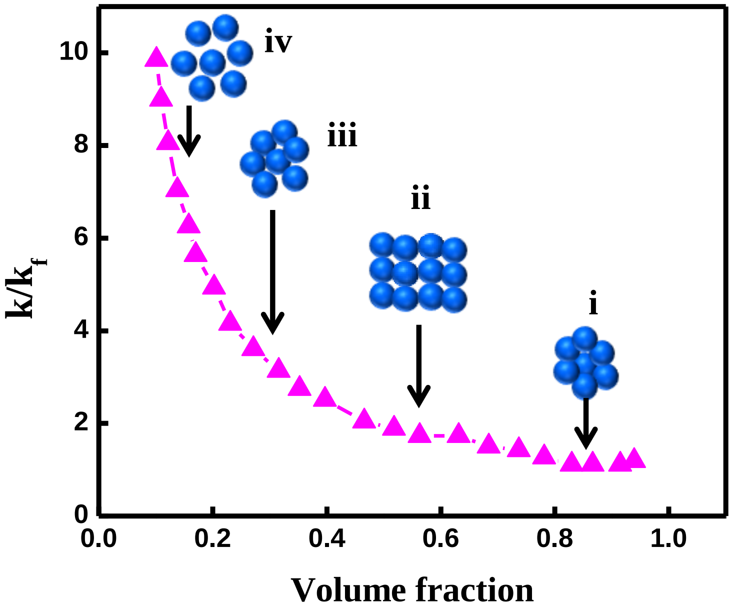

Figure 1.9 Thermal conductivity ratio due to increased effective volume of highly conducting clusters. Schematic diagrams indicate (from right to left) (i) closely packed FCC arrangement of particles, (ii) simple cubic arrangement, (iii) loosely packed irregular structure of particles in physical contact, and (iv) clusters of particles separated by liquid layers thin enough to allow for rapid heat flow among particles.[2]

With decrease in φ, the effective volume of the cluster increases, thus enhancing the thermal conductivity. For a cluster of close packed spherical particles, ~ 25 % volume is filled with liquid in the space between particles, which increases the effective volume of highly conductive region by ~ 30 % with respect to a dispersed nanoparticle system. For loosely packed clusters the effective volume increase will be larger than the closely packed clusters.[2] For increase in *k*, particle needs not to be in physical contact, but at a specific distance, allowing rapid heat flow between them. Such "Liquid mediated" clusters have shown to have very larger effective volume because of low packing fraction and are capable of enhancing of *k*. However, in general clustering results in a decrease in thermal conductivity due to the settling of particles in the liquid, creating larger regions of "particle free" liquid with high thermal resistance and particle rich regime at the bottom of the container.[2]

Due to the larger surface area to volume ratio, the nanoparticles can be also exothermally reactive. In addition the diffusion accompanied by chemical reactions can also enhance the thermal conductivity. If chemical equilibrium is reached before any appreciable transport, the effective thermal conductivity in such case is [121]

$$\frac{k}{k_f} = \frac{\rho_f D^{sl} \left(\Delta h\right)^2}{T\left(\frac{\partial \mu^s}{\partial c^s}\right)} \tag{1. 14}$$

where Δh is the reaction heat which is of the order of the gradient in the chemical potential μ^s for the nanoparticles.[121] With a bounding Δh of 10^5 J/kg for reaction rates for nanoparticles[122] in solutions, k/k_f is again several orders less than that of the base fluid. There are convincing theoretical reasons[2, 23, 123] to believe that the Brownian motion of the nanoparticles has a negligible role in the *k* enhancement in nanofluid. Also, the effectiveness of ballistic phonon transport over the diffusion phonon transport is also not convincing as the temperature within the solid particle will be a constant, providing the same boundary conduction for heat flow in liquids for either ballistic or diffusive phonon transport.[2] All the interfacial layer models, assumed a complex bare nanoparticle with an interfacial fluid nanolayer, however, the assumptions are at variance with the theoretical and experimental studies[124-126] which indicate that the interfacial layers are limited to a few molecular dimensions and cannot account the larger enhancements repoted. Taking into consideration of various mechanisms that are responsible for the observed enhancement in *k*, heat transport through percolating conduction path has emerged as one of the most effective means of heat transport.[11, 59] **Table 1.1** shows different thermal conductivity models for nanofluids.

Table 1.1: Thermal conductivity models for nanofluids.

S. No	Thermal conductivity		Remarks
	Model	Mathematical Expression	
1.	Maxwell[103]	$\frac{k}{k_f} = \frac{1+2\beta\phi}{1-\beta\phi}$, $\beta = \frac{(k_p - k_f)}{(k_p + 2k_f)}$	Suitable for dilute spherical particles/composites
2.	Bruggeman[105]	$\frac{k}{k_f} = k_f \frac{\left[(3\varphi - 1)\frac{k_p}{k_f} + (2 - 3\varphi) + \sqrt{\Delta}\right]}{4}$, $\Delta = (3\varphi - 1)^2 \left(\frac{k_p}{k_f}\right)^2 + (2 - 3\varphi)^2 + 2(2 + 9\varphi - 9\varphi^2)\left(\frac{k_p}{k_f}\right)$	Considered the interparticle interaction
3.	Hamilton and Crosser[107]	$\frac{k}{k_f} = k_f \left[\frac{k_p + (n-1)k_f - (n-1)(k_f - k_p)\varphi}{k_p + (n-1)k_f + (k_f - k_p)\varphi}\right]$	Considered two-component systems of different particle shapes and particle sizes

4	Yu et al.[108]	$\frac{k}{k_f}=\left(1+\frac{n\varphi A}{1-\varphi A}\right)k_1$, $A=\frac{1}{3}\sum_{j=a,b,c}\frac{k_{pj}-k_f}{k_{pj}+(n-1)k_f}$	Renovated H-C model, considered particle-liquid interfacial layer
5.	Hashin and Shtrikman[106]	$k_f\left[1+\frac{3\varphi[k]}{3k_f+(1-\varphi)k}\right]\le k\le\left[1-\frac{3(1-\varphi)[k]}{3k_p-\varphi[k]}\right]k_p$	Based on EMT
6.	Xuan et al. [109]	$\frac{k}{k_f}=\frac{k_p+2k_f-2(k_f-k_p)\varphi}{k_p+2k_f+(k_f-k_p)\varphi}k_f+\frac{\rho_p\varphi c_p}{2}\sqrt{\frac{k_BT}{3\pi r_c\mu}}$	Considered Brownian motion
7.	Kumar et al. [110]	$\frac{k}{k_f}=k_b+c\frac{2k_BT}{\pi\nu d_p^2}\frac{\varphi r_b}{k_b(1-\varphi)r_b}k_b$	Considered Brownian motion and temperature
8.	Prasher et al. [26]	$\frac{k}{k_f}=\left(1+A\mathrm{Re}^m\mathrm{Pr}^{0.333}\varphi\right)\left[\frac{k_p+2k_f+2(k_p-k_f)\varphi}{k_p+2k_f-(k_p-k_f)\varphi}\right]k_p$, $h=\frac{k_p}{a\left(1+A\mathrm{Re}^m\mathrm{Pr}^{0.333}\varphi\right)}$	Considered convection caused by Brownian motion of nanoparticles
9.	Yamada et al. [111]	$\frac{k}{k_f}=\frac{\frac{k_p}{k_f}+K-K\varphi(1-k_p/k_f)}{\frac{k_p}{k_f}+K+\varphi(1-k_p/k_f)}k_f$, $K=2\varphi^{0.2}(l_p/d_p)$	Suitable for cylindrical particels
10.	Hesselman et al. [112]	$\frac{k}{k_f}=\frac{[\alpha(1+2\beta+2)]+2\varphi[\alpha(1-\beta)-1]}{[\alpha(1+2\beta+2)]-\varphi[\alpha(1-\beta)-1]}$	Considered the thermal barrier resistance at the interface between the materials for spherical, cylindrical and flat plate

			particles
11.	Xie et al.[116]	$$\frac{k}{k_f} = 1 + 3\Theta\varphi_T + \frac{3\Theta^2\varphi_T^2}{1-\Theta\varphi_T}$$	Considered the effect of nanolayer
12.	Jang et al. [320]	$$\frac{k}{k_f} = k_f + (1-\varphi) + k_p\varphi + \varphi h\delta_T$$	Considered the thickness liquid layer and Brownian motion of dispersed particles
13.	Wang et al.[113]	$$\frac{k}{k_f} = \frac{(1-\varphi) + 3\varphi\int_0^\infty \frac{k_{cl}(r)n(r)}{k_{cl}(r)+2k_f}dr}{(1-\varphi) + 3\varphi\int_0^\infty \frac{k_f n(r)}{k_{cl}(r)+2k_f}dr}$$	Considered the effect of clusters
14.	Emami et al. [114]	$$\frac{k}{k_f} = \frac{\alpha^{'}(1+\frac{\Delta}{d})}{1+\frac{\alpha^{'}\Delta}{d}}$$	Considered thermal resistance
15.	Corcione[115]	$$\frac{k}{k_f} = 1 + 4.4\,\mathrm{Re}^{0.4}\,\mathrm{Pr}^{0.66}\left(\frac{T}{T_{fr}}\right)^{10}\left(\frac{k_p}{k_f}\right)^{0.03}\varphi^{0.66}$$	Considered the freezing point

1.3.2 Experimental Studies on Thermal Properties of Nanofluid

Nanofluids have been a topic of great interest during the last one decade primarily due to the initial reports of anomalous thermal conductivity enhancement (i.e. beyond Maxwell's limit) in nanofluids with a small percentage of nanoparticles.[35, 37, 38] E.g. Masuda[127] reported a thermal conductivity enhancement of 30 % with 4.3 vol% of Al_2O_3 nanoparticle. A 40 %

enhancement was observed in 0.3 vol% of CuO nanofluid by Eastman et al.[38] Also, the thermal conductivity of nanofluids depends on many factors such as particle volume fraction, particle material, particle size, particle shape etc. Detailed literature reviews on the effect of these parameters on thermal properties of nanofluids are presented below.

1.3.2.1 Effect of Concentration

Several studies show that the thermal conductivity increases with particle loading beyond the EMT predictions.[10, 128-135] Bjorneklett[136] observed 790 % thermal conductivity enhancement in silver-filled epoxy adhesive of 25 vol% due to the large thermal conductivity difference between the silver (429 $W/m^{-1}\cdot K^{-1}$) and epoxy. An enhancement of 32.4 % was observed in the effective thermal conductivity of water based Al_2O_3 nanofluids for a volume fraction about 4.3 %.[127] Lee et al.[66] observed 20 % k enhancement for the 4 vol% for ethylene glycol based CuO nanofluid. Xuan et al.[61] reported that the thermal conductivity ratio increases from 1.2 to 1.8 as the φ of the particle increases from 2.5 to 8 % in transformer oil (TO) based Cu nanofluid. For water based Cu nanofluid, k/k_f were varied from 1.1 to 1.6 as φ of the particle increases from 1 to 5 %.[61] Shin et al.[137] studied the thermal conductivity of polyethylene and polypropylene particles dispersed in a mixture of silicon oil and kerosene. They have observed a thermal conductivity enhancement of 13 % for 10 vol% particle loading. An anomalous thermal conductivity enhancement of 150 % was observed in synthetic polyalphaolefin oil based MWCNTs nanofluid for a very low particle loading of 1 vol%.[138] Ethylene glycol based carbon nanotube (CNT) nanofluids showed a thermal conductivity enhancement of 12 % at a particle loading of 1 vol% and synthetic engine oil based CNT nanofluids showed a 30 % k enhancement at a particle loading of 2 vol%.[63] Cho et al.[139] reported an anomalous increase in thermal conductivity of 18 % with a very low particle loading of Ag nanoparticle of 10000 ppm. For water based MWCNT nanofluid, the thermal conductivity enhancement was found to be 11 % for a volume fraction of 1 vol%.[140] A maximum thermal conductivity enhancement of 74 % for was observed at a particle loading of 0.3 vol% in water based Cu nanofluids.[141] An enhancement of 16.5 % was observed in ethylene glycol based iron (Fe) nanofluid for a particle loading of 0.3 vol%.[142] For ethylene glycol based MWCNT nanofluid, a considerable thermal conductivy enhancement of 17 % was observed at 1 vol%.[143] A 20 % increase in k at 2.5 vol% of carbon nanotubes was observed in ethylene glycol based CNT nanofluids.[143] Methanol based Al_2O_3, silicon dioxide (SiO_2) and TiO_2 nanofluids showed an increase in k with increase in φ.[144] A 30 % k enhancement is observed in water based iron oxide (Fe_3O_4) nanofluid as φ increases from 0-0.04.[145]

Table 1.2: Reported values of k/k_f as a function of concentration for different nanofluids.

Nanoparticle/ Size (nm)	Base fluid	Concentration φ %	k/k_f	% enhancement	Ref
Silver	Epoxy	25	-	790	136
Al_2O_3	Water	4.3	1.32	32	127
CuO/ 18.6	EG	4	1.2	20	66
Polyethylene	Silicon oil	10	1.13	13	137
Copper/ 100	TO	1.5	1.12	12	61
		8	1.45	45	
Copper/ 100	Water	2.5	1.23	23	
		7.5	1.78	78	
Silver/ 200	EG	10000 ppm	1.18	18	139
CNT/ ID:5-10 OD: 20-50	EG	1	1.12	12	63
	Engine oil	2	1.3	30	
Copper	Water	0.3	1.74	74	141
Fe_3O_4	EG	0.3	1.165	16.5	142
CNT/ Dia - 10 Length 5–10 μm	Water	0.3	1.02	2	143
		1	1.10	10	
SiC/ 170	Water	1	1.04	4	146

		4	1.22	22	
Al_2O_3/ 10	PAO	0.4	1.05	5	147
		2.8	1.15	15	
Fe_3O_4/ 8.7	Kerosene	1.71	1.06	0.6	148
		5.03	1.125	12.5	
CuO/ 10	EG	0.18	1.07	7	
		0.92	1.12	12	
		1.14	1.14	14	
Nanodiamond	MO	0.5	1.025	2.5	149
		1.9	1.12	12	
	EG	0.2	1.01	1	
		0.85	1.11	11	
Fe_3O_4/ 15	Kerosene	0.25	1.04	4	150
		1	1.32	32	
Fe_3O_4	Kerosene	2	1.06	6	151
		5	1.18	18	
GNP/ Thickness 2µm	Water	0.012	1.07	7	135
		0.05	1.21	21	
ND-Ni/ 25	Water	0.62	1.03	3	134
		3.03	1.2	20	
ND-Ni/ 25	EG	0.62	1.001	0.1	134
		3.03	1.08	8	
TiO_2/ 13	Water	1	1.08	8	152
		2	1.12	12	
		4	1.15	15	
CuO/ <50 nm	Water	0.01	1.27	27	153
		0.05	1.53	53	
ZnO/ <50 nm		0.02	1.09	9	
		0.08	1.12	12	
Cu	N-tetradecane	0.01	1.05	5	154
		0.02	1.13	13	
Nitrogen doped Graphene	Water	0.01	1.24	24	155
		0.06	1.33	33	
Graphene	EG	0.05	1.041	4.1	156
		0.2	1.119	11.9	

At a particle loading of 4 vol%, water based Fe_3O_4 nanofluids exhibited a 38 % enhancement in thermal conductivity which was attributed to particle clustering.[157] An increase in *k* with increase in concentration was observed in EG based Cu nanofluid of particle size 12 and 3 nm.[158] A study on graphene oxide nanosheets[131] showed a thermal conductivity enhancement of 30, 62 and 76 % at a particle loading of 5 vol% for three different base fluids distilled water, propyl glycol and liquid paraffin, respectively. The observed *k* enhancement was above the EMT prediction. Reports showed that the thermal conductivity of MWCNT nanofluids increases with increase in volume fraction and the *k* enhancement observed were well above the EMT predictions.[159-166] **Table 1.2** shows the summary of the reported values of k/k_f as a function of concentration for different nanofluids. A plot showing the reported percentage of *k* enhancement with concentration of nanoparticles in different nanofluids is shown in **Fig. 1.10.**

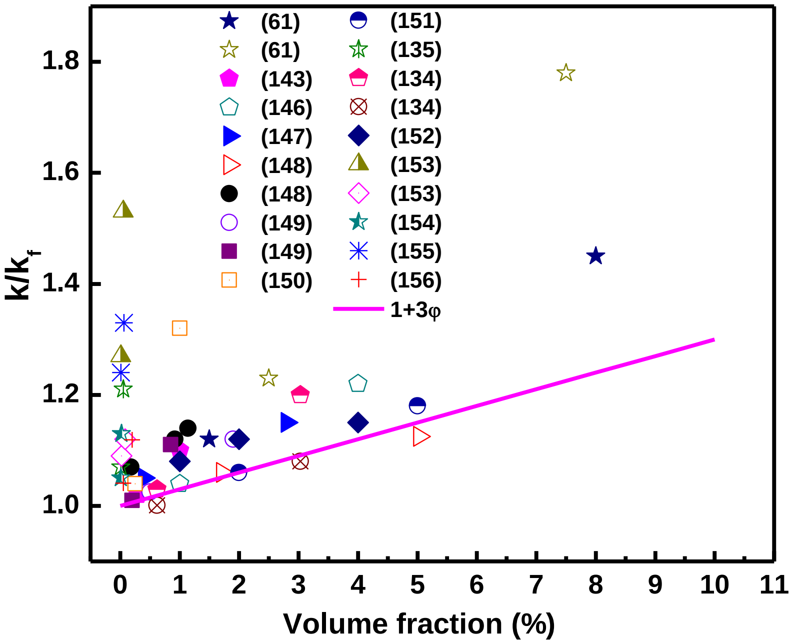

Figure 1.10 : Reported k/k_f with the concentration of nanoparticles in different nanofluids. The EMT prediction is shown by the solid line.

1.3.2.2 Effect of Particle Size

One of the important physical parameters which play a major role in nanofluid thermal properties and the stability is the size of the nanoparticles used. A few reports showed an increase in *k* with a decrease in size of the nanoparticle[3, 167-169] whereas other reports showed a decrease in *k* with increase in particle size.[10, 170, 171] An increase in *k* with decrease in particle size was reported in water based Al_2Cu and ethylene glycol based Ag_2Al.[172] A decrease in *k* with increase in particle size was reported in water based TiO_2 nanofluids.[173] The *k* enhancement was found to decrease with decreasing particle size in water and ethylene glycol based Al_2O_3 nanofluids of particle size varying from 8 to 282 nm.[174] Minsta et al.[169] reported that zero *k* enhancement in water based Al_2O_3 nanofluids of particle size 36 and 47 nm at room temperature but an increase in thermal conductivity was observed for small particle size than the larger one at elevated temperature.

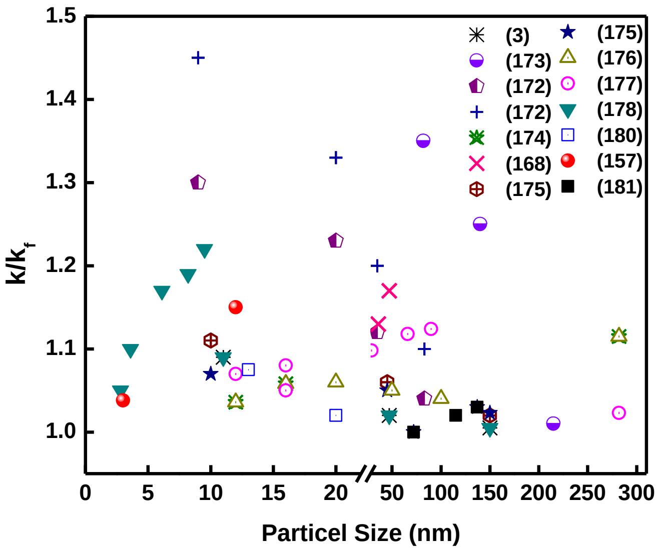

Figure 1.11: Reported value of effective thermal conductivity as a function of particle size for various nanofluids. It should be noted that volume fraction are quite different in each study **(Table 1.3)**

An enhancement in *k* with decrease in particle size was reported in water based Al_2O_3 nanofluids with three different particle diameters of 20, 50 and 100 nm.[176] Similarly, the thermal conductivity study in ethylene glycol based nanofluid showed an increases in *k* with a decrease in particle size.[175] A larger *k* was observed for larger particle size in water based silicon carbide SiC nanofluids with four different particle size 20,30, 35 and 90 nm.[177]

Table 1.3: Reported values of k/k_f as a function of size and concentration for different nanofluids.

Nanoparticle	Concentration (φ%)	Size (nm)	k/k_f	% enhancement	Ref
Al_2O_3/ Water	1	11	1.09	8	3
		47	1.02	2	
		150	1.005	0.5	
TiO_2/ Water	0.6	82	1.35	3.5	173
		140	1.25	25	
		215	1.01	1	
Al_2Cu/ Water	0.5	9	1.3	30	172
		20	1.23	23	
		25	1.19	19	
		35	1.12	12	
		83	1.04	4	
Al_2Cu/ EG	0.5	9	1.45	45	172
		20	1.33	33	
		25	1.27	27	
		35	1.2	20	
		83	1.10	10	
Al_2O_3/ Water	2	12	1.036	3.6	174
		16	1.058	5.8	
		282	1.115	11.5	
Al_2O_3/ Water	14	36	1.13	13	169
		47	1.17	17	
Al/EG	1	10	1.11	11	175
		45	1.06	6	
		150	1.02	2	
Al/ Water	1	10	1.07	7	
		45	1.05	5	
		150	1.023	2.3	
Al_2O_3/ Water	0.51	20	1.06	6	176
		50	1.05	5	

		100	1.04	4	
α- SiC/ Water	4.1	16	1.08	8	177
		29	1.098	9.8	
		66	1.118	11.8	
		90	1.124	12.4	
Fe_3O_4/ Kerosene	5.5	2.8	1.05	5	178
		3.6	1.10	10	
		6.1	1.17	17	
		8.2	1.19	19	
		9.5	1.22	22	
SiO_2/ Water	8	10	1.08	8	179
		20	1.09	9	
		40	1.09	9	
		60	1.11	11	
Al_2O_3/ Water	0.5	13	1.075	7.5	180
		20	1.020	2	
Cu/ EG	0.03	12	1.15	15	158
	0.0035	3	1.038	3.8	
Al_2O_3/ Water	0.51	72	1	0	181
		115	1.02	2	
		137	1.03	0.3	

A decrease in k with decrease in particle size (in the size range of 2−40 nm) was reported in water based gold nanofluids.[182] Similarly, a decrease in k with decrease in particle size from 2.8 – 9.5 nm was observed in kerosene based Fe_3O_4 nanofluid.[178] **Table 1.3** shows the summary of the reported values of k/k_f as a function of size and concentration for different nanofluids. A plot of the k/k_f as a function of particle size reported in different nanofluids is shown in **Fig. 1.11.**

1.3.2.3 Effect of Particle Aspect Ratio

Several studies showed an increase in k enhancement with increase in particle aspect ratio.[27, 160, 163, 166, 183-185] For the same particle loading of 5 vol% rod shaped TiO_2 nanoparticle in water with an aspect ratio of 4 showed an enhancement of 32 % where as nanofluids containing spherical nanoparticles of diameter 15 nm showed an enhancement of 29 %.[27] An increase in *k* with increase in nanotube length was reported in water based MWCNT.[166] The *k* enhancement was about 14, 18, 38 and 48 % for the nanotube length of 0.5, 1, 1.7 and 5 µm, respectively. The *k* studies in Al_2O_3 nanofluids with different particle morphologies showed that the *k* enhancement coefficients follow the sequence cylinders> bricks >platelets~blades.[185]

Table 1.4: The reported values of k/k_f as a function of particle morphology for different nanofluids.

Nanoparticle/ Base fluid	Concentration (φ %)	Shape/Aspect ratio (AR)	k/k_f	% enhancement	Ref
TiO_2/ Water	5	15 nm	1.29	29	27
		10 nm × 40nm^2	1.32	32	
MWCNT/ Water	0.24	0.5 µm length	1.14	14	166
		1 µm length	1.18	18	
		1.7 µm length	1.38	38	
		5 µm length	1.48	48	
CNT/ Water	1	18.8 AR	1.43	43	186
		666 AR	2.08	108	
Al_2O_3	1	10 nm	1.039	3.9	147
		80×10 nm^2	1.051	5.1	
CuO/ Engine oil (SAE 20W50)	0.28	Sphere	1.045	4.5	187
		Nanorhombic	1.053	5.3	
		Nanorod	1.061	6.1	
MWCNT/ Water	1	-	1.35	35	160
DWCNT/ Water			1.03	3	
CNT		35 AR	1.32	32	163
SiC/ Water	4	Sphere	1.10		183
		Cylinder	1.20		
CNF/ Water	2.5	10 (Avg. Dia)	1.08	8	184
		20 (Avg. Dia)	1.06	6	
		40 (Avg. Dia)	1.025	2.5	
Al_2O_3/ Water/EG	7	Cylinders	1.26	26	185
		Bricks	1.24	24	
		Platelets	1.18	18	
		Blades			

The observed *k* enhancement of nanorods Al_2O_3/PAO was greater than that of PAO based alumina nanofluids having spherical particles.[147] For the same particle loading of 1 vol%, the CNT nanofluids with an aspect ratio of 666 showed a *k* enhancement 2.08 where as CNT with an aspect ratio of 18.8 showed a k/k_f of 1.43.[186] These experimental results suggest that particle having higher aspect ratio can give a higher *k* enhancement than the spherical particle due to the effective heat transfer along the length of the rod shaped particle**. Table 1.4** shows the summary of the reported values of k/k_f as a function of particle morphology for different nanofluids.

1.3.2.4 Effect of Aggregation

On aggregation aspect, recent studies reveal that the effective heat conduction through nanoparticle agglomerates can result in an enhanced *k* in nanofluids,[11, 59, 151, 188-191] and the sedimentation of aggregates in base fluids, results in a lower *k*.[141, 164] Water based untreated diamond nanofluids showed a decrease in *k* with time, whereas plasma treated stable diamond nanofluids showed a time independent *k*.[192] Nasiri et al.[193] observed a decrease in *k* with time due to the formation of agglomerates. With time, a decrease in *k* is observed in water based Cu and CNT nanofluids due to sedimentation and agglomeration.[141] Timofeeva et al.[10] showed a larger *k* with time in water based Al_2O_3 nanofluids due to the formation of larger agglomerates. A time independent *k* was observed in ethylene glycol based ZnO,[194] graphene oxide nanofluids[130] and kerosene based Fe_3O_4 nanofluids.[150]

Conduction through Linear Aggregates (Controlled Aggregation): Recent studies showed that the conduction through linear agglomerates of nanoparticle in basefluids can lead to a dramatic enhancement of *k*.[11, 47, 178, 195, 196] Philip et al.[11] observed 300 % *k* enhancement in kerosene based Fe_3O_4 nanofluid at a particle loading of 6.3 vol%. at an applied field of 80 G. The observed enhancement in *k* was shown to be due to the effective heat transport through chainlike aggregates of the nanoparticle. Similarly 130 % *k* enhancement was observed in kerosene based Fe_3O_4 (0.0171 φ%) nanofluids at an applied magnetic field of 350 G.[197] Li et al.[195] observed an enhancement of k/k_f in water based magnetic nanofluids of size 26 nm in the presence of an external magnetic field along the field direction. Horton et al.[196] showed that the thermal conductivity of magnetic-metal-coated carbon nanotubes can significantly enhance under applied magnetic field due to the controlled aggregation of magnetic nanoparticle along the field direction. Similar results were reported in Ni and Fe_2O_3 incorporated in water based SWCNT.[9, 189, 191] Recent studies shows that the stable nanofluids exhibits thermal conductivity within EMT prediction whereas aggregating nanofluids shows enhancement beyond EMT predictions.[148]

1.3.2.5 Effect of Nanoinclusions

In general the thermal conductivity of the nanofluid will be higher when the dispersed nanoparticles have a higher *k*.[140, 142, 175, 198, 199] Shima et al.[199] showed the effect of suspended particle *k* on enhancement in nanofluids. They observed that in the dilute limit, the thermal conductivity of nanoparticle does not influence the *k* enhancement and the *k* of nanofluids is solely dependent on the volume fraction of the nanoparticle. Some researchers reported that the thermal conductivity of the nanoparticle is not a primary factor for the observed enhancement in nanofluid *k*.[22, 29, 157, 200] For the same particle loading of 4 vol%, water based Fe_3O_4 nanofluids exhibited 38 % *k* enhancement, while water based nanofluids containing TiO_2 or Al_2O_3 nanoparticles showed 30 % enhancement even though bulk Fe_3O_4 crystal has a lower *k* than Al_2O_3, CuO, and TiO_2 crystals.[157] Studies on water based CuO, MWCNT and SiO_2 nanofluids showed that MWCNT has the highest k enhancement and SiO_2 the lowest *k* enhancement.[140] For the same concentration of nanoparticle (1 vol%), the *k* enhancement for water based TiO_2 was higher than that of Al_2O_3 nanofluids, though the bulk *k* is higher for Al_2O_3 nanoparticle.[142]

Table 1.5: The reported values of k/k_f for nanofluids having different nanoparticle.

Base fluid	Concentration (φ %)	Nanoparticle	Bulk *k* (W/m.K)	k/k_f	% enhancement	Ref
Water	1	SiO_2	1.4	1.03	3	140
		MWCNT	6600	1.11	11	
		CuO	385	1.05	5	
Water	4	Fe_3O_4	9	1.38	38	157
		TiO_2	15	1.3	30	
		Al_2O_3	35	1.3	30	
Water	1	Al_2O_3	35	1.14	14	142
		TiO_2	15	1.03	3	
Water	1.8	Ag_2Al		2.4	140	201
		Al_2Cu		2.2	120	
EG	1	Cu	386	1.60	60	202
		Fe	9	1.27	27	
Water	0.09	Cu	385	1.15	15	203
	0.2	Al_2O_3	35	1.18	18	
Water	4	Al_2O_3	35	1.08	8	152
		SiO_2	1.4	1.09	9	
		TiO_2	15	1.15	15	
Kerosene	0.01	Fe_3O_4	9	1.02	2	199
		Ag	429	1.04	4	
Hexadecane	0.01	Fe_3O_4	9	1.05	5	
		Ag	429	1.05	5	
Water	2	Al_2O_3	35	1.045		175
Transformer oil		CuO	385	1.11		
EG		Cu		1.17		

Chopkar et al.[201] reported that for the same particle concentration, the *k* enhancement for water based Ag_2Al nanofluid is slightly more than Ag_2Cu nanoparticle suspensions. Sinha et al.[202] reported a *k* enhancement of 48-70 % for the same concentration of 1 vol% the Cu nanofluids whereas Fe nanofluids showed a *k* enhancement of around 21-33 %. Wang et al.[203] reported that water based Cu nanofluid have a higher *k* enhancement compared to water based Al_2O_3 nanofluids, and the reason for the larger *k* enhancement in Cu nanofluid was attributed to the higher *k* of copper nanoparticles. Patel et al.[175] observed that metallic nanofluids exhibit higher *k* enhancement than the oxide nanofluids, which was proved to be wrong later. **Table 1.5** summarizes of the reported values of k/k_f for nanofluids with different nanoparticle.

1.3.1.6 Effect of Additives

Most of the reports show that the optimum concentration of additives will enhance the *k* of nanofluids.[38, 203, 204]

Table 1.6: The reported values of k/k_f for nanofluids with different additives

Nanoparticle	Base fluid	Concentration (φ %)	Additives	k/k_f	% enhancement	Ref
CuO	EG	4	Thioglycolic acid	1.4	40	38
			Without acid	1.1	10	
Al_2O_3	Water	0.08	SDBS	1.09	9	203
Cu		0.033		1.12	12	
Al_2O_3	Water	0.5	SDS (0 wt%)	1.05	8	180
			SDS (0.2 wt%)	1.06	6	
			SDS (1 wt%)	1.07	7	
			SDS (2 wt%)	1.05	5	
			PVA (0 wt%)	1.07	7	
			PVA (0.2 wt%)	1.03	3	
			PVA (1 wt%)	1.07	7	
			PVA (1.5 wt%)	1.06	6	
			PVA (2 wt%)	1.04	4	
Al_2O_3	Water	4	NP9	1.18	18	205
			SDS	1.13	13	
SiO_2	Water	4	NP9	1.09	9	
			CTAB	1.10	10	

Eastman et al.[38] observed an enhancement in *k* in ethylene glycol based Cu nanofluid stabilized with thioglycolic acid, compared to non acid-containing nanofluids. However, it was reported that, CTAB has no effect on *k* enhancement in water based CNT nanofluids.[160] Another report showed that at an optimum concentration of polyisobutene succinimide (3 wt %) provide a better *k* enhancment in PAO based MWCNT nanofluid.[163] Wang et al.[203] also reported that an optimal concentration of sodium dodecylbenzenesulfonate (SDBS) can result in an enhanced k in water based Cu and Al_2O_3 nanofluids. **Table 1.6** summarizes the reported values of k/k_f for nanofluids with different additives.

1.3.2.7 Effect of Temperature

A water based Al_2O_3 nanofluids (1 vol%) showed a *k* enhancement from 2 to 10 % as the temperature was increased from 21 to 50 °C.[206] The increase in *k* with increase in temperature from 10 to 60 ^oC was observed water and ethylene glycol based Al_2O_3 nanofluid (5 vol%).[10] The temperature independent *k* enhancement was also reported in ethylene glycol and water based nanofluids.[143, 166] A temperature independent *k* enhancement was observed in water based SiC nanofluids.[146] Shima et al.[207] showed that for both aqueous and non-aqueous ferrofluids with average particle diameter of 6 nm over the temperature range of 25 to 50 °C, *k* was independent of temperature. Their findings show that the microconvection has a less dominant role on thermal conductivity enhancement of nanofluids. The *k* enhancement in hexadecane (HD) based Al_2O_3 was constant in the temperature range 25 to 50 ^oC.[208] Similarly, a temperature independent *k* enhancement was observed for kerosene based Fe_3O_4 nanofluids.[150, 151] There are reports showing a decrease in *k* with increase in temperature in water based TiO_2[209] and hexane based Bi_2Te_3 nanorods.[17] Aqueous nanofluids over the temperature range of 25 to 50 °C showed an increase in *k* with temperature whereas a decrease in *k* was observed in non-aqueous (kerosene and hexadecane based) nanofluids.[207] Thermal conductivity of dibenzyl toluene based MoS_2 nanofluids was found to increase from 1.175 to 1.375 as the temperature increased from 40 – 180 °C.[210] Ghozatloo et al. [211] observed that the *k* of water based surface modified CNT increases with increase in temperature. Ethylene glycol based graphene nanofluids showed a *k* enhancement quite independent of temperature.[156] EG based nanodiamond nanofluid also showed a temperature independent *k*.[149] **Table 1.7** gives a summary of the reported values of k/k_f as a function of temperature for different nanofluids.

Table 1.7: Summary of the studies on the effect of temperature on thermal conductivity in nanofluids

Nanoparticle/ Base fluid	Concentration (φ %)	Temperature (°C)	k/k_f	% enhancement	Ref
Al_2O_3/ Water	1	21	1.02	2	206
		50	1.10	10	
Bi_2Te_3/ HD		10	1.13	13	17
		24	1.11	11	
		36	1.09	9	
		47	1.08	8	
Al_2O_3/ Water	5	20	1.08	8	10
		60	1.13	12	
CNT/ Water	0.28	10	1.13	13	143
		65			
MWCNT/ Water	1.45	15	1.36	36	166
		75	1.68	68	
SiC/ Water	2	25	1.09	9	146
		70			
Al_2O_3/ HD	2	2	1.11	11	208
		23	1.068	6.8	
		32			
		42			
		52			
TiO_2/Water	1	15	1.01	1	209
		25	1.02	2	
		35	1.02	2	

Fe_3O_4/ Kerosene	4.1	25	1.19	19	151
		75			
Fe_3O_4/ Kerosene	1	10	1.35	35	150
		60			
Fe_3O_4/ Kerosene	0.095	25	1.3	30	207
		50			
Fe_3O_4/ Hexadecane	0.061	25	1.2	20	
		50			
Fe_3O_4/ Water	0.0102	25	1.03	3	
		50			
Al/ Water/ EG	1	20	1.055	5.5	175
		30	1.065	6.5	
		40	1.08	8	
		50	1.1	10	
Al/ EG	1	20	1.023	2.3	
		30	1.033	3.3	
		40	1.041	4.1	
		50	1.054	5.4	
Cu/ Water	1	20	1.113	11.3	
		30	1.156	15.6	
		40	1.184	18.4	
		50	1.194	19.4	
Cu/ TO	1	20	1.07	7	
		30	1.114	11.4	
		40	1.13	13	
		50	1.15	15	
ND/ MO	0.5	20	1.06	6	149
		40			
		60			
		80	1.05	5	
		100	1.04	4	
MoS_2	Dibenzyl toluene	40	1.175	17.5	210
		180	1.375	37.5	
ND-Ni/ Water	3.03	20	1.12	12	134
		60	1.32	32	
ND-Ni/EG	3.03	20	1.05	5	134
		60	1.153	15.3	
Graphite/ EG	0.2	25	1.119	11.9	156
		35	1.113	11.3	
		45	1.123	12.3	
		55	1.137	13.7	
Cu/ N-tetradecane	0.01	33	1.05	5	154
		173	1.65	65	

In addition to the above mentioned factors, pH of the nanofluids,[40, 203, 212, 213] sonication time[6, 63, 159, 163, 198, 214-216] and basefluid properties[63, 131, 140, 143, 147, 190, 198, 217] also influence on *k* enhancement in nanofluids.

1.3.3. Specific Heat Capacity of Nanofluid

Although the addition of nanoparticles to a base fluid enhances its thermal conductivity, it sometimes decreases the heat capacity of nanofluid,[218] which hampers the effective use of such nanofluids as a coolant. To make the heat transfer processes cost effective and clean, significant increase in the heat capacity of the heat transfer fluids is needed. However, many studies show no increase in heat capacity larger than the experimental error upon the addition of particles.[219] For effective utilization of nanofluids for practical heat transfer applications, a synergetic balance of various thermophysical properties such as thermal conductivity, viscosity, heat capacity, density and diffusion coefficient is a prerequisite. There are multiple reports on a strong[220-222] and weak[218] dependence of C_p on the volume fraction of nanoparticles. There are also some reports on a decrease in the heat capacity with increase in volume fraction.[220-222] Though the thermal properties of nanofluids are investigated intensely, the studies on heat capacity of nanofluids are scarce.[221, 223, 224] A knowledge of specific heat capacity and thermal conductivity is important in order to understand the heat transfer properties of nanofluids. Studies on specific heat capacity kerosene based iron oxide nanofluids showed a decrease in the heat capacity of nanofluid with increase in volume concentration and an increase with temperature.[218] Such a behavior was also observed in CuO nanofluids and water-based Al_2O_3 nanofluid.[220] Ho et al.[225] reported a highest enhancement of specific heat capacity of 19.9 % in Hitec melt at an optimal concentration of 0.063 wt % of Al_2O_3 nanoparticles. A specific heat capacity enhancement of 50 % in 0.6

wt% of graphite nanoparticle fibers suspended in polyalphaolefin was observed.[226] Increase in heat capacity with increase concentration of nanoparticle were reported by many researchers.[227, 228] Specific heat capacity of nanofluids is also dependent on size of dispersed particles.[229, 230] Xiong et al. [229] reported that specific heat capacity is more for small size particle (5 nm size Ag nanoparticle) compared to the bigger size particle (50 nm). In the case of CuO nanoparticle the specific heat capacity of nanoparticle increased with decrease in particle size.[223] A decrease in the specific heat capacity with increase in the nanoparticle size was reported by Novotny et al.[230] Unlike large thermal conductivity contrast between the suspended particles and base fluids, the C_p contrast between them was not significant on addition of particle loading is not anticipated. As the studies on various parameters affecting C_p of nanofluid are limited, a systematic study on the effect of volume fraction, properties of dispersed particle (density, thermal conductivity, morphology etc.) on the specific heat capacity of nanofluids is warranted for a better understanding of their utility in heat transfer applications such as concentrating solar power and waste heat recovery.

1.3.4 Thermal Conductivity of Phase Change Materials

From the initial focus on thermophysical properties of nanofluids (both experimental and theoretical modeling), the attention is now shifted to tailoring of novel nanofluids with large thermal conductivities and their applications. To overcome the limitations of traditional heat transfer media, phase change materials (PCMs) are being considered as effective media for thermal energy storage.[231] The use of organic phase change materials as continuous phases (base fluids) has attracted much attention in the recent years due to their self nucleating properties, chemical stability, high heat of fusion, safe and non reactive nature and ability to freeze without much super cooling.[232] The energy charge/discharge rate is one of the most crucial factors to meet the cooling and heating capacity demand and the storage size. One of the drawbacks of PCM is its poor thermal conductivity which hampers the fast thermal charging and discharging during the phase change. To enhance the thermal conductivity of pure PCM, several methods have been attempted, e.g. placing a metal structure in PCM,[233] impregnating porous material[234] and dispersing high thermal conductivity particles in PCM.[235] Though there are some studies[236-238] on thermal conductivity of PCM with nanoinclusion in the recent years, there are no reports on the effect of aggregation of such nanoinclusions on the thermal conductivity of PCMs. A suitable phase change temperature and a large melting enthalpy are two major requirements of a phase change material. Sutherland[239] and Powell[240] observed that a sudden increase in the thermal conductivity of n-octadecance shows when it transformed from liquid to solid state. Lyeo et al.[241] showed that the thermal conductivity of thin film of the phase-change material $Ge_2Sb_2Te_5$ increases irreversibly with increasing temperature and undergoes large changes with phase transformations. Molecular dynamic studies on PCM showed that, upon crystallization a nanocrystalline structure develops leading to a thermal conductivity doubling.[242] Zheng et al.[237] reported a large contrast in electrical and thermal conductivities using first-order phase transitions in percolated composite materials. Harish et al.[238] reported a large contrast in the thermal conductivity enhancement of phase change alkane in liquid and solid state with single-walled carbon nanotube inclusions. Tunable electrical and thermal conductivity through freezing rate control in hexadecane based nanocomposite were reported by Schiffres et al.[243] Thermal conductivity studies on CNT/Hexadecane composites showed a 3 times increment in thermal conductivity at the phase change point of hexadecane.[236] Though there are several studies on thermal conductivity of PCM with nanoinclusion in the recent years, the effect of clusters on the thermal conductivity of PCMs is still unclear.

1.4 Motivation

The researchers tried to explain the reported anomalous enhancement in thermal conductivity in nanofluids by considering mechanisms such as liquid layering at the liquid/particle interface,[2, 244] Brownian motion of nanoparticles,[26, 32] ballistic heat transport [245] and effective heat transfer through nanoparticle clusters.[6, 246] After considering various mechanisms for the observed enhancement in thermal conductivity, one of the most probable mechanisms considered is the effective conduction of heat through percolating aggregating nanoparticle paths.[26, 59] However, there are conflicting reports on the contributions from micro-nano convection and agglomeration of particles.[2] This field has been quite controversial, with multiple reports of anomalous enhancement in thermal conductivity, i.e. many report showing k enhancement well above those predicted from classical models[27, 36, 101, 201, 247], and many other reports of the thermal conductivity increase within the classical Maxwell Mixing model.[11, 14, 246, 248]

One of the grey areas in the understanding of thermal property variations in nanofluids is the role of interfacial resistance and morphology of suspended nanoparticles on k enhancement. The former aspect is extremely important, as suspensions are often stabilized using surface active species. Though the mechanism of stabilization of nanoparticles by surfactants is quite well understood, their precise role on interfacial thermal resistance, on thermal and rheological properties of nanofluids is still unclear.[108, 116, 249-251] Also, aggregation is a very complex issue in nanofluids as subtle changes in the solvent properties and interfacial properties of nanoparticles can affect it. Therefore, a systematic study to understand the effect of interfacial resistance, aggregation and other physico-chemical properties such as viscosity, specific heat capacity and density on thermal conductivity of nanofluid is warranted. To make the heat transfer processes cost effective and clean, a significant increase in the heat capacity of heat transfer fluids is needed. Although the addition of nanoparticles to the base fluid enhances its thermal conductivity, it sometimes decreases the heat capacity of nanofluid,[218] which hampers the effective use of such nanofluids as a coolant. Hence a systematic study on volume fraction, bulk properties of dispersed particle (density, thermal conductivity, morphology etc.) on the specific heat capacity of nanofluids is a prerequisite for the effective utilization of these materials in heat transfer applications such as concentrating solar power and waste heat recovery. Though there are several studies on increase in thermal conductivity of organic phase change materials using different nanoinclusions, the role of aggregation, particle morphology and particle concentration is not yet very clear. This thesis attempts to provide a systematic study on the factors influencing the thermal properties of nanofluids and phase change materials.

1.5 Objectives

The main objectives of the thesis are:

- ❖ To study the role of particle size, volume fraction and morphology, interfacial resistance, density and viscosity on the thermal properties of nanofluids.
- ❖ To study the effect of aggregation of dispersed nanomaterials on the thermal and electrical properties of stable and unstable nanofluid.
- ❖ To probe the role of size, morphology and concentrations of nanoinclusion on specific heat capacity of nanofluids.

- To develop new methodologies to achieve extremely large tunable thermal conductivity in phase change alkane using inverse micellar templating.
- To study the role of aggregation of dispersed nanomaterials on thermal conductivity of phase change alkane using nanoinclusions.

1.6 Overview of the thesis

This thesis consists of 8 chapters and the details of each chapter are summarized. **Chapter 1** gives a brief introduction about the nanofluids and their applications. Literature survey on classical theories, experimental findings in various nanofluids, motivation and the objectives of the present work are also presented. **Chapter 2** describes the details of sample preparation methods, the experimental tools used to study thermal conductivity, rheology, hydrodynamic size and associated properties. **Chapter 3** describes the effect of adsorbing moieties on thermal conductivity, rheology, density, contact angle and refractive index of ‘soft’ and ‘hard’ nanofluids. The role of surface morphology, initial thermal conductivity of solid particles and their number density in base fluids on thermal property enhancement of nanofluids is also discussed. **Chapter 4** describes the thermal conductivity, electrical conductivity (σ), viscosity and refractive index of two non-aggregating nanofluids of γ-Al_2O_3 and SiO_2 and two aggregating nanofluids of TiO_2 and α- Al_2O_3. **Chapter 5** describes the effect of particle size, particle morphology and volume fraction of nanoparticles on the temperature dependent specific heat capacity of metal oxide nanofluids. **Chapter 6** describes a new approach to achieve large tunable thermal conductivity in phase change alkane using inverse micellar templating. **Chapter 7** describes the thermal conductivity changes in phase change alkane incorporated with copper nanowire, multiwalled carbon nanotube, graphite nanofibers and graphene nanoplatelets. **Chapter 8** summarizes the results obtained, conclusions drawn and recommendations for future work.

Chapter II

Materials and Experimental Techniques

2.1 Materials

An anionic surfactant, sodium dodecyl sulfate ($C_{12}H_{25}$-SO_4 Na-, SDS), cationic surfactant, cetyltrimethylammonium bromide (CTAB) and non-ionic surfactants, nonylphenol ethoxylate (NP9 & NP10) were purchased from Sigma and used as such. These surfactants are water soluble at room temperature. For the studies, 16 vol% stock solutions of SDS, CTAB, NP9 and NP10 surfactants were prepared using milli-Q water with a resistivity value of 18.2 MΩ cm, from which different concentrations were prepared. Oil based surfactants, oleylamine, oleic acid (OA), a monounsaturated fatty acid ($C_{18}H_{34}O_2$), dioctyl sodium sulfosuccinate ($C_{20}H_{37}NaO_7S$, AOT) and sorbitan Oleate ($C_{24}H_{44}O_6$, Span 80) were also purchased from Sigma, and used without further purification. For the studies, stock solutions of OA, AOT and Span 80 surfactants were prepared in n-hexadecane, from which different concentrations were prepared. The molecular structure of the surfactants used are shown in **Fig. 2.1** Graphite nanofiber (GNF) purchased from Nanoamor (USA), had an outer diameter of 200-600 nm, length of 5-50 μm and purity > 95 %. Multiwalled carbon nanotubes purchased from Nanoamor had an outer diameter < 8 nm and length 10-30 μm. Copper nanowire (CuNW) and Graphene nanoplatelets (GNP) in powder form were purchased from Reinste.

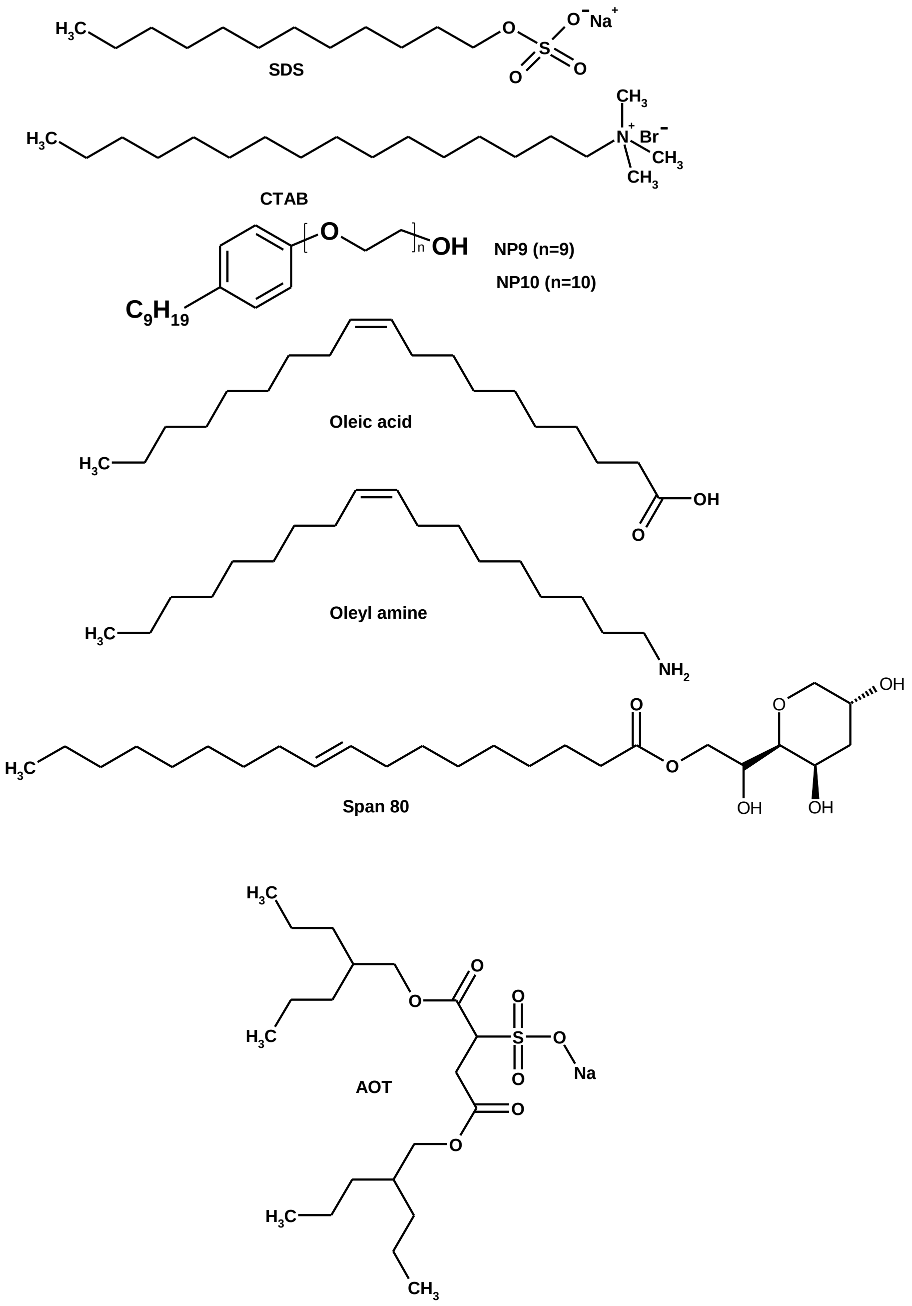

Figure 2.1: Molecular structure of surfactants SDS, CTAB, NP9 & NP10, Oleic acid, oleylamine, Span 80 and AOT.

The former has an outer diameter of 50 nm and length 10 – 50 µm and the latter has a lateral size of 2 µm and thickness in the range of 1 – 4 nm. The TEM and SEM images of the nanoinclusions CuNW, GNP, MWCNT and GNF are shown in **Fig. 2.2 (a-d)**.

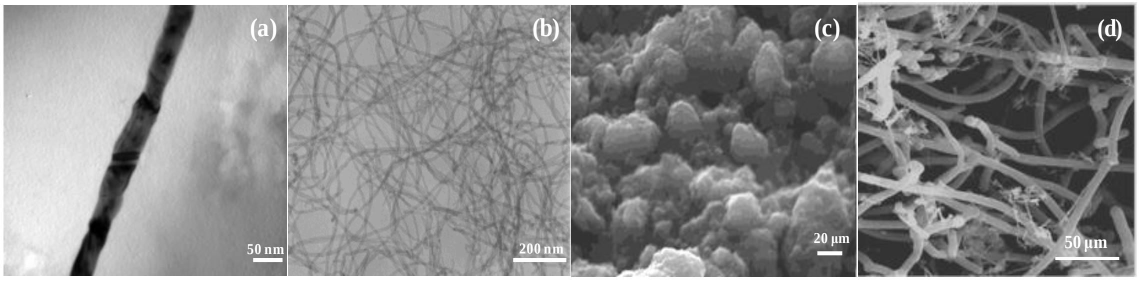

Figure 2.2: TEM images of (a) Copper nanowire, (b) Multi walled carbon nanotube and SEM images of (c) Graphene nanoplatelets and (d) Graphite nanofibres.

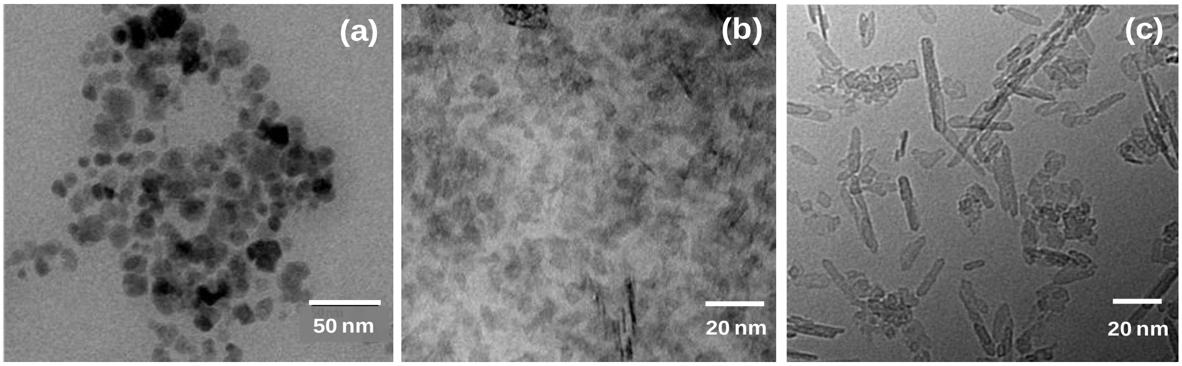

Figure 2.3: TEM images of the (a) Fe_3O_4[207] (b) Al_2O_3 nano spheres[147] and (c) Al_2O_3 nano rods[147] nanoparticles.

The water based γ- Al_2O_3 and TiO_2 nanofluids were purchased from Numex Private Limited and aqueous SiO_2 and α- Al_2O_3 nanofluid were purchased from Chempure Private Limited. The Al_2O_3 nanoparticles dispersed in polyalphaolefin (PAO) was obtained from Sasol and used as such. The Al_2O_3 nanorods (NR) with an aspect ratio of 8 and nanospheres (NS) of size 10 nm dispersed in PAO were stabilized using a surfactant solsperse 21000 (Lubrizol Chemical). Kerosene based Fe_3O_4 nanofluids were synthesized in our lab.[252] The TEM images of nanoparticles, nanorods and nanospheres are shown in **Fig. 2.3 (a-c).**

2.1.1 Preparation of Ferrofluid

For kerosene based nanofluids, Fe_3O_4 nanoparticles were prepared by chemical coprecipitation technique.[207, 252] The details are briefly discussed. The freshly prepared iron salt solutions of 0.2 M $FeCl_2.4H_2O$ and 0.4 M $FeCl_3.6H_2O$ were mixed at 1:1 ratio at a constant stirring speed of 1000 rpm. After the addition of ammonium solution, the pH of the solution reached a value of 10. When the solution turned black, 20 mL of oleic acid was added and the dispersion pH was adjusted to 9.5 with the temperature increased to 70 °C. At the same pH, temperature and stirring speed, the solution was kept for 30 min to finish the coating process. After this step, the temperature was increased to 79 °C in order to eliminate the excess ammonia and the protonation of adsorbed and un-adsorbed ammonium oleate as oleic acid. The surfactant coated particles were washed with triply distilled water at 60 °C, until the pH became 7 to remove the ionic impurities and later dispersed in hexane. The hexane dispersion was treated with acetone to induce aggregation of particles. The aggregated particles were then separated from the dispersion by centrifugation at 2500 rpm for 30 min. The precipitated magnetite nanoparticles were again dispersed in hexane for further treatment. The hexane, acetone mixture washing procedure was repeated again to remove excess surfactant in the dispersion. The surfactant-coated Fe_3O_4 nanoparticles were dried at 35 °C for 48 hours in inert atmosphere and the dried particles were dispersed in kerosene.[252]

The Fe_3O_4 nanoparticles of different particle sizes were synthesized by changing the solvent polarity during chemical coprecipitation using a mixed solvent of ethanol and water at four different ratios of 20:80; 40:60, 50:50 and 60:40.[252, 253]

2.1.2 Preparation of Dispersion of Nanoparticles in Hexadecane

The dispersions of CuNW and GNP in hexadecane were prepared by sonication using horn sonicator (Sonic Vibra-Cell) for 2 hours at 30 % amplitude of power. The dispersions of MWCNTs and GNFs in the PCM liquid were produced by two methods. In method I, 0.0038 φ nanomaterials was added to 0.16 φ of the already prepared surfactant solution (Span 80) and the dispersion was sonicated by a horn sonicator for 30 min at 30 % amplitude of power. In method 2, the surface modification of the nanomaterial was performed in a mixture of two strong acids, concentrated sulfuric acid (98 %) and nitric acid (70 %) at 3:1 volume ratio[254]. The nanomaterial was first added to the acid mixture and sonicated at ~ 65 °C for 7 h. After cooling the sample to room temperature, the acid treated dispersion was diluted with Milli Q water and the nanomaterial was centrifuged for 30 mins at 10,000 rpm. The solid nanomaterials were dried at 100 °C in an oven for 1 h. Then the surface-modified GNFs were re-dispersed in hexadecane by horn sonication for 30 mins at 30 % amplitude of power with the addition of 2 wt% oleylamine as surfactant.

The dispersions of CuNW, MWCNTs and GNFs in the hexadecane were obtained as follows. CuNW nanofluid was prepared by dispersing 0.33 wt% of CuNW in hexadecane and the dispersion was sonicated by a horn sonicator for 30 mins at 30 % amplitude of power. In the case of MWCNT, 0.5 wt% of nanomaterial was dispersed in hexadecane and sonicated under the same condition. The Al_2O_3 nanorods and nanospheres dispersed in polyalphaolefin were stabilized using a surfactant solsperse 21000 (Lubrizol Chemical).

2.2 Experimental Techniques

2.2.1 Thermal Conductivity Measurements

Different techniques such as transient hot wire method (THW), thermal constants analyzer (TCA), steady state parallel plate method and 3ω method have been used for measuring the thermal conductivity of nanofluids. Among these techniques, the transient hot-wire method has been used most extensively.

2.2.1.1 Transient Hot Wire Method

The Transient Hot Wire method[255] is based upon using a long, thin platinum wire as a dual line heat source and the temperature sensor. This is possible due to the relatively unique relationship between the temperature and thermal characteristics of platinum. The sensor is immersed in the fluid whose thermal conductivity is to be measured and is heated up by a step increase in the electric power through resistive heating. Heat from the sensor is transferred to the surrounding fluid through conduction. Simultaneously, the relative change in resistivity of the wire is measured through four wire resistive measurement system. The thermal conductivity of the fluid is obtained from the relative change in resistivity of the wire using Fourier's law,

$$\Delta T = \frac{q}{4\pi k} E_i\left(\frac{-r^2}{4Dt}\right) \quad 0 < t < t_1 \tag{2. 1}$$

where, r is the distance from the line at which temperature is measured, D is the thermal diffusivity and E_i is the exponential integral which is given as,

$$-E_i(\alpha) = \int_{\alpha}^{\infty} \frac{1}{u}\exp(-u)du = -\beta - \ln\alpha - \frac{\alpha^2}{4} + \ldots\ldots \tag{2. 2}$$

where, β =0.5772… is the Euler's constant and $\alpha = r^2/4Dt$ is the temperature coefficient.

If α becomes negligibly small when r is small and D is large, **Eqn. 2.1** becomes

$$\Delta T \approx \frac{q}{4\pi k}\left[-\beta - \ln\left(\frac{r^2}{4Dt}\right)\right] = \frac{q}{4\pi k}\left[\ln t - \ln\left(\frac{r^2}{4DC_E}\right)\right] \tag{2. 3}$$

where $C_E = \exp\beta$. After some delay, ΔT versus $\ln t$ becomes a straight line with slope equal to $q/4\pi k$. Therefore k can be computed from

$$k = \left[\frac{q}{4\pi(\Delta T_2 - \Delta T_1)}\right]\ln\left(\frac{t_2}{t_1}\right) \tag{2. 4}$$

Fig. 2.4 shows the schematics of transient hot wire experimental setup. R_1, R_2 and R_3 are the resistors and R_w is the resistance in the nanofluid

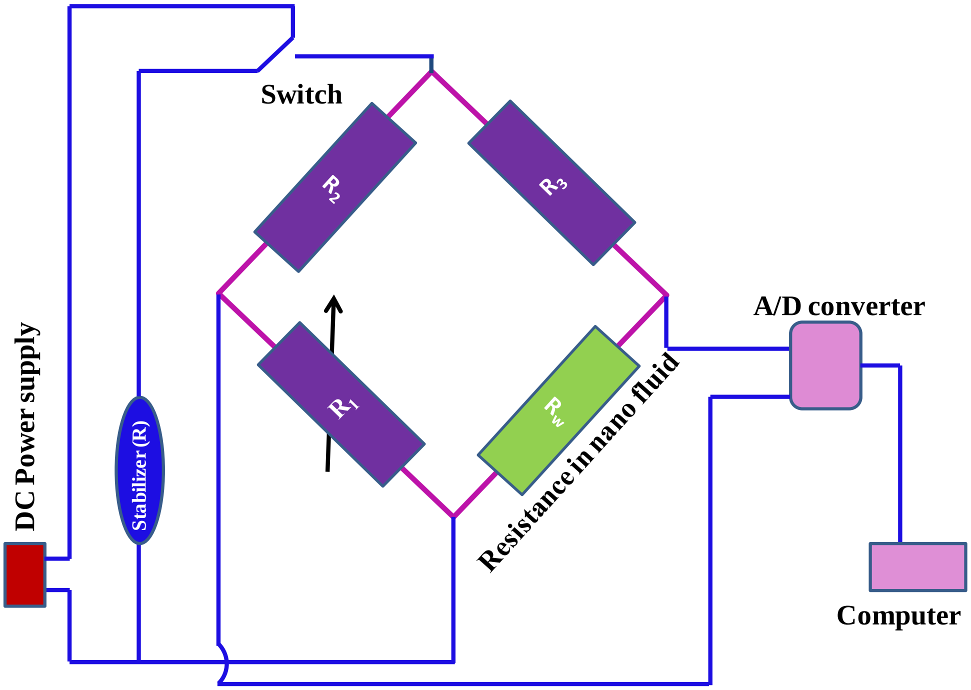

Figure 2.4: Schematics of transient hot wire experimental setup.

2.2.1.2 Thermal Constants Analyzer Techniques

Thermal Constants Analyzer technique is also used to measure the thermal conductivity of nanofluids.[186, 256-258] The thermal constants analyzer utilizes the transient plane source (TPS) theory to calculate the thermal conductivity of nanofluids. In this method, the TPS acts as both sensor and the heat source. In TPS method the thermal conductivity is measured using Fourier law of heat conduction. The main advantages are it is fast, it can measure wide ranges of thermal conductivity (0.02 – 200 W/mK), no sample preparation is required and sample size can be flexible.

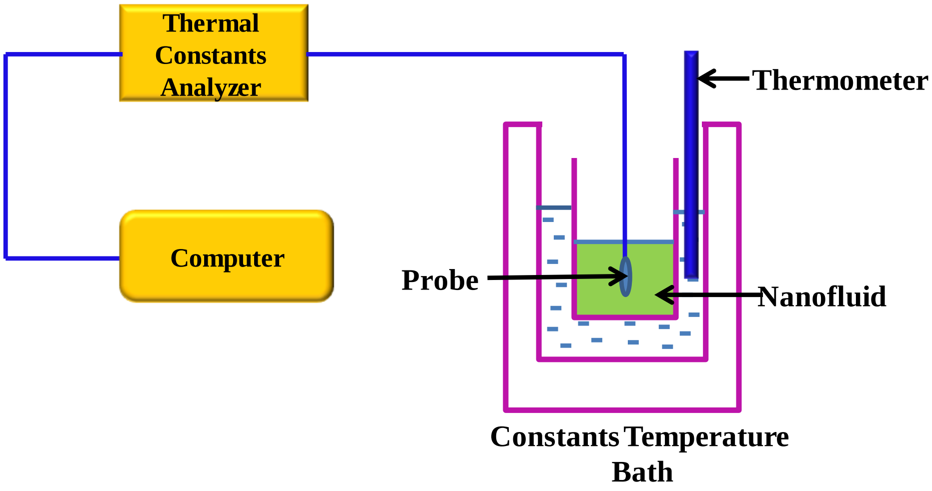

Figure 2.5 : Schematic representation of the experimental setup for Thermal constant analyzer measurement.

The experimental setup of measuring thermal conductivity of nanofluid using TCA is shown in **Fig. 2.7.** It consists of thermal constant analyzer, a vessel, a temperature bath and a thermometer. The probe is immersed vertically in the vessel containing the nanofluid which is kept in a constant temperature bath and the temperature sensor is immersed in the vessel to measure the temperature of the nanofluid. By measuring the resistance of the probe, the thermal conductivity of the nanofluid is determined. When a constant electric power is supplied to the probe, the temperature rise of the probe $\Delta T(\tau)$ is measured by the probe resistance with time $R_p(\tau)$ as,

$$\Delta T(\tau) = \frac{1}{\alpha}\left[\frac{R_p(\tau)}{R_0} - 1\right] \tag{2. 5}$$

where, R_0 is the electric resistance of the probe when $\tau = 0$ and τ is the variable on the time of electrification, $\tau = \sqrt{\frac{tD}{r_p^2}}$, where t is the measuring time and r_p is the radius of the probe. According to Fourier law, in case of no natural convection of a fluid, $\Delta T(\tau)$ is given as,

$$\Delta T(\tau) = \frac{W}{\pi^{1.5} r_p k} D(\tau) \tag{2. 6}$$

where,

$$D(\tau) = \int_0^{\tau} d\sigma\left(\sigma^{-2}\right)\int_0^1 v dv \int_0^1 u du \times \exp\left(\frac{-u^2 - v^2}{4\sigma^2}\right) I_0\left(\frac{uv}{2\sigma^2}\right) \tag{2. 7}$$

where, W is the electric power supplied to the probe, I_0 is the modified Bessel function and $D(\tau)$ is a geometric function. In such case the experimental data can be fitted with the above equation and the thermal conductivity of the nanofluid is obtained from the slope of the curve. If natural convection of the fluid occurs, the thermal conductivity will vary with $D(t)$, and the result is incorrect. In this case, the thermal constants analyzer automatically gives an alarm to avoid using the unreliable result. In order to avoid the happening of natural convection, the parameters of the analyzer should be controlled properly.

2.2.1.3 Steady-State Parallel Plate Method

Challoner et al.[259] developed the steady state parallel-plate method. A schematic representation of the experimental setup is shown in the **Fig. 2.6**, where the sample is placed between the two round parallel copper plates.

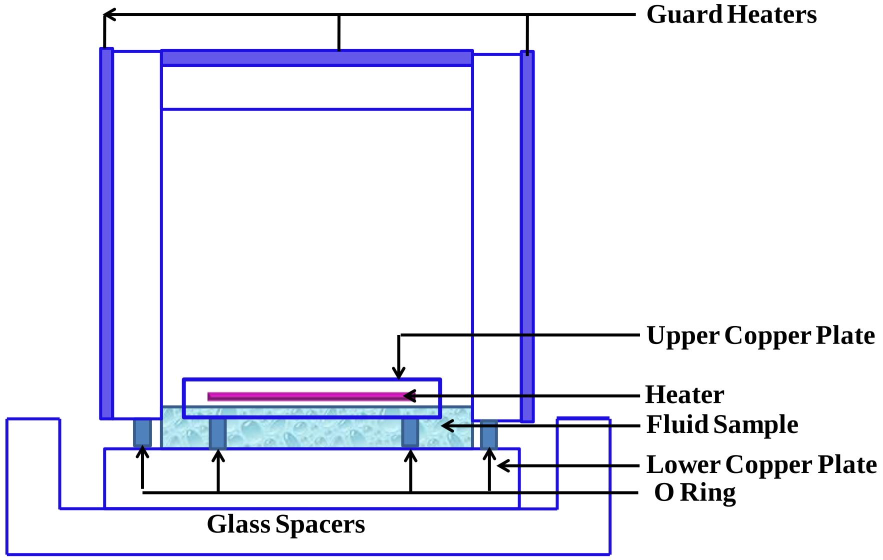

Figure 2.6: Schematic of the experimental setup for steady-state parallel-plate method.

The temperature increase in each thermocouple is measured accurately. When the thermocouples are at the same temperature, the difference in temperature readings is minimized. As the total heat supplied by the main heater flows through the liquid between the upper and lower copper plates, the overall thermal conductivity across the two copper plates, including the effect of the glass spacer, is calculated from the one-dimensional heat conduction equation relating the power $\dot{q}$ of the main heater, the temperature difference ΔT between the two copper plates, and the geometry of the liquid cell as,

$$k = \frac{\dot{q} L_g}{S \Delta T} \tag{2. 8}$$

where, L_g is the thickness of the glass spacer between the two copper plates and S is the cross- sectional area of the top copper plate. The thermal conductivity of the liquid is calculated by the **Eqn. (2.9)**

$$k_e = \frac{kS - k_g S_g}{S - S_g} \tag{2. 9}$$

where, k_g and S_g are the thermal conductivity of the glass spacer and cross- sectional area of the glass spacer, respectively. In order to avoid heat loss from the fluid to the surrounding, guard heaters are used to maintain a constant temperature of the fluid.

2.2.1.3 3ω Method

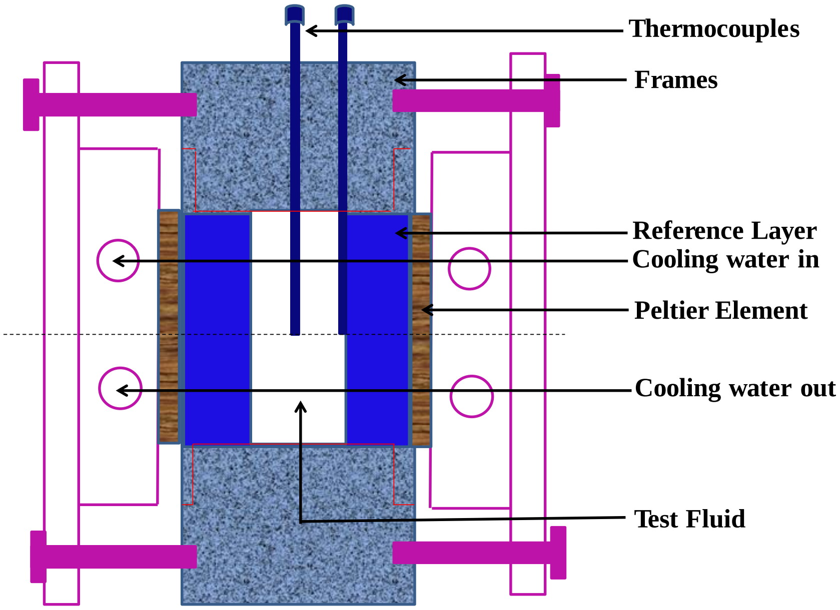

Figure 2.7 : Schematic of the experimental setup for 3ω method.

In the 3ω method, a single element is used as a heat source which acts as the heater and the sensor.[260] A sinusoidal current of frequency ω passing through the metal wire generates a heat wave of frequency 2ω which is deduced to the frequency 3ω by the voltage component. The temperature oscillation at a distance r = $(x^2+y^2)^{1/2}$ from an infinitely narrow line-source of heat on the surface of an infinite half-volume is given by,

$$\Delta T(r) = \frac{P}{l\pi k} K_0(qr) \qquad (2.\ 10)$$

where, P/l is the amplitude of the power per unit length generated at a frequency 2ω in the line source of heat and K_0 is the zeroth-order modified Bessel function. The magnitude of the complex quantity, $\frac{1}{q} = \left(\frac{D}{i2\omega}\right)^{1/2}$, is the wavelength of the diffusive thermal well or the thermal penetration depth.

In the limit, $|qr| \langle\langle 1$

$$\Delta T = \frac{P}{l\pi k}\left(\frac{1}{2}\ln\frac{D}{r^2} + \ln 2 - 0.5772 - \frac{1}{2}\ln 2\omega - \frac{i\pi}{4}\right) \qquad (2.\ 11)$$

Either the real or the imaginary part of the temperature oscillations is used to find the thermal conductivity. The temperature oscillation is related to the heat generation by,

$$\Delta T = \frac{P}{l\pi k}\int_0^\infty \frac{\sin^2 kb}{(kb)^2\left(k^2+q^2\right)^{1/2}}dk \qquad (2.\ 12)$$

The 3ω device is fabricated by metal deposition and patterning. The device is connected to metal heaters by electrical wires. A well is created around the heater which contains the nanofluid. The microdevice is placed inside a temperature controller. This method is used for the temperature dependent thermal conductivity studies. The schematic representation of 3ω method is shown in **Fig. 2.7.**

In the present study thermal conductivity was measured using KD2 pro thermal property analyzer from Decagon devices Inc., USA. Here, the thermal conductivity of the nanofluid was measured by monitoring the heat dissipation from a line heat source. The length of the line heat source is 60 mm and the diameter is 1.28 mm. The thermal conductivity range of the probe and the accuracy of the k measurement are 0.02–2 W m^{-1} C^{-1} and 5 %, respectively. The vial, in which the sample is taken, had a diameter of 24 mm. Calibration of the probe was carried out by measuring the thermal conductivities of four standard liquids - water, glycerol, ethylene glycol and kerosene; the measured values are in good agreement with the literature values. The k measurements were made 10 mins after achieving the desired temperature. For measuring the thermal conductivity at different temperatures, the sample vial with the thermal conductivity probe was immersed in a circulating water bath and the temperature of the water bath was maintained within ± 0.1 °C. The entire sample assembly is insulated for temperature gradient and vibrations.

2.2.2 Rheometer

Rheology deals with the deformation and flow of matter. Solids have an ‘elastic’ response, and can resist an applied stress, while fluids do not have an elastic response, and deform continuously under stress.[261] Viscosity is a measure of a fluid’s resistance to flow. Under the action of an external force, a fluid starts to flow which results in a shearing stress in the fluid that tends to oppose the motion. As one layer of the fluid moves past an adjacent layer, the fluid molecules interact with each other, transmit the momentum from the faster layer to the slower layer in order to resist the relative motion. If an external (shearing) force is applied to a fluid, the fluid will move and continue to move as long as the force acts on it. Instrument used to measure rheological properties of materials is called rheometer. Many factors affect the stability of nanofluids, e.g. hydrodynamic forces, Brownian motion, strength of interparticle interactions, volume fraction, electrostatic forces, steric repulsion, size and shape of particles. Measuring the rheology of nanofluids gives an indication of their properties and interactions that are occurring. Rheology based measurements can help to predict which formulations might exhibit flocculation, coagulation or coalescence in nanofluids that can result in undesired effects such as settling, phase separation, etc.

High-precision, continuously-variable-shear instruments in which the test fluid is sheared between rotating cylinders, cones, or plates, under controlled-stress or controlled-rate conditions, are termed as rotational rheometers. Rheometers are capable of producing oscillatory strains, and measuring the normal stress. The basic rotational system consists of four parts: (i) a measurement tool with a well-defined geometry, (ii) a device to apply a constant torque or rotation speed to the tool over a wide range of shear stress or shear rate values, (iii) a device to determine the stress or shear rate response, and (iv) a temperature control for the test fluid and tool. Depending on the design specifications, rheometers may also include built-in corrections or compensations for inertia, drift, and temperature fluctuations during measurement. Most rheometers are based on the relative rotation about a common axis of one of three tool geometries. The schematic representation of these geometries are shown in **Fig. 2.8**. In the present study Viscosity measurements are carried out using Anton Paar MCR 301 strain controlled rotational Rheometer, Germany. The air-bearing-supported synchronous Electrically Commutated (EC) motor (also called DC motor) is the key component of the MCR rheometer series. The EC motor of the MCR series ensures accuracy across a wide viscosity range – from solids to liquids with viscosities lower than water. The rotor of the EC motor drive is equipped with permanent magnets. In the stator, coils with opposite polarity produce magnetic poles.

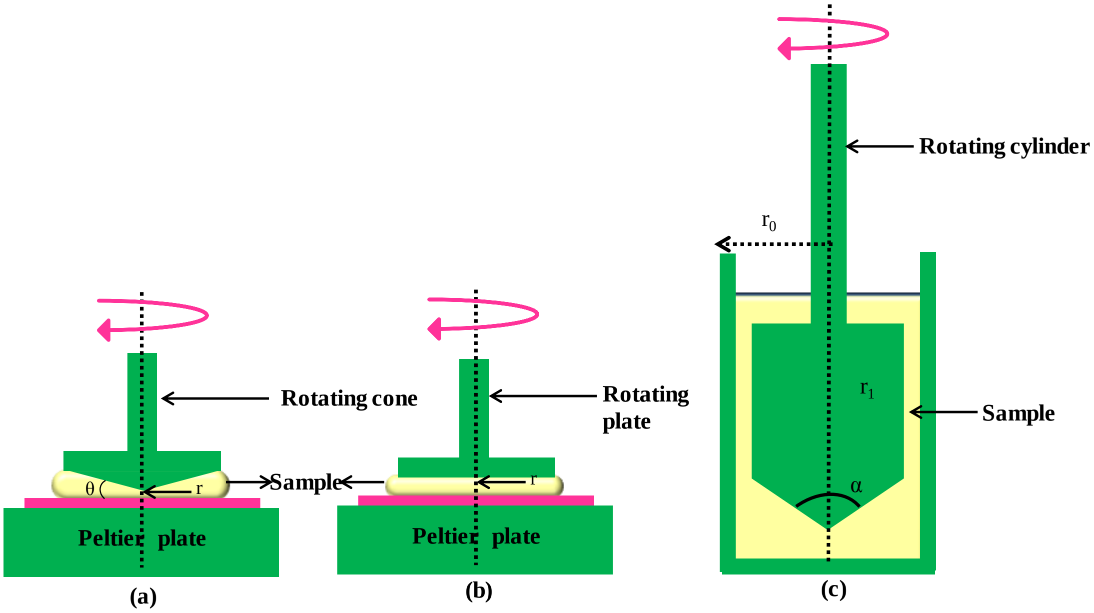

Figure 2.8: Schematic diagram of basic tool geometries for the rotational rheometer: (a) cone and plate (b) parallel plates and (c) concentric cylinder.

The magnets in the rotor and the stator coils attract each other, so that a rotating flux of current in the coil windings produces a frictionless synchronous movement of the rotor. The torque of the motor is set and measured via the input current to the stator coils. Due to its unique design, the EC motor features a linear relation between the torque and the input current to the stator coil, which is advantageous for precise torque control and measurement.

2.2.3 Dynamic Light Scattering

Dynamic light scattering (DLS), also referred to as Quasi-Elastic Light Scattering (QELS), is a non-invasive technique for measuring the hydrodynamic size and size distribution of molecules and particles typically in the submicron range. Typical applications of dynamic light scattering are the characterization of particles or molecules, which have been dispersed in a liquid. The Brownian motion of the particles or molecules in suspension causes laser light to be scattered at different intensities. Analysis of these intensity fluctuations yields the velocity of the Brownian motion and the particle size calculated by using the Stokes-Einstein relationship. In light scattering experiments, a monochromatic light source, usually a laser passes through a polarizer and into sample. The scattered light then goes through a second polarizer where it is collected by a photomultiplier tube (PMT). The instantaneous scattered field can be regarded as the superposition of waves scattered from the individual scattering centers. The scattered electric field at a given scattering wave vector *q* is expressed as,

$$E(q,t)\alpha\sum_{j=1}^{N}\exp\left(i\vec{q}.r_j\vec{(t)}\right) \qquad (2.\ 13)$$

where $\vec{r}(t)$ is the center- of-mass position of the jth scatterer. The scattered field given by **Eqn. 2.13** therefore fluctuates in response to the motions of the scatterers. If the fluctuations are faster than 10^{-6} sec, filter method is used to detect and analyze the time scale of these fluctuations. Optical mixing or beating methods are usually used for processes that occur on time scales slower than about 10^{-6} sec. In optical mixing methods no “filter” is inserted between the scattering medium and the detector (PMT). The scattered light impinges directly on the PMT cathode. In the homodyne (self-beat) method only the scattered light impinges on the photocathode, while in the heterodyne method a local oscillator (a small portion of the unscattered laser beam) is mixed with the scattered light on the cathode surface. Since PMT is a square-law detector, its instantaneous current output is proportional to the square of the incident electric field $I(t) \alpha ||E(t)||^2$. The PMT output is fed to a digital correlator, which calculates the intensity-intensity auto correlation function (also known as homodyne correlation function), which is defined as,

$$\langle I(q,0)I(q,t)\rangle = B\left\langle |E(q,0)|^2 |E(q,t)|^2 \right\rangle \tag{2. 14}$$

here *B* is the proportionality constant. The normalized intensity autocorrelation function $g^{(2)}(q,t)$ is defined as,

$$g^{(2)}(q,t) = \frac{\langle I(q,0)I(q,t)\rangle}{\langle I(q)\rangle^2} \tag{2. 15}$$

and the normalized electric field auto-correlation function (also known as heterodyne correlation function) as,

$$g^{(1)}(q,t) = \frac{\langle E(q,0)E(q,t)\rangle}{\langle |E(q)|\rangle^2} \tag{2. 16}$$

with the assumption that the scattering volume can be divided into a large number of statistically independent sub-regions and the scattered electric field is a Gaussian random variable, $g^{(2)}(q,t)$ is related to $g^{(1)}(q,t)$ by,

$$g^{(2)}(q,t) = 1 + \beta\left|g^{(1)}(q,t)\right|^2 \tag{2. 17}$$

The above equation is known as Siegert relation and the constant β depends on the coherence area set by the optics of the instrument and is obtained from the fit. The heterodyne correlation function $g^{(1)}(q,t)$, which is related to the position of the particles, can be redefined as the intermediate scattering function (dynamic structural factor), $F(q,t)$ using **Eqn.2.13**,

$$F(q,t)\ \alpha\ \langle E(q,0)E(q,t)\rangle \tag{2. 18}$$

$$F(q,t) = \frac{1}{N}\sum_{I=1}^{N}\sum_{J=1}^{N}\langle\exp\left(i\,\vec{q}.\left[\vec{r}_i(0) - \vec{r}_j(t)\right]\right) \tag{2. 19}$$

Hence,

$$g^{(1)}(q,t) = \frac{F(q,t)}{S(q)} \tag{2. 20}$$

where, $S(q) = F(q,0)$. Since for an non-interacting suspension $S(q)=1$, by measuring $g^{(1)}(q,t)$ (either by homodyne or heterodyne method), one can determine the self-diffusion coefficient D_0 of colloidal particles. In the present study hydrodynamic size measurements were carried out using Zetasizer Nano ZS from Malvern Instruments, UK.

2.2.4 Phase Contrast Optical Microscopy

In phase contrast optical microscopy, a phase object causes a small phase shift in the light passing through a transparent specimen which is converted into amplitude or contrast changes in the image. As light travels through a medium other than vacuum, interaction with the medium can cause amplitude and phase changes which depend on the properties of the medium. The basic principle to make phase changes visible in phase contrast microscopy is to separate the illuminating background light from the specimen scattered light, which make up the foreground details, and to manipulate these differently. The ring shaped illuminating light (orange) that passes through the condenser annulus is focused on the specimen by the condenser. Some of the illuminating light is scattered by the specimen (Blue). The remaining light is unaffected by the specimen and form the background light (Pink).

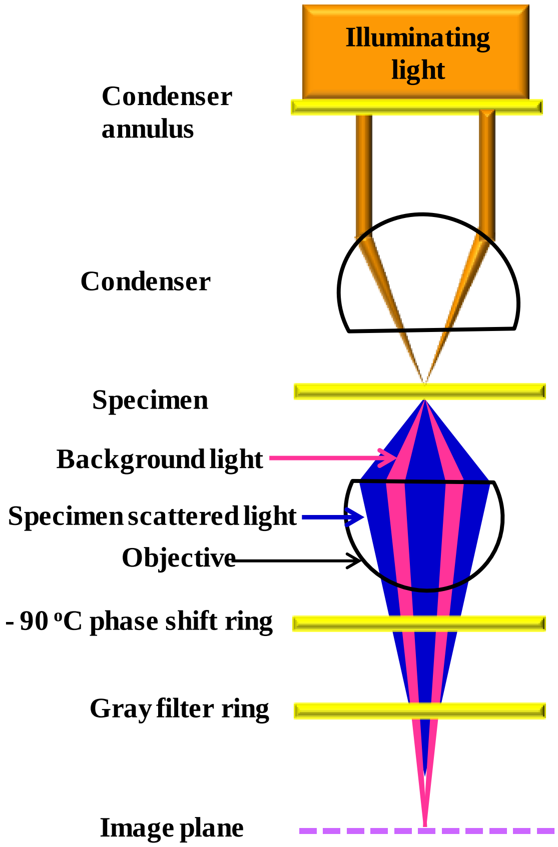

Figure 2.9: Schematic representation of phase contrast optical microscope showing the arrangement of light source lenses, specimen, phase ring and image plane.

When observing the unstained biological specimen, the scattered light is weak and typically phase shifted by -90°, relative to the background light. This leads to that the foreground and the backgrounds nearly have the same intensity, resulting in a low image contrast. In a phase contrast microscope, the image contrast is improved in two steps. The background light is phase shifted -90° by passing it through a phase shift ring. This eliminates the phase difference between the background and the scattered light, leading to an increased intensity difference between foreground and background. To further increase the contrast, the background is dimmed by a gray filter ring. Some of the scattered light will be phase shifted and dimmed by the rings. However, the background light is affected to a much greater extent, which creates the phase contrast effect. The above describes negative phase contrast. In its positive form, the background light is instead phase shifted by +90°. The background light will thus be 180° out of phase relative to the scattered light. This results in that the scattered light will be subtracted from the background light to form an image where the foreground is darker than the background. The performance of modern phase contrast microscopes is so refined that it enables specimens containing very small internal structures, or even just a few protein molecules, to be detected when the technology is coupled to electronic enhancement and post-acquisition image processing. The schematic representation of phase contrast microscope is shown in **Fig. 2.9.**

In the present study, the aggregation effect in nanofluids and phase change materials are studied using Lecia inverted optical microscope (Germany) attached with a JVC camera and frame grabber card. The obtained images are processed using Lecia Win software.

2.2.5 Fourier Transform Infrared Spectroscopy

In Fourier Transform Infrared (FTIR), the preferred method of infrared spectroscopy, IR radiation is passed through a sample. Some of the infrared radiation is absorbed by the sample and some of it is transmitted. The resulting spectrum represents the molecular absorption and transmission, creating a molecular fingerprint of the sample. Like a fingerprint no two unique molecular structures produce the same infrared spectrum. This makes infrared spectroscopy useful for several types of analysis. The total internal energy of a molecule in a first approximation is the sum of rotational, vibrational and electronic energy levels. In Infrared spectroscopy the interactions between matter and electromagnetic (EM) fields in the IR region is studied where the EM waves mainly couple with the molecular vibrations. In other words, excitation of molecules to the higher vibrational state can occur by absorbing IR radiation. For FTIR studies, a small amount of solid sample is mixed thoroughly with potassium bromide in the ratio 1:100 (by weight). Then the mixture is compressed into a thin transparent pellet using a hydraulic press. These pellets are transparent to IR radiation and it is used for analysis. If the photon energy coincides with the vibrational energy levels of the molecule the frequency is absorbed by the molecule. Hence the IR spectroscopy is a very powerful technique which provides fingerprint information on the chemical composition of the sample. In the present study FTIR measurements were done using ABB Bomem MB 3000 instrument, Canada.

2.2.6 Thermogravimetric Analysis and Differential Scanning Calorimetry

Specific heat capacity is a material property describing the energy required to induce a change in the temperature of a unit mass of the material. A differential scanning calorimeter (DSC) is used to measure this quantity. The C_p is measured using DSC by heating a sample and measuring the temperature difference between the sample and a reference. The sample material is subjected to a linear temperature program, and the heat flow rate into the sample is continuously measured which is proportional to the instantaneous specific heat of the sample. Reference and sample crucibles are placed on a sample holder placed inside a furnace which generates heat radially toward the center. Thermocouples in contact with each crucible measure the temperature. One thermo element is shared between the crucibles allowing the temperature difference to be measured as a voltage. Here the methodology of specific heat measurements using differential scanning calorimetry has been employed according to the ASTM standard (E 1269-05).[262, 263] It measures the heat changes associated with the temperature rise of the sample at a given heating rate. The instrument was calibrated with heat of fusion of indium, zinc, aluminum and using sapphire as an external standard. For this the standard and the sample were run over the desired temperature range and heating rate. The effect of variables such as sample weight, heating rate and calorimeter sensitivity on the measurements is considered. For this the blank (crucibles alone) were run several times for the specific method to standardize the instruments avoiding any artifacts. The crucible with sapphire along with a blank reference was run followed by the samples. The C_p by sapphire was determined using the STARe software. The heating rates were fixed at 2 °/min for each of the samples to study its effect on the specific heat capacity. The deflections from the base line, corrected from the empty platinum sample pan (crucible), are proportional to the sample weights and the specific heats of the sample and the standard, respectively provided both are run at the calorimeter settings (same temperature range and heating rates). Specific heat is measured by direct comparison with a standard to reduce the effects of instrumental variation.[264] An accuracy of 2 % is achieved by this method. In our present study, the thermogravimetric analysis (TGA) of nanofluids was carried out using Mettler Toledo TGA-DSC-1, 1100LF system, (Switzerland) under inert atmosphere.

2.2.7 Contact Angle Meter

A charge coupled device (CCD) based contact angle meter (Holmarc, Kochi) was used for measuring contact angles of liquids over substrates. Contact angle (θ) is a quantitative measure of wetting of a solid by a liquid. It is defined geometrically as the angle formed by a liquid at the three phase boundary where a liquid, gas and solid intersect. The shape of the drop is controlled by the three forces of interfacial tension i.e., solid-liquid (γ_{sl}), solid-vapour (γ_{sv}) and liquid-vapour (γ_{lv}) interfacial tension. The shape of a liquid droplet on a flat horizontal solid surface is determined by the Young-Laplace equation. The relationship between interfacial tensions and contact angle is given by, [265]

$$\gamma^{sl} = \gamma^{sv} - \gamma^{lv} \cos\theta \tag{2. 21}$$

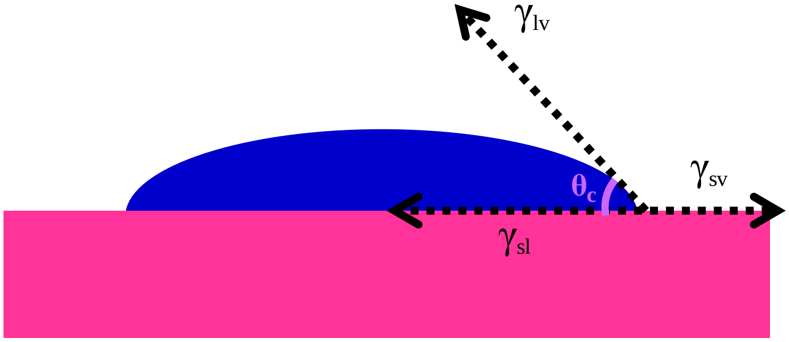

Figure 2.10: Schematic representation of contact angle of the liquid drop on a smooth solid surface.

Image Analysis software (Image J) is used for measurement and further calculations. The instrument makes use of a CCD sensor for imaging the droplet. The manual dispensing syringe pump is used for liquid dispensing. The CCD sensor and imaging optical assembly are mounted on a translation stage for fine adjustment of image position on the sensor. The dispensing system which consists of a syringe along with linear stage is held on a vertical translator for initial setting of the distance of the needle from the solid surface. Back light is provided by a high bright light emitting diode (LED). The illumination intensity of the back light LED has a controllable feature. The substrate holder can be rotated ±180° from the horizontal position. This enables a detailed study in contact angle variation for liquids with varying properties and also helps in finding out the contact angle hysteresis of the fluid. The instrument is compact and rigid and has leveling screws for stable setting on any platform. All surfaces have a black finish to avoid unwanted reflection of light during measurement. The schematic representation of contact angle of the liquid drop on a smooth solid surface is shown in **Fig.2.10**

2.2.8 Temperature Controlled Water Bath

To measure the thermal conductivity at different temperatures (25 – 4 °C), the sample vial with the thermal conductivity probe is immersed in a circulating water bath (ANM Alliance, India) and the temperature of the water bath is maintained within ± 0.1 °C. The entire sample assembly is insulated for temperature gradient and vibrations. The thermal conductivity measurements are made 10 mins after achieving the desired temperature for better temperature equilibrium.

Chapter III

Role of Adsorbing Moieties on Thermal Conductivity and Associated Properties of Nanofluids

3.1 Introduction

Thermal properties of materials are extremely important for heat transfer applications.[266, 267] Nanofluids and nanomaterials have been a topic of great interest during the last decade primarily due to the initial reports of anomalous thermal conductivity enhancement (i.e. beyond Maxwell's limits) in nanofluids with a small percentage of nanoparticles.[38] Several recent studies in stable nanofluids show thermal conductivity enhancement within Maxwell's limits.[11, 14, 147, 275] The reasons for the reported anomalous enhancement in thermal conductivity in nanofluids are still a topic of debate.[147, 276] After considering various mechanisms responsible for the observed enhancement in *k*, one of the most probable aspects considered in the recent years is the effective conduction of heat through percolating aggregating nanoparticle paths.[208, 273, 277] However, many researchers still believe that the micro-nano convection could be another plausible cause for thermal conductivity enhancement.[278, 279] Another grey area in the understanding of thermal property variations in nanofluids is the role of interfacial resistance[267, 280] and the morphology of suspended nanoparticles in fluids. The former aspect is extremely important because most of the suspensions are stabilized using surface active species or surfactant. Though the mechanism of stabilization of nanoparticles by surfactants is quite well understood, their precise role on the interfacial thermal resistance, on thermal and rheological properties of nanofluids is still unclear.[15, 108, 177, 249-251, 270, 281] Therefore, a systematic study to understand the effect of interfacial resistance on thermal conductivity of liquids and suspensions is warranted, which is one of the key issues addressed in this study.

Nanofluids are thermodynamically unstable systems. However, they can be made kinetically stable with the aid of suitable surface active species. Unlike molecular fluids, production of well stabilized nanofluids is a difficult task. For the production of stable nanofluids, one has to produce fairly monodisperse nanoparticles and functionalize them with a suitable stabilizing moiety to prevent interparticle attractions. Owing to the large surface area to volume ratio of fine nanomaterials, the dispersed particles (even with stabilizing entities) have a tendency to aggregate because of van der Waals attraction. Even with the best available production route, it is difficult to produce nanoparticles with polydispersity less than 5 %. However, to unravel the exact mechanism of heat conduction in nanofluids, model systems with high degree of monodispersity and well controlled morphology is necessary. To resolve the problem of high polydispersity of nanoparticles, model systems of micellar fluids with remarkable monodispersity, along with other nanofluids are chosen for the present study.

Though there are several studies on viscosity of nanofluids, a proper understanding of the role of η on k enhancement is still missing that is a very important aspect for thermal engineering. The particle concentration, particle-particle interactions, agglomeration and clustering of suspended entities play a major role in the reduced viscosity (η/η_0) where, η_0 is the viscosity of the basefluid.[282] The rheological properties of nanofluids are strongly related to the conformation of suspended particles in the basefluids. Agglomeration in nanofluids is an undesirable effect that is difficult to control. Since agglomeration issue is practically negligible in micellar systems due to electrostatic or steric forces, it is one of the best model systems to study the role of viscosity on thermal and related properties.

The questions that are addressed in this study are the following (a) Do the *k* enhancements in 'soft' and 'hard' nanofluids follow the effective medium theory? (b) What is the role of initial thermal conductivity, morphology and number density of suspended particles on thermal conductivity enhancement? (c) Do surface active moieties at nanoparticle interfaces enhance or reduce the *k* of nanofluids? (d) What is the role of the aspect ratio of particles and their orientation with respect to heat flow direction on *k* enhancement? For these studies, model soft systems of micelles in the size range of 2.5 to 7 nm with different head group charges and commercially obtained water based alumina, silica and non-aqueous kerosene based iron oxide nanofluids with particle size in the range of 12 to15 nm were used. Through these systematic studies, the effect of surface active species on thermal conductivity, rheology, density, contact angle and refractive index are studied.

3.2 Materials and Methods

3.2.1 Materials

SDS , CTAB, NP9 and NP10 were used in this study**.** The critical micellar concentrations (CMC) for SDS, CTAB, NP9 and NP10 are 8×10^{-3} M, 9×10^{-4} M, 6×10^{-5} M and 7×10^{-5} M, respectively. The reported micellar diameter of SDS, CTAB, NP9 and NP10 are approximately 3.7, 5.0, 6.3 and 6.8 nm, respectively.[283-287] The average aggregation number of micelles for SDS, CTAB, NP9 and NP10 are 64, 95, 350 and 144, respectively.[283, 288-290] For the studies, 16 vol% stock solutions of SDS, CTAB, NP9 and NP10 surfactants were prepared using milli-Q water with a resistivity value of 18.2 MΩ cm, from which different concentrations were prepared.

Water based γ-Al_2O_3, SiO_2 nanofluids and oil based Fe_3O_4 nanofluid were used to study the effect of adsorbed surfactant layer on thermal conductivity. Fe_3O_4 nanoparticles were prepared by chemical coprecipitation technique.[207, 252] The details of the materials used for this study are discussed in **Chapter 2**.

3.2.2 Methods

The thermal conductivity of the samples was measured by using a hot wire probe as per the procedure described in **Chapter 2**. Viscosity, FTIR, Contact angle and thermogravimetric analysis were carried out. DMA 35 portable densitometer from Anton Paar (Germany) was used for density measurements. Refractive index measurements were done using a Rudolph digital refractrometer with peltier based temperature controller. Small angle X-ray scattering (SAXS) studies for nanofluids were carried out using Rigaku Ultima IV instrument. It uses Cu K_α (λ =1.5418 Å) as X-ray source. The scattering intensity $I(q)$ was measured as a function of the scattering vector $\left(q = \frac{4\pi \sin\theta'}{\lambda} \right)$. The scattering intensity plot was fitted with the spherical model equation, $I(q) = |\Delta\rho|^2 \left\{ \frac{4\pi}{q^3} \left[\sin\left(\frac{qd}{2}\right) - \frac{qd}{2} \cos\left(\frac{qd}{2}\right) \right] \right\}^2$ where, $\Delta\rho$ is the difference in electron density of particle and the suspended medium. The most probable particle size was obtained from the distance distribution function.

3.3 Results and Discussion

3.3.1 DLS, SAXS, FTIR and TGA Analysis

Fig. 3.1 shows the hydrodynamic diameter of the water-based and kerosene based nanofluids. The average hydrodynamic sizes are found to be 13, 15 and 12.5 nm for γ-Al_2O_3, SiO_2 and Fe_3O_4 nanoparticles, respectively. The size distribution is found to be narrow for all the three nanofluids.

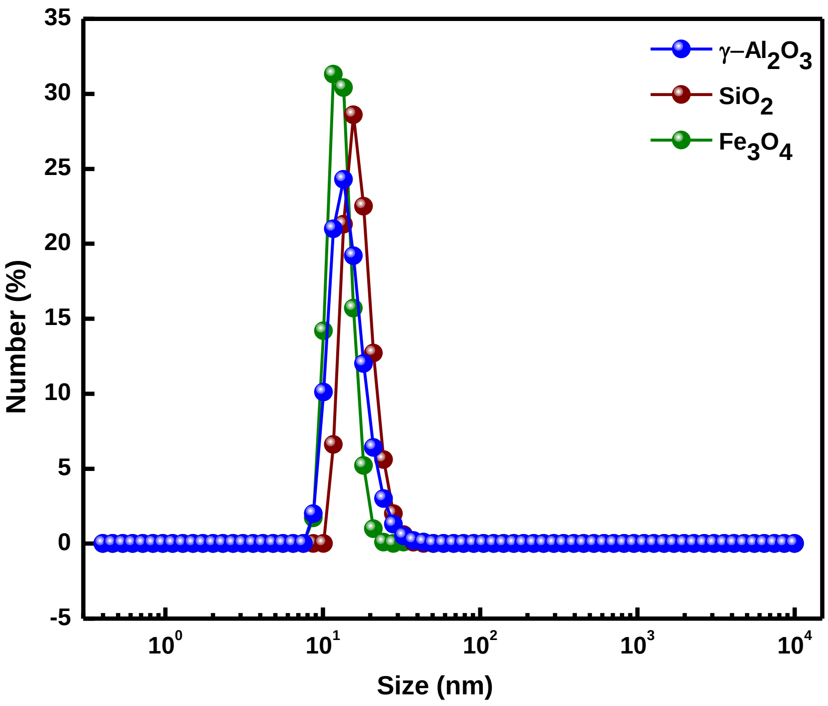

Figure 3.1: Hydrodynamic size distribution of water based uncoated γ- Al_2O_3, SiO_2 and oleic acid coated kerosene based Fe_3O_4 nanofluids.

Fig. 3.2(a) shows the X-ray scattering intensity as a function of scattering vector and **Fig. 3.2(b)** shows the particle size distribution obtained from the best fit on SAXS data for water based **γ-** Al_2O_3 and SiO_2 nanofluids and kerosene based Fe_3O_4 nanofluids. The most probable particle size is found to be 10.74 nm for **γ-** Al_2O_3 nanoparticle, 14.7 nm for SiO_2 nanoparticles and 11.66 nm for Fe_3O_4 nanoparticles. The average hydrodynamic diameter measured by DLS was slightly higher than that obtained from the SAXS results.

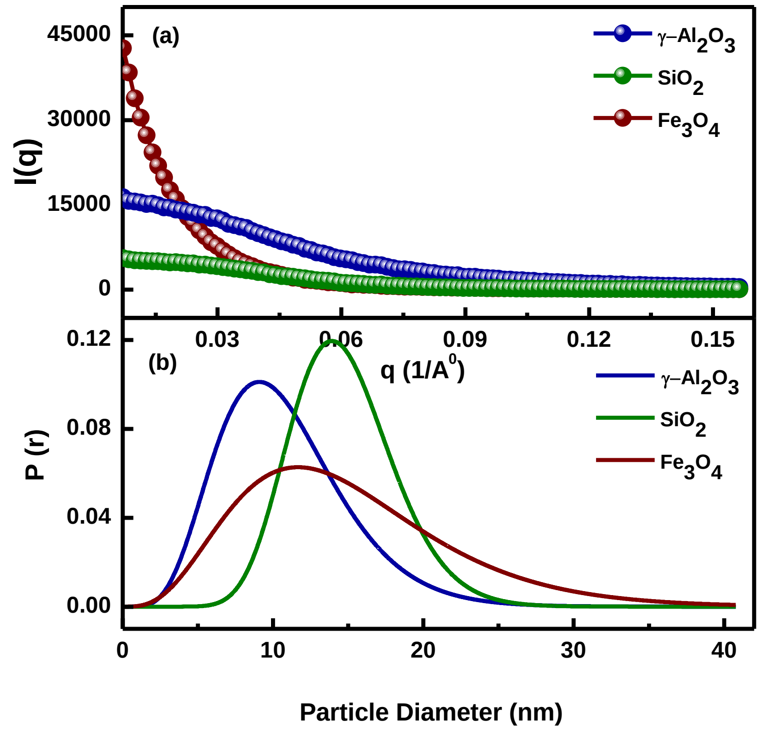

Figure 3.2: (a) The X-ray scattering intensity as a function of scattering vector and (b) the particle size distribution obtained from the best fit on SAXS data for water based γ- Al_2O_3 and SiO_2 nanofluids and kerosene based Fe_3O_4 nanofluid.

The thermogravimetric curves for γ-Al_2O_3 and SiO_2 nanofluids and Fe_3O_4 nanoparticles are shown in **Fig. 3.3**. The thermogravimetric curves for water based γ-Al_2O_3 and SiO_2 nanofluids **(Fig. 3.3 (a&b))** show a single step weight loss at ≈ 103 °C (~75 wt%) and ≈ 105 °C (~71 wt%), respectively, corresponding to the loss of most of the water. Thereafter, a gradual decrease in weight is observed till 600 °C in both the cases. The gradual decrease in weight observed beyond 100 °C (till 600 °C) was about ~ 4 wt% and 6 wt%, respectively for γ- Al_2O_3 and SiO_2 nanofluids. The decrease in weight observed beyond 100 °C in the cases of γ- Al_2O_3 may be due to the dehydroxylation of the alumina surface.[291]

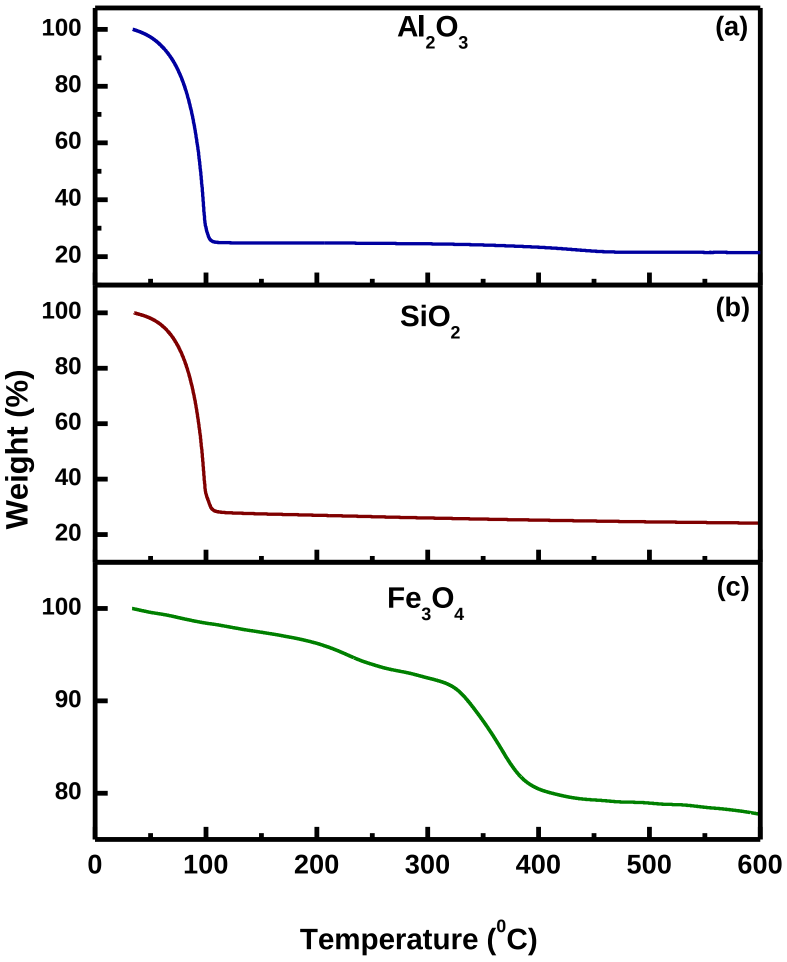

Figure 3.3: The thermogravimetric curves for water based (a) γ- Al_2O_3 (b) SiO_2 nanofluids and (c) Fe_3O_4 nanoparticles.

The weight loss observed in γ- Al_2O_3 in the temperature range of 100-600 °C was similar to that observed by Costa et al.[291] A similar trend in the thermogram was also observed in SiO_2 nanofluids. The TGA curve for the Fe_3O_4 nanoparticles shows a two-step weight loss between 199 to 310 °C (~ 4 wt%) and between 310 to 400 ˚C (~12 wt%) **(Fig. 3.3(c))**. The first step should be due to the removal of loosely bound or free surfactant and the second step should be due to the removal of strongly bound surfactant molecules.

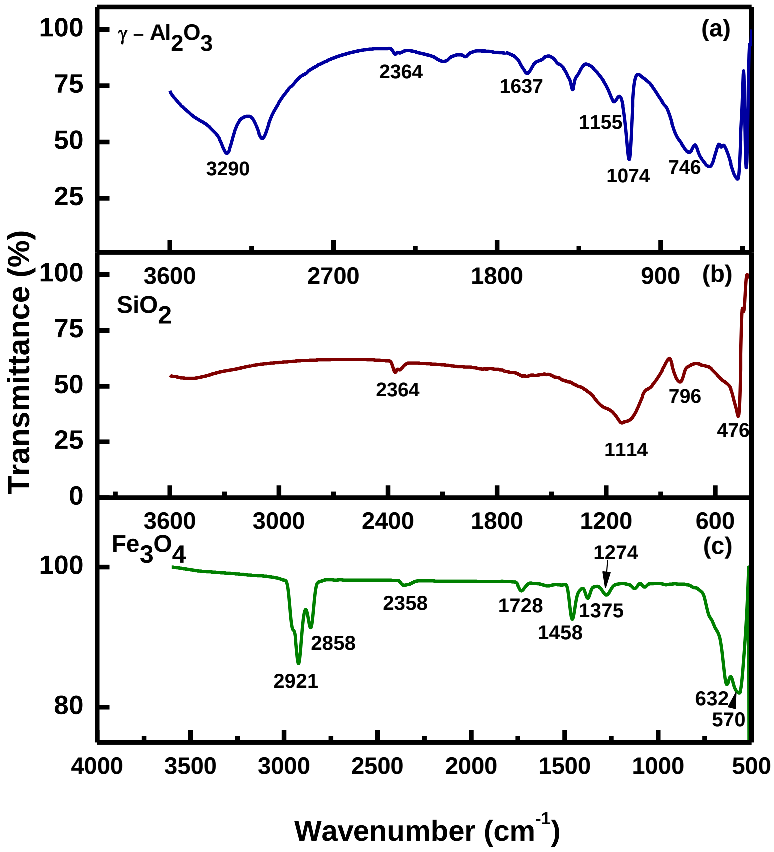

Figure 3.4: FTIR spectrum of (a) γ- Al_2O_3 (b) SiO_2 and (c) oleic acid coated Fe_3O_4 nanofluids.

The FTIR spectrum for Al_2O_3, SiO_2 and Fe_3O_4 nanofluids are shown in **Fig. 3.4**. **Fig. 3.4 (a)** corresponds to the FTIR spectrum of water based γ- Al_2O_3 nanofluid. The transmittance band at 746 cm^{-1} corresponds to the stretching vibration of Al-O.[292] The spectrum shows characteristic peaks at 1074 and 1155 cm^{-1} which corresponds to the Al-O-Al symmetric bending and stretching vibrations and Al-O-Al asymmetric bending modes, respectively.[292] The transmittance band at 1637 and 3290 (3575) cm^{-1} correspond~~s~~ to bending[291] and stretching modes of water, respectively. **Fig. 3.4 (b)** corresponds to the FTIR spectrum of SiO_2 nanofluid. The rocking, symmetric and asymmetric stretching of Si-O-Si are observed at

476, 796 and 1114 cm^{-1}, respectively.[293] The FTIR spectrum of oleic acid coated iron oxide nanoparticles dispersed in kerosene is shown in **Fig. 3.4 (c).** The spectrum shows characteristic peaks at 2921, 2858, 2358, 1728, 1458, 1375, 1274, 632 and 570 cm^{-1}. The symmetric and asymmetric stretching mode of the methylene group of the oleic acid appears at 2858 and 2921 cm^{-1}, respectively. The peak at 1458 cm^{-1} corresponds to the asymmetric stretching of the carboxylate (COO^-) group. The peak at 570 cm^{-1} is attributed to the stretching of bonds between octahedral and tetrahedral metal ions to oxide ions while the one at 1728 cm^{-1} is due to the presence of free oleic acid molecules. The rest of the peaks are attributed to the vibrations in kerosene. In all the three cases, a peak is noticed around 2360 cm^{-1} that corresponds to asymmetric stretching mode of carbon dioxide.

3.3.2 Effect of Number Density of Dispersed Particle on Thermal Conductivity

Fig. 3.5 shows the variation of k/k_f and the percentage of decrease in thermal conductivity as a function of surfactant concentration for SDS, CTAB, NP9 and NP10 in water. It should be noted that the surfactants are amphiphilic molecules with hydrophilic and hydrophobic parts. The surfactant molecules exist as unimers at concentrations below CMC and form spherical micelles above CMC. The driving forces for micelle formation are the hydrophobic force and entropy. The forces opposing micelle formation are concentration gradient, thermal motion and electrostatic repulsion between ionic polar heads (applicable to CTAB and SDS only). In all the four systems, the k/k_f is found to decrease with increase in surfactant concentration. The micellar system is a disordered system. As the surfactant concentration increases the number of micelles in the system increases, leading to an increase in the degree of disorder, which has resulted in a decrease in k/k_f with increase in surfactant concentration.

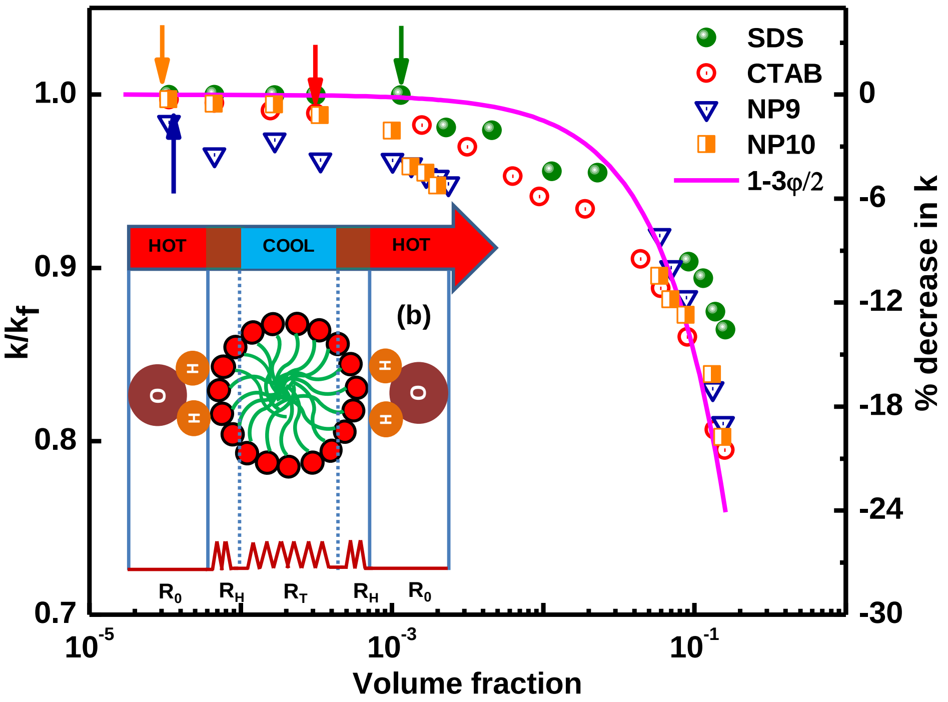

Figure 3.5: The variation of thermal conductivity as a function of volume fraction for SDS, CTAB, NP9 and NP10 along with the theoretical fit (The CMC values of surfactants are shown by arrows of respective symbol colors). Inset shows the schematic representation of micelles and the possible thermal resistive contributions from different moieties (head group, tail and water molecules). R_0, R_H, R_T represents the resistance offered by water molecules, head group and tail, respectively.

Similar results were reported by Anderson,[294] who observed that an increase in the disorder of the system can decrease the thermal conductivity. Muller[295] suggested that the strength of the interatomic binding force is related to the thermal conductivity. The greater the strength of this binding force, the higher the thermal conductivity. The higher interatomic binding force in metals results in higher thermal conductivity. The binding force is weak in the case of micellar systems due to its disordered structures leading to a lower thermal conductivity. The number density for the micellar system is given by, $n = \frac{6\varphi}{\pi d^3}$.

The experimental data are fitted with Maxwell model as shown by the solid line in **Fig. 3.5**. It can be seen that the experimental data show large deviations from effective medium theory at low volume fractions of micelles, especially for CTAB and NP9. At lower volume fraction, the number of micelles in the system is less and therefore, the interfacial thermal resistance is also less. As the volume fraction increases, the number of micelles in the system increases, which leads to higher interfacial thermal resistance. The lower interfacial thermal resistance at lower concentration might be a probable reason for the observed large deviation from theoretical fit at lower volume fractions. For volume fractions above 0.06, the experimental data fit quite well with the effective medium theory.

In general, the interfacial thermal resistance reduces the effective thermal conductivity. When $\alpha \rightarrow \infty$, k/k_f reduces to $(1\text{-}3\varphi/2)$, where the effective thermal conductivity becomes smaller than that of the base fluid. A negative interfacial thermal resistance means an interfacial thermal gradient that is lower than that of the bulk region. A positive R_k leads to a decrease in the effective thermal conductivity. Simulation studies in the nanofluids showed that a positive Kapitza, due to a weak solid-fluid interaction, can lead to a negligible or negative thermal conductivity enhancement.[23, 296] The non-equilibrium molecular dynamics simulations show that the thermal conductivity of a well-dispersed nanofluid can be enhanced beyond the Maxwell limit through a percolating amorphous like fluid structure at the cluster interface, due to the strong cluster-fluid interaction.[246] Our experimental data suggest that the interfacial resistance in the presence of surfactant is positive but far from infinity. The interfacial thickness as given by Yan [113] is $h=\frac{1}{\sqrt{3}}\left(\frac{4M_f}{\rho_f N_a}\right)^{1/3}$ where, M_f and ρ_f are the molecular weight and density, respectively of the surrounding fluid medium around a nanocluster and N_a is Avogadro's number. Using the above expression, the calculated values of the interfacial thickness for water, SDS, CTAB, NP9 and NP10 are found to be 2.84, 71.5, 77, 90.9 and 93.7 nm, respectively. The observed larger reduction of thermal conductivity, especially at lower surfactant concentrations in NP9 and NP10, followed by CTAB and SDS are consistent with the theoretical values of interfacial thickness.

According to kinetic theory, the thermal conductivity is defined as, $k=\frac{1}{3}\sum_{pol}\int Cv\Lambda_{eff}\,d\omega$ where, C, v, ω, Λ_{eff} are the heat capacity, group velocity, frequency and the effective mean free path over all phonon polarizations, respectively. The thermal conductivity reduction in solids originates from scattering from the grain boundaries where the mean free path is a function of the average grain size and phonon frequency. Further, it also depends on the grain boundary structure and the impurity atoms at the boundary that affect the phonon transmission and reflection at each interface.[297-300] Very recently, it was reported that a substantial reduction in thermal conductivity in $FeSb_2$ occurs as the grain size decreases from micrometers to nanometers due to dominant scattering from smaller grains.[301] The porosity and phonon scattering at grain boundaries are found to be the dominant mechanisms for thermal conductivity reduction in nanocrystalline materials.[302] Isotopic doping [303-305] and a decrease in the phonon group velocity[306] can also cause reduction in thermal conductivity. In porous materials, thermal conduction through the solid phase, radiation across the pores and convection through the porous phase etc., contributes to the effective thermal conductivity.

The scattering of phonons by interaction with the surroundings or the presence of defects produced by the surfactant micelles in solutions can also lead to a decrease in thermal conductivity.[307] Since phonons are scattered at surfaces and interfaces, a reduction in k is anticipated with increase in the surface area-to-volume ratio. Experimental studies show that the excess SDS surfactants on the CNT surface can decrease the thermal conductivity enhancement of nanofluids due to an increase in the interfacial resistance.[249] Assal et al.[160] also reported a considerable decrease in thermal conductivity of water as the surfactant (CTAB) concentration increases.

It should be noted that the spherical micellar size of SDS is much smaller than that of CTAB, NP9 and NP10. Therefore, the total interfacial area (~$1/r$ dependence) available for SDS is much larger than the other three. If the concept of phonon scattering at interfaces is invoked, k should decrease with increase in the surface-to-volume ratio. However, the k decrease was almost the same at high volume fraction for all the four surfactants. The average CTAB inter-micellar spacing (IPS) reduces from 32 to 2.9 nm as the concentration is increased from φ = 0.002 to 0.16 where the micellar number density increases from 2.41×10^{22} to 2.43×10^{24}. For NP9, the IPS reduces from 36 to 3.7 nm as the concentration is increased from φ = 0.002 to 0.16 where the micellar number density increases from 1.58×10^{22} to 1.21×10^{24}. For NP10, the IPS reduces from 41 to 4.2 nm as the concentration is increased from φ = 0.002 to 0.16 where the micellar number density increases from 1.11×10^{22} to 8.54×10^{23}. For SDS, the IPS reduces from 20 to 2 nm as the concentration is increased from φ = 0.002 to 0.16 where the micellar number density increases from 8.64×10^{22} to 6.1×10^{24}. Among all the four surfactant micelles, SDS seems to have the highest number density and lowest IPS. Therefore, SDS is expected to have the maximum thermal conductivity enhancement compared to the other surfactant. But from the experimental results it is clear that the thermal conductivity enhancement for non-ionic and cationic surfactant is more when compared to that of SDS for the same volume fraction. This may be due to the fact that the number of micelles present in the system for the same surfactant concentration is more in the case of non-ionic and cationic surfactants when compared to that of SDS, since the CMC for SDS is 8×10^{-3} M, where as for CTAB, NP9 and NP10 the CMC are 9×10^{-4} M 6×10^{-5} M and 7×10^{-5} M, respectively. Therefore the number of holes (disorder) in the systems studied follow the trend, NP10 ≈ NP9 > CTAB > SDS for the same volume fraction. Hence the decrease in thermal conductivity should be more for non ionic surfactant followed by cationic and anionic system, which was consistent with our experimental results.

3.3.3 Effect of Concentration of Dispersed Phase on Interfacial Tension

To study the effect of interfacial tension, the contact angle measurements were carried out for all the four surfactant solutions on a stainless steel substrate. Steel substrate is chosen as the hotwire probe used has a stainless steel body. **Fig. 3.6 (a)** shows the variation of contact angle as a function of concentration of surfactant solutions. As the surfactant concentration increases, the contact angle is found to decrease for all the four surfactant solutions.

It is known that the addition of surfactant to water reduces its surface tension or interfacial tension and causes it to spread on a substrate.[308] The relationship between interfacial tension and contact angle is given by [265] $\gamma^{sl} = \gamma^{sv} - \gamma^{lv}\cos\theta$ γ_{lv} is calculated using the following formula[309]

$$\cos\theta = -1 + \sqrt{\frac{\gamma^{sv}}{\gamma^{lv}}}e^{-0.0001247\left(\gamma^{lv} - \gamma^{sv}\right)^2} \tag{3. 1}$$

On conversion of the solid to liquid surface tension using the above equations, the solid-liquid interfacial tension for SDS at $\varphi = 0.002$ is 1.625 mJ/m^2, which reduces to 0.225 mJ/m^2 at $\varphi = 0.09$.

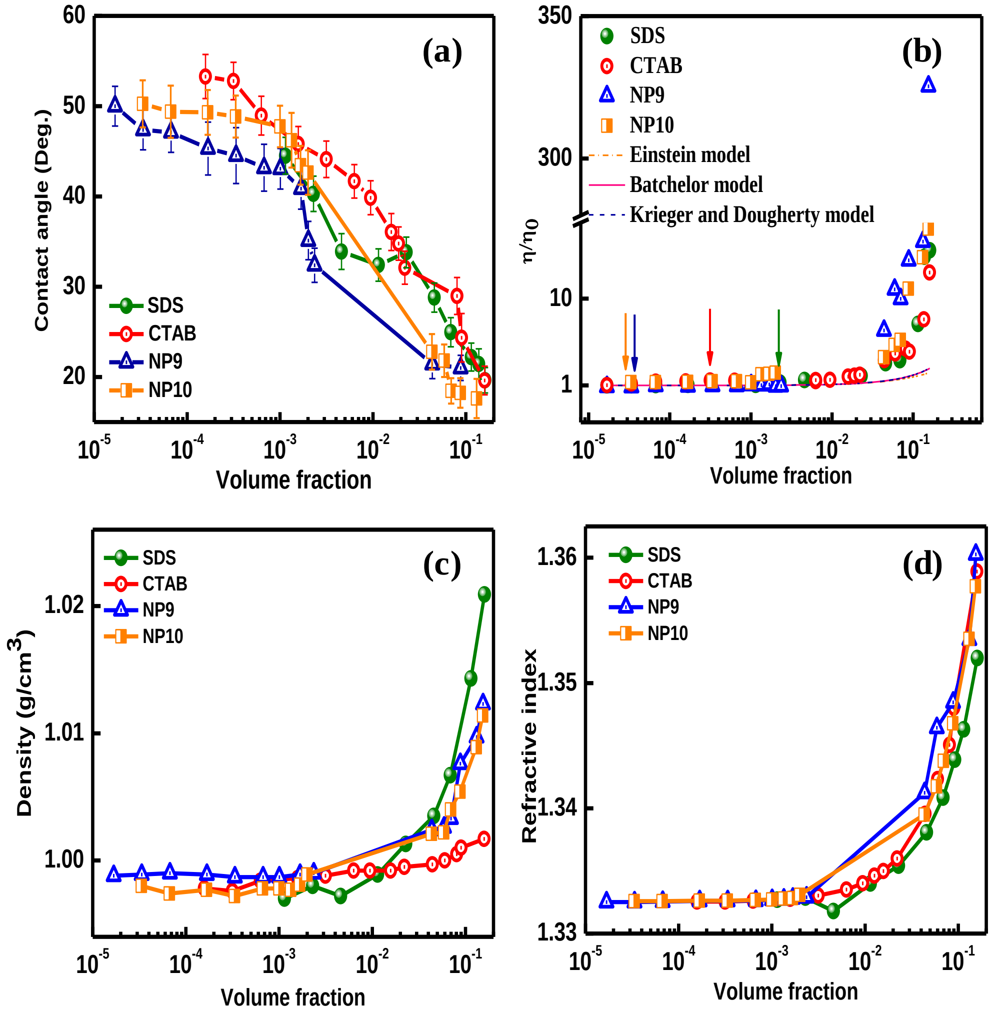

Figure 3.6: (a) Contact angle as a function of volume fraction, (b) The reduced viscosity as a function of volume fraction along with the theoretical fits using Einstein, Batchelor and Krieger & Dougherty models (The CMC values of each surfactant are shown by arrows of respective symbol colors), (c) density and (d) refractive index as functions of surfactant concentration for SDS, CTAB, NP9 and NP10.

Similarly the interfacial tension of CTAB, NP9 and NP10 solutions decreased from 2.734 to 0.228 mJ/m^2, 0.913 to 0.074 mJ/m^2 and 1.98 to 0.06 mJ/m^2, respectively as the surfactant concentration decreases from $\varphi = 0.02$ to 0.09. From our contact angle measurements, the calculated value of γ_{sl} of water is 72.7 mJ/m^2 which is in good agreement with the reported value of 72.75 mJ/m.^{2} [310, 311] The reported value of γ^{sl} for CTAB on mica substrate is 1.5 ± 1 at one CMC concentration.[312] This clearly shows that the presence of surfactant micelles makes the fluid more hydrophilic. Theoretical studies show that R_k attains a relatively larger value only when the liquid is more hydrophobic to the solid surface.[296, 313] Studies show that the orientation of adsorbed moieties of non-ionic surfactants changes with surfactant concentrations that results in changes in the free energy of adsorption.[314] An early study shows that the thermal conductivity of zinc-sulphide is increased when large particles of highly conducting diamond are added, but k lowered when submicron size particles of diamond is added, which was attributed to the change in the interfacial thermal resistance at larger surface to volume ratio.[315] According to Debye model $R_{BD} = \frac{4}{\rho C_p v \eta}$ where R_{BD} is the phonon boundary resistance. Therefore, thermal conductivity of the dispersion is $K_m = \frac{1}{3}\rho C v l$ where 'l' is the phonon mean free path. The Kapitza radius, a_k (~ l/q) depends on the probability of phonon crossing at the interface. When particle size is less than the Kapitza radius, the effective conductivity of the dispersion is lowered by the particles.

3.3.4 Effect of Concentration of Dispersed Phase on Viscosity Enhancement

Fig. 3.6 (b) shows the reduced viscosity as a function of surfactant concentration for SDS, CTAB, NP9 and NP10. In all the four systems, the viscosity increase was nominal up to 0.05

(φ). The percentage of enhancement in viscosity at $\varphi = 0.002$ was 7, 13, 3 and 40 % for SDS, CTAB, NP9 and NP10, respectively. Further increase in the concentration of the surfactant leads to a dramatic enhancement in reduced viscosity for all the four surfactants. The reduced viscosity values at $\varphi = 0.08$ for SDS, CTAB, NP9 and NP10 are 1.95, 2.65, 27.59 and 13.03, respectively. What is the reason for the observed sharp increase in viscosity above a certain surfactant concentration? The large increase in the viscosity above 0.08 volume fraction of surfactant solutions can be understood in terms of the structural changes of the micelles. It is known that upon increasing the surfactant concentration well beyond CMC, the motion of charged micelles are inhibited by their crowding, and the hydrated spherical micelles are deformed to rod-shaped micelles, resulting in an increase in viscosity.[289] A sphere to rod transition in SDS solution occurs at a concentration of 0.25 mole/litre ($\sim\varphi = 0.07$) at a temperature of 27 ºC.[316] The reported value of the aggregation number of SDS spherical micelle is 60 and for rod shaped micelles [formed above $\varphi = 0.07$ with a semi minor axis 17 Å (b=c) and semi major axis 35.8 Å] is approximately 106.[317] In the case of CTAB, the sphere to rod transition occurs at a concentration above $\varphi = 0.075$. [289, 318] The dramatic increase in the viscosity observed in SDS and CTAB micellar solution above $\varphi = 0.08$ confirms the formation of rod shaped micelles that are randomly packed. Such a sharp increase in the viscosity of the surfactant solution due to the formation of rod-like micelles was reported eailer.[317, 319, 320] A similar dramatic increase in viscosity due to rod shaped micelles is observed for NP9 and NP10 systems, above $\varphi = 0.07$. In general, the viscosity data follows Einstein model at dilute concentrations, where it assumes that the particles are rigid, uncharged, without attractive forces and are small enough so that the dilatational perturbation of the flow is unbounded to decay to zero.[321] A particle moves at the velocity of the streamline in line with the particle centre in such a suspension. The Einstein equation describes the dependence of viscosity increase with concentration of particles in the simplest case of dilute suspensions (≤ 0.01) as $\frac{\eta}{\eta_0} = 1 + 2.5\varphi$. For $\varphi \geq 0.01$, hydrodynamic interactions between particles become important as the disturbance of the fluid around one particle interacting with those around other particles. The viscosity in such a case is given by Batchelor equation $\frac{\eta}{\eta_0} = 1 + 2.5\varphi + 6.5\varphi^2$.[322] For $\varphi \geq 0.1$, the multi-particle collisions become increasingly important, a semi-empirical relationship for the shear viscosity covering the full range of particle volume fraction was obtained by Krieger and Dougherty $\frac{\eta}{\eta_0} = \left(1 - \frac{\varphi}{\varphi_m}\right)^{-[\eta]\varphi_m}$,[323] where, $[\eta]$ is the intrinsic viscosity, which is 2.5 for hard spheres and φ_m is the maximum packing fraction. For randomly mono-dispersed spheres, the maximum close packing fraction is approximately 0.64.

The Einstein, Batchelor and Krieger-Dougherty (KD) fit on the experimental data points are shown in the **Fig. 3.6 (b)**. The result shows that the enhancement in viscosity ratio with φ is much more than the values predicted by models at relatively large volume fractions. Since the number density increases with concentration, the interaction between the micelles at higher concentration becomes stronger, which has contributed to the observed deviation from the theoretical fit. It should be noted that the effectiveness of the nanofluid coolants depends on the flow modes (laminar or turbulent). Lower viscosity implies lower pumping power, which is advantageous from an industrial application standpoint. A quantitative expression derived for fully developed laminar flow that compares the relative coefficients of viscosity and *k* enhancement shows that the use of nanofluid will be beneficial if the increase in the viscosity is less than four times of the increase in *k*. Viscosity and thermal conductivity enhancements can be described by linear dependence on the particle volume fraction as $\frac{k}{k_f} = 1 + C_k \phi$ and $\frac{\eta}{\eta_0} = 1 + C_\eta \phi$ where C_k and C_η are constants. At low volume fractions, for the nanofluid to be beneficial for heat transfer applications, the ratio of coefficients (C_η/C_k) should be < 4.93. At 10 CMC (and 30 CMC), the ratio of viscosity to thermal conductivity increase for SDS, CTAB and NP9 are -6 (and -13), -3.7 (and -2.8) and 0.39 (and -0.26), respectively. These results suggest that the cationic and non ionic surfactants are better emulsifiers for optimal value of thermal to rheological property enhancements.

3.3.5 Effect of Surface Morphologies on Thermal Conductivity, Viscosity, Density and Refractive Index

The viscosity measurements clearly show that a morphological change (sphere to rod transition) occurs for all the surfactants above $\varphi = 0.07$. It may be seen from **Fig. 3.5** that the *k* is reduced drastically after $\varphi = 0.07$, which may be possibly due to the sphere to rod transition. **Fig. 3.6 (c&d)** shows the density and refractive index variation as a function of surfactant concentration for SDS, CTAB, NP9 and NP10. The morphological transitions in the surfactant solutions above $\varphi = 0.08$ is also evident in the density and refractive index measurements. From **Fig. 3.6 (c)**, it is seen that the density increases from 1.0013 to 1.0143 g/cm^3 as the concentration of SDS increases from $\varphi = 0.002$ to 0.08. Similarly in the case of CTAB, the density increases from 0.9988 to 1.0005 g/cm^3 while in the case of NP9, it increases from 0.999 to 1.0076 g/cm^3 for an increase in φ from 0.002 to 0.08. For the same increase in volume fraction, the density of NP10 increases from 0.9989 to 1.0054 g/cm^3. The large variation in the density of the surfactant solutions above 0.08 φ further corroborates the formation of rod shaped micelles. The refractive index **(Fig. 3.6 (d))** of the solutions also shows a systematic increase with concentration of surfactants in all four cases. Again a dramatic increase in the refractive index is observed above 0.08 φ. In the microconvection model, the convection velocity is taken to be the root-mean-square (rms) velocity of the nanoparticle. The root-mean-square velocity (v_N) of a Brownian particle can be defined as $v_N = \sqrt{\frac{18k_BT}{\pi\rho d^2}}$. Considering the micellar size, the maximum convection velocity is expected in SDS (size ~2.5 nm) and the least in NP9 (size ~6.5 nm). Therefore, in terms of micro-convection theory, the observed negative enhancement in k with volume fractions is consistent. However, it is intriguing that the effective medium theory holds good even after the morphological transformation (spherical to cylindrical micelles). Studies show that the cylindrical structure with large aspect ratio enhances the thermal conductivity of nanofluids compared to the spherical ones.[27, 147, 183] The aspect ratio of the suspended particles and the orientation of the particles with respect to the heat flow direction play a crucial role in k enhancement. In the case of magnetic nanofluids, alignment of nanostructures along the field direction can cause dramatic enhancement in the thermal properties due to parallel mode of conduction.[324] It should be noted that the aspect ratio, in the case of magnetic nanofluids, increases several orders of magnitude when they are subjected to a magnetic field. However, aspect ratio change in the case of surfactant micelles after transformation from spherical to cylindrical micelle is very small. In the case of SDS at 0.07 vol%, the semiminor and major axis are 1.7 nm and 3.58 nm, respectively.[317] Probably, the small changes in the aspect ratio and the lower k of the micelles have contributed to the observed good agreement between the experimental data and EMT prediction. On the basis of these results, the possible thermal resistance contributions from different moieties of the micelles (head group, tail and water molecules) are schematically shown in the inset in **Fig. 3.5**. The maximum interfacial resistance is offered by the hydrophobic tail part and minimum by the fluid molecules.

3.3.6 Effect of Surfactant on *k* Enhancement in Aqueous and Non Aqueous Metal Oxide Nanofluid

Aqueous Alumina Nanofluid: Fig. 3.7 shows the variation of k/k_f as a function of φ of Al_2O_3 nanofluids without surfactant and with surfactants CTAB and NP9 of 10, 70 CMC. The k/k_f for pure surfactants of CTAB and NP9 of same volume fractions (10 and 70 CMC) are also shown in the **Fig. 3.7** for comparison. The best fit using effective medium theory is shown by the solid line. Over all the experimental data fits fairly well with the EMT theory for various volume fractions of alumina nanofluids with and without surfactants, except a small deviation observed at higher volume fractions. The maximum thermal conductivity enhancement for nanofluids with a particle loading of 0.06 was ~14.4 %. The most striking observation was that though the k/k_f of the surfactant micellar solutions was lower than that of the basefluid, the k/k_f of the nanofluids with the same amount of soft spheres (micelles) is dictated by the thermal conductivity of the nanofluids. This is a very promising result in terms of industrial applications of surfactant stabilized nanofluids. To verify these intriguing results, the experiments are repeated for other nanofluids. The schematic representation of the system containing charged Al_2O_3 nanoparticles and surfactant micelles is depicted in the inset of **Fig. 3.7**.

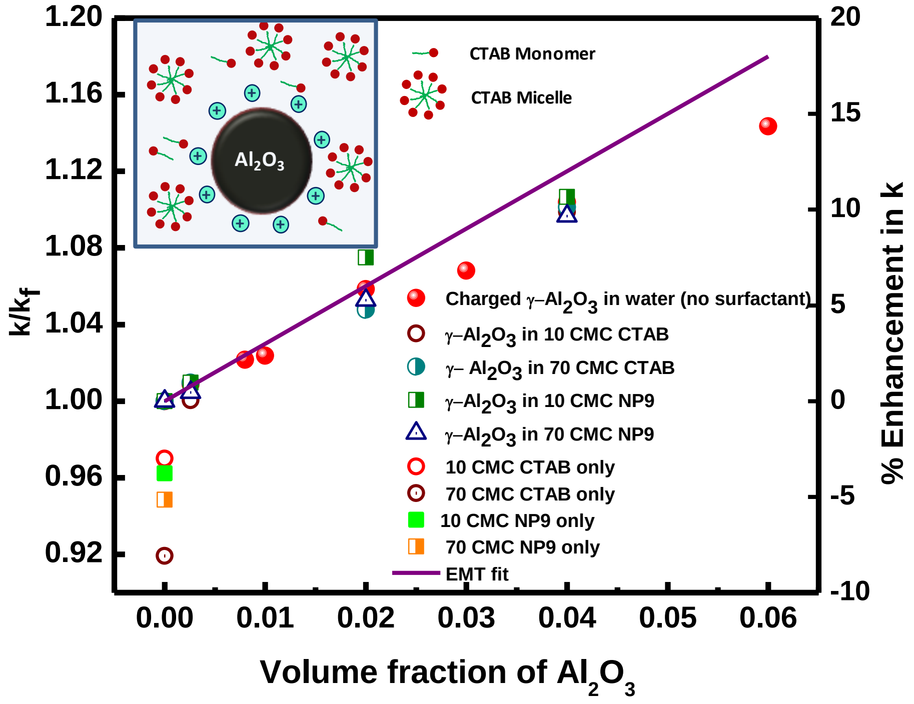

Figure 3.7: The variation of effective thermal conductivity as a function of alumina nanoparticle volume fraction without and with CTAB and NP9 along with the theoretical fit using (solid line) EMT. The inset in the figure shows the schematics of charged γ-Al_2O_3 in CTAB micellar solution.

Aqueous Silica Nanofluid: Fig. 3.8 shows the variation of k/k_f as a function of φ of SiO_2 nanofluids without surfactant and with surfactants SDS and NP9 of 5, 10 and 70 CMC. The k/k_f for pure surfactants of SDS and NP9 of the same volume fractions (5, 10 and 70 CMC) are also shown in the **Fig. 3.8** for comparison. The best fit using effective medium theory is shown by the solid line. The experimental data fits fairly well with the EMT theory upto 0.04 φ of SiO_2 with and without surfactants and the fit was poor at higher volume fractions. The maximum thermal conductivity enhancement for nanofluids with a particle loading of 0.1 was ~12.6 %.

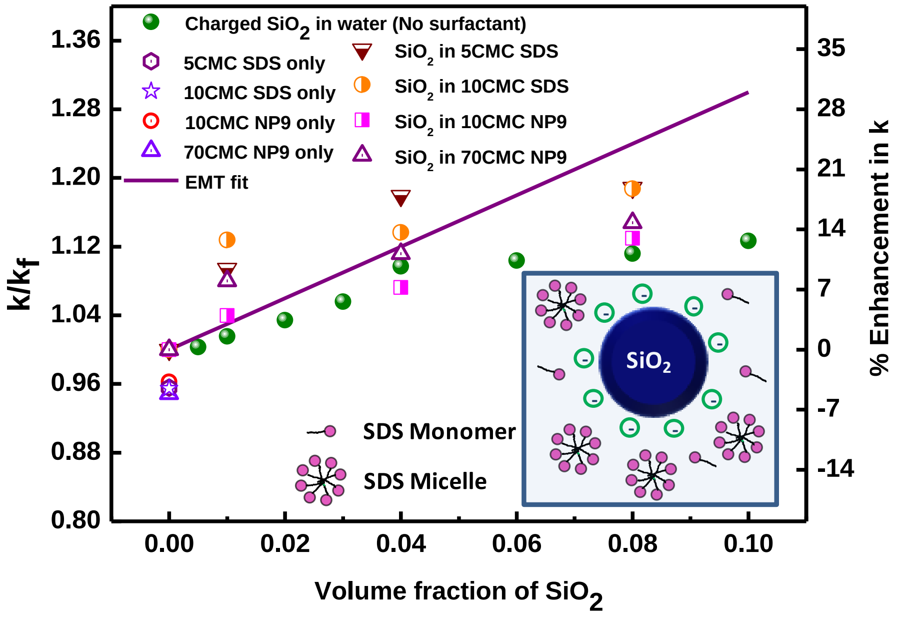

Figure 3.8: The variation of effective thermal conductivity as a function of SiO_2 nanoparticle volume fraction without and with SDS and NP9 along with the theoretical fit (solid line) using EMT. The inset in the figure shows the schematics of charged SiO_2 in SDS micellar solution.

Again, the k/k_f of the nanofluids with the same amount of soft spheres is dictated by the thermal conductivity of the nanofluids. The schematic representation of the system containing charged SiO_2 nanoparticles and surfactant micelles are depicted in the inset of **Fig. 3.8**.

Non-Aqueous Fe_3O_4 Nanofluid: Fig. 3.9 shows the variation of k/k_f as a function of φ of Fe_3O_4 nanofluids coated with 10 % oleic acid and 5,10 wt % of oleic acid in basefluid (kerosene). The best fit using effective medium theory is shown by the solid line. The experimental data fits fairly well with the EMT theory, especially above 0.04 φ of Fe_3O_4. The maximum thermal conductivity enhancement for nanofluids with a particle loading of 0.08 φ

was ~ 23.4 %. These results were consistent with the *k* enhancement observed in magnetic nanofluids, without external magnetic field.[11] On the contrary, very large enhancement in *k* is observed under magnetic field due to a parallel mode of conduction. Again, the k/k_f of the basefluid with the same amount of surfactant alone shows much lower value compared to the one with nanoparticles. The carboxylic acid group of oleic acid binds to the magnetite while the aliphatic chain extends out into the non-polar solvent thus providing steric hindrance between the particles. The charges at the carboxylate ion of oleic acid, de-localizes in between two oxygen atoms because of resonance effect.

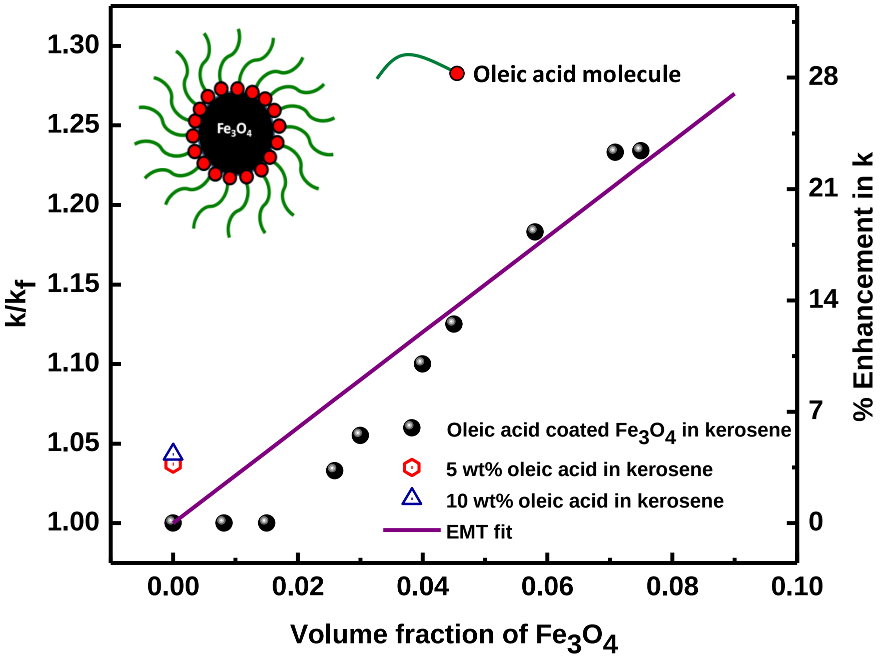

Figure 3.9: The variation of effective thermal conductivity as a function of Fe_3O_4 nanoparticle volume fraction along with the theoretical fit (solid line) using EMT. The schematic in the figure shows the oleic acid coated Fe_3O_4 particle.

The surfactant coating thus prevents the agglomeration of particles against van der Waals and magnetic attractive interactions. Besides, it passivates the nanocrystals against further oxidation. This once again confirms that the thermal conductivity of nanofluid is dictated by the thermal conductivity of the suspended particles. The schematic representation of the nanoparticles with adsorbed surfactant moieties is depicted in the inset of **Fig. 3.9**.

With and without surfactant, the k/k_f enhancement was almost the same in the case of alumina, silica and iron oxide nanofluids. It can be seen that the value of k/k_f enhancement with pure surfactant was negative, while it is positive at all concentrations of nanoparticles for all the three systems. In general the excess surfactant did not show a lowering of k of the nanofluid, though the surfactant alone in base fluids showed a negative enhancement. For example, SiO_2 nanofluid of 0.08 φ shows an enhancement of 13 % without any surfactant and an 18 % enhancement with SDS. This shows that the thermal conductivity of a nanofluid in presence of surfactant and nanoparticles simply follows the thermal conductivity of nanoparticles in the fluid and the addition of surfactant, even beyond optimal concentration would not lower the thermal conductivity of nanofluids significantly. Besides, the surfactant moieties on nanoparticles aid thermal conductivity enhancement and also improve the stability of nanofluids against agglomeration of suspended particles.

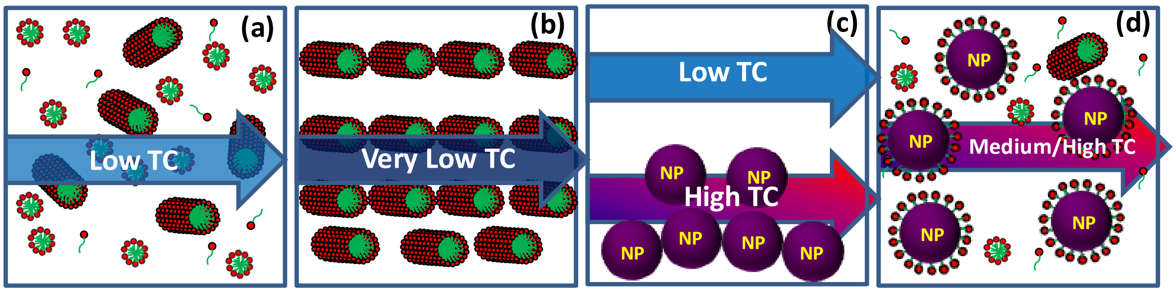

Figure 3.10: Schematic representation of nanofluids (a) ‘soft’ system with spherical and cylindrical micelles randomly arranged ($k_p<k_f$). (b) aligned cylindrical micelles ($k_p<k_f$). (c)

bare nanoparticle in basefluid ($k_p>>k_f$) and (d) surfactant coated nanoparticle in base fluid ($k_p>> k_f$).

Fig. 3.10 shows the schematic representation of nanofluids drawn based on the experimental findings. (a) 'soft' micellar system with spherical and cylindrical micelles randomly arranged ($k_p<k_f$). This scenario arises when the surfactant concentration is above the critical micellar concentration. Because $k_p<k_f$, the system shows a k/k_f <1 (b) Aligned cylindrical micelles at extremely large concentrations of surfactants (C>>CMC). Again, because $k_p<k_f$, the system shows a k/k_f <1. (c) Bare nanoparticle in basefluid ($k_p>>k_f$) where no surface active species are used. Due to agglomeration and subsequent settling, the heavy nanoparticles settles at the bottom of container.

Table 3.1: Thermal conductivity of bulk particle, base fluid, thermal conductivity ratio of nanofluid of different volume fraction and their corresponding % enhancement.

S. No	Material	*k* of bulk particle (W/m.k)	Base fluid	*k* of base fluid (W/m.k)	k/k_f of Nanofluid	% enhancement
1.	Fe_3O_4	9.7	Kerosene	0.116	1.1 (φ=0.04) 1.18(φ=0.06) 1.23(φ=0.07)	10 18 23
2.	Al_2O_3	35	Water	0.6	1.09(φ=0.02) 1.10(φ=0.04) 1.14(φ=0.06)	9 10 14
3.	SiO_2	1.4	Water	0.6	1.09(φ=0.04) 1.10(φ=0.06) 1.13(φ=0.08)	9 10 13

Here, two different conduction pathways are possible- one though the nanoparticle pathway where the k/k_f is high and the other through liquid pathway where the k/kf is low and (d) surfactant coated nanoparticle in base fluid (k_p>>k_f). Here, the surfactant moieties stabilize the nanoparticles thereby providing a stable suspension, where the k/k_f enhancement will be modest or high. However, conduction through percolating nanoparticle paths can carry heat much more effectively.[207] Thermal conductivity values of bulk particle, base fluid, nanofluids of different volume fractions and their respective percentage enhancement are listed in **Table 3.1**

3.4 Conclusions

The thermal properties of nanofluids containing soft spheres of surfactants with different head group charges and alkyl chain length are investigated. The contributions of interfacial resistance, density, viscosity and surface morphology of dispersed particles on thermal conductivity are also studied by using model soft systems of micelles in the size range of 2.5 to 7 nm. Our results show that the thermal conductivity variation of surfactant micelles with volume fraction fits well with the effective medium theory of poor thermal conductors. The long alkyl chain group of non-ionic surfactant micelles is found to be very poor thermal conductors at very low concentrations, with large interfacial tension compared to their anionic counterparts. Though a dramatic enhancement in viscosity is noticed at high concentrations, due to transformation of spherical micelles into cylindrical, the effective medium theory still holds good even after the morphological transformation. This may be probably due to the minor changes in the aspect ratio and poor k of the micelles as such. The k measurement in alumina, silicon dioxide and iron oxide nanofluids in presence of ionic and non ionic surfactants shows that the adsorbed surfactant does not influence the thermal conductivity enhancement in nanofluids. Further, the stabilizing moieties on nanoparticles do not reduce the thermal properties of nanofluids but it enhances the dispersibility and stability of nanoparticles in the base fluids. These finding will have important implications for producing efficient nanofluids with superior heat transfer properties.

Chapter IV

Effect of Nanoparticles Aggregation on Thermal and Electrical Conductivities of Nanofluids

4.1 Introduction

Nanofluids, which are colloidal dispersions of nanoparticles in traditional heat transfer fluids, have been attempted as a new class of coolants.[3, 5, 6, 11, 14, 19, 20, 24, 26-29, 32, 34, 38-40, 147, 260, 325, 326] The initial reports of anomalous thermal conductivity enhancement in nanofluids containing a small percentage of nanoparticles triggered interest in these material.[35, 38] Besides, nanofluids have several interesting applications in diverse fields, e.g. drug delivery and targeting,[327] cation and defect sensors,[328-330] mechanical sealing[54] etc. Along with the reported anomalous enhancement of k in nanofluids, several recent studies in stable nanofluids show enhancement within the Maxwell's limits.[10, 11, 14, 205, 207, 246, 248] Earlier reports suggest that linear and fractal aggregates lead to extra conduction paths which enhance the thermal conductivity of nanofluids.[9, 11, 191] Very recently, magnetically polarizable nanofluids have been shown to have tunable thermal properties,[178, 331] which are being exploited for innovative smart cooling applications.[133, 197, 332] Though there are some studies on electrical conductivity (σ) measurements in nanofluids,[333-337] the role of aggregation on σ of nanofluids is not investigated yet. To throw more light into the effect of aggregation on the physical properties of nanofluids, investigation of k, σ, viscosity and refractive index of four different aqueous nanofluids containing particles of similar size. Two of the nanofluids chosen for the present study were unstable (they phase separate within a short span of time after sonication) and the other two were stable (without sedimentation for a long period of time).

4.2 Materials and Methods

The water based γ-Al_2O_3 and TiO_2 nanofluids and aqueous SiO_2 and α- Al_2O_3 nanofluids are used in the present study. The thermal conductivity, electrical conductivity, size, viscosity, refractive index and TGA measurements were carried out. All the electrical conductivity measurements have been carried out at 25 °C. An inverted phase contrast microscope was used to obtain the microscopic images of nanofluids.

4.3 Results and Discussion

4.3.1 Dynamic Light Scattering and Thermogravimetric Analysis

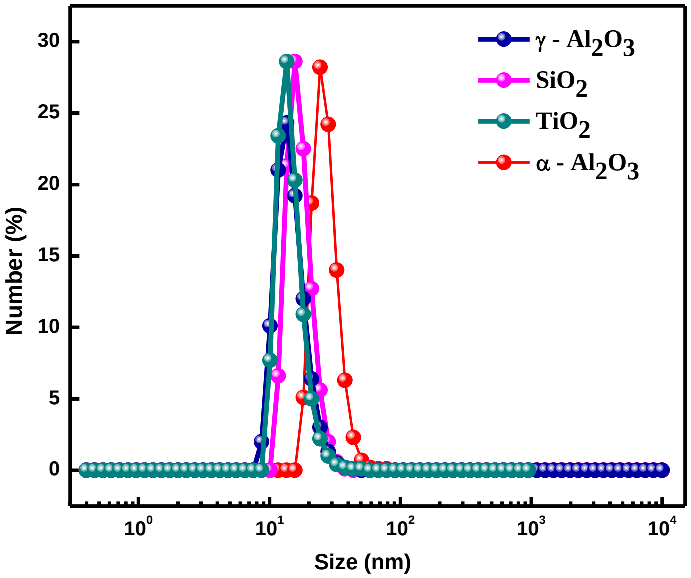

Figure 4.1: Hydrodynamic size distribution obtained for γ- Al_2O_3 , SiO_2, TiO_2 and α – Al_2O_3 nanofluids.

Fig. 4.1 shows the hydrodynamic size distribution of γ- Al_2O_3, SiO_2, TiO_2 and α – Al_2O_3 nanofluids. The average hydrodynamic sizes are found to be 13, ~15, ~13.5 and ~24.4 nm for γ-Al_2O_3, SiO_2, TiO_2 and α-Al_2O_3 nanoparticles, respectively. Overall, the size distribution is narrow for all the four nanofluids. The hydrodynamic size includes the contributions of surfactant and the hydration layer on the nanoparticles. The zeta potential values of γ- Al_2O_3 and SiO_2 were -30 and +25 mV, respectively. In TiO_2 and α – Al_2O_3 the zeta potential values were not measurable.

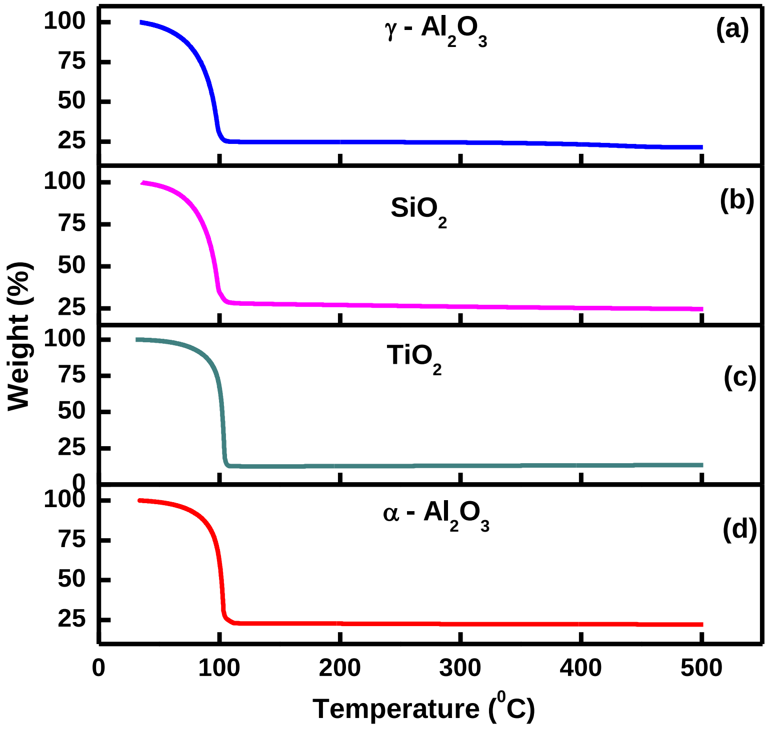

Figure 4.2: Thermogravimetric curves for (a) γ- Al_2O_3 (b) SiO_2, (c) TiO_2 and (d) α - Al_2O_3 nanofluids.

The thermogravimetric curves for water based γ- Al_2O_3, SiO_2, TiO_2 and α – Al_2O_3 nanofluids are shown in **Fig. 4.2**. The single step weight loss observed at ≈ 103 °C (~75 wt%), ≈ 105 °C (~72 wt%) , ≈ 108 °C (~87.4 wt%) and ≈ 110 °C (~77 wt%), for γ- Al_2O_3, SiO_2, TiO_2 and α – Al_2O_3, respectively is attributed to the loss of water (the amount is indicated in the respective brackets). Thereafter, a gradual decrease in weight is observed till 500 °C. The weight loss from 100 to 500 °C is about ~ 1, 4, 6 and 0.7 wt % for TiO_2, γ- Al_2O_3, SiO_2 and α – Al_2O_3 nanofluids, respectively. The higher weight loss observed in the case of γ- Al_2O_3 and SiO_2 system is due to the removal of surface active species present.

4.3.2 Thermal Conductivity

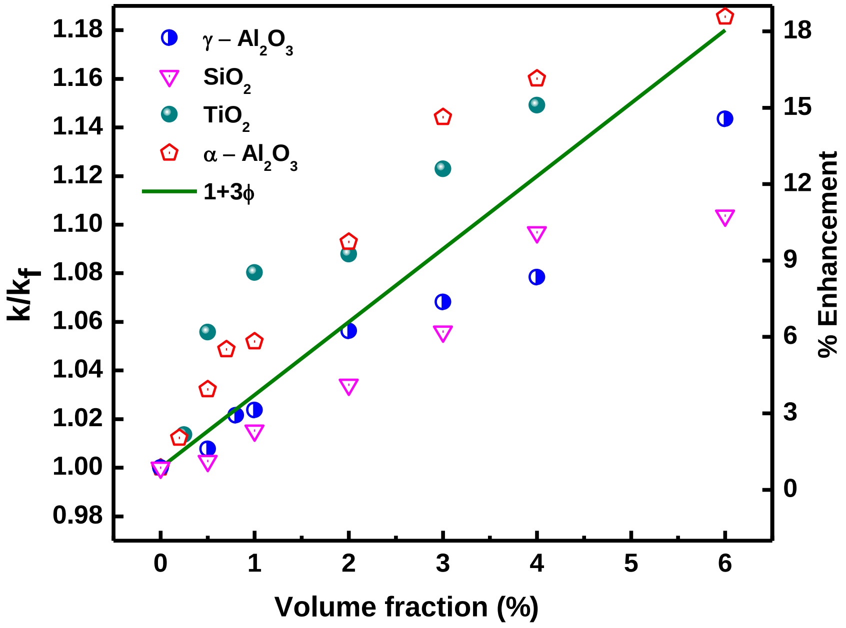

Figure 4.3: Variation of effective thermal conductivity as a function of volume fraction for γ- Al_2O_3, SiO_2, TiO_2 and α-Al_2O_3 along with the EMT theoretical fit.

Fig. 4.3 shows the k/k_f of nanofluids along with EMT theoretical fit as a function of volume fraction of γ- Al_2O_3, SiO_2, TiO_2 and α-Al_2O_3 nanoparticle. In all the four systems, the thermal conductivity increases with increase in volume fraction of nanoparticles. The experimental data are fitted with the effective medium theory. For γ- Al_2O_3 and SiO_2 nanofluids, the experimental data points falls within the EMT fit at lower concentration whereas the data points falls below the EMT fit at higher concentration. But in the case of TiO_2 and α Al_2O_3, the experimental data points are well above the theoretical fit for all concentrations.

The maximum thermal conductivity enhancement observed in 6 vol% of γ- Al_2O_3 and SiO_2 nanofluids are 14.3 and 10.4 %, respectively whereas it was 15 and 18.6 %, respectively for 4 vol% of TiO_2 and 6 vol% α-Al_2O_3 nanofluids. These results suggest that the non-aggregating nanofluids exhibit *k* within Maxwell limit while aggregating nanofluids exhibit *k* enhancement beyond the Maxwell limit. This was in good agreement with some of the earlier experimental findings.[148] These results suggest that the nature of the aggregates and the percolating conduction path dictate the *k* enhancement in nanofluids.

4.3.3 Electrical Conductivity

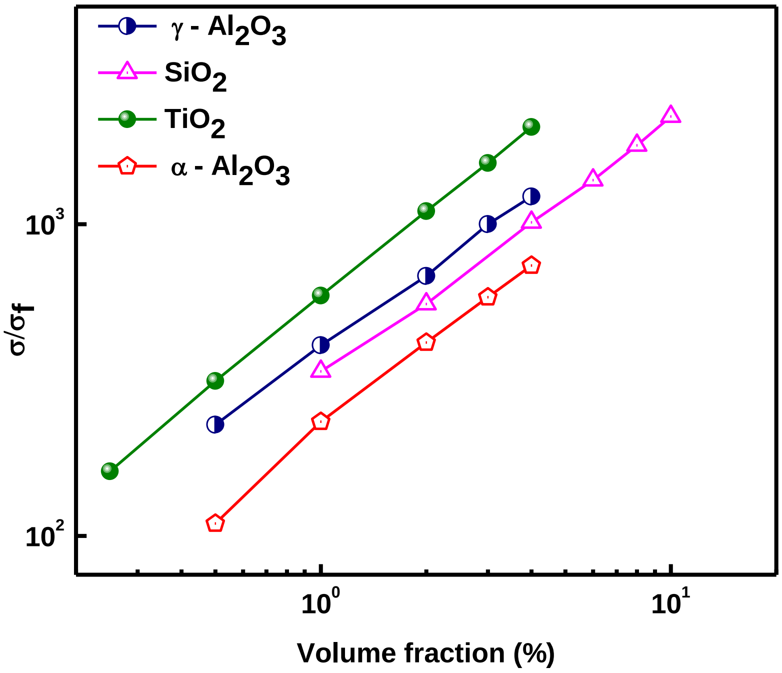

Figure 4.4: The variation of effective electrical conductivity as a function of volume fraction for γ- Al_2O_3, SiO_2, TiO_2 and α-Al_2O_3.

Fig. 4.4 shows the effective electrical conductivity (σ/σ_f) of four water based nanofluids as a function of volume fraction. The electrical conductivity of water, Al_2O_3, SiO_2 and TiO_2 are 5.5×10^{-6}, 10^{-14}, 10^{-18} and 10^{-12} S/cm, respectively. Though the electrical conductivity values of the base fluid, γ- Al_2O_3, SiO_2, TiO_2 and α-Al_2O_3 are low, the σ of the nanofluids are extremely high. This large enhancement cannot be explained using Maxwell theoretical model, which severely underestimates the observed enhancement. Therefore, the observed enhancement in σ should solely originate from the variation of electric double layer around each nanoparticle. The electrical double layer depends on the Debye length and the size of the particle. For larger electrical double layer, the larger the bulk electrical conductivity. The concentration of the ions in the base fluid, the particle size, and the charge on the nanoparticles dictates the conductivity of the nanofluid. Our study clearly shows that (a) the electrical conductivity of nanofluid increases almost linearly with the volume fraction of the nanoparticles (b) σ has a strong dependence on volume fraction of the particles and (c) the electrical conductivity of nanofluid cannot be explained by Maxwell theoretical model. The electrical conductivity enhancement observed is 5218 %, 4366 %, 3142 % and 8876 % for 4 vol% of γ- Al_2O_3, SiO_2, α- Al_2O_3 and TiO_2, respectively. No clear trend is observed in the σ enhancement in stable and unstable nanofluids. Also, it is not clear how the agglomeration of particle affects the electrical conductivity of the nanofluids. More systematic studies are required to obtain further insights.

4.3.4 Viscosity

Fig. 4.5 shows the viscosity as a function of shear rate for the water based nanofluids of different volume fractions. In all the four systems, the viscosity increases with increase in volume fraction of nanoparticles. In general, the addition of nanoparticles in the base fluid increases the viscosity of the nanofluid, as a result of either the occlusion of the solvent within the temporary nanoparticle clusters or due to the increase in the number density. The liquid occluded within the clusters does not participate in the flow, thus increasing the effective solid phase concentration.[338-341] This is the reason for the observed increase in viscosity. The γ- Al_2O_3 and SiO_2 nanofluids exhibit almost Newtonian behavior for all volume fractions in the shear rate range of 1 to 100 s^{-1}. This is yet another confirmation that the particles in these nanofluids are non-aggregating. However, in the case of TiO_2 and α-Al_2O_3 nanofluids a shear thinning behavior is observed.

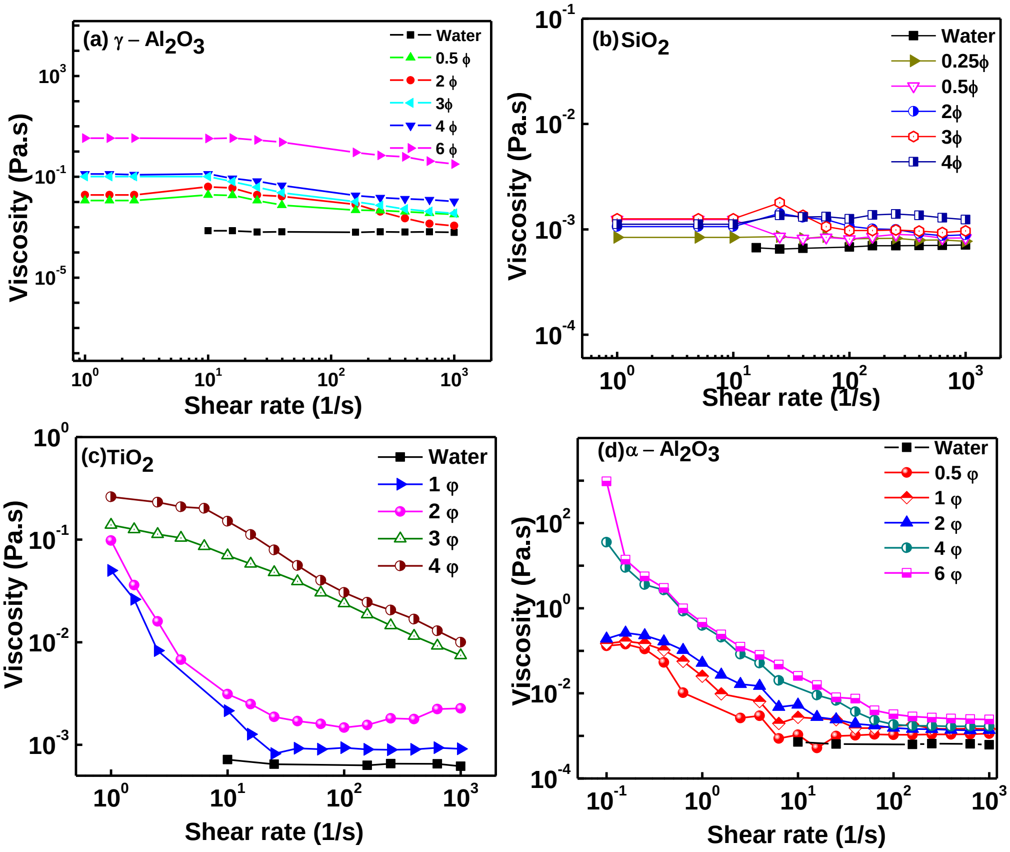

Figure 4.5: Viscosity as a function of shear rate for (a) γ – Al_2O_3, (b) SiO_2, (c) TiO_2 and (d) α- Al_2O_3 nanofluids of different concentrations.

The van der Waals attraction between the particles leads to the formation of dense aggregates (reversible) with a significant number of nearest neighbors which exhibit complex responses to applied flows and osmotic stresses. In such cases, the hydration layer between the particles within the aggregates provides a slippery bond that is not shear resistant.[342] Tsenoglou [338] reported that with increasing shear rates the clusters are broken down by the hydrodynamic forces allowing the entrapped solvent to flow, thus reducing the viscosity. Thus, the sample exhibits a shear thinning behavior. The shear thinning behavior is observed up to a shear rate of 10 s^{-1} followed by a Newtonian region for α-Al_2O_3 nanofluid. At higher shear rate, Newtonian regime occurs due to the breaking down of clusters into primary particles. But in the case of TiO_2 nanofluids shear thinning behaviors is observed even at the higher shear rates for higher volume fraction (3φ & 4φ), which indicates that the clusters are not fully destroyed by the hydrodynamic forces. The rheological results provide the evidence for the presence of aggregates or clusters in α-Al_2O_3 and TiO_2 nanofluids. This is in agreement with the thermal conductivity result where the thermal conductivity of γ- Al_2O_3 and SiO_2 nanofluids are well below the Maxwell's model whereas the thermal conductivity of TiO_2 and α-Al_2O_3 nanofluids are well above the Maxwell's model. **Fig. 4.6** shows the reduced viscosity as a function of nanoparticle concentration for γ- Al_2O_3, SiO_2, TiO_2 and α-Al_2O_3. In all the four systems, the viscosity increases with increase in nanoparticle concentration. The Einstein, Batchelor and Krieger-Dougherty (KD) fit on the experimental data points are also shown in the **Fig. 4.6**. The experimental data points show large deviation from the theoretical model at higher volume fractions for all the four nanofluids. Since the number density increases with concentration, the interaction between the nanoparticles at higher concentration becomes stronger, which would have contributed to the observed deviation from the theoretical fit.

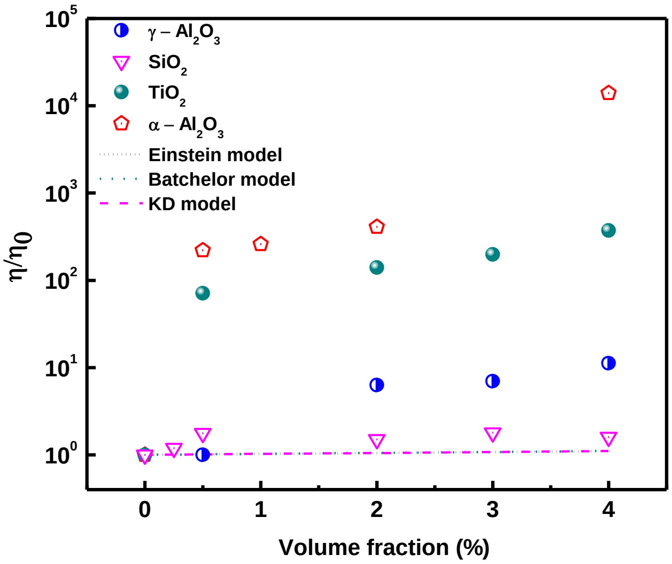

Figure 4.6: The reduced viscosity as a function of volume fraction of nanoparticles along with the theoretical fits using Einstein, Batchelor and Krieger & Dougherty models.

It is worth to note that the theoretical models are ideal for dilute suspension where the interaction between the nanoparticle is less or negligible. At the highest volume fraction (4φ) the reduced viscosity is about two to four orders of magnitude higher than that of the base fluid for TiO_2 and α-Al_2O_3, while only a moderate increase in reduced viscosity is observed for γ- Al_2O_3 and SiO_2 nanofluids.

4.3.5 Phase Contrast Optical Microscopy

To obtain macroscopic evidence of the aggregation in nanofluids, the phase contrast microscopic images are taken for different volume fractions for all the four nanofluids. **Fig. 4.7** shows the microscopy images of water based nanofluids taken at different volume fractions after sonication for 2 mins. The micrographs confirm that the cluster formation takes place in the case of TiO_2 and α-Al_2O_3 nanofluids whereas in the case of γ- Al_2O_3 and SiO_2 nanofluids no such clusters are observed. Even at very high concentrations, no micron sized aggregates are seen in the case of γ- Al_2O_3 and SiO_2 nanofluids.

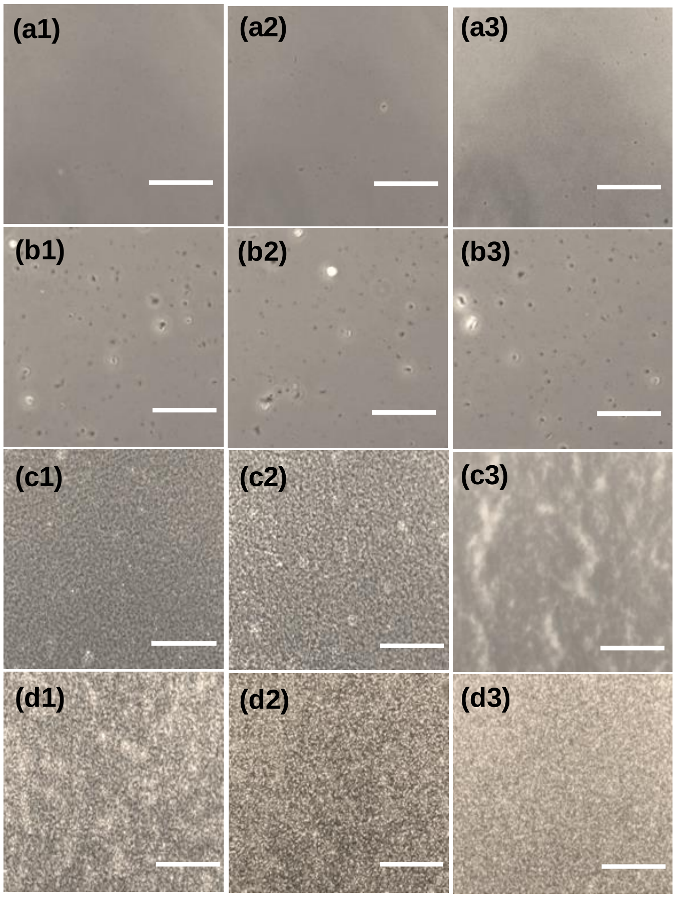

Figure 4.7: Phase contrast optical microscopic images of γ–Al_2O_3 (a1= 0.5φ, a2=2φ and a3= 6φ), SiO_2 (b1= 0.5φ, b2=4φ and b3= 6φ), TiO_2 (c1= 0.7φ, c2= 2φ and c3= 4φ) and α- Al_2O_3 (d1= 0.25φ, d2= 2φ and d3= 4φ) at different volume fractions. The scale bar in each figure corresponds to 10 microns.

This means that if at all aggregates exist in these nanofluids, their size is much less than a micron. But in the case of TiO_2 and α-Al_2O_3 nanofluids, the electrostatic stabilization seems to be not effective which leads to van der Waals attraction and aggregation of particles.

4.3.6 Refractive Index

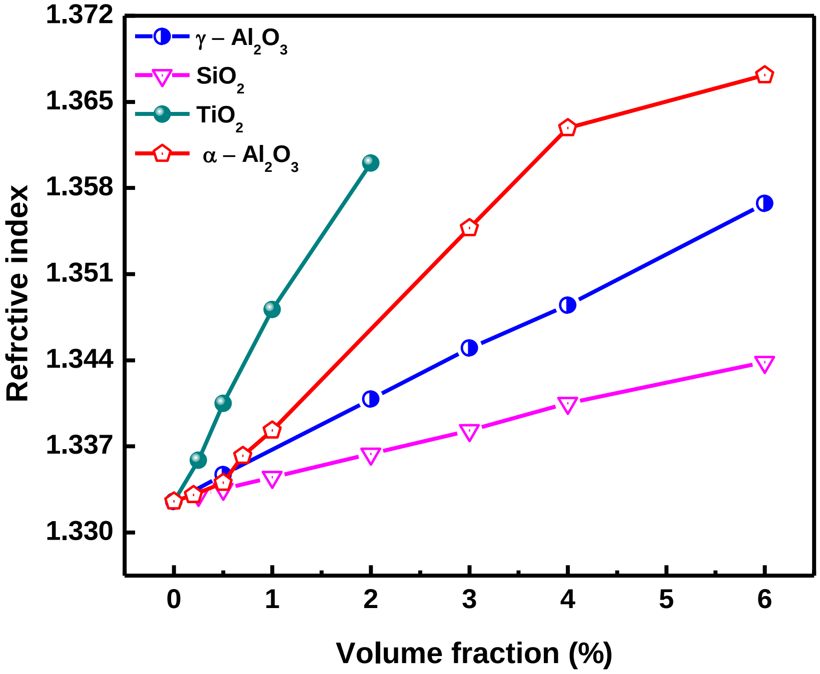

Figure 4.8 : Refractive index as a function of volume fraction for γ – Al_2O_3, SiO_2, TiO_2 and α- Al_2O_3 nanofluids.

Fig. 4.8 shows the variation of refractive index with volume fraction of γ –Al_2O_3, SiO_2, TiO_2 and α- Al_2O_3. In all the four systems the refractive index increases with increase in volume fraction of nanoparticle. The refractive index value is very high in the case of TiO_2 and α-Al_2O_3 nanofluids when compared to that of γ- Al_2O_3 and SiO_2 for the same volume fraction of nanoparticles. The dramatic increase in refractive index observed should be due to the presence of aggregates in these systems as the nanomaterial always has a higher refractive index than that of the base fluid.[343, 344] The presence of aggregates in the system increases the local density of TiO_2 and α-Al_2O_3 nanofluid resulting in a dramatic increase in refractive index. The refractive index measurements further confirm the presence of aggregates in TiO_2 and α-Al_2O_3 nanofluids.

4.3.7 Time Dependant Thermal Conductivity Measurements

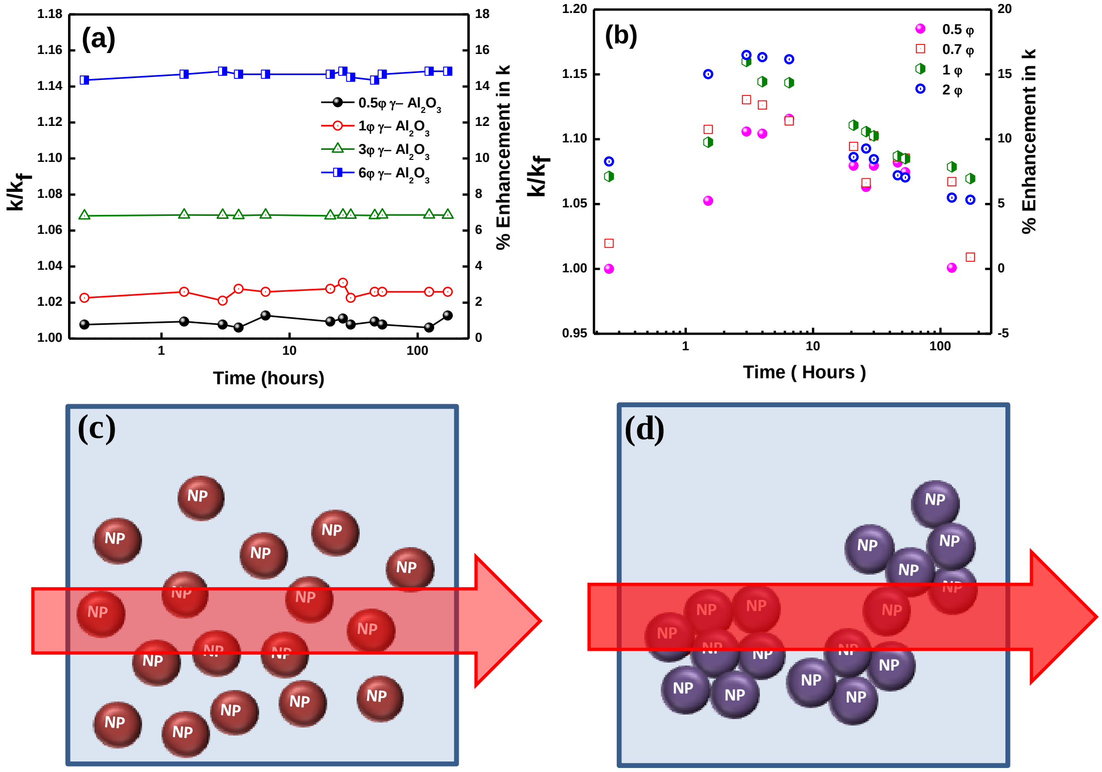

Figure 4.9: Time dependent effective thermal conductivity for (a) γ – Al_2O_3 and (b) α- Al_2O_3 nanofluids for different volume fractions. Schematic representation of the distribution of particles in (c) non-aggregating and (d) aggregating nanofluids.

In order to understand the effect of aggregates on the thermal conductivity of nanofluids, time dependent thermal conductivity measurements were done in γ- Al_2O_3 and α-Al_2O_3 nanofluids. The **Fig. 4.9 (a)** shows the variation of k/k_f and the % of enhancement with time, after 2 min of sonication at four different particle concentrations of 0.5, 1, 3 and 6 vol% for γ- Al_2O_3 nanofluid. Here, k/k_f increases with the particle loading and is found to be time independent. **Fig. 4.9 (b)** shows the variation of k/k_f and the percentage of enhancement in k with time, after 2 min of sonication at four different particle concentrations (0.5, 0.7, 1, and 2 vol%) for α-Al_2O_3 nanofluid. The k/k_f increases with time and reaches a peak value after a time interval of about 3 hours and then starts decreasing with time. Both, the increase and decrease in k/k_f can be explained on the basis of cluster formation. Immediately after sonication the particles are well dispersed. With time, the particles start forming clusters which leads to an increase in thermal conductivity because the conduction is effective through percolating conducting path of aggregates.[59] With increasing time, due to strong interaction between the clusters, the clusters tend to come closer and form thick agglomerates, which eventually sediment due to gravitational force. The maximum enhancement observed (~3 hours) for particle loading of 0.5, 0.7, 1 and 2 vol% are 10.6, 13, 16 and 16.5 %, respectively. After 3 hours, the k/k_f starts decreasing. Earlier studies show that the nanoparticles tend to aggregate when the surface charge on the nanoparticle is relatively small leading to a decrease in thermal conductivity of nanofluids.[189] The aggregation and the subsequent settling of clusters leads to a decrease in k with elapsed time. The schematic representation of distribution of particles in the non-aggregating and aggregating nanofluids is shown in **Fig. 4.9 (c-d).**

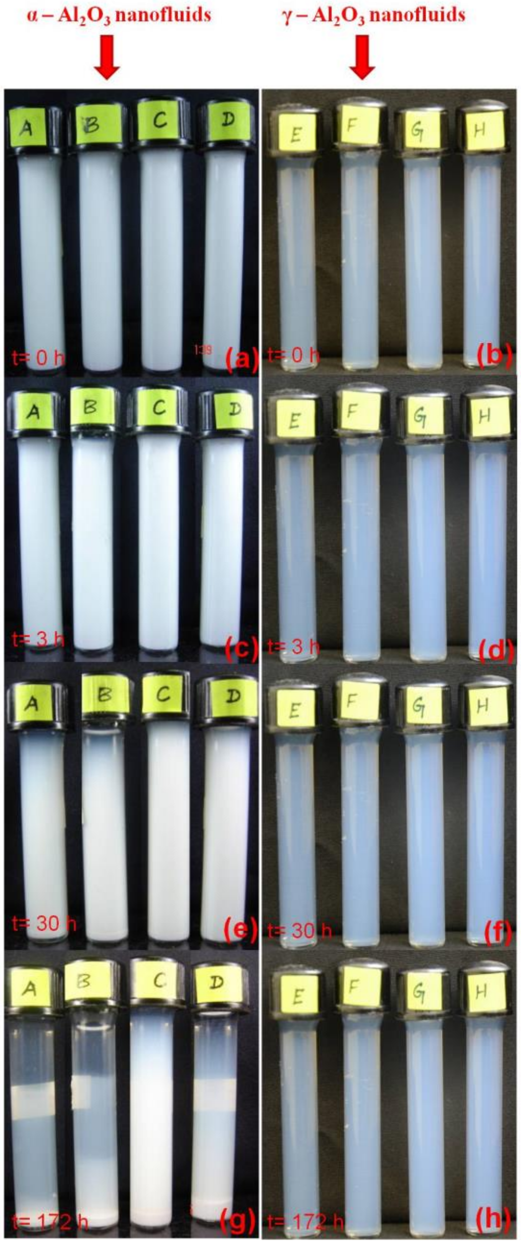

Figure 4.10: Photographs of different volume fractions (0.5, 0.7, 1 and 2φ) of α- Al_2O_3 (A-D) and γ- Al_2O_3 nanofluids (E-H) at different volume fractions (0.5, 1, 3 and 6φ). **Fig. 4.**10 (a&b) are taken immediately after sonication, **Fig. 4.10** (c&d), (e&f) and (g&h) are taken at 3, 30 and 172 hours, respectively after sonication.

Fig. 4.10 (a, c, e & g) shows the photographs of 0.5, 0.7, 1 and 2φ of α- Al_2O_3 nanofluids. **Fig. 4.10 (b, d, f & h)** shows the photographs of 0.5, 1, 3 and 6φ of γ- Al_2O_3 nanofluids at different time intervals. **Fig. 10 (a & b)** is taken immediately after sonication, **Fig. 4.10 (c & d), (e & f) and (g & h)** are taken at 3, 30 and 172 hours, respectively after sonication. From the photographs it is clearly seen that no noticeable phase separation occurs until 3 hours in both the systems. On the contrary, the particles start settling in the case of α- Al_2O_3 nanofluids. After 172 hours, there is a complete phase separation for all volume fractions of α- Al_2O_3 (**Fig. 4.10 g**). This is in agreement with our time dependent thermal conductivity measurements, where the thermal conductivity is less, immediately after sonication but starts increasing with time and achieves the maximum value around 3 hours after sonication. As time increases further, the thermal conductivity decreases again. This is due to the fact that immediately after sonication, the particles are well dispersed. As time elapses the particles tend to come closer and start forming aggregates due to weak van der Waals attraction. Hence, the thermal conductivity increases with time due to the effective conduction of heat through the nanoparticle aggregates. As the time increases further, the aggregates coalesce to form bigger aggregates or clusters that eventually settle down due to gravity leading to a decrease in the thermal conductivity. On the other hand no visible settling is observed in the case of γ- Al_2O_3 (**Fig. 4.10 (b, d, f & h**)).

4.4 Conclusions

Thermal and electrical conductivity measurements were carried out in four water based γ-Al_2O_3, SiO_2, TiO_2 and α-Al_2O_3 nanofluids at different particle loading. It is observed that the thermal conductivity increases with increase in volume fraction in all the four cases. The thermal conductivity values of stable nanofluids are found to be well below EMT predictions whereas it is above EMT predictions for unstable nanofluids. The aggregating behavior of TiO_2 and α-Al_2O_3 nanoparticles was evident from the shear thinning behavior whereas a Newtonian behavior is observed in γ- Al_2O_3 and SiO_2 nanofluids. Electrical conductivity of the nanofluids is found to increase with increase in volume fraction. The refractive index and phase contrast microscopic results also confirm the aggregation in TiO_2 and α-Al_2O_3 nanofluids. The microscopy study confirms no noticeable aggregate formation in γ- Al_2O_3 and SiO_2 nanofluids. Time dependent studies show that the non-aggregating nanofluids exhibit time independent k/k_f whereas aggregating nanofluids exhibit a time dependant k/k_f.

Chapter V

Effect of Nanoparticle Size, Morphology and Concentration on Specific Heat Capacity of Nanofluids

5.1 Introduction

Nanofluids have been a topic of intense research during the last one decade due to their interesting thermophysical properties and anticipated applications in heat transfer.[2, 5, 12, 18-20, 23, 38, 147, 345-349] Several factors affect the heat transfer properties of nanofluids that include thermal conductivity, viscosity, heat capacity, density and diffusion coefficient. For effective utilization of nanofluids for practical heat transfer applications, a synergetic balance of these thermophysical properties is a prerequisite. Though the thermal properties of nanofluids are investigated intensely, the studies on heat capacity of nanofluids are scarce.[221, 223, 224, 227, 350] A knowledge of specific heat capacity and thermal conductivity is important in order to understand the heat transfer properties of nanofluids. Nanofluids with higher heat capacities are necessary to enhance heat transfer efficiency at lower operating costs. Thermal diffusivity, thermal conductivity and specific heat capacity are inter-related as $C_p = \frac{k}{D\,\rho}$.

Unlike solids and gases, the accurate determination of heat transfer parameters in nanofluids is complex. So far, thermal conductivity studies have been the main focus of nanofluid research.[220] An increase of thermal conductivity is necessary but not a sufficient condition for achieving high performance in heat exchange equipments. The specific heat capacity determines the rate at which the substance will heat up or cool down.[351] As the heat capacity of a material is directly related to the atomic structure, measurements of heat capacity as a function of temperature could provide structural properties of nanostructured materials.[352] In ultrafine particles, both bulk and surface phonon modes contribute to the vibrational specific heat. As the surface area to volume ratio increases, the surface mode contribution plays a prominent role over the bulk modes. Studies show that the specific heat in nanocrystals increases upto 20 % under an increase of atomic-level strain due to changes in the vibrational and configurational entropy due to large anharmonic atomic vibrations at grain boundaries and disordered lattice sites.[353]

There are several studies which reports the strong and weak dependence of C_p on the volume fraction of nanoparticles. Yang et al.[354] reported that at low volume fraction and moderate temperature change, the heat capacity of nanofluid doesn't change much when compared to the base fluid. Several studies report a decrease in the heat capacity with increase in volume fraction.[220-222] Yang et al.[355] reported an increase in specific heat capacity with the increase in temperature. Shin et al.[224] observed a 32 % increase in specific heat capacity in a eutectic salt mixture on dispersing alumina nanoparticles at 1 % mass concentration. The objective of the present work is to systematically study the effect of volume fraction, properties of dispersed particle (density, thermal conductivity, morphology etc.) on the specific heat capacity of nanofluids for a better understanding of their utility in heat transfer applications such as concentrating solar power and waste heat recovery.

5.2 Materials and Methods

For the present study, kerosene based Fe_3O_4 and PAO based Al_2O_3 nanofluids (nanospheres and nanorods) are used. The Fe_3O_4 nanofluids are prepared in our laboratory using coprecipitation approach. The synthesis procedure is briefly discussed in **Chapter 2**. Fe_3O_4 nanoparticles and Al_2O_3 nanospheres were used to study the effect of particle volume fraction on the specific heat capacity. The effect of particle morphology on the specific heat capacity of nanofluids was studied using Al_2O_3 nanospheres and nanorods. The effect of particle size on the specific heat capacity of nanofluids was studied using Fe_3O_4 nanoparticles of size varying from 2.3 to 8.5 nm. The Al_2O_3 and Fe_3O_4 nanoparticles were characterized for their phase identity by XRD. The size distribution of the nanoparticles was determined by DLS. The thermogravimetric analysis of the nanofluids was carried out under inert atmosphere from 40 – 100 ºC at a heating rate of 2 ºC/min. Measurements of Specific Heat Capacity is carried out as described in **Chapter 2**.

5.3 Results and Discussion

5.3.1 Nanoparticles Characterization by XRD, DLS and TGA

Fig. 5.1 (a) and **5.1 (b)** show the XRD patterns of Al_2O_3 (sphere) and Fe_3O_4 nanoparticles, respectively. The diffraction peaks of (120), (031), (051), (151), and (002) were indexed to an orthorhombic structure of Al_2O_3 (JCP DS card no: 21-1307).

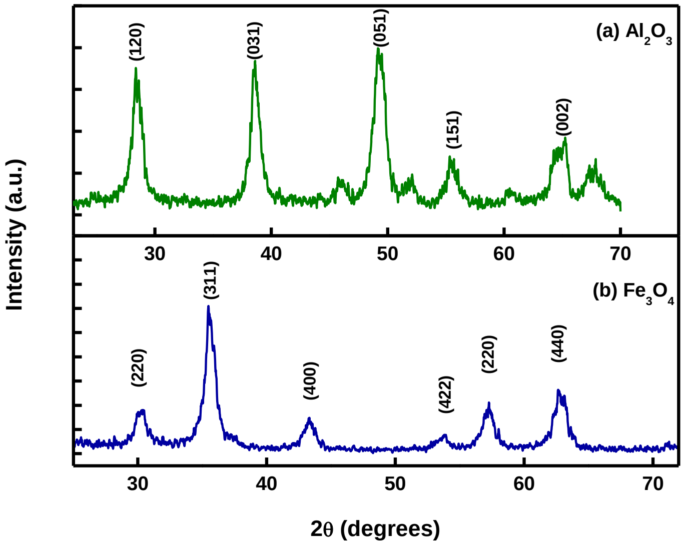

Figure 5.1: XRD patterns of (a) Al_2O_3 and (b) Fe_3O_4 Nanoparticles.

The diffraction peaks of (220), (311), (400), (422), (511), and (440) were indexed to a cubic spinel structure of Fe_3O_4 (JCP DS card no: 89-3854). An inverse spinel structure consists of oxide ions that form a cubic close-packed arrangement in which 1/3 of tetrahedral interstices and 2/3 of octahedral interstices coordinate with oxygen. The parallel alignment of Fe^{2+} and Fe^{3+} ions spin in the adjacent octahedral sites leads to a net magnetization and thus a ferri-magnetic behavior[356].

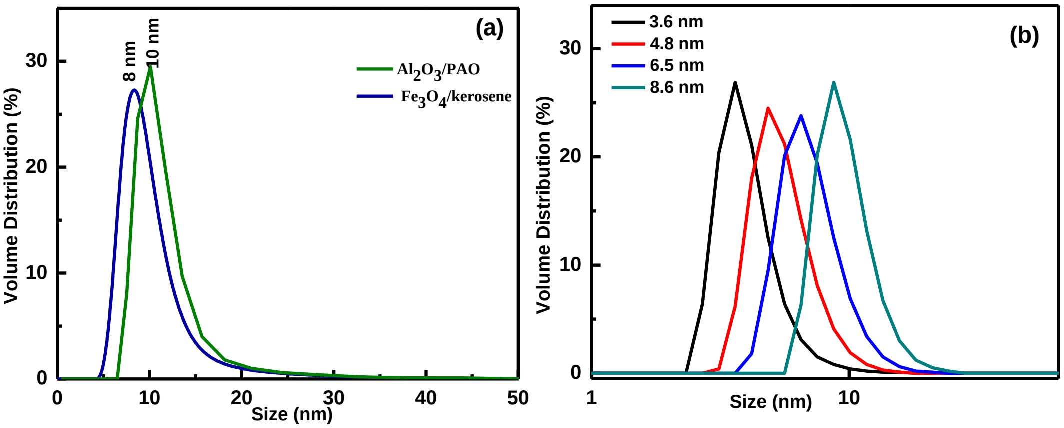

Figure 5.2: (a) Volume averaged hydrodynamic size distribution of Fe_3O_4 and Al_2O_3 nanoparticles. (b) Volume averaged hydrodynamic size distribution of Fe_3O_4 nanoparticles of different size.

Fig. 5.2 (a) shows the hydrodynamic diameter of the PAO based Al_2O_3 and kerosene based Fe_3O_4 nanofluids. The average hydrodynamic sizes are found to be 10 and ~ 8 nm for Al_2O_3 and Fe_3O_4 nanoparticles, respectively. The size distribution is found to be narrow for both Al_2O_3 and Fe_3O_4 nanofluids. The time dependent hydrodynamic measurements carried out in these systems showed a time independent hydrodynamic size, which indicate the good stability of the dispersions.[148] **Fig. 5.2 (b)** shows the hydrodynamic size distribution of

Fe_3O_4 nanoparticles of different sizes synthesized with different solvent dielectric constants. The hydrodynamic diameters of particles prepared with ethanol water ratio of 20:80, 40:60, 50:50 and 60:40 are found to be 3.6, 4.8, 6.5 and 8.6 ± 0.8 nm, respectively.

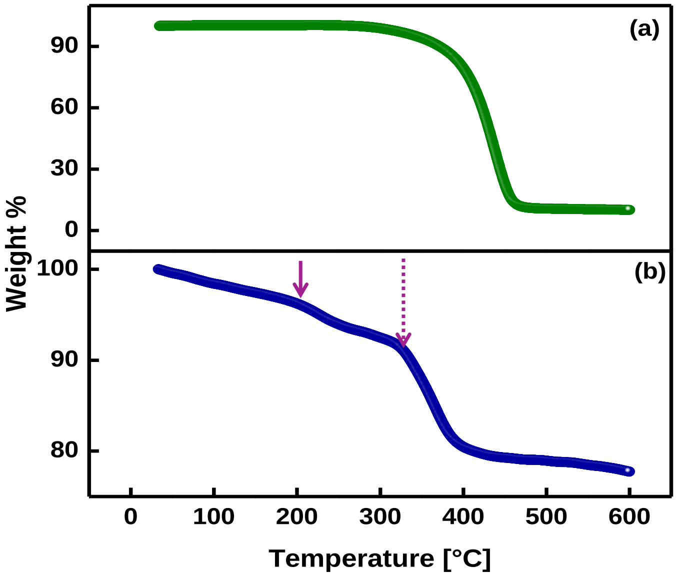

Figure 5.3 : Thermogravimetric curves for (a) PAO based Al_2O_3 nanofluid and (b) oleic acid coated Fe_3O_4 nanoparticle.

The thermogravimetric curve for PAO based Al_2O_3 nanofluid in **Fig. 5.3 (a)** shows a single step weight loss at ≈ 468 °C (~88 wt%) due to the decomposition of PAO. The TGA curve for the Fe_3O_4 nanoparticles shows a two-step weight loss between 199-310 °C (~ 4 wt%) and 310-400 °C (~12 wt%) **Fig. 5.3 (b)**. The first step (solid arrow) is due to the removal of loosely bound or free surfactant and the second step (dotted arrow) should be due to the removal of strongly bound surfactant molecules.

5.3.2 Effect of Volume Fraction of Nanoparticles on the Specific Heat Capacity of Nanofluids

The variation of absolute specific heat capacity with temperature for different concentrations and the ratio of the specific heat capacity of nanofluid ($C_{p,nf}/C_{p,bf}$) with respect to the C_p of base fluid for kerosene based nanofluids are shown in **Fig. 5.4 (a)** and **Fig. 5.4 (b)**, respectively.

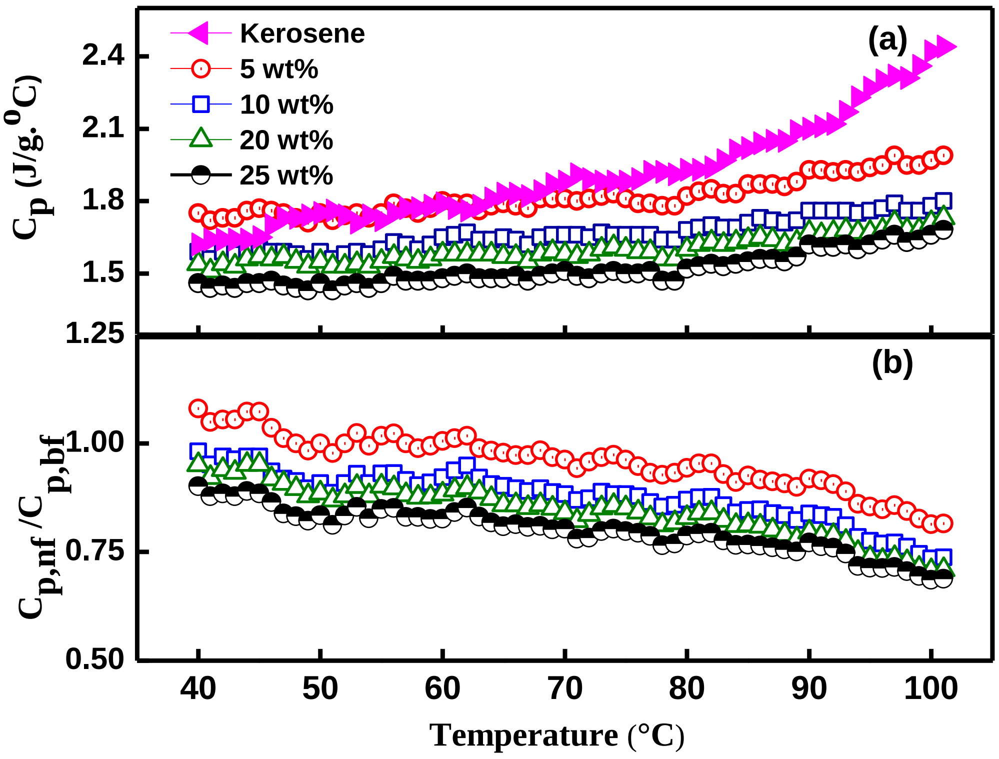

Figure 5.4: (a) The variation of specific heat capacity with temperature for different concentration of kerosene based Fe_3O_4 nanofluids. (b) Specific heat capacity ratio as a function of temperature for different concentration of Fe_3O_4 nanoparticles.

Fig. 5.4 shows a marginal increase in the specific heat capacity with increase in temperature. As the nanoparticle concentration increases, the specific heat capacity of the kerosene based

Fe_3O_4 nanofluid is found to decrease. In general, the specific heat capacity of nanofluids can be explained using two models. The model I, which is similar to the mixing theory for ideal gas mixtures,[228] calculates the specific heat of nanofluids ($C_{p,nf}$) by averaging the C_p of the base fluid ($C_{p,bf}$), the C_p of nanoparticle ($C_{p,np}$) and its volume fraction. According to model I,

$$C_{p,nf} = \varphi C_{p,np} + (1-\varphi)C_{p,bf} \tag{5. 1}$$

This equation has been used for the evaluation of heat transfer behavior of nanofluids in many experiments[37, 357] and also in theoretical simulations.[358-360]

In Model II, $C_{p,nf}$ is derived by assuming thermal equilibrium between particles and the surrounding fluid, using classical and statistical mechanics.[220] According to Model II,

$$C_{p,nf} = \frac{\varphi(\rho c_p)_n + (1-\varphi)(\rho C_p)_f}{\varphi\rho_n + (1-\varphi)\rho_f} \tag{5. 2}$$

where, ρ_n and ρ_f are the particle and fluid densities, respectively and the nanofluid density ρ_{nf} is given by,

$$\rho_{nf} = \frac{m_{nf}}{V_{nf}} = \rho_n + (1-\varphi)\rho_f \tag{5. 3}$$

where, m_{nf} and V_{nf} are the mass and volume, respectively of the nanofluid. The specific heat of the bulk and nanosized Fe_3O_4 are 0.6512 and 0.79 J/g. °C, respectively.[361] The specific heat capacity of pure kerosene is 2.01 J/g. °C.[362] According to the theoretical model I, the effective specific heat of the nanofluid should be lower than the specific heat of pure kerosene. Here, the lower specific heat of nanoparticles in the base fluid results in a decrease in specific heat capacity of the nanofluid with increase in particle concentration. An earlier study showed a similar decrease in the heat capacity of nanofluid with increase in volume concentration and an increase with temperature in kerosene based iron oxide nanofluids.[218] Such a behavior was also observed in CuO nanofluids where the constrained liquid layering at the surface of nanoparticle free boundary is attributed as the cause for the variations in the Gibbs free energy and change in specific heat capacity. Studies on the effect of volume fraction on the specific heat capacity of water-based Al_2O_3 nanofluid showed that the specific heat capacity decreases with increase in particle concentration.[220] Studies also conclude that, the solid-liquid interfacial conformation plays a critical role in the heat capacity changes because of the changes in the phonon vibration mode at the interface.[223] Murshed et al.[20] reported that the thermal diffusivity of nanofluids increases significantly with increasing volume fraction of nanoparticles in the case of TiO_2, Al_2O_3 and aluminum nanoparticles dispersed in ethylene glycol and engine oil. Their study revealed that the particle size and shape can influence the effective thermal diffusivity of nanofluids. Zhang et al.[363] observed an increase in the thermal diffusivity with particle concentration in Au/toluene, Al_2O_3/water and CNT/water nanofluids.

Fig. 5.5 shows the variation of $C_{p,nf}$ of kerosene based Fe_3O_4 nanofluids along with theoretical fit using Model I and Model II at different temperatures. **Fig. 5.5** shows that the experimental data fits better with the Model II than Model I. Similar agreement with model II was observed by Zhou et al. [220] in water based Al_2O_3 nanofluid and Higano et al.[218] in kerosene based Fe_3O_4 nanofluid.

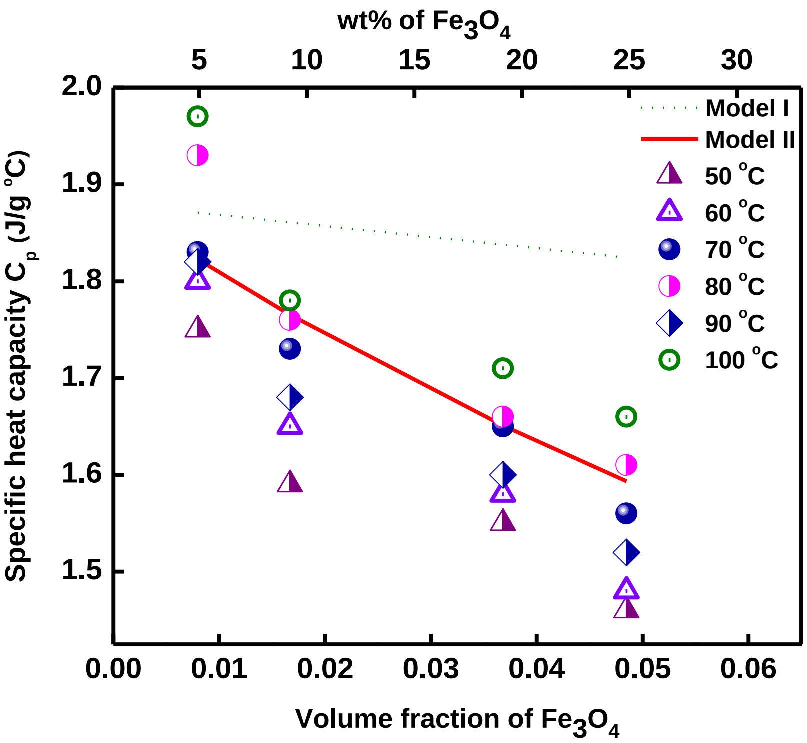

Figure 5.5: Variation of specific heat capacity as a function of volume fraction of kerosene based Fe_3O_4 nanofluid at different temperatures along with Model I (dotted line) and Model II (solid line) fits. The corresponding wt% is shown in the top x- axis.

Fig. 5.6 (a) and **(b)** shows the variation of specific heat capacity with temperature for different concentration of PAO based Al_2O_3 nanofluids and the variation of specific heat capacity ratio, respectively. Surprisingly, the specific heat capacity of Al_2O_3 / PAO increases upto 4 wt% nanoparticle concentration. Further increase in Al_2O_3 concentration led to a decrease in the $C_{p,nf}$ but larger than the $C_{p,bf}$. These results suggest that PAO molecules strongly modify the interfacial thermal characteristics of Al_2O_3 nanoparticles that increases the heat capacity of PAO based Al_2O_3 nanofluids.

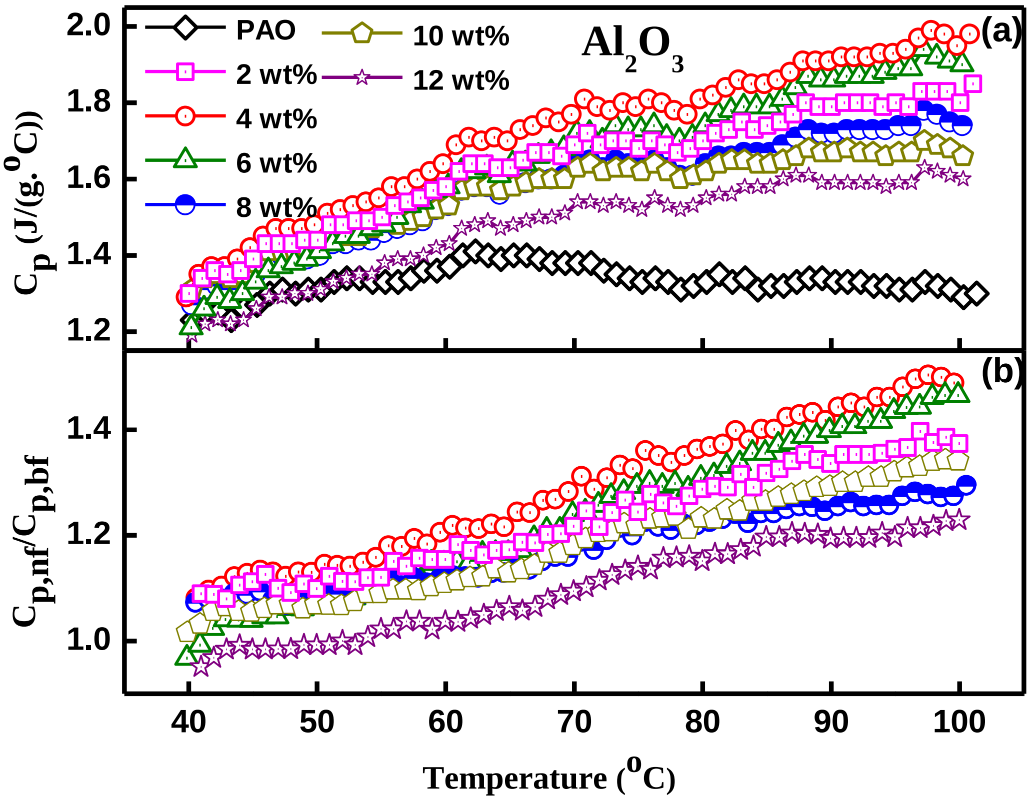

Figure 5.6: (a) Specific heat capacity of alumina nanofluids with different weight percentage of Al_2O_3 nanoparticles in PAO and (b) Specific heat capacity ratio of alumina nanofluid with respect to PAO.

In general, the mechanisms considered for the unusual enhancement of the specific heat capacity are: (1) enhanced specific heat capacity of nanoparticle due to higher specific surface energy (compared with bulk material); (2) additional thermal storage mechanisms due to interfacial interactions (e.g., such as interfacial thermal resistance and capacitance) between nanoparticle and the adhering liquid molecules because of the extremely high specific surface area of the nanoparticle; and (3) the existence of semi-solid liquid layer adhering to the nanoparticles, which are likely to enhance the specific heat capacity due to the smaller intermolecular spacing similar to the nanoparticle lattice structure on the surface (compared to the higher intermolecular spacing in the bulk liquid).

Nelson et al.[226] reported a specific heat capacity enhancement of 50 % in 0.6 % exfoliated graphite nanoparticle fibers suspended in PAO. The specific heat capacity of Al_2O_3 nanoparticle was found to increase up to 25 % compared with the bulk value of Al_2O_3.[352] A volumetric heat capacity (C_v) enhancement with increase in temperature in Al_2O_3 and ZnO dispersed in 60:40 by mass of ethylene glycol/water and in water based SiO_2 nanofluids is reported.[228] The enhancement of specific heat capacity of the silica nanocomposite is attributed to the high surface energy of nanoparticles that includes a phase transformation in the solvent material (liquid ordering). Such ordering of liquids on nanoparticles are expected to have semi-solid properties that gives rise to an increase in specific heat capacity of nanofluids.[350, 364] The heat capacities of ionic salts are shown to increase with molar mass due to an increase in number of translational, vibrational and rotational modes[365].

5.3.3 Effect of Nanoparticle Size on the Specific Heat Capacity of Nanofluids

The variation of specific heat capacity and the normalized specific heat capacity of nanofluids with temperature with respect to particle size is shown in **Fig. 5.7 (a & b)**. From the **Fig. 5.7** it is clearly seen that the specific heat capacity ratio decreases with increase in particle size. A similar trend was reported by Xiong et al.[229] for Ag nanoparticles of size ranging from 5 to 50 nm suggesting that the enhanced C_p in smaller sized nanoparticle is caused by the larger atomic thermal vibrational energies of surface atoms. Wang et al.[223] reported that the specific heat capacity of nanoparticle increases with decrease in size of the particle in the case of CuO nanoparticle of size ranging from 3.4 to 50 nm.

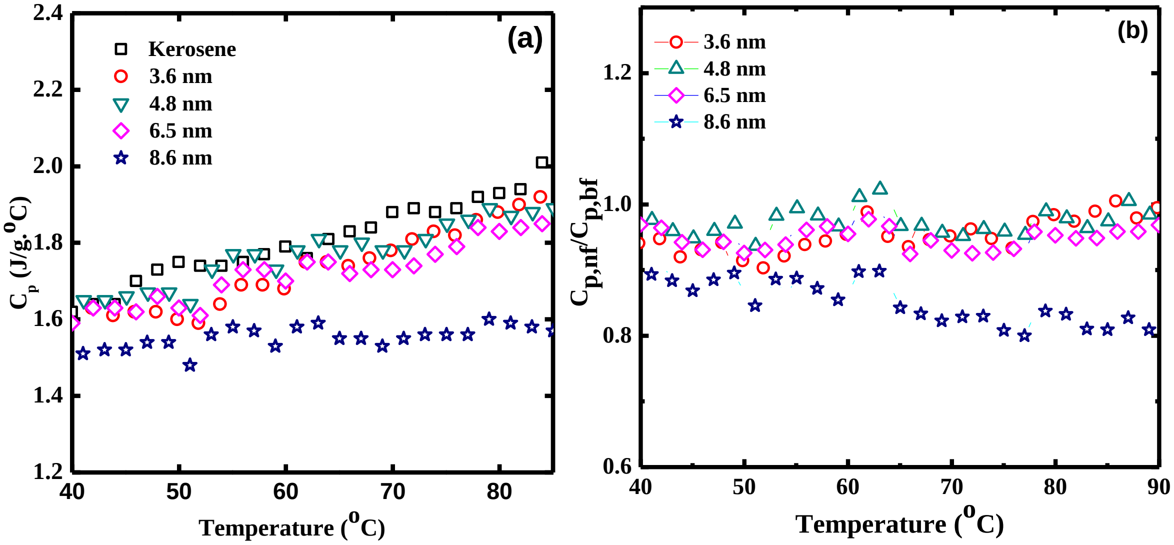

Figure 5.7: (a) Specific heat capacity of kerosene based Fe_3O_4 nanofluids with different average particle sizes and (b) the corresponding specific heat capacity ratio.

The major contribution to the specific heat capacity above ambient temperature is determined by the vibrational degrees of freedom, and the peculiarities of surface phonon spectra of nanoparticles are responsible for the anomalous behavior of specific heat capacity. The vibrational states with lower frequencies make a larger contribution to heat capacity.[366] Studies on the effect of nanoparticle size on the specific heat capacity by Dudda et al.[50] showed 8, 12, 19 and 27 % enhancement of specific heat capacity for the SiO_2 nanoparticle size of 5, 10, 30 and 60 nm, respectively**.** Novotny et al.[367] reported a decrease in the specific heat capacity with increase in the nanoparticle size which is attributed to the absence of low frequency modes and the increase in the specific heat capacity at low temperatures was attributed to the additional vibrational mode of surface phonon. More heat is required to raise the temperature of surface atoms because of larger vibrational amplitude of surface atoms, compared to the bulk atoms.[368] A study on high-energy ball milled Ruthenium (Ru) and

Aluminum-Ruthenium (AlRu) nanoparticles of size ranging from 7 to 12 nm, with large atomic-level strain, showed a specific heat increase of ~20 %, which was attributed to the large changes in the vibrational and configurational part of the entropy.[353]

5.3.4 Effect of Shape of Nanostructures on the Specific Heat Capacity of Nanofluids

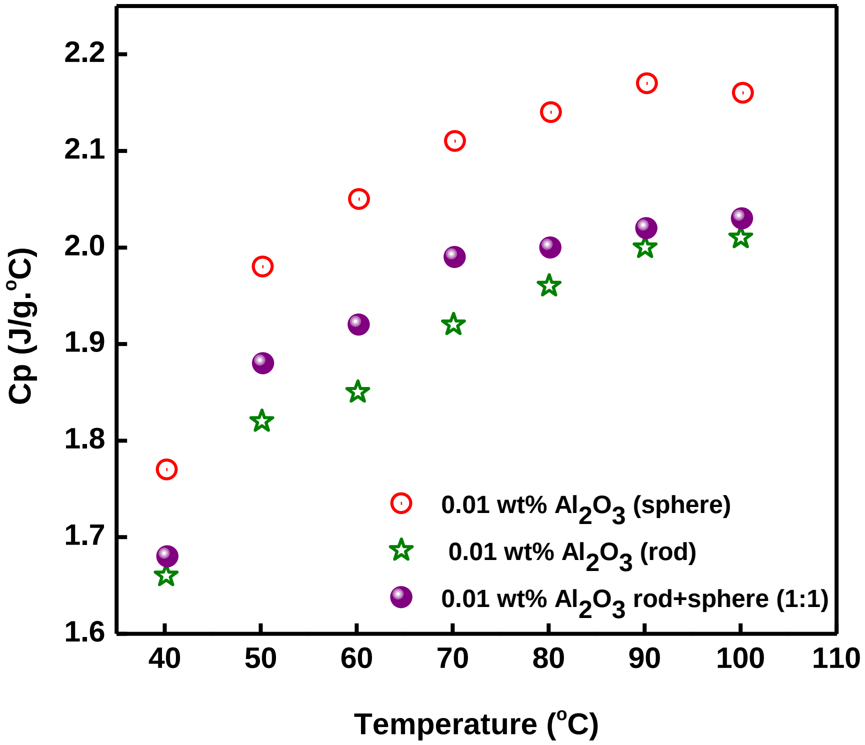

Figure 5.8: Variation of specific heat capacity as a function of temperature for PAO based Al_2O_3 nanofluids with spherical and rod shaped particles of concentration 0.01 wt%.

Fig. 5.8 shows the variation of C_p as a function of temperature for PAO based Al_2O_3 with different particle morphologies. A concentration of 0.01 wt% was used in the case of spherical Al_2O_3 and rod shaped Al_2O_3 in PAO. For both the nanofluids, C_p increases with temperature. At the same concentration (0.01 wt%), the specific heat capacity of the nanofluid containing spherical particles was more compared to that of rod shaped Al_2O_3 nanoparticles. In the present case, the aspect ratio of the nanorods was ~ 8 (80 x 10 nm^2), while the nanospheres diameter was 10 nm. The surface area to volume ratio for nanorods is 425×10^6 while that of nanospheres (diameter 10 nm) is 600×10^6. Therefore, the surface atoms are more in the case of nanospheres compared to that of nanorods. This means more heat is required to raise the temperature of surface atoms by one degree.

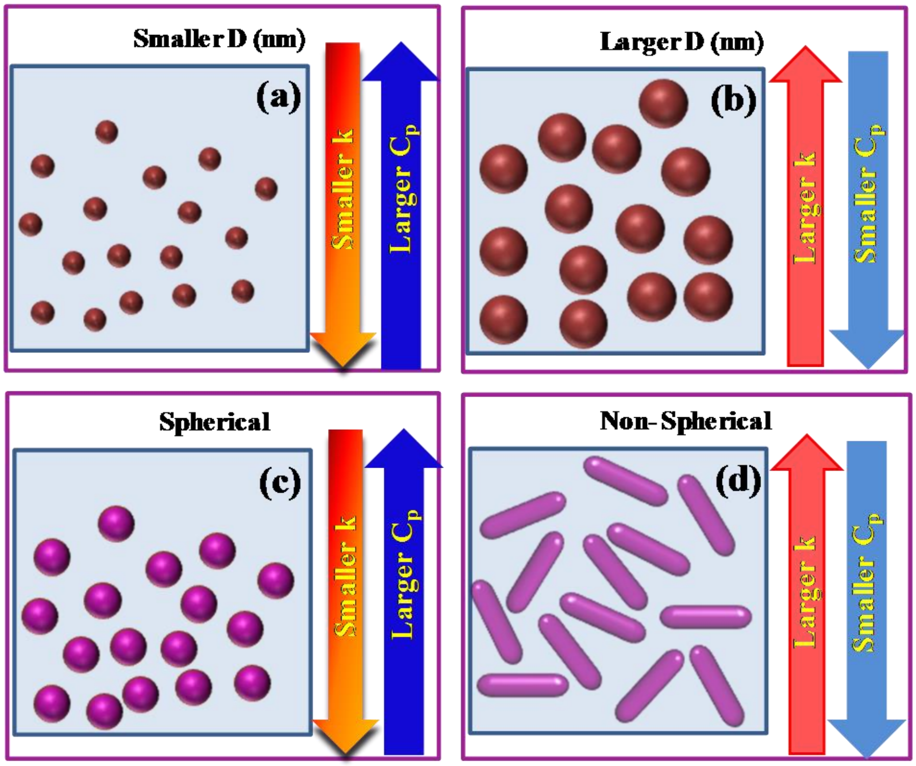

Figure 5.9: Schematic representation of the effect of (a) smaller d, (b) larger d, (c) spherical particle and (d) non spherical particle on the specific heat capacity and thermal conductivity of the nanofluid.

Therefore, the observed larger specific heat capacity of nanospheres than that of nanorods is in good agreement with surface atomic consideration. This study hence shows that the particle morphology also plays a major role in the specific heat capacity of nanofluids. The observed reduction in C_p with increasing aspect ratio of nanoparticles is in sharp contrast with the increase in thermal conductivity in several nanofluids.[130, 346, 369-375] The schematic representation of the effect of particle size and morphology on the specific heat capacity and thermal conductivity of the nanofluid is shown in **Fig. 5.9**.

5.4. Conclusions

The thermophysical properties of nanofluids with different types of nanoparticles as a function of concentration, shapes, size and base fluids are studied. The present work concludes that the nanoparticle concentration, shape and size play a major role in specific heat capacity of nanofluid. In the Fe_3O_4 nanofluids, the specific heat capacity is found to decrease with increasing particle concentration while an increase in the specific heat capacity is observed in Al_2O_3/PAO based nanofluid. This suggests that PAO molecules strongly modify the interfacial thermal characteristics of Al_2O_3 nanoparticles. The size dependent studies on specific heat capacity suggest that the C_p increases with decreasing dispersed nanoparticle size. The study shows that the particle morphology also plays a major role in specific heat capacity of nanofluids and the C_p decreases with increasing aspect ratio of nanoparticles due to reduced surface atomic contributions.

Chapter VI

Tunable Thermal Transport in Phase Change Materials Using Inverse Micellar Templating and Nanofillers

6.1. Introduction

The use of organic phase change materials as heat transfer media has attracted much attention in the recent years due their ability to freeze without much supercooling.[232] The crystallization of the n-alkane chain releases a large amount of latent heat, which is the key to heat transfer applications. Another material of focus, for such cooling applications over the past one decade, was dispersions of nanomaterials, popularly known as nanofluids[38]. The intense research on various nanofluids led to the conclusion that traditional nanofluids show only modest thermal conductivity enhancement.[40, 147, 182, 246, 278] During the last decade, several new promising approaches to achieve extremely large thermal conductivity enhancement using carbon nanotubes,[376] graphene,[337, 369, 377, 378] magnetic materials [276, 331, 379] and composites [191, 373, 377, 380] have been demonstrated.

The recent finding of reversible tuning of electrical and thermal conductivities using first-order phase transitions in percolated composite materials[236-238, 243] have attracted much interest among nanofluid research community because of their important applications in heat management in various industrial sectors. Zheng et al.[237] have observed large contrasts in the electrical and thermal conductivities at the phase transition temperature in graphite/water and carbon nanotube/hexadecane suspensions, which was attributed to the modulations in the electrical and thermal contact resistances due to the internal stress generated during the phase transition. Harish et al.[238] reported a large enhancement in the thermal conductivity in the solid phase (~250 %) of an alkane (n-octadecane) containing 0.25 wt% of single-walled carbon nanotubes, compared to the nominal enhancement in the liquid state (~10 %).

Schiffres et al.[243] demonstrated tunable electrical and thermal conductivities by controlling the crystal growth through freezing rate control in solution-based nanocomposites where nanoparticles are driven into concentrated intercrystal regions to increase the percolation pathways and to reduce the interparticle resistance. Sun et al.[236] studied the room temperature electrical and thermal switching in CNT/Hexadecane composites and found 5 orders of electrical and 3 times of k variations at the phase change point of hexadecane. Though significant enhancement in thermal and electrical conductivities are observed in nanocomposites during phase change, the reversible switching under long repeated cycling is strongly affected due to the agglomeration of nanomaterials because of the strong van der Waals interaction and the high reactivity of nanomaterials. Also, aggregation not only hampers the long term stability of such nanocomposites but also reduces their switching time. Here, a novel strategy is disclosed to overcome these difficulties by templating alkanes with inverse micelles. Since agglomeration issue is negligible in micellar systems due to steric interactions, such systems offer promising heat transfer applications. For these studies, soft systems of inverse micelles of size ranging from 1.5 to 6 nm, with different head groups were prepared. The k tunability of the micellar systems with dispersions of multiwalled carbon nanotubes and graphite nanofibers in n-hexadecane under identical experimental conditions were compared and the effect of functionalization of nanomaterials on stability, agglomeration and thermal conductivity enhancement was studied.

6.2 Materials and Methods

6.2.1 Materials

The surfactants OA, AOT and Span 80 were used in this study. The critical micellar concentrations (CMC) for OA, AOT and Span 80 are 0.72, 0.077 and 0.019 mM, respectively.[381-384] For the studies, stock solutions of OA, AOT and Span 80 surfactants were prepared in n-hexadecane from which different concentrations were prepared. The structures of these three surfactants are shown in **Fig. 2.1**. The n-Hexadecane is chosen as the phase change material and graphite nanofibers and multiwalled carbon nanotubes are used as nanoinclusions. Preparation method to produce dispersion of MWCNT and GNF in hexadecane is discussed in **Chapter 2**.

6.2.2 Methods

The k of the dispersion was measured by using a hot wire probe[207]. An inverted phase contrast microscope was used to obtain the microscopic images of the nanofluids. Details of these equipments are discussed in **Chapter 2**.

6.3 Results and Discussion

6.3.1 Effect of Inverse Micellar Templating on *k* Contrast in Hexadecane under Freezing

Fig. 6.1 shows the variation of k/k_f and the percentage of increase in k as a function of temperature for different volume fractions of oleic acid in hexadecane. Here, k_f is the thermal conductivity of hexadecane. The surfactants are amphiphilic molecules with hydrophilic and hydrophobic parts. They exist as unimers at concentrations below the critical micellar concentration and form spherical inverse micelles just above the CMC. The hydrophobic force and entropy are the driving forces for the inverse micelle formation.

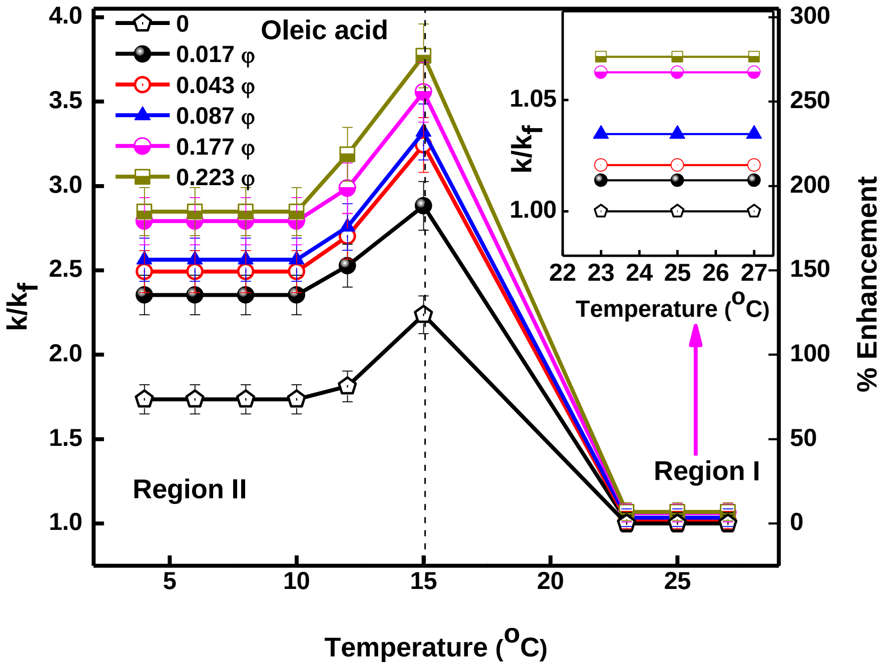

Figure 6.1: Variation of effective thermal conductivity and the percentage of increase in thermal conductivity as a function of temperature for different volume fractions of oleic acid in hexadecane. Inset shows the magnified view of region I (23 to 27 °C).

In a normal micelle, the surfactant molecules are oriented in such a way that the hydrophobic hydrocarbon chains (tails) face towards the interior of the micelle, leaving the hydrophilic groups (head) in contact with the aqueous medium. In the case of non-polar solvent, the hydrophilic groups are sequestered in the micelle core and the hydrophobic groups extend away from the center. The CMC for OA is 0.72 mM (i.e. $\varphi = 0.0002$).[381] The diameter of the oleic acid inverse micelle is ~ 6 nm.[385] All the concentrations studied here are well above the CMC and hence inverse micelles are present in all these cases.

Fig. 6.1 can be divided into two regions, I and II, where region I ($T > 22$ °C) corresponds to the liquid phase and region II ($T < 18$ °C) corresponds to the solid phase. The k increases with increase in OA concentration in both regions I and II. In the liquid state, the k enhancement was nominal, i.e., from 1 to 6.9 %, as the φ of the OA is increased from 0.017 to 0.223. In the solid state, immediately after freezing, the k enhancement increases from 188 to 277 % as the OA φ increases from 0.017 to 0.223. With further decrease in temperature, beyond the freezing point, the k is found to decrease a little and then becomes constant for all the concentrations of OA. In the solid phase, a larger enhancement of 277 % is observed immediately after freezing of the base fluid (T =16 °C) for a φ□of 0.223. With further decrease in temperature below freezing point, the k decreases and reaches ~150.9 % at T=10 °C and remains constant thereafter. The k of nanofluids increases with the micellar loading in both the regions, which can be understood as follows:

The critical micellar concentration for oleic acid is 0.72 mM[381] corresponding to a volume fraction 0.0002. As the concentration of oleic acid in the present study is much above the CMC, inverse micelles are present in the solutions. The increase in k with the concentration of OA in both the regions indicates that the presence of inverse micelles increase the k of the alkane. The k of pure hexadecane and OA are 0.144 and 0.164 W/m-K, respectively. To check the universality of micellar templating on k enhancement during freezing transitions, the experiments in two other inverse micellar systems were also performed.

Fig. 6.2 shows the variation of k/k_f and the percentage of increase in k as a function of temperature for different φ of AOT in hexadecane. The AOT forms inverse micelles in hexadecane above $\varphi > 2.1\times10^{-5}$ (i.e., 0.077 mM).[382, 383] The φ values used in our experiments were well above the CMC which ensure inverse micelles in the system. The linear length of the AOT molecule is 1.2 nm and the typical inverse micellar size of AOT is 1.5 nm.[386] The *k* increases with concentration of AOT in both the regions as observed in the case of OA.

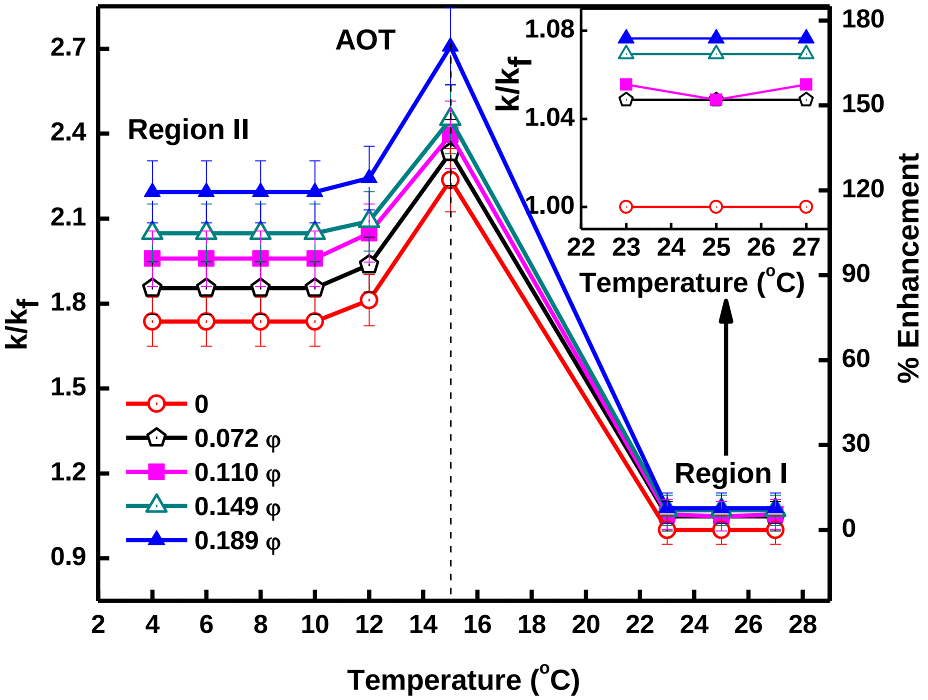

Figure 6.2: Variation of effective thermal conductivity and the percentage of increase in thermal conductivity as a function of temperature for different volume fractions of AOT in hexadecane. Inset shows the zoomed view of region I (23 – 27 °C).

In the liquid state, the *k* increases from 4.8 to 7.6 % as the *φ* of AOT is increased from 0.072 to 0.189. In the solid phase, the *k* enhancement increases from 133 to 170 % as the *φ* of AOT is increased from 0.072 to 0.189, immediately after freezing. With further decrease in the temperature, the *k* is found to decrease slightly and then remains constant. This can be explained in terms of the variations in the aspect ratio of the needlelike crystals formed.[243] It has been shown by Schiffres et al.[243] that rapid cooling can result in a larger aspect ratio of the needles and a larger *k* enhancement.

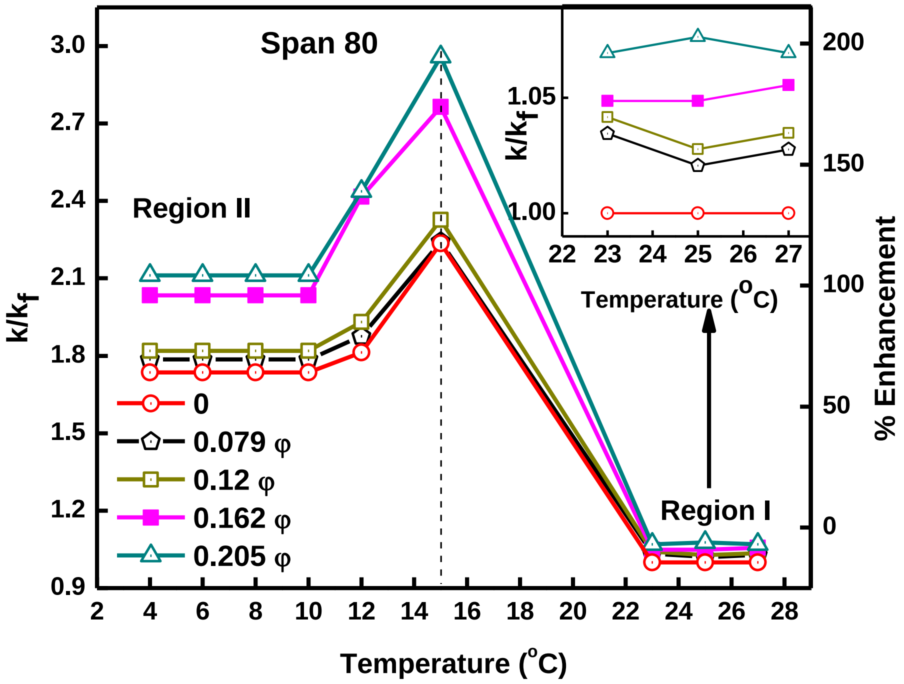

Figure 6.3: Variation of effective thermal conductivity and the percentage of increase in thermal conductivity as a function of temperature for different volume fractions of Span 80 in hexadecane. Inset shows the zoomed view of region I (23 – 27 °C).

Fig. 6.3 shows the variation of k/k_f and the percentage of enhancement in *k* as a function of temperature for different volume fractions of Span 80 in hexadecane. The *k* values of pure hexadecane and Span 80 are 0.144 and 0.182, respectively. The CMC value of Span 80 is approximately 0.019 mM[384] which corresponds to a φ of 6.24×10^{-6}. The typical inverse micellar size of Span 80 is 5 nm.[387] Like in the previous two cases, the *k* increases with φ in both the regions. In the liquid state, the *k* enhancement increases from 2.7 to 7.3 % as the φ

increases from 0.079 to 0.205. In the solid state, the *k* enhancement increases from 124 to 196 % as the φ is increased from 0.079 to 0.205, immediately after freezing. With further decrease in temperature beyond freezing point, the *k* is found to decrease a little and attains a constant value. In solid phase a larger enhancement of 196 % is observed immediately after freezing of base fluid (T = 16 °C and φ of 0.205). With further decrease in temperature, the *k* decreases and reaches 103 % and remains constant at $T \leq 10$ °C.

The aggregation number is the ratio of micellar core volume to the volume of one chain. The presence of surfactant micelles may have affected the freezing/melting point of hexadecane due to thermodynamic effects and also due to the different crystal structures formed. Studies show that the dispersed oil droplet size has an effect on the freezing point of hexadecane (bulk freezing point of hexadecane is 18 °C) in agreement with the Gibbs−Thomson equation.[388] On the contrary, in the presence of normal micelles, *k* decreases with increase in concentration of micelles, and the mechanism of conduction of heat through normal micelle is discussed in **Chapter 3**. The molecular dynamics simulations studies show that the interfaces of organic liquids with surfactant tail groups are highly conductive.[389] The large conductance of the organic liquid-surfactant interface was attributed partly to the penetration of alkane molecule into the surfactant tail regions, which is more prominent for linear surfactant molecules. The very similar molecular and vibrational structures of the surfactant tails and the alkane molecules lead to the optimization of the van der Waals interactions between the chains in the two species.

The composite system has a matrix of alkane base fluid with surfactant micelles dispersed. As the net thermal resistance of inverse micelle is much lower than that of the alkanes because of the highly ordered packing of the linear chain surfactant within the sphere, the effective interfacial resistance along the conduction path should be much lower than that of pure alkane. Further, the cores of the micelles have polar head groups, which might entrap hydrophilic moieties (e.g. moisture, ions etc.) within the cores, which is again more thermally conducting than the alkane (e.g. water has a thermal conductivity of 0.6 W/m-K compared to 0.12 W/m-K for alkanes). With increase in oleic acid concentration, the numbers of inverse micelles in the system will also increase which in turn reduces the effective interfacial thermal resistance along the heat conduction pathways. The observed increase in *k* with increase in volume fraction of the micelles is in very good agreement with the above hypothesis.

When the alkane undergoes first order phase transition during cooling, it forms crystals[237] of different morphologies, whose aspect ratio can vary from micro to millimeter scale depending on the rate of cooling.[243] This suggests that, during the freezing transition, the nanosized frozen inverse micelles with highly packed linear chain surfactant within the sphere are pushed to the inter crystal boundaries, thereby filling the heat conduction path that reduces the effective thermal resistance.[238] Studies show that the presence of surface active species in long-chain alkanes can induce or alter surface freezing to become oriented chains.[390] An earlier study suggests that the internal stress generated during freezing also improves the conduction among the crystals.[237] Molecular dynamics simulations of the structure of paraffins in solid and liquid states shows that, upon crystallization, the *k* doubles due to the formation of nanocrystallites paraffin.[242]

Among the three micellar systems studied, oleic acid based templating showed the highest *k* enhancement. The matched alkyl chain length (or vibrational spectrum) of both oleic acid and hexadecane seems to optimize the van der Waals interactions between the chains in the two species, thereby lowering the interfacial thermal resistance, in agreement with earlier theoretical predictions.[390] Simulations results further show that penetration of alkane molecules in the tail region of a straight chain surfactant is more (with less thermal resistance) compared to less-ordered unsaturated, kinked surfactant or double-tailed lipid molecules. The molecular surface structure of liquid alkanes changes with alterations in a solvent's molecular structure due to surface free energy considerations.[391] In the presence of inclusions, the surface structure is altered due to changes in the van der Waals interactions between adjacent solvent molecules and the net ordering of liquid molecules at an interface due to intrinsic interfacial anisotropy. The greater efficiency of thermal vibration waves (phonons) through straight and densely packed chains are expected to provide a better heat conduction. Molecular dynamics simulations predict a larger interfacial thermal resistance for dissimilar structured base fluid (alkane) and surfactant molecules.[389] Based on our experimental results, the conclusions drawn are graphically illustrated in **Fig. 6.4 (a-d)**.

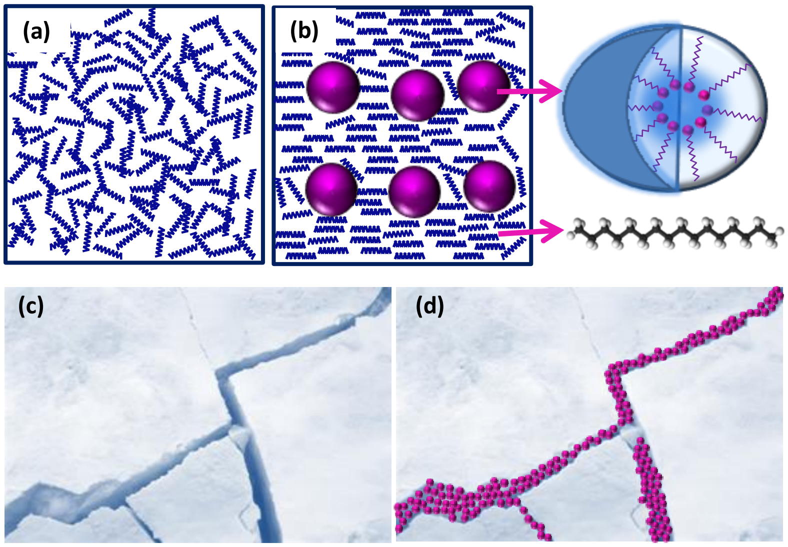

Figure 6.4: (a&b) The atomic structure of alkanes without and with inverse micelles, respectively. The magnified views of a single hexadecane molecule and the inverse micelles are shown by arrows. **Figure 6.4 (c&d)** shows the configuration of the crystals without and with inverse micelles, respectively.

Fig. 6.4 (a) and **(b)** shows the atomic structure of alkanes without and with inverse micelles, respectively. The magnified view of a single hexadecane molecule and the inverse micelles are shown by arrows. **Fig. 6.4 (c)** and **(d)** shows the configuration of the crystals without and with inverse micelles, respectively. During freezing transition, the inverse micelles are pushed to the microcracks and the intercrystal boundaries, leading to a better heat conduction path. The alkane molecules may also undergo some ordering around the inverse micelles, which can restrict translational diffusions of alkane molecules. These findings are consistent with the ice-templating and nanoparticle-induced molecular alignment of alkane.[243] In order to compare the micellar templating to that of nanofillers, the temperature dependent *k* measurements are carried out using MWCNTs and GNF. Also, effect of nanomaterial type and their aggregation on *k* enhancement under freezing conditions are studied.

6.3.2 Effect of Graphite Nanofiber Inclusions on *k* Contrast in Hexadecane under Freezing

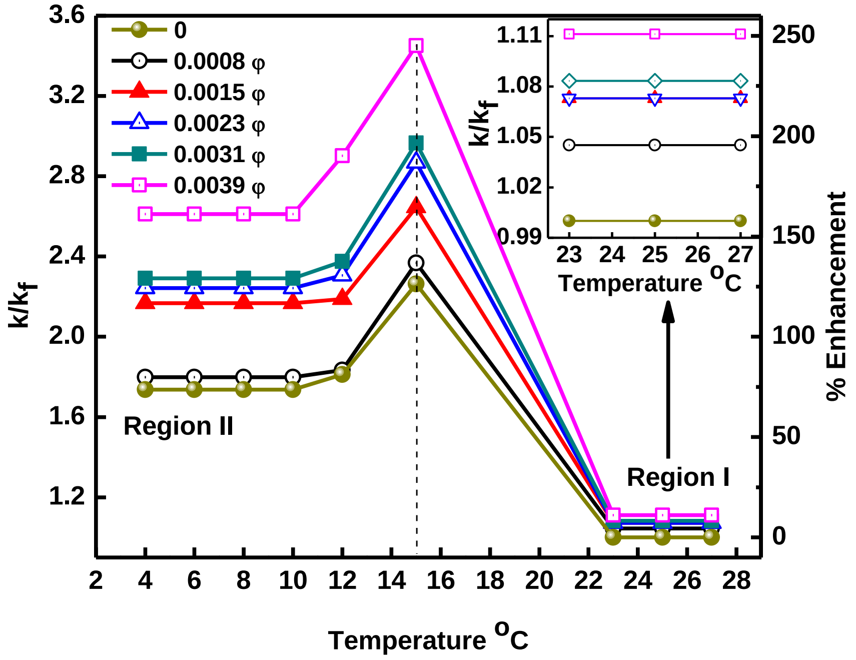

Figure 6.5: Variation of effective thermal conductivity and the percentage of increase in thermal conductivity as a function of temperature for different volume fractions of GNF in hexadecane. Inset shows the zoomed view of region I (23 – 27 °C).

Fig. 6.5 shows the variation of k/k_f and the percentage of increase in *k* as a function of temperature for different volume fractions of GNF in hexadecane. As the volume fraction of GNF increases, the *k* also increases in both the liquid and solid phase. This observation was in agreement with the earlier reports.[236, 237, 243] In liquid state, the *k* enhancement increases from 4.5 to 11 % whereas in the solid state the *k* enhances from 136 to 245 % as the F-GNF concentration increases from 0.0008 to 0.0039. With further decrease in temperature beyond freezing point, the k decreases a little and remains constant for all concentration of GNF. In solid phase, a larger enhancement of 245 % is observed immediately after freezing of the alkane basefluid (T=16 °C) at a GNF loading of φ = 0.0039. With a further decrease in temperature, the k decreases and reaches 161 % at $T \leq$ 10 °C. Earlier study in graphite/HD suspension[237] shows that the k increases to 220 % in the solid state with a graphite loading of φ□□= 0.008. The large contrast observed in the k in the solid state was attributed to the effective transfer of heat through percolation structures and the internal stress generated during freezing. Schiffres et al.[243] demonstrated the tuning of electrical conductivity and k by varying freezing rate control between 10^2 and 10^{-3} °C/min, where they achieved a thermal conductivity contrast ratio varying between 2.3 and 3.0 for a φ of 0.01 in multilayer graphene suspended in hexadecane at solid-liquid transition while k varies between 2.1 and 2.6 in pure hexadecane. The larger k contrast at slower cooling rate was attributed to the formation of larger crystals and the accumulation of more nanoparticles at the intercrystal regions thereby creating additional percolation pathways for heat transport. Harish et al.[238] observed a 250 % enhancement of k in the solid state with a SWCNT loading of 0.25 wt%. It was suggested that the alkane molecules surrounding the nanotubes, when frozen to solid phase, exhibit a tendency to form lamellar layers along the nanotubes axis leading to a 2D structural ordering in the planes perpendicular to the nanotube axis which is similar to the crystalline polymer.[238]

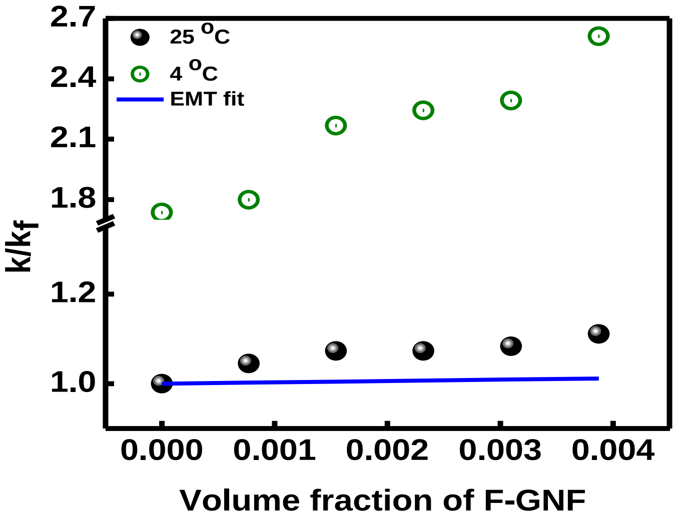

Figure 6.6: Effective thermal conductivity of GNF nanofluids as a function of volume fraction in the solid and liquid state. EMT fit is shown by the solid line.

Fig. 6.6 shows the k/k_f of GNF nanofluids as a function of volume fraction in the solid and liquid state. The Maxwell model is shown by the solid line. At room temperature, the thermal conductivity of the GNF and the base fluid (hexadecane) are ~ 1500 W/m-K[392] and 0.144 W/m-K, respectively. The theoretical fit shows that at room temperature the experimental data are well above the Maxwell's theory. These results show an extremely large thermal conductivity enhancement in both liquid and solid phase in the presence of F-GNF nanoinclusions. Similar enhancement beyond the EMT predictions are observed in multilayer graphene suspended in hexadecane.[243] in hexadecane based graphite and CNT dispersions[237, 393] and in n-octadecane based single-walled carbon nanotube dispersions.[238] **Table 6.1** shows the comparison of the thermal conductivity results in nanofluids with different phase change materials and the dispersed materials.

Table 6.1 : Comparison of the thermal conductivity values in nanofluids with different phase change materials and dispersed materials.

Sl. No	Dispersed phase	Dispersion medium	Volume fraction	k/k_f		Ref
				Liquid (25 °C)	Solid (4 °C)	
1.	Multilayer graphene	Hexadecane	0.01	-	3.0	[243]
2.	Functionalized MWCNT	Hexadecane	0.01	1.42	3.93	[236]
	Original MWCNT		0.008	1.07	2.71	
3.	Graphite	Hexadecane	0.01	2.9	8.57	[237]
4.	SWCNT	Octadecance	0.001	1.1	2.5	[238]
	Exfoliated graphite nanoplatelets		0.0004	1.43	3.2	
			0.002	1.14	2.71	
5	Oleic acid	Hexadecane	0.223	1.069	2.85	Present work
	AOT		0.19	1.076	2.19	
	Span 80		0.205	1.03	2.1	
	F-GNF		0.0039	1.11	2.6	
	F- MWCNT		0.0039	1.13	2.05	

The k changes in hexadecane under repeated freezing and melting cycles for φ□□= 0.223 of OA, φ□□= 0.189 of AOT and φ□□= 0.205 of Span 80 are shown in **Fig. 6.7**. During repeated cycles of freezing and melting, the k/k_f in liquid state are found to be 1, 1.069, 1.076 and 1.076 for HD, OA, AOT and Span 80, respectively. The k/k_f of solid states are found to be 1.74, 2.8, 2.19 and 2.11 for HD, OA, AOT and Span 80, respectively. These results show that the freezing and melting are completely reversible for all the systems studied owing to the monodispersity and non-aggregating nature of micelles.

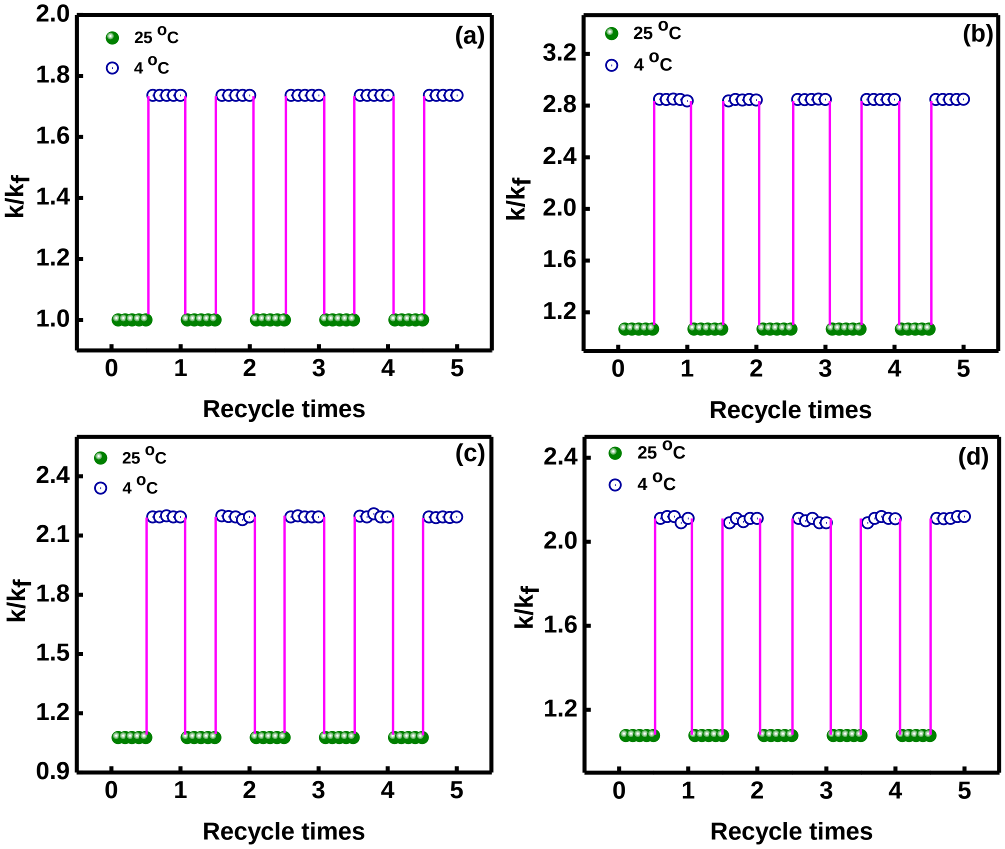

Figure 6.7 : Effective thermal conductivity of (a) pure n-Hexadecane with, (b) $\varphi = 0.223$ of OA (c) $\varphi = 0.189$ of AOT and (d) $\varphi = 0.205$ of Span 80 after different cycles, closed circles and open circles indicate the k/k_f measured at 25 °C and 4 °C, respectively.

6.3.3 Effect of Aggregation of Nanoinclusions on *k* Enhancement during Freezing

6.3.3.1 Bare, Surfactant Stabilized and Surface Modified GNF

Fig. 6.8 shows the variation of *k* as a function of temperature for pure alkane, span stabilized GNFs and F-GNFs of $\varphi = 0.0038$. In liquid state, the *k* of base fluid and nanofluids follows the usual trend.

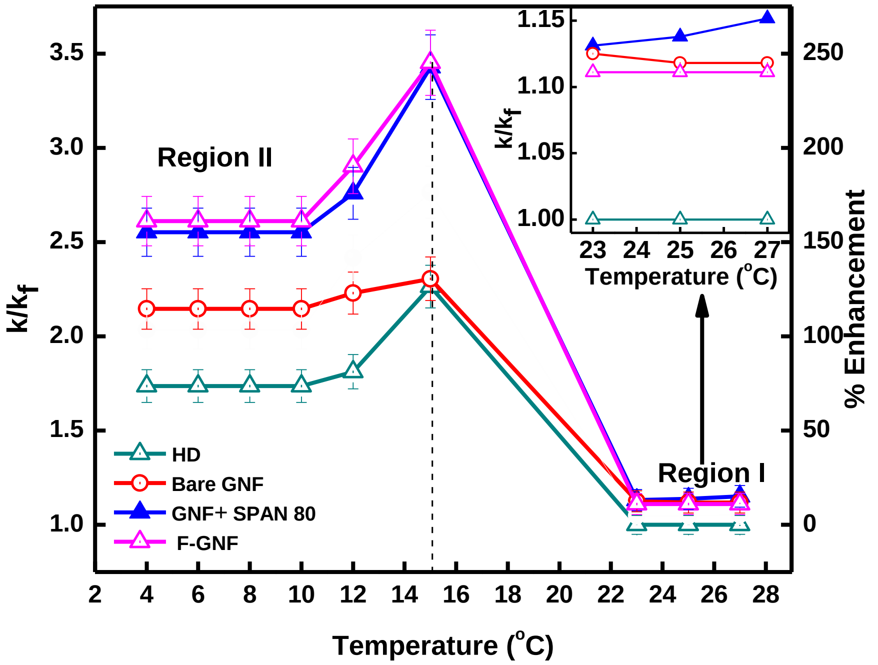

Figure 6.8: Variation of effective thermal conductivity as a function of temperature for pure HD, surfactant stabilized GNFs (GNF+Span80), and F-GNFs. Inset shows the zoomed view of region I.

After freezing, the enhancement of *k* of the base fluid was 126 % at 15 °C. Further, a decrease in temperature results in a decrease in *k*, to a value of 73 %, which remains constant at $T \leq 10$ °C. In the case of HD containing bare graphite nanofibers ($\varphi = 0.0038$ GNF), the *k* enhancement was almost the same as that of the base fluid at 15 °C and remains constant with further decrease in temperature. On the other hand, GNF (φ = 0.0039) stabilized with Span 80 showed an enhancement of around 242 % at 15 °C and the value decreases gradually and reaches 155 % enhancement at $T \leq 10$ °C. F-GNF (φ = 0.0039) also showed an enhancement of around 245 % at 15 °C and decreases gradually and reaches 161 % at $T \leq 10$ °C. These results suggest that the functionalized nanomaterials provide a higher k enhancement than that of bare nanomaterials. Among the stabilized ones, the surface modified (F-GNF) gave higher enhancement on freezing. It is known that the dispersibility of nanomaterials improves with functionalization, which should be the main reason for the observed enhancement in stabilized nanofluids.[148, 331] It is believed that the distribution of GNF's at the grain boundaries are uniform during the crystallization of alkanes in the case of F-GNF compared to the bundled one in the case of bare GNF. This finding shows that the well dispersed GNF are stable and provides better percolated nanofiber network pathways for the effective heat conduction.[243]

6.3.3.2 Bare, Surfactant Stabilized and Surface Modified MWCNTs

Fig. 6.9 shows the variation of k/k_f as a function of temperature for pure HD, Span 80 stabilized MWCNTs and F-MWCNTs. In the latter two cases the φ of MWCNTs is 0.0038. In the liquid state both the surfactant stabilized and the surface modified MWCNTs show a higher k than that of base fluid. The % of k enhancement was 8 and 13 % for nanofluids containing Span 80 stabilized and functionalized MWCNTs, respectively. Like the GNF, the F- MWCNTs showed a better k enhancement than the surfactant stabilized nanofluid. For F-MWCNTs, the maximum enhancement observed is 157 and 69 % at 15 and 10 °C, respectively. In the case of nanofluid stabilized with Span 80, the % of *k* enhancement is 48 and 17 % at 15 and 10 °C, respectively.

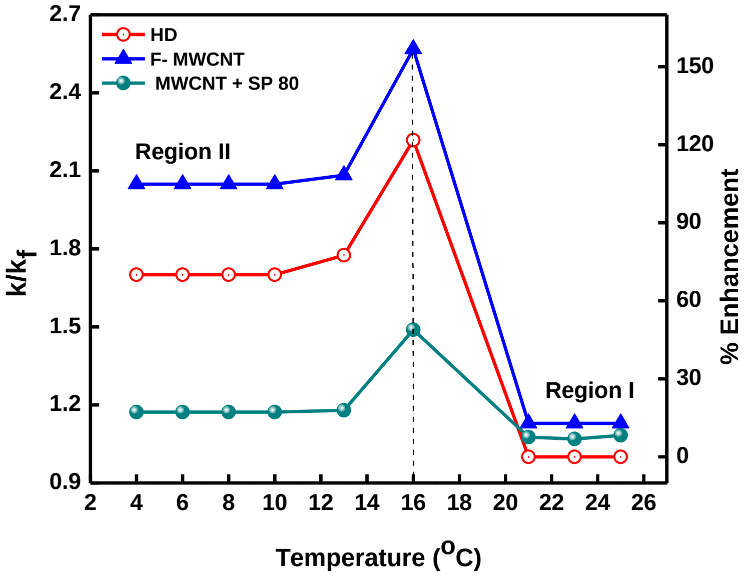

Figure 6.9: The variation of effective thermal conductivity as a function of temperature for pure HD, Span 80 stabilized MWCNTs and F-MWCNTs of $\varphi = 0.0038$.

The reason for the higher *k* enhancement in F-MWCNT dispersion is attributed to the better dispersibility of MWCNTs, as evident from the microscopic images, where the percolated nanofibers networks are uniformly distributed, which enables better conduction pathways. The molecular dynamics simulation studies on structural phase transition and crystallization process of alkane molecules in carbon nanotube dispersions show an isotropic-to-nematic or smectic transition with molecules aligned with embedded nanotubes.[394] Under certain situations, the alkane molecules can even form lamellar layers or two-dimensional structure ordering that can affect the translational diffusions and rotation freedom.

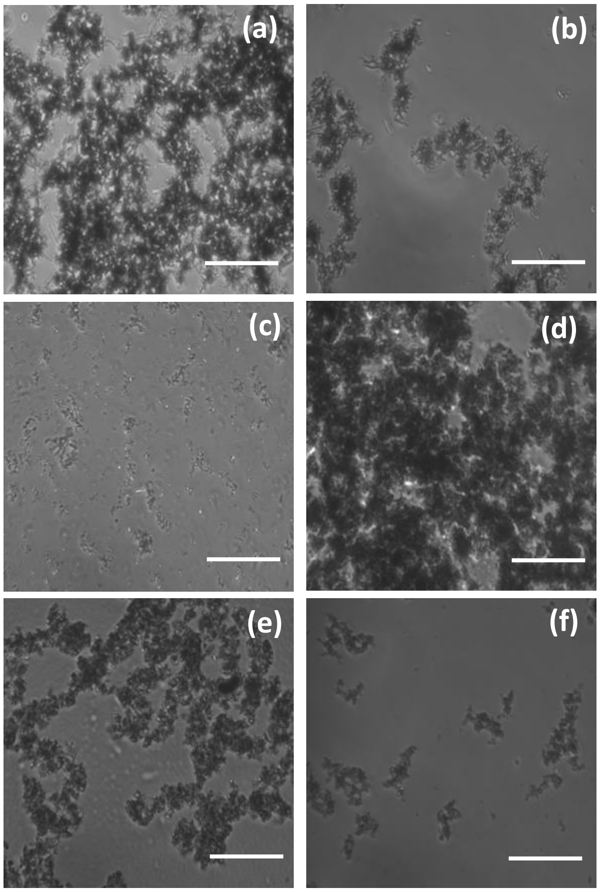

Figure 6.10: Phase contrast optical microscopic images of (a) bare GNFs, (b) Span stabilized GNFs, (c) F-GNFs, (d) bare MWCNTs, (e) Span stabilized MWCNTs and (f) F-MWCNTs in hexadecane. In all the cases, the volume fraction is 0.0038. The scale bar corresponds to 50 μm.

To obtain macroscopic evidence for the dispersibility of nanofillers in the PCM matrix and their aggregation under different stabilization conditions, the phase contrast microscopic images of bare GNF, Span 80 stabilized MWCNTs and GNFs and F-MWCNTs and F-GNFs in hexadecane are taken. **Fig. 6.10** shows the optical microscopic images of (a) bare GNFs, (b) Span stabilized GNFs, (c) F-GNFs, (d) bare MWCNTs, (e) Span stabilized MWCNTs and

(f) F-MWCNTs in hexadecane. In all the cases, the volume fraction of dispersed nanomaterial is the same φ□ = 0.0038 and the microscopy images were taken after sonication for 2 mins. The images confirm the presence of very large aggregates in the case of nanofluids with bare GNFs and bare MWCNTs compared to the other four cases. The Span 80 stabilized and functionalized GNF are fairly well dispersed. Large clusters are observed in the case of Span 80 stabilized MWCNTs nanofluids whereas F-MWCNTs nanofluids showed only a few small clusters, confirming better dispersibility under surface functionalization. Therefore, the observed larger k enhancement in stabilized nanofillers dispersions are indeed due to better distribution of nanofillers in the intercrystal boundaries.

6.4 Conclusions

Extremely large tunable thermal conductivity in a phase change alkane is achieved using inverse micellar templating. The thermal conductivity enhancement between the solid and liquid phase in presence of inverse micelles of size ranging from 1.5 – 6 nm can vary between 111 to 185 %. These results suggest that during the freezing transition, the nanosized frozen inverse micelles with highly packed linear chain surfactant are pushed to the inter crystal boundaries, thereby paving effective heat conduction path. Comparison of results with that of nanofillers in alkanes showed that the k contrast in surface modified graphite and multiwalled carbon nanotube in n-hexadecane at 15 °C for $\varphi \sim 0.0039$ are found to be 161 and 157 %, respectively. The phase contrast optical microscopic images confirm better dispersibility under surface functionalization, which enables better distribution of nanofillers in the intercrystal boundaries and higher thermal conductivity enhancement. Further, these results suggest interesting possibilities of using micellar templated phase change materials for applications in latent heat thermal storage systems (e.g. solar engineering, seasonal regulation of building temperature, and thermal storage) and new insight into the role of aggregation of nanofillers in *k* enhancement under freezing conditions.

Chapter VII Role of Nanoinclusions on Thermal Conductivity enhancement in Phase Change Materials under Freezing.

7.1 Introduction

Latent heat storage has been on the frontiers of research with an aim of obtaining a heat storage system with a high heat capacity and good heat transfer property. Use of appropriate material to store the heat is the key to the development of heat storage systems. The last decade witnessed several new methods that were employed to enhance the thermal conductivity of nanofluids using carbon nanotubes,[346, 351, 371] metal oxides,[27, 152, 173, 268, 395, 396] graphene,[374, 377, 397] magnetic materials[178] and composites.[280, 398-401] The use of organic phase change materials as continuous phases (base fluids) has attracted much attention in the recent years due to the advantages of phase change materials such as self nucleating properties, chemical stability, high heat of fusion, safe and non reactive nature and ability to freeze without much super cooling [232]. The PCMs used for ambient temperature related applications are hydrocarbons with different chain lengths. Most of the phase change materials (organic) have low thermal conductivity which limits their utility in practical applications. The increase of the thermal conductivity of organic phase change materials using different nanoinclusions has been a topic of research in recent years. The nanoinclusions can be ceramic particles,[402] metallic particles,[403] and carbon materials[404] with higher thermal conductivity. Reversible tuning of electrical and thermal conductivity using phase change material in percolated composite materials[236-238, 405] has drawn considerable attention owing to their applications in heat management systems in various industrial sectors such as construction, textile, food packaging industry, medical packaging industry, automobile, transportation etc. A sudden increase in thermal conductivity of n-octadecance occurs when it transforms from liquid to solid phase. Zheng et al.[237] reported a large contrast in electrical and thermal conductivities using first-order phase transitions in percolated composite materials. Thermal conductivity studies on CNT/Hexadecane composites shows a 3 times enhancement in thermal conductivity at the phase change point of hexadecane[236]. Harish et al.[238] reported a large contrast in the thermal conductivity enhancement of phase change alkane in liquid and solid phase with single-walled carbon nanotube inclusions. Tunable electrical and thermal conductivities through freezing rate control in hexadecane based nanocomposite was reported by Schiffres et al.[243] Though there are studies on thermal conductivity of PCM with nanoinclusions in the recent years, the effect of clusters on the thermal conductivity of PCMs is not studied systematically. In the present work, the role of aggregates on the thermal conductivity in liquid and solid phase of PCM is studied.

7.2 Materials and Methods

7.2.1 Materials

Hexadecane used as phase change material, copper nanowire, graphene nanoplatelets and multiwalled carbon nanotubes are used for the present study. The details of the materials used and the preparation of dispersions of CuNW, MWCNT and graphene nanoplatelets in hexadecane are discussed in **Chapter 2**.

7.2.2 Methods

The thermal conductivity of the dispersion was measured by using a hot wire probe.[207] An inverted phase contrast microscope was used to obtain the microscopic images of the nanofluids.

7.3 Results and Discussion

7.3.1 Effect of Aggregation of Nanomaterials on Thermal Conductivity Contrast in Hexadecane during Freezing Transition

7.3.1.1 Copper Nanowire Additives

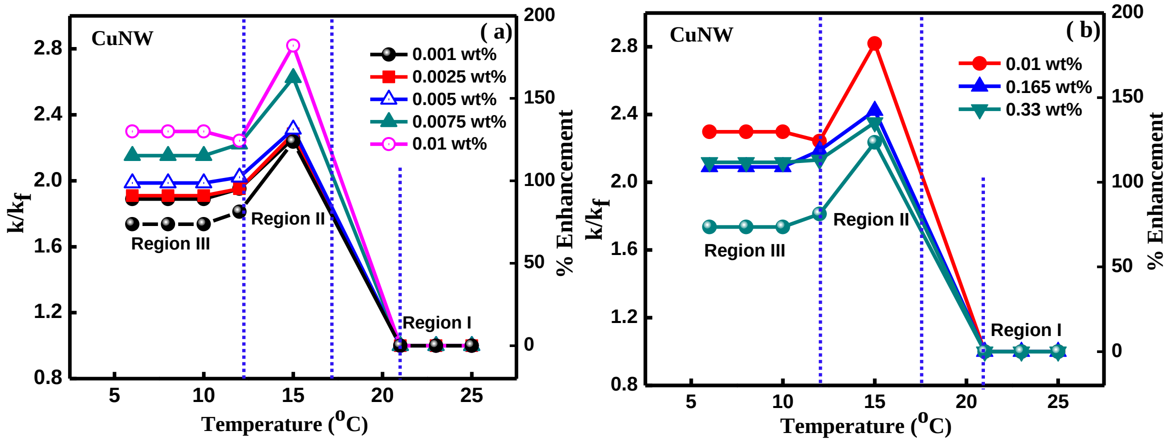

Figure 7.1: Variation of effective thermal conductivity and the percentage of increase in thermal conductivity as a function of temperature for different wt% of copper nanowire in hexadecane (a) lower particle loading and (b) higher particle loading.

Fig. 7.1 shows the variation of k/k_f and the percentage of increase in thermal conductivity as a function of temperature for different wt.% CuNW in hexadecane. **Fig. 7.1** can be divided into three regions named I, II and III. $T > 22$ °C corresponds to region I, where the nanofluid is in the liquid phase, the temperature just above and below the freezing point correspond to the region II and region III, respectively. In all the regions, the thermal conductivity increases with increase in CuNW concentration. In liquid phase, the thermal conductivity enhancement increases from 1 to 3 % as the CuNW concentration increases from 0.001 to 0.33wt %. In solid phase, immediately after freezing (region II), the thermal conductivity enhancement increases from 126 to 182 % as the CuNW concentration increases from 0.001 to 0.01wt %. With further decrease in temperature beyond freezing point (region III), the thermal conductivity is found to decrease and become constant for all concentrations of CuNW. In the solid phase (region II), a larger enhancement of 182 % was observed immediately after freezing of base fluid (T =16 ^{o}C) for a particle loading of 0.01 wt% of CuNW. With further decrease in temperature below freezing point (region III) the thermal conductivity decreases and reaches a steady enhancement value of 130 % at T =10 ^{o}C or below. With further increase in concentration of CuNW beyond 0.01 wt%, the thermal conductivity starts decreasing. For a maximum particle loading of 0.33 wt%, the thermal conductivity in the region II is 135 %. With further decrease in temperature below the freezing point (region III), the thermal conductivity decreases and reaches an enhancement of 118 % at T =10 ^{o}C. The observed higher thermal conductivity in the solid phase is attributed to the effective heat transfer through the continuous networking structure present during the phase transition. The hexadecane crystals are known to exhibit strong anisotropic growth kinetics[237] where needle like structures are formed which is expected to increase the contact area of the dispersed particle.[237] During freezing, when the crystals begin to nucleate and form needle-like structures; particles are gradually pushed to the grain boundaries,[238] resulting the formation of a continuous quasi-2D network of bundles. The internal stresses generated during the phase transition can reduce the thermal contact resistances[237] in the percolated nanoinclusions, which causes the enhancement in the effective thermal conductivity of the frozen phase.[237, 240] In contrast to the small molecular liquids, the long linear molecular liquids can form ordered interfacial structures that can significantly alter the thermal conductivity of the fluid.[242]

7.3.1.2 Multi Walled Carbon Nanotubes Additives

Fig. 7.2 shows the variation of k/k_f and the percentage of increase in thermal conductivity as a function of temperature for different wt% of bare MWCNT in hexadecane. The thermal conductivity variation of pure hexadecane is also shown for comparison.

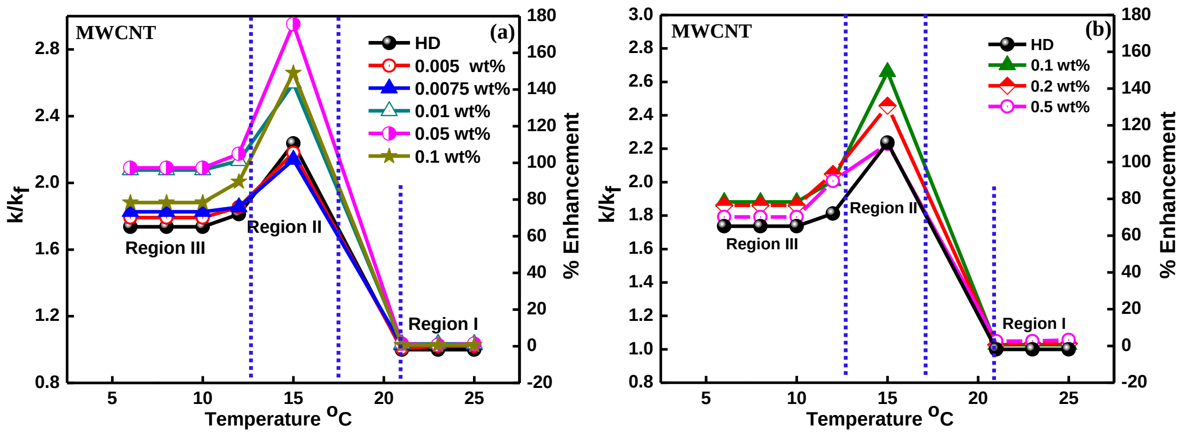

Figure 7.2: Variation of effective thermal conductivity and the percentage of increase in thermal conductivity as a function of temperature for different wt% of bare multi-walled carbon nanotube in hexadecane.

The thermal conductivity increases with concentration of MWCNT in all the three regions (I, II & III). In region I, the thermal conductivity enhances from 1 to 3 % as the MWCNT concentration increases from 0.005 to 0.05 wt%, whereas in region II the thermal conductivity increases from 123 to 195 %. As seen in the previous case, with further decrease in temperature, beyond freezing point (region III), the thermal conductivity decreases and becomes a constant. The concentration beyond 0.05 wt%, a decrease in the thermal conductivity is observed in the solid phase (region II and III) whereas in liquid phase (region I) the thermal conductivity continues to increase with increase in concentration. In region II, a larger *k* enhancement of 195 % was observed immediately after freezing of the base fluid (*T*=16 °C) for a particle loading of 0.05 wt% of MWCNT. With further decrease in temperature the thermal conductivity decreases and becomes a constant value of 109 % at *T*=10 °C. Irrespective of the phase, the thermal conductivity of nanofluids increases with particle loading in all the regions. Decreasing the temperature beyond freezing point results in a decrease in thermal conductivity for all concentrations of MWCNT. The observed decrease in thermal conductivity above a particle loading is expected to be due to the presence of aggregates formed in the system, which do not form a favorable conduction pathway for heat transport.

7.3.1.3 Graphene Nanoplatelets Additives

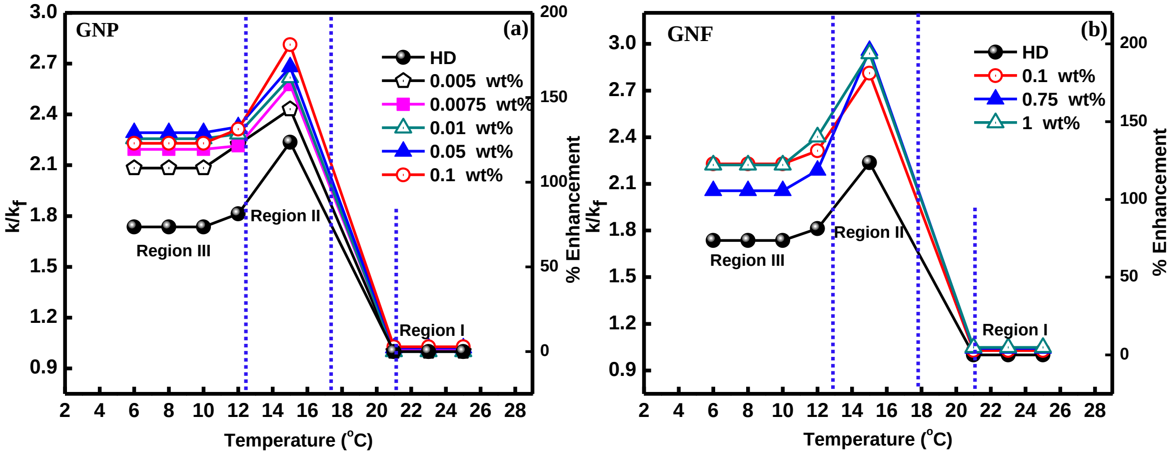

Figure 7.3: Variation of effective thermal conductivity and the percentage of increase in thermal conductivity as a function of temperature for different wt% of graphene nanoplatelets in hexadecane.

Fig. 7.3 shows the variation of k/k_f and the percentage of increase in thermal conductivity as a function of temperature for different wt% of GNP in hexadecane. The thermal conductivity increases with the concentration of GNP in all the three regions. In the liquid phase, the thermal conductivity enhancement increases from 1 to 4.8 % as the GNP concentration is increased from 0.005 to 0.05 wt% and in region II the thermal conductivity increases from 143 to 180 % for the same GNP concentration range. With further decrease in temperature beyond the freezing point (region III), the thermal conductivity is found to decrease for all the concentrations of GNP and then becomes constant. For concentrations beyond 0.1 wt%, a decrease in thermal conductivity in region II & III is observed, whereas in region I the thermal conductivity increases with increase in concentration beyond 0.1 wt%. In region II, a larger enhancement of 80 % was observed after freezing of base fluid (T=16 ^{o}C) for a particle loading of 0.75 wt% of GNP and reaches a constant value of 105 % at T=10 ^{o}C. The thermal conductivity of nanofluids increases with particle loading in all the regions. The decreasing in temperature beyond freezing point results in a decrease in thermal conductivity for all the concentrations of GNP. The presence of aggregates at higher particle loading leads to an unfavorable conduction pathway which is responsible for the decrease in thermal conductivity above a certain concentration under freezing. The values of k/k_f of CuNW, MWCNT and GNP in the three regions I, II and III at different concentrations are listed in **Table 7.1.**

Table 7.1 : k/k_f values of CuNW, MWCNT and GNP in the regions I, II and III at different concentrations.

Particle	Concentration (wt %)	k/k_f		
		Region I	Region II	Region III
CuNW	0.001	1	2.26	1.89
	0.0075	1	2.63	2.15
	0.01	1	2.82	2.3
	0.33	1	2.35	2.12
MWCNT	0.005	1.02	2.18	1.79
	0.01	1.035	2.6	2.07
	0.05	1.035	2.95	2.09
	0.1	1.028	2.66	1.88
	0.5	1.056	2.22	1.79
GNP	0.005	1	2.43	2.08
	0.01	1	2.61	2.25
	0.1	1.028	2.8	2.22
	0.2	1.03	2.45	1.86
	0.5	1.056	2.22	1.79

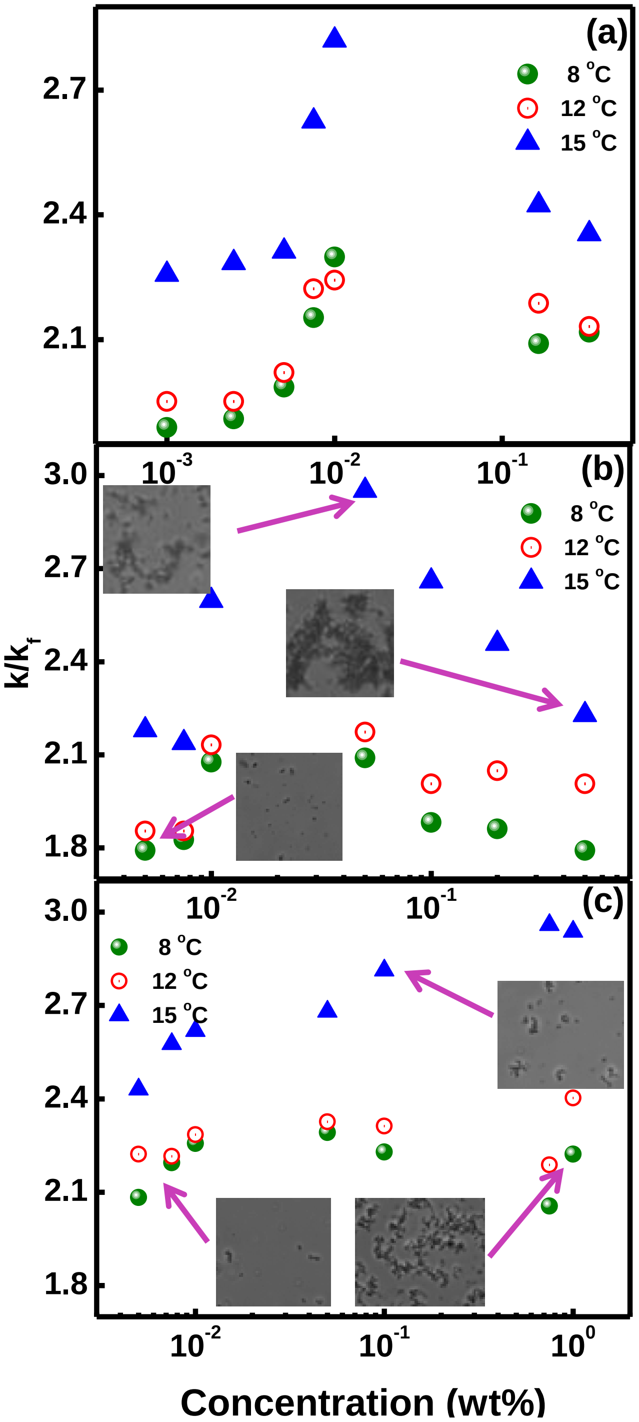

Figure 7.4: Effective thermal conductivity as a function of concentration at different temperatures for (a) CuNW, (b) MWCNT and (c) GNP (Closed circle, open circle and closed

triangle correspond to measurements at 8, 12 and 15 ^{o}C, respectively). The observed microstructures at certain concentrations are shown in the inset.

Fig. 7.4 shows the k/k_f as a function of concentration at different temperatures below freezing point for copper nanowire, multi-walled carbon nanotube and graphene nanoplatelets dispersed in hexadecane. In all the three systems, as the concentration of the nanoinclusion increases, the thermal conductivity starts increasing and reaches a maximum, followed by a decrease above a certain concentration. In the case of bare CuNW the thermal conductivity increases and reaches the maximum enhancement of 182 % at 15 ^{o}C for 0.01 wt %, but with further increase in concentration, the thermal conductivity starts decreasing. Similarly in the case of bare MWCNT and GNP, the maximum enhancements observed are 195 and 180 % at 15 ^{o}C for 0.05 and 0.1 wt%, respectively. With further increase in concentration of nanoparticle the thermal conductivity decreases.

Table 7.2 shows the size range, density and bulk thermal conductivity of CuNW, MWCNT and GNP used in the present study. As the density of CuNW is very high, it is prone to sedimentation (sedimentation velocity at infinite dilution is given by $V_0 = \frac{2\Delta\rho g d^2}{9\eta}$), as compared to the other two nanomaterials. Among the three, the MWCNT possesses the highest bulk thermal conductivity of 6600 W/m.K. Yet, the thermal conductivity enhancement for concentrations above 0.1 wt% of particle loading was comparable in all the three cases. This again goes in agreement with the classical EMT theory, where the thermal conductivity in dispersions is solely dependent on the volume fraction of dispersed phase and not the thermal properties of suspended materials.[199] In order to achieve a parallel mode of conduction, the interparticle spacing and interfacial thermal resistance are to be very small.[26] Since the particles are not stabilized, they have a tendency to form agglomerates due to weak van der Waals attraction. In such scenario, an increase in thermal conductivity is anticipated because of the effective conduction of heat through the percolating conducting path of aggregates.[59]

Table 7. 2: The size range, density and bulk thermal conductivity of CuNW, MWCNT and GNP.

S.No	Particle	Size	Density (g/cm^3)	*k* (bulk) W/m.K
1.	CuNW	Length – 10-50 µm Diameter – 50nm	8.94	385
2	MWCNT	Length - 10-30 µm Diameter < 8nm	1.3-1.4	6600
3	GNP	Lateral size : 2µm Thickness : 1 – 4 nm	2.25	3000

Among the three nanofluids CuNW gives the largest enhancement at very low particle loading under freezing. The maximum enhancement observed immediately after freezing is 181 % for a particle loading of 0.01 wt% (8.61×10^{-6} φ) CuNW. In the case of MWCNT and GNPs, the enhancement observed immediately after freezing is 195 and 182 % for particle loading of 0.05 wt% (0.000275φ) and 0.1 wt% (0.000342φ), respectively. The larger enhancement at very low concentrations observed in the case of CuNW was quite reproducible. However, this enhancement is quite puzzling and it is not clear if it is due to the larger length and diameter or due to the inherent large bulk thermal conductivity value. A large enhancement was reported by Wang et al.,[406] in CuNW – polyacrylate composites where a thermal conductivity enhancement of ~ 1350 % was observed at an ultralow loading of 0.9 φ%, which was attributed to the large aspect ratio and single-crystalline structure of CuNW. Studies in magnetic nanofluids[178] and soft sphere nanofluids[326] also shows increase in k with aspect ratio. Cherkasova et al.[407] studied the influence of particle anisotropy on the thermal conductivity of the nanofluids and reported that the thermal conductivity of the suspensions is enhanced with larger aspect-ratio of particles. Evans et al.[408] also found that the high aspect ratio particles give larger thermal conductivity enhancement than spherical particles. Another study show that the high interfacial thermal resistance in the case of high aspect ratio particles can inhibits the thermal conductivity increase.[409]

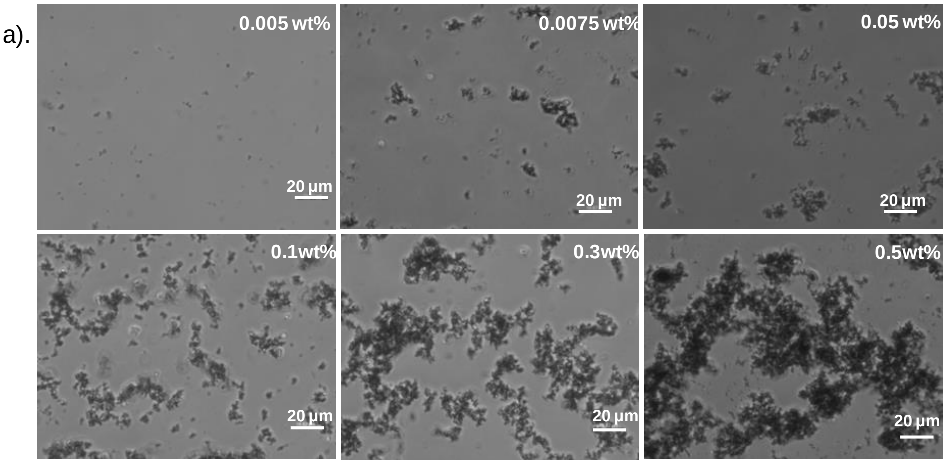

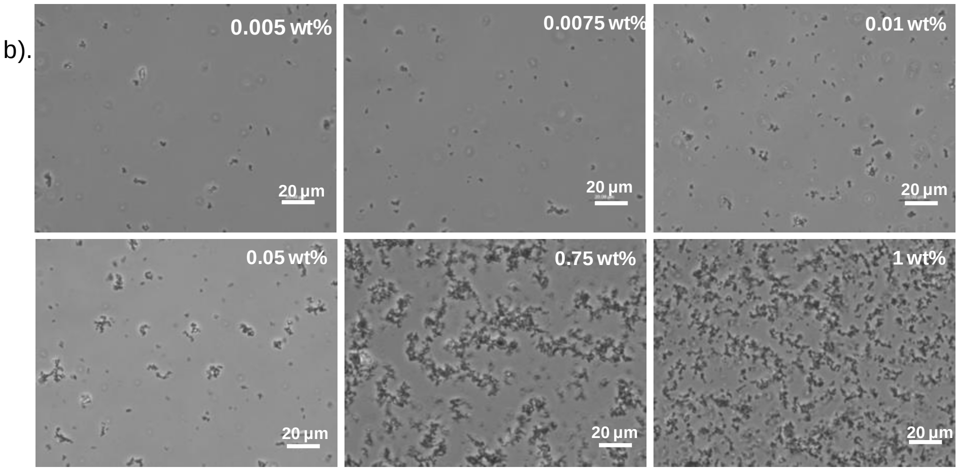

Figure 7.5: Phase contrast optical microscopic images of (a) bare MWCNT and (b) GNP in hexadecane at different particle loadings.

To obtain insight into the microstructural evolution of nanomaterials in basefluids, the phase contrast microscopic images are taken for the bare MWCNT and GNP in hexadecane at room temperature. **Fig. 7.5 (a)** and **(b)** show the microscopic images of MWCNT/hexadecane and GNP/hexadecane taken after sonication for 2 mins. The evolution of aggregates with increase in concentrations was evident from the microscopy images in both cases. However, the size of the aggregates present in GNP/ hexadecane system was less compared to that of MWCNT/hexadecane.

The repeated cycles of the thermal conductivity of pure hexadecane and with 0.005 wt% of MWCNT and GNP during melting and freezing is shown in **Fig. 7.6**. The freezing and melting cycles are found to be perfectly reversible in the case of hexadecane but showed some deviations with nanofillers, mainly in the freezing condition. The thermal conductivity enhancements of MWCNT nanofluid in the liquid phase during the first, second, third and fourth cycles are 1.023, 1.02, 1.012, and 1, respectively and during freezing, the enhancement were 2.1, 2.43, 2.36, and 1.75, respectively.

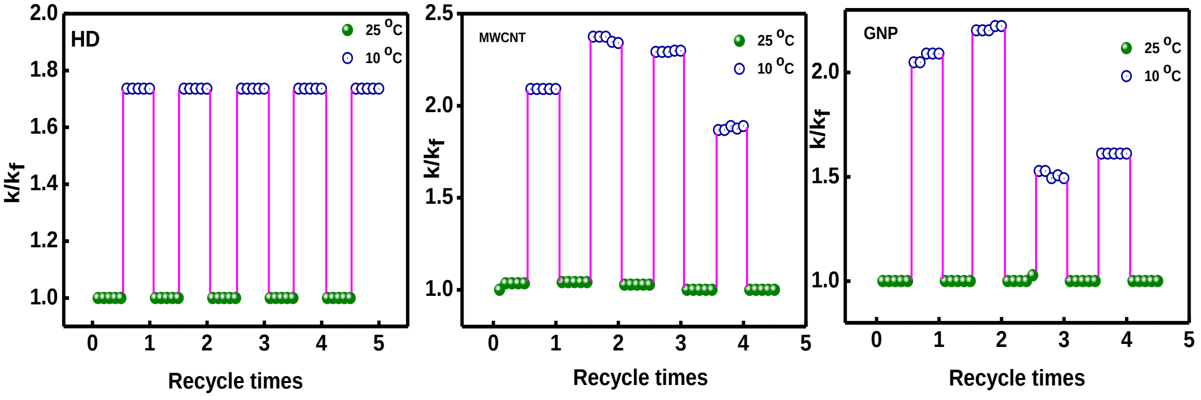

Figure 7.6: Thermal conductivity of (a) Hexadecane, (b) 0.005 wt% MWCNT and (c) 0.005 wt% GNP after different cycles of melting and freezing. Closed and open circles indicate the *k* measured at 25 °C and 10 °C during different thermal cycles, respectively.

The thermal conductivity enhancements of GNP nanofluid in the liquid phase during the first, second, third and fourth cycles are 1.02, 1, 1, and 1, respectively and during freezing, the enhancement were 2.15, 2.20, 1.5, and 1.57, respectively.

7.4 Conclusions

The thermal conductivity changes in phase change alkane incorporated with copper nanowire, multiwalled carbon nanotube and graphene nanoplatelets inclusions with different loading were studied. The phase contrast microscopic results show aggregate formation with increase in concentration of dispersed nanomaterials due to weak van der Waals attraction. These results suggest that at an optimal nanoparticle loading, the space filling agglomerates in a phase change alkane can provide extremely large tunable thermal conductivity. The thermal conductivity decreases with temperature and stabilizes several degrees below the freezing point. About two orders of thermal conductivity enhancement are observed at very low concentrations of nanofillers during the liquid to solid phase change. The increase in thermal conductivity during the first order phase transition is attributed to the reduction in the interfacial thermal resistance and the internal stress generated in the presence of nanomaterials at the grain boundaries of alkane crystals. An anomalously large thermal contrast is observed at very low concentration of copper nanowire which should have applications in heat transfer. Further studies are required to understand the reason behind this anomalous enhancement at very low concentration of Cu nanowires.

Chapter VIII | Conclusions and Recommendations for Future Work

8.1 Conclusions

The factors influencing the thermal properties of nanoparticle suspensions and phase change materials are studied systematically. The key findings are summarized below.

The thermal conductivity studies in model soft micellar system of average size 2.5 to 7 nm with different head group charges, show that the thermal conductivity of ionic surfactant micelles follows effective medium theory of poor thermal conductors (i.e. $1-3\varphi/2$, with the interfacial resistance tending to infinity). The long alkyl chain groups of non-ionic surfactant micelles are poor thermal conductors at very low concentrations with large interfacial tension compared to their anionic counterparts. The k measurements in aqueous alumina, silica and non-aqueous iron oxide nanofluids with particle size in the range of 12-15 nm, show that the presence of excess surfactant does not lower the thermal conductivity enhancement in nanofluids significantly, though the latter has a much lower conductivity than the basefluid. The adsorbed moieties on nanoparticles do not lower their thermal properties significantly but they enhance the dispersibility and stability of nanoparticles in the base fluids. For ‘hard’ spheres, the thermal conductivity follows effective medium theory for good conductors. The orientation of cylindrical nanomaterials along heat flow direction and their aspect ratio are found to have significant influence on the thermal conductivity enhancement of nanofluids. While the higher aspect ratio with random ordering gives a lower thermal conductivity, the orientated cylinders with high aspect ratio provides a dramatic enhancement in the thermal conductivity.

The thermal conductivity, electrical conductivity, viscosity and refractive index are found to increase with increase in volume fraction of nanoparticles in aggregating and non-aggregating nanofluids. For stable nanofluids, the experimental *k* data fitted well with the Maxwell's non-interacting model at lower concentration but deviated at higher concentration. For aggregating nanofluids, the experimental *k* values are found to be higher than the EMT predictions. The *k* is found to be time independent and dependent, respectively for stable and unstable nanofluids. The phase contrast microscopic study showed the presence of micron sized aggregates in TiO_2 and α- Al_2O_3 nanofluids and the absence of such aggregates in γ-Al_2O_3 and SiO_2 nanofluids. It is also observed that the aggregation in unstable nanofluids leads to a strong modification of their viscosity and refractive index.

The effect of particle size and volume fraction of nanoparticles on the temperature dependent specific heat capacity of metal oxide nanofluids show that the specific heat capacity decreases with increase in volume fraction and particle size in kerosene based Fe_3O_4 nanofluids but enhances in the case of PAO based Al_2O_3 nanofluids. These results suggest that PAO molecules strongly modify the interfacial thermal characteristics of Al_2O_3 nanoparticles that in turn increases the heat capacity of PAO based Al_2O_3 nanofluids. For kerosene based nanofluids, the C_p data was in reasonable agreement with thermal equilibrium model for specific heat (Model II) but showed a large deviation from the mixing model (Model I). This study also showed that the particle morphology plays a major role in specific heat capacity of nanofluids and the C_p decreases with increasing aspect ratio of nanoparticles due to a reduced surface atomic contribution.

A new approach was developed to achieve large tunable thermal conductivity in phase change alkane using inverse micellar templating. Thermal properties of n-hexadecane basefluids containing inverse micelles of different volume fractions have been studied using two ionic and non-ionic surfactants. For 0.223, 0.19 and 0.205 vol% of oleic acid, dioctyl sodium sulfosuccinate and sorbitan oleate inverse micelles, the thermal conductivity contrast between the solid and liquid phase were 185, 119 and 111%, respectively. Unlike the nanofluids, the thermal conductivity enhancement of micellar templated alkanes were perfectly reversible under repeated thermal cycling because of monodispersity and non aggregation of micelles due to effective intermolecular repulsion between micelles. These results suggest that during the first order phase transition, the inverse micelles are pushed to the grain boundaries of alkane crystals thereby reducing the interfacial thermal resistance. In addition to this, the internal stress generated during freezing improves the heat conduction through the alkane crystallites.

The thermal conductivity changes in phase change alkane incorporated with copper nanowire, multiwalled carbon nanotube, graphite nanofibers and graphene nanoplatelets showed that at an optimal nanoparticle loading, the space filling agglomerates in a phase change alkane can provide extremely large tunable thermal conductivity. The thermal conductivity decreases with temperature but stabilizes several degrees below the freezing point. About two orders of magnitude thermal conductivity enhancement is observed at a very low concentration of nanofillers during the liquid to solid phase change. The increase in thermal conductivity during the first order phase transition is attributed to the reduction in the interfacial thermal resistance and the internal stress generated in the presence of nanomaterials at the grain boundaries of alkane crystals. The thermal conductivity enhancement with volume fraction showed a large deviation from EMT theory in these nanofluids, which confirms the effective conduction of heat through percolated pathways. An anomalously large thermal contrast is observed at a very low concentration in copper nanowire suspensions. The phase contrast microscopic results show an increase in the aggregate growth with increase in concentration of dispersed particles, which corroborates the effective heat transport through percolated nanoparticle pathways.

8.2 Recommendations for Future Work

- To study the effect of bulk k of suspended nanomaterial on thermal conductivity of phase change material under freezing.
- To study the thermal conductivity of coreshell nanofluids, binary nanofluids, nano emulsions etc..
- To develop suitable approaches to design PCM based cooling circuits.
- Probing the effect of heating and cooling rates on k enhancement in PCM.
- Development of superior nanocomposite for effective heat transfer applications

Reference:

1. Bhushan, B., *Springer Handbook of Nanotechnology*. Spinger: New York, 2004.

2. Keblinski, P.; Phillpot, S. R.; Choi, S. U. S.; Eastman, J. A., Mechanism of heat flow in suspensions of nano-sized particles (nanofluids). *Int. J. Heat Mass Transfer* **2002,** 45, 855-863.

3. Chon, C. H.; Kihm, K. D.; Lee, S. P.; Choi, S. U., Empirical correlation finding the role of temperature and particle size for nanofluid (Al_2O_3) thermal conductivity enhancement. *Appl. Phys. Lett.* **2005,** 87, 153107.

4. Taylor, R.; Coulombe, S.; Otanicar, T.; Phelan, P.; Gunawan, A.; Lv, W.; Rosengarten, G.; Prasher, R.; Tyagi, H., Small particles, big impacts: A review of the diverse applications of nanofluids. *J. Appl. Phys.* **2013,** 113, 011301.

5. Philip, J.; Shima, P. D.; Raj, B., Evidence for enhanced thermal conduction through percolating structures in nanofluids. *Nanotechnology* **2008,** 19, 305706.

6. Karthikeyan, N. R.; Philip, J.; Raj, B., Effect of clustering on the thermal conductivity of nanofluids. *Mater. Chem. Phys.* **2008,** 109, 50-55.

7. Gharagozloo, P. E.; Eaton, J. K.; Goodson, K. E., Diffusion, aggregation, and the thermal conductivity of nanofluids. *Appl. Phys. Lett.* **2008,** 93, 103110.

8. Garg, J.; Poudel, B.; Chiesa, M.; Gordon, J. B.; Ma, J. J.; Wang, J. B.; Ren, Z. F.; Kang, Y. T.; Ohtani, H.; Nanda, J.; McKinley, G. H.; Chen, G., Enhanced thermal conductivity and viscosity of copper nanoparticles in ethylene glycol nanofluid. *J. Appl. Phys.* **2008,** 103, 074301.

9. Wright, B.; Thomas, D.; Hong, H.; Groven, L.; Puszynski, J.; Duke, E.; Ye, X.; Jin, S., Magnetic field enhanced thermal conductivity in heat transfer nanofluids containing Ni coated single wall carbon nanotubes. *Appl. Phys. Lett.* **2007,** 91, 173116.

10. Timofeeva, E. V.; Gavrilov, A. N.; McCloskey, J. M.; Tolmachev, Y. V.; Sprunt, S.; Lopatina, L. M.; Selinger, J. V., Thermal conductivity and particle agglomeration in alumina nanofluids: Experiment and theory. *Phys. Rev. E* **2007,** 76, 061203

11. Philip, J.; Shima, P. D.; Raj, B., Enhancement of thermal conductivity in magnetite based nanofluid due to chainlike structures. *Appl. Phys. Lett.* **2007,** 91, 203108.

12. Li, C. H.; Peterson, G. P., The effect of particle size on the effective thermal conductivity of Al2O3-water nanofluids. *J. Appl. Phys.* **2007,** 101, 044312

13. Jang, S. P.; Lee, J. H.; Hwang, K. S.; Choi, S. U. S., Particle concentration and tube size dependence of viscosities of Al2O3-water nanofluids flowing through micro- and minitubes. *Appl. Phys. Lett.* **2007,** 91, 243112.

14. Eapen, J.; Williams, W. C.; Buongiorno, J.; Hu, L. W.; Yip, S.; Rusconi, R.; Piazza, R., Mean-field versus microconvection effects in nanofluid thermal conduction. *Phys. Rev. Lett.* **2007,** 99, 095901.

15. Zhou, X. F.; Gao, L., Effective thermal conductivity in nanofluids of nonspherical particles with interfacial thermal resistance: Differential effective medium theory. *J. Appl. Phys.* **2006,** 100, 024913.

16. Zhang, X.; Gu, H.; Fujii, M., Effective thermal conductivity and thermal diffusivity of nanofluids containing spherical and cylindrical nanoparticles. *J. Appl. Phys.* **2006,** 100, 044325.

17. Yang, B.; Han, Z. H., Temperature-dependent thermal conductivity of nanorod-based nanofluids. *Appl. Phys. Lett.* **2006,** 89, 083111

18. Rusconi, R.; Rodari, E.; Piazza, R., Optical measurements of the thermal properties of nanofluids. *Appl. Phys. Lett.* **2006,** 89, 261916

19. Prasher, R.; Song, D.; Wang, J.; Phelan, P., Measurements of nanofluid viscosity and its implications for thermal applications. *Appl. Phys. Lett.* **2006,** 89, 133108.

20. Murshed, S. M. S.; Leong, K. C.; Yang, C., Determination of the effective thermal diffusivity of nanofluids by the double hot-wire technique. *J. Phys. D: Appl. Phys.* **2006,** 39, 5316-5322.

21. Kim, S. J.; Bang, I. C.; Buongiorno, J.; Hu, L. W., Effects of nanoparticle deposition on surface wettability influencing boiling heat transfer in nanofluids. *Appl. Phys. Lett.* **2006,** 89, 153107.

22. Hong, K. S.; Hong, T. K.; Yang, H. S., Thermal conductivity of Fe nanofluids depending on the cluster size of nanoparticles. *Appl. Phys. Lett.* **2006,** 88, 031901.

23. Evans, W.; Fish, J.; Keblinski, P., Role of brownian motion hydrodynamics on nanofluid thermal conductivity. *Appl. Phys. Lett.* **2006,** 88, 093116

24. Buongiorno, J., Convective Transport in Nanofluids. *ASME J. Heat Transfer* **2006,** 128, 240.

25. Abdallah, P. B., Heat transfer through near-field interactions in nanofluids. *Appl. Phys. Lett.* **2006,** 89, 113117.

26. Prasher, R.; Bhattacharya, P.; Phelan, P. E., Thermal Conductivity of Nanoscale Colloidal Solutions (Nanofluids). *Phys. Rev. Lett.* **2005,** 94, 025901.

27. Murshed, S. M. S.; Leong, K. C.; Yang, C., Enhanced thermal conductivity of TiO_2—water based nanofluids. *Int. J. Therm. Sci.* **2005,** 44, 367-373.

28. Keblinski, P.; Eastman, J. A.; Cahill, D. G., Nanofluids for thermal transport. *Mater. Today* **2005,** 8, 36-44.

29. Hong, T. K.; Yang, H. S.; Choi, C. J., Study of the enhanced thermal conductivity of Fe nanofluids. *J. Appl. Phys.* **2005,** 97, 064311.

30. Zhou, D. W., Heat transfer enhancement of copper nanofluid with acoustic cavitation. *Int. J. Heat Mass Transfer* **2004,** 47, 3109.

31. Wen, D.; Ding, Y., Experimental investigation into convective heat transfer of nanofluids at the entrance region under laminar flow conditions. *Int. J. Heat Mass Transfer* **2004,** 47, (24), 5181-5188.

32. Jang, S. P.; Choi, S. U. S., Role of brownian motion in the enhanced thermal conductivity of nanofluids. *Appl. Phys. Lett.* **2004,** 84, 4316.

33. Bhattacharya, P.; Saha, S. K.; Yadav, A.; Phelana, P. E.; Prasher, R. S., Brownian dynamics simulation to determine the effective thermal conductivity of nanofluids. *J. Appl. Phys.* **2004,** 95, 6492.

34. Xue, Q. Z., Model for effective thermal conductivity of nanofluids. *Phys. Lett. A* **2003,** 307, 313.

35. Xie, H.; Lee, H.; Youn, W.; Choi, M., Nanofluids containing multiwalled carbon nanotubes and their enhanced thermal conductivities. *J. Appl. Phys.* **2003,** 94, 4967-4971.

36. Patel, H. E.; Das, S. K.; Sundararajan, T.; Nair, A. S.; George, B.; Pradeep, T., Thermal conductivities of naked and monolayer protected metal nanoparticle based

nanofluids: Manifestation of anomalous enhancement and chemical effects. *Appl. Phys. Lett.* **2003,** 83, 2931-2933.

37. Das, S. K.; Putra, N.; Thiesen, P.; Roetzel, W., Temperature Dependence of Thermal Conductivity Enhancement of Nanofluids *ASME J. Heat Transfer* **2003,** 125, 567-574.

38. Eastman, J. A.; Choi, S. U. S.; Li, S.; Yu, W.; Thompson, L. J., Anomalously increased effective thermal conductivities of ethylene glycol-based nanofluids containing copper nanoparticles. *Appl. Phys. Lett.* **2001,** 78, 718-720.

39. Xuan, Y.; Roetzel, W., Conceptions for heat transfer correlation of nanofluids. *Int. J. Heat Mass Transfer* **2000,** 43, 3701-3707.

40. Younes, H.; Christensen, G.; Luan, X.; Hong, H.; Smith, P., Effects of alignment, pH, surfactant, and solvent on heat transfer nanofluids containing Fe_2O_3 and CuO nanoparticles. *J. Appl. Phys.* **2012,** 111, 064308.

41. Thang, B. H.; Quang, L. D.; Hong, N. M.; Khoi, P. H.; Minh, P. N., Application of Multiwalled Carbon Nanotube Nanofluid for 450 W LED Floodlight. *J.Nano Mat.* **2014,** 2014, 1-6.

42. Mahendran, V.; Philip, J., Naked eye visualization of defects in ferromagnetic materials and components. *NDT&E International* **2013,** 60, 100-109.

43. Liakos, I.; Grumezescu, A. M.; Holban, A. M., Magnetite Nanostructures as Novel Strategies for Anti-Infectious Therapy. *Molecules* **2014,** 19, (8), 12710-12726.

44. Khullar, V.; Tyagi, H.; Hordy, N.; Otanicar, T. P.; Hewakuruppu, Y.; Modi, P.; Taylor, R. A., Harvesting solar thermal energy through nanofluid-based volumetric absorption systems. *Int. J. Heat Mass Transfer* **2014,** 77, 377-384.

45. Taylor, R. A.; Otanicar, T.; Rosengarten, G., Nanofluid-based optical filter optimization for PV/T systems. *Light Sci. Appl.* **2012,** 1, 1-7.

46. Rosenzweig, R. E., *Ferrohydrodynamics*. Cambridge University Press: Cambridge, 1985.

47. Philip, J.; Shima, P. D.; Raj, B., Nanofluid with tunable thermal properties. *Appl. Phys. Lett.* **2008,** 92, 043108.

48. Kao, M. J.; Lo, C. H.; Tsung, T. T.; Wu, Y. Y.; Jwo, C. S.; Lin, H. M., Copper-oxide brake nanofluid manufactured using arc-submerged nanoparticle synthesis system. *J. Alloys Compd.* **2007,** 134-435, 672-674.

49. Yu, W.; Xie, H., A Review on Nanofluids: Preparation, Stability Mechanisms, and Applications. *J. Nanomater.* **2012,** 2012, 1-17.

50. Dudda, B.; Shin, D., Effect of nanoparticle dispersion on specific heat capacity of a binary nitrate salt eutectic for concentrated solar power applications. *Int. J. Thermal Sci.* **2013,** 69, 37-42.

51. Mahian, O.; Kianifar, A.; Kalogirou, S. A.; Pop, I.; Wongwises, S., A review of the applications of nanofluids in solar energy. *Int. J. Heat Mass Transfer* **2013,** 57, 582-594.

52. Yang, D.; Yang, F.; Hu, J.; Long, J.; Wang, C.; Fu, D.; Ni, Q., Hydrophilic multi-walled carbon nanotubes decorated with magnetite nanoparticles as lymphatic targeted drug delivery vehiclesw *Chem. Commun.* **2009**, 4447.

53. Hernández, R. In *Polymer gels with magnetic nanoparticles. Applications in magnetic hyperthermia.*, POLYSOLVAT-9, 9th International IUPAC Conference on Polymer-Solvent Complexes & Intercalates, Ukraine, 11-14 September 2012, 2012; Ukraine, 2012.

54. Raj, K.; Moskowitz, R., Commercial applications of Ferrofluis. *J. Magn. Magn. Mater.* **1990,** 85, 233-245.

55. Hyning, D. L. V.; Klemperer, W. G.; Zukoski, C. F., Silver nanoparticle formation: Predictions and verification of the aggregative growth model. *Langmuir* **2001,** 17, 3128-3135.

56. Chen, Y.; Luo, X.; Yue, G.-H.; Luo, X.; Peng, D.-L., Synthesis of iron–nickel nanoparticles via a nonaqueous organometallic route. *Mat. Chem. Phys.* **2009,** 113, 412-416.

57. Pati, S. S.; Mahendran, V.; Philip, J., A simple approach to produce stable ferrofluids without surfactants and with high temperature stability. *J. Nanofluids* **2013,** 2, 94-103.

58. Gnanaprakash, G.; Mahadevan, S.; Jayakumar, T.; Sundaram, P. K.; Philip, J.; Raj, B., Effect of initial pH and temperature of iron salt solutions on formation of magnetite nanoparticles. *Mater. Chem. Phys.* **2007,** 103, 168-175.

59. Prasher, R.; Phelan, P. E.; Bhattacharya, P., Effect of aggregation kinetics on the thermal conductivity of nanoscale colloidal solutions (nanofluid) *Nano. Lett.* **2006,** 6, 1529-1534.

60. Bonnemann, H.; Richards, R. M., Nanoscopic Metal Particles 2 Synthetic Methods and Potential Applications. *Eur. J. Inorg. Chem.* **2001**, 2455-2480.

61. Xuan, Y.; Li, Q., Heat transfer enhancement of nanofluids. *Int. J. Heat Fluid Flow* **2000,** 21, 58-64.

62. Kwak, K.; Kim, C., Viscosity and thermal conductivity of copper oxide nanofluid dispersed in ethylene glycol. *Korean-Australia Rheology Journal* **2005,** 17, (2), 35-40.

63. Liu, M. S.; Lin, M. C. C.; Huang, I. T.; Wang, C. C., Enhancement of thermal conductivity with carbon nanotube for nanofluids. *Int. Commu. Heat Mass Transfer* **2005,** 32, 1202-1210.

64. Wang, X. B.; Liu, Z. M.; Hu, P. A.; Liu, Y. Q.; Han, B. X.; Zhu, D. B., Nanofluids in carbon nanotubes using supercritical CO_2: a first step towards a nanochemical reaction. *Appl. Phys. A* **2005,** 80, 637-639.

65. Bom, D.; Andrews, R.; Jacques, D.; Anthony, J.; Chen, B.; Meie, M. S.; Selegue, J. P., Thermogravimetric Analysis of the Oxidation of Multi-Walled Carbon Nanotubes: Evidence for the Role of Defect Sites in Carbon Nanotube Chemistry. *Nano Lett.* **2002,** 2, 615-619.

66. Lee, S.; Choi, S. U. S.; Li, S.; Eastman, J. A., Measuring Thermal Conductivity of Fluids Containing Oxide Nanoparticles. *ASME J. Heat Transfer* **1999,** 121, 280-289.

67. Suresh, S.; Venkitaraj, K. P.; Selvakumar, P.; Chandrasekar, M., Synthesis of Al2O3–Cu/water hybrid nanofluids using two step method and its thermo physical properties. *Colloids Surf., A* **2011,** 388, 41-48.

68. Ghosh, M. M.; Ghosh, S.; Pabi, S. K., On Synthesis of a Highly Effective and Stable Silver Nanofluid Inspired by Its Multiscale Modeling. *Nanosci. Nanotechnol. Lett.* **2012,** 4, 1-6.

69. Hwang, Y.; Lee, J. K.; Lee, J. K.; Jeong, Y. M.; Cheong, S.; Ahn, Y. C.; Kim, S. H., Production and dispersion stability of nanoparticles in nanofluids. *Powder Technol.* **2008,** 186, 145-153.

70. Moosavi, M.; Goharshadi, E. K.; Youssefi, A., Fabrication, characterization, and measurement of some physicochemical properties of ZnO nanofluids. *Int. J. Heat Fluid Flow* **2010,** 31, 599-605.

71. Choi, C.; Yoo, H. S.; Oh, J. M., Preparation and heat transfer properties of nanoparticle-in-transformer oil dispersions as advanced energy efficient coolants. *Curr. Appl. Phys.* **2007,** 8, 710.

72. Wen, D.; Ding, Y., Natural convective heat transfer of suspensions of titanium dioxide nanoparticles (nanofluids). *IEEE Trans. Nanotech.* **2006,** 5, 220-227.

73. Salehi, J. M.; Heyhat, M. M.; Rajabpour, A., Enhancement of thermal conductivity of silver nanofluid synthesized by a one-step method with the effect of polyvinylpyrrolidone on thermal behavior. *Appl. Phys. Lett.* **2013,** 102, 231907.

74. Li, Y.; Zhou, J. e.; Tung, S.; Schneider, E.; Xi, S., A review on development of nanofluid preparation and characterization. *Powder Technol.* **2009,** 196, 89.

75. Chen, Y.; Peng, D.-L.; Lin, D.; Luo, X., Preparation and magnetic properties of nickel nanoparticles via the thermal decomposition of nickel organometallic precursor in alkylamines. *Nanotechnology* **2007,** 18, 505703.

76. Zhu, J.; Li, D.; Chen, H.; Yang, X.; Lu, L.; Wang, X., Highly Dispersed CuO Nanoparticles, Prepared by a Novel Quick Precipitation Method. *Mater. Lett.* **2004,** 58, 3324-3327.

77. Sandhya, S. U.; Nityananda, S. A., A Facile One Step Solution Route to Synthesize Cuprous Oxide Nanofluid. *Nanomater. Nanootechnol.* **2013,** 3, 1-7.

78. Kumar, S. A.; Meenakshi, K. S.; Narashimhan, B. R. V.; Srikanth, S.; Arthanareeswaranc, G., Synthesis and characterization of copper nanofluid by a novel one-step method. *Mater. Chem. Phys.* **2009,** 113, 57-62.

79. Patel, K.; Kapoor, S.; Dave, D. P.; Mukherjee, T., Synthesis of nanosized silver colloids by microwave dielectric heating. *J. Chem. Sci.* **2005,** 117, 53-60.

80. Akoh, H.; Tsukasaki, Y.; Yatsuya, S.; Tasaki, A., Magnetic properties of ferromagnetic ultrafine particlesprepared by vacuum evaporation on running oil substrate. *J. Cryst. Growth* **1978,** 45, 495-500.

81. Sridhara, V.; Satapathy, L. N., Al_2O_3-based nanofluids: a review. *Nanoscale Res. Lett.* **2011,** 6, (456), 1-16.

82. Choi, S. U. S.; Eastman, J. A. Enhanced heat transfer using nanofluids. 2001.

83. Kanaras, A. G.; Kamounah, F. S.; Schaumburg, K.; Kiely, C. J.; Brust, M., Thioalkylated tetraethylene glycol: a new ligand for water soluble monolayer protected gold clusters. *Chem. Comm.* **2002,** 20, 2294-2295.

84. Lo, C.-H.; Tsung, T.-T.; Chen, L.-C., Shape-controlled synthesis of Cu-based nanofluid using submerged arc nanoparticle synthesis system (SANSS). *J. Cryst. Growth* **2005,** 277, 636-642.

85. Lo, C.-H.; Tsung, T.-T.; Lin, H.-M., Preparation of silver nanofluid by the submerged arc nanoparticle synthesis system (SANSS). *J. Alloys Compd.* **2007,** 434-435, 659-662.

86. Kim, H. J.; Bang, I. C.; Onoe, J., Characteristic stability of bare Au-water nanofluids fabricated by pulsed laser ablation in liquids. *Optics and Lasers in Eng.* **2009,** 47, 532.

87. Lee, S. W.; Park, S. D.; Bang, I. C., Critical heat flux for CuO nanofluid fabricated by pulsed laser ablation differentiating deposition characteristics. *Int. J. Heat Mass Transfer* **2012,** 55, (23-24), 6908-6915.

88. Phuoc, T. X.; Soong, Y.; Chyu, M. K., Synthesis of Ag-deionized water nanofluids using multi-beam laser ablation in liquids. *Optics and Lasers in Eng.* **2007,** 45, 1099.

89. Wang, H.; Xu, J. Z.; Zhu, J. J.; Chen, H. Y., Preparation of CuO Nanoparticles by Microwave Irradiation. *J. Cryst. Growth* **2002,** 244, 88-94.

90. Zhu, H. t.; Lin, Y. s.; Yin, Y. s., A novel one-step chemical method for preparation of copper nanofluids. *J. Colloid Interface Sci.* **2004,** 277, 100-103.

91. Bönnemann, H.; Botha, S. S.; Bladergroen, B.; Linkov, V. M., Monodisperse copper- and silver-nanocolloids suitable for heat-conductive fluids. *Appl. Organomet. Chem.* **2005,** 19, (6), 768-773.

92. Singh, A. K.; Raykar, V. S., Microwave synthesis of silver nanofluids with polyvinylpyrrolidone (PVP) and their transport properties. *Colloid. Polym. Sci.* **2008,** 286, 1667-1673.

93. Bonet, F.; Tekaia-Elhsissen, K.; Sarathy, K. V., Study of interaction of ethylene glycol/PVP phase on noble metal powders prepared by polyol process. *Bull. Mater. Sci.* **2000,** 23, (3), 165-168.

94. Sun, Y.; Mayers, B.; Herricks, T.; Xia, Y., Polyol Synthesis of Uniform Silver Nanowires: A Plausible Growth Mechanism and the Supporting Evidence. *Nano Lett.* **2003,** 3, (7), 955-960.

95. Hsin, Y. L.; Hwang, K. C.; Chen, F. R.; Kai, J. J., Production and in-situ Metal Filling of Carbon Nanotubes in Water. *Adv. Mat.* **2001,** 13, 830-833.

96. Wanga, C.; Yanga, J.; Ding, Y., Phase transfer based synthesis and thermophysical properties of Au/Therminol VP-1 nanofluids. *Prog. Nat. Sci.* **2013,** 23, (3), 338-342.

97. Yang, J.; Sargent, E.; Kelley, S.; Ying, J. Y., A general phase-transfer protocol for metal ions and its application in nanocrystal synthesis. *Nat. Mat.* **2010,** 8, 683-689.

98. Kumar, A.; Joshi, H. M.; Mandale, A. B.; Srivastava, R.; Adyanthaya, S. D.; Pasricha, R.; Sastry, M., Phase transfer of platinum nanoparticles from aqueous to organic solutions using fatty amine molecules. *J. Chem. Sci.* **2004,** 116, 293-300.

99. Wang, X.; Xu, S.; Zhou, J.; Xu, W., A rapid phase transfer method for nanoparticles using alkylamine stabilizers. *J. Colloid Interf. Sci.* **2010,** 348, 24-28.

100. Yu, W.; Xie, H.; Wang, X.; Wang, X., Highly Efficient Method for Preparing Homogeneous and Stable Colloids Containing Graphene Oxide. *Nanoscale Res. Lett.* **2011,** 6, 1-7.

101. Zhu, H.; Zhang, C.; Tang, Y.; Wang, J.; Ren, B.; Yin, Y., Preparation and thermal conductivity of suspensions of graphite nanoparticles. *Carbon* **2007,** 45, (1), 226-228.

102. Muthukumaran, T.; Gnanaprakash, G.; Philip, J., Synthesis of Stable Magnetic Nanofluids of Different Particle Sizes. *J. Nanofluids* **2012,** 1, 85-92.

103. Maxwell, J. C., *A treatise on electricity and magnetism*. II ed.; Clarendon: 1881.

104. Merrill, W. M.; Diaz, R. E.; LoRe, M. M.; Squires, M. C.; Alexopoulos, N. G., Effective Medium Theories for Artificial Materials Composed of Multiple Sizes of Spherical Inclusions in a Host Continuum. *(IEEE) Trans. Antennas Propagat.* **1999,** 47, (1), 142-148.

105. Bruggeman, D. A. G., Berechnung verschiedener physikalischer Konstanten von heterogenen Substanzen. I. Dielektrizitätskonstanten und Leitfähigkeiten der Mischkörper aus isotropen Substanzen. *Ann. Phys.* **1935,** 416, (7), 636-664.

106. Hashin, Z.; Shtrikman, S., A variational approach to the theory of the effective magnetic permeability of multiphase materials. *J. Appl. Phys* **1962,** 33, 3125.

107. Hamilton, R. L.; Crosser, O. K., Thermal conductivity of heterogeneous two-component systems. *Ind. Eng. Chem. Fundam.* **1962,** 1, 187-191.

108. Yu, W.; Choi, S. U. S., The role of interfacial layers in the enhanced thermal conductivity of nanofluids: A renovated Hamilton–Crosser model. *J. Nanopart. Res.* **2004,** 6, 355-361.

109. Xuan, Y.; Li, Q., Investigation on Convective Heat Transfer and Flow Features of Nanofluids. *J. Heat Transfer* **2003,** 125, 151-155.

110. Kumar, D. H.; Patel, H. E.; Kumar, V. R. R.; Sundararajan, T.; Pradeep, T.; Das, S. K., Model for heat conduction in nanofluids. . *Phys. Rev. Lett.* **2004,** 93, (14), 144301.

111. Yamada, E.; Ota, T., Effective thermal conductivity of dispersed materials. *Heat and Mass Transfer* **1980,** 13, (1-2), 27-37.

112. Hesselman, D. P. H.; Johnson, L. F., Effective thermal conductivity of nanocomposites with interfacial thermal barrier resistance. *J. Compos. Mater.* **1987,** 21, (6), 508-515.

113. Wang, B. X.; Zhou, L. P.; Peng, X. F., A fractal model for predicting the effective thermal conductivity of liquid with suspension of nanoparticles. *Int. J. Heat Mass Transfer* **2003,** 46, 2665.

114. Meibodi, M. E.; Sefti, M. V.; Rashidi, A. M.; Amrollahi, A.; Tabasi, M.; Kalal, H. S., A model for thermal conductivity of nanofluids. *Mater. Chem. Phys.* **2010,** 123, 639-643.

115. Corcione, M., Empirical correlating equations for predicting the effective thermal conductivity and dynamic viscosity of nanofluids. *Energ. Convers. Manage.* **2011,** 52, 789-793.

116. Xie, H.; Fujii, M.; Zhang, X., Effect of interfacial nanolayer on the effective thermal conductivity of nanoparticle-fluid mixture. *Int. J. Heat Mass Transfer* **2005,** 48, 2926-2932.

117. Yu, C. J.; Richter, A. G.; Datta, A.; Durbin, M. K.; Dutta, P., Molecular layering in a liquid on a solid substrate: an X-ray reflectivity study. *Physica B* **2000.,** 283, 27-31.

118. Hendersona, J. R.; Swol, F. v., On the Interface between a Fluid and a Planar Wall: Theory and Simulations of a Hard Sphere Fluid at a Hard Wall. *Mol. Phys.* **1984,** 51, (4), 991-1010.

119. Joshi, A. A.; Majumdar, A., Transient ballistic and diffusive phonon heat transport in thin films. *J. Appl. Phys.* **1993,** 74, 31-39.

120. Ye, L.; Liu, J.; Sheng, P.; Huang, J. S.; Weitz, D. A., Sound propagation in colloidal systems. *J. Physique IV* **1993,** 3, 183-196.

121. DeGroot, S. R.; Mazur, P., *Nonequilibrium thermodynamics*. Dover Publications: New York, 1984.

122. Eapen, J.; Rusconi, R.; Piazza, R.; Yip, S., The Classical Nature of Thermal Conduction in Nanofluids. *ASME J. Heat Transfer* **2010,** 132, 102402.

123. Keblinski, P.; Cahill, D. G., Comment on ‘‘Model for Heat Conduction in Nanofluids’’. *Phys. Rev. Lett.* **2005,** 95, 209401.

124. Mo, H.; Evmenenko, G.; Dutta, P., Ordering of liquid squalane near a solid surface. *Chem. Phys. Letters* **2005,** 415, 106-109.

125. Reedijk, M. F.; Arsic, J.; Hollander, F. F. A.; Vries, S. A. d.; Vlieg, E., Liquid Order at the Interface of KDP Crystals with Water: Evidence for Icelike Layers. *Phys. Rev. Lett.* **2003,** 90, (9), 066103.

126. Yu, C. J.; Richter, A. G.; Kmetko, J.; Dugan, S. W.; Datta, A.; Dutta, P., Structure of interfacial liquids: X-ray scattering studies. *Phys. Rev. E* **2001,** 63, 021205.

127. Masuda, H.; Ebata, A.; Teramae, K.; Hishinuma, N., Alteration of Thermal Conductivity and Viscosity of Liquid by Dispersing Ultra-Fine Particles (Dispersion of γ–Al2O3, SiO2, and TiO2 Ultra-Fine Particles). *Netsu Bussei* **1993,** 7, 227-233.

128. Murshed, S. M. S.; Leong, K. C.; Yang, C., Investigations of thermal conductivity and viscosity of nanofluids. *Int. J. Therm. Sci.* **2008,** 47, 560-568.

129. Yu, W.; Xie, H.; Wang, X.; Wang, X., Significant thermal conductivity enhancement for nanofluids containing graphene nanosheets. *Phys. Lett. A* **2011,** 375, 1323-1328.

130. Yu, W.; Xie, H.; Bao, D., Enhanced thermal conductivities of nanofluids containing graphene oxide nanosheets. *Nanotechnology* **2010,** 21, 055705.

131. Yu, W.; Xie, H.; Chen, W., Experimental investigation on thermal conductivity of nanofluids containing graphene oxide nanosheets. *J. Appl. Phys.* **2010,** 107, 094317

132. Reinecke, B. N.; Shan, J. W.; Suabedissen, K. K.; Cherkasova, A. S., On the anisotropic thermal conductivity of magnetorheological suspensions. *J. Appl. Phys.* **2008,** 104, 023507.

133. Cha, G.; Ju, Y. S.; Ahure, L. A.; Wereley, N. M., Experimental characterization of thermal conductance switching in magnetorheological fluids. *J. Appl. Phys.* **2010,** 107, 09B505.

134. Sundar, L. S.; Singh, M. K.; Ramana, E. V.; Singh, B.; Gracio, J.; Sousa, A. C. M., Enhanced Thermal Conductivity and Viscosity of Nanodiamond-Nickel Nanocomposite Nanofluids. *Sci. Rep.* **2014,** 4, 14.

135. Mehrali, M.; Sadeghinezhad, E.; Latibari, S. T.; Kazi, S. N.; Mehrali, M.; Zubir, M. N. B. M.; Metselaar, H. S. C., Investigation of thermal conductivity and rheological properties of nanofluids containing graphene nanoplatelets. *Nanoscale Res. Lett.* **2014,** 9, (15), 1-12.

136. Bjorneklett, A.; Halbo, L.; Kristiansen, H., Thermal conductivity of epoxy adhesives filled with silver particles *Int. J. Adhes. Adhes.* **1992,** 12, 99-104.

137. Shin, S.; Lee, S.-H., Thermal conductivity of suspensions in shear flow fields. *Int. J Heat Mass Transfer* **2000,** 43, 4275-4284.

138. Choi, S. U. S.; Zhang, Z. G.; Yu, W.; Lockwood, F. E.; Grulke, E. A., Anomalous thermal conductivity enhancement in nanotube suspensions. *Appl. Phys. Lett.* **2001,** 79, 2252-2254.

139. Cho, T.; Baek, I.; Lee, J.; Park, S., Preparation of nanofluids containing suspended silver particles for enhancing fluid thermal conductivity of fluids. *J. Ind. Eng. Chem.* **2005,** 11, 400.

140. Hwang, Y. J.; Ahn, Y. C.; Shin, H. S.; Lee, C. G.; Kim, G. T.; Park, H. S.; Lee, J. K., Investigation on characteristics of thermal conductivity enhancement of nanofluids. *Curr. Appl. Phys.* **2006,** 6, 1068.

141. Jana, S.; Khojin, A. S.; Zhong, W. H., Enhancement of fluid thermal conductivity by the addition of single and hybrid nano-additives. *Thermochim. Acta* **2007,** 462, 45.

142. Yoo, D. H.; Hong, K. S.; Yang, H. S., Study of thermal conductivity of nanofluids for the application of heat transfer fluids. *Thermochim. Acta* **2007,** 455, 66-69.

143. Chen, L.; Xie, H.; Li, Y.; Yu, W., Nanofluids containing carbon nanotubes treated by mechanochemical reaction. *Thermochim. Acta* **2008,** 477, 21-24.

144. Mostafizur, R. M.; Bhuiyan, M. H. U.; Saidur, R.; Aziz, A. R. A., Thermal conductivity variation for methanol based nanofluids. *Int. J. Heat Mass Transfer* **2014,** 76, 350-356.
145. Khedkar, R. S.; Kiran, A. S.; Sonawane, S. S.; Wasewar, K. L.; Umare, S. S., Thermo-physical properties measurement of water based Fe_3O_4 nanofluids. *Carbon-Sci. Tech.* **2013,** 5, (1), 187-191.
146. Singh, D.; Timofeeva, E.; Yu, W.; Routbort, J.; France, D.; Smith, D.; Cepero, J. M. L., An investigation of silicon carbide-water nanofluid for heat transfer applications. *J. Appl. Phys.* **2009,** 105, 064306.
147. Buongiorno, J.; Venerus, D. C.; Prabhat, N.; McKrell, T.; Townsend, J.; Christianson, R.; Tolmachev, Y. V.; Keblinski, P.; Hu, L.-w.; Alvarado, J. L.; Bang, I. C.; Bishnoi, S. W.; Bonetti, M.; Botz, F.; Cecere, A.; Chang, Y.; Chen, G.; Chen, H.; Chung, S. J.; Chyu, M. K.; Das, S. K.; Paola, R. D.; Ding, Y.; Dubois, F.; Dzido, G.; Eapen, J.; Escher, W.; Funfschilling, D.; Galand, Q.; Gao, J.; Gharagozloo, P. E.; Goodson, K. E.; Gutierrez, J. G.; Hong, H.; Horton, M.; Hwang, K. S.; Iorio, C. S.; Jang, S. P.; Jarzebski, A. B.; Jiang, Y.; Jin, L.; Kabelac, S.; Kamath, A.; Kedzierski, M. A.; Kieng, L. G.; Kim, C.; Kim, J.-H.; Kim, S.; Lee, S. H.; Leong, K. C.; Manna, I.; Michel, B.; Ni, R.; Patel, H. E.; Philip, J.; Poulikakos, D.; Reynaud, C.; Savino, R.; Singh, P. K.; Song, P.; Sundararajan, T.; Timofeeva, E.; Tritcak, T.; Turanov, A. N.; Vaerenbergh, S. V.; Wen, D.; Witharana, S.; Yang, C.; Yeh, W.-H.; Zhao, X.-Z.; Zhou, S.-Q., A benchmark study on the thermal conductivity of nanofluids. *J. Appl. Phys.* **2009,** 106, 094312.
148. Shima, P. D.; Philip, J.; Raj, B., Influence of aggregation on thermal conductivity in stable and unstable nanofluids. *Appl. Phys. Lett.* **2010,** 97, 153113.
149. Branson, B. T.; Beauchamp, P. S.; Beam, J. C.; Lukehart, C. M.; Davidson, J. L., Nanodiamond nanofluids for enhanced Thermal conductivity. *ACS Nano* **2013,** 7, (4), 3183-3189.
150. Yu, W.; Xie, H.; Chen, L.; Li, Y., Enhancement of thermal conductivity of kerosene-based Fe_3O_4 nanofluids prepared via phase-transfer method. *Colloids Surf. A* **2010,** 355, 109-113.
151. Parekh, K.; Lee, H. S., Magnetic field induced enhancement in thermal conductivity of magnetite nanofluid. *J. Appl. Phys.* **2010,** 107, 09A310.
152. Angayarkanni, S. A.; Philip, J., Effect of Nanoparticles Aggregation on Thermal and Electrical Conductivities of Nanofluids. *J. Nanofluids* **2014,** 3, (1), 17-25.
153. Ponmani, S.; William, J. K. M.; Samuel, R.; Nagarajan, R.; Sangwai, J. S., Formation and characterization of thermal and electrical properties ofCuO and ZnO nanofluids in xanthan gum. *Colloids Surf., A: Physicochem. Eng. Aspects* **2014,** 443, 37-43.
154. Jiang, H.; Xu, Q.; Huang, C.; Shi, L., Effect of temperature on the effective thermal conductivity ofn-tetradecane-based nanofluids containing copper nanoparticles. *Particuology* **2015**, In press.
155. Mehrali, M.; Sadeghinezhad, E.; Latibari, S. T.; Mehrali, M.; Togun, H.; Zubir, M. N. M.; Kazi, S. N.; Metselaar, H. S. C., Preparation, characterization, viscosity, and thermal conductivity of nitrogen-doped graphene aqueous nanofluids. *J. Mater. Sci.* **2014,** 49, 7156-7171.

156. Ma, L.; Wang, J.; Marconnet, A. M.; Barbati, A. C.; McKinley, G. H.; Liu, W.; Chen, G., Viscosity and Thermal Conductivity of Stable Graphite Suspensions Near Percolation. *Nano Lett.* **2014,** 15, 127-133.
157. Zhu, H.; Zhang, C.; Liu, S.; Tang, Y.; Yin, Y., Effects of nanoparticle clustering and alignment on thermal conductivities of Fe_3O_4 aqueous nanofluids. *Appl. Phys. Lett.* **2006,** 89, 023123.
158. Jiang, H.; Li, H.; Xu, Q.; Shi, L., Effective thermal conductivity of nanofluids considering interfacial nano-shells. *Mater. Chem. Phys.* **2014,** 148, 195-200.
159. Assael, M. J.; Metaxa, I. N.; Kakosimos, K.; Constantinou, D., Thermal Conductivity of Nanofluids – Experimental and Theoretical. *Int. J. Thermophys.* **2006,** 27, 999-1017.
160. Assael, M. J.; Metaxa, I. N.; Arvanitidis, J.; Christofilos, D.; Lioutas, C., Thermal conductivity enhancement in aqueous suspensions of carbon multi-walled and double-walled nanotubes in the presence of two different dispersants. *Int. J. Thermophys.* **2005** 26, 647-664.
161. Han, Z. H.; Yang, B.; Kim, S. H.; Zachariah, M. R., Application of hybrid sphere/carbon nanotube particles in nanofluids. *Nanotechnology* **2007,** 18, 105701.
162. Shaikha, S.; Lafdi, K.; Ponnappan, R., Thermal conductivity improvement in carbon nanoparticle doped PAO oil:An experimental study. *J. Appl. Phys.* **2007,** 101, 064302.
163. Yang, Y.; Grulke, E. A.; Zhang, Z. G.; Wu, G., Thermal and rheological properties of carbon nanotube-in-oil dispersions. *J. Appl. Phys.* **2006,** 99, 114307.
164. Kim, Y. J.; Ma, H.; Yu, Q., Plasma nanocoated carbon nanotubes for heat transfer nanofluids. *Nanotechnology* **2010,** 21, 295703.
165. Jha, N.; Ramaprabhua, S., Thermal conductivity studies of metal dispersed multiwalled carbon nanotubes in water and ethylene glycol based nanofluid *J. Appl. Phys.* **2009,** 106, 084317.
166. Glory, J.; Bonetti, M.; Helezen, M.; Hermite, M. M. L.; Reynaud, C., Thermal and electrical conductivities of water-based nanofluids prepared with long multiwalled carbon nanotubes. *J. Appl. Phys.* **2008,** 103, 094309.
167. Vajjha, R. S.; Das, D. K., Experimental determination of thermal conductivity of three nanofluids and development of new correlations. *Int. J. Heat Mass Transfer* **2009,** 52, 4675-4682.
168. Kim, S. H.; Choi, S. R.; Kim, D., Thermal Conductivity of Metal-Oxide Nanofluids: Particle Size Dependence and Effect of Laser Irradiation. *ASME J. Heat Transfer* **2007,** 129, 298-307.
169. Mintsa, H. A.; Roy, G.; Nguyen, C. T.; Doucet, D., New temperature dependent thermal conductivity data for water-based nanofluids. *Int. J. Therm. Sci.* **2009,** 48, 363-371.
170. Beck, M. P.; Yuan, Y.; Warrier, P.; Teja, A. S., The thermal conductivity of alumina nanofluids in water, ethylene glycol, and ethylene glycol + water mixtures. *J. Nanopart. Res.* **2010,** 12, 1469–1477.
171. Beck, M. P.; Yuan, Y.; Warrier, P.; Teja, A. S., The thermal conductivity of aqueous nanofluids containing ceria nanoparticles. *J. Appl. Phys.* **2010,** 107, 066101.
172. Chopkar, M.; Kumar, S.; Bhandari, D. R.; Das, P. K.; Mannaa, I., Development and characterization of Al_2Cu and Ag_2Al nanoparticle dispersed water and ethylene glycol based nanofluid. *Mater. Sci. Eng. B* **2007,** 139, 141-148.

173. He, Y.; Jin, Y.; Chen, H.; Ding, Y.; Cang, D.; Lu, H., Heat transfer and flow behaviour of aqueous suspensions of TiO2 nanoparticles (nanofluids) flowing upward through a vertical pipe. *Int. J. Heat Mass Transfer* **2007,** 50, 2272-2281.
174. Beck, M. P.; Yuan, Y.; Warrier, P.; Teja, A. S., The effect of particle size on the thermal conductivity of alumina nanofluids *J. Nanopart. Res.* **2008,** 11, 1129-1136.
175. Patel, H. E.; Sundararajan, T.; Das, S. K., An experimental investigation into the thermal conductivity enhancement in oxide and metallic nanofluids. *J. Nanopart. Res.* **2010,** 12, 1015–1031.
176. Teng, T. P.; Hung, Y. H.; Teng, T. C.; Moa, H. E.; Hsu, H. G., The effect of alumina/water nanofluid particle size on thermal conductivity. *App. Therm. Eng.* **2010,** 30, 2213-2218.
177. Timofeeva, E. V.; Smith, D. S.; Yu, W.; France, D. M.; Singh, D.; Routbort, J. L., Particle size and interfacial effects on thermo-physical and heat transfer characteristics of water-based α-SiC
nanofluids. *Nanotechnology* **2010,** 21 215703.
178. Shima, P. D.; Philip, J., Tuning of Thermal Conductivity and Rheology of Nanofluids Using an External Stimulus. *J. Phys. Chem. C* **2011,** 115, 20097-20104.
179. Sun, C.; Bai, B.; Lu, W.-Q.; Liu, J., Shear-rate dependent effective thermal conductivity of H2O+SiO2 nanofluids. *Phys. Fluids* **2013,** 25, 052002.
180. Xia, G.; Jiang, H.; Ran Liu, Y. Z., Effects of surfactant on the stability and thermal conductivity of Al_2O_3/de-ionized water nanofluids. *Int. J. Therm. Sci.* **2014,** 84, 118-124.
181. Lee, J.-H.; Lee, S.-H.; Jang, S. P., Do temperature and nanoparticle size affect the thermal conductivity of alumina nanofluids? *App. Phys. Lett.* **2014,** 104, 161908.
182. Shalkevich, N.; Escher, W.; Burgi, T.; Michel, B.; Ahmed, L. S.; Poulikakos, D., On the Thermal Conductivity of Gold Nanoparticle Colloids. *Langmuir* **2010,** 26, 663–670.
183. Xie, H.; Wang, J.; Xi, T.; Liu, Y., Thermal conductivity of suspensions containing nanosized SiC particles. *Int J Thermophys.* **2002,** 23, (2), 571-580.
184. Lee, K. J.; Yoon, S. H.; Jang, y., Carbon Nanofibers: A Novel Nanofiller for Nanofluid Applications. *Small* **2007,** 3, 1209-1213.
185. Timofeeva, E. V.; Routbort, J. L.; Singh, D., Particle shape effects on thermophysical properties of alumina nanofluids. *J. Appl. Phys.* **2009,** 106, 014304.
186. Jiang, W.; Ding, G.; Peng, H., Measurement and model on thermal conductivities of carbon nanotube nanorefrigerants. *Int. J. Therm. Sci.* **2009,** 48, 1108-1115.
187. Farbod, M.; asl, R. K.; abadi, A. R. N., Morphology dependence of thermal and rheological properties of oil-based nanofluids of CuO nanostructures. *Colloids Surf. A: Physicochem. Eng. Aspects* **2015,** 474 71-75.
188. Li, Q.; Xuan, Y.; Wang, J., Experimental investigations on transport properties of magnetic fluids. *Exp. Therm Fluid Sci.* **2005,** 30, 109-116.
189. Wensel, J.; Wright, B.; Thomas, D.; Douglas, W.; Mannhalter, B.; Cross, W.; Hong, H.; Kellar, J.; Smith, P.; Roy, W., Enhanced thermal conductivity by aggregation in heat transfer nanofluids containing metal oxide nanoparticles and carbon nanotubes. *Appl. Phys. Lett.* **2008,** 92, 023110
190. Xuan, Y.; Huang, Y.; Li, Q., Experimental investigation on thermal conductivity and specific heat capacity of magnetic microencapsulated phase change material suspension. *Chem. Phys. Lett.* **2009,** 479, 264-269.

191. Hong, H.; Wright, B.; Wensel, J.; Jin, S.; Ye, X. R.; Roy, W., Enhanced thermal conductivity by the magnetic field in heat transfer nanofluids containing carbon nanotube. *Synth. Met.* **2007,** 157, 437.

192. Yu, Q.; Kim, Y. J.; Ma, H., Nanofluids with plasma treated diamond nanoparticles. *Appl. Phys. Lett.* **2008,** 92, 103111.

193. Nasiri, A.; Niasar, M. S.; Rashidi, A.; Amrollahi, A.; Khodafarin, R., Effect of dispersion method on thermal conductivity and stability of nanofluid. *Exp. Therm. Fluid Sci.* **2011,** 35, 717-723.

194. Yu, W.; Xie, H.; Chen, L.; Li, Y., Investigation of thermal conductivity and viscosity of ethylene glycol based ZnO nanofluid. *Thermochim. Acta* **2009,** 491, 92-96.

195. Li, D.; Zhao, W.; Liu, Z.; Zhu, B., Experimental investigation of heat transfer enhancement of the heat pipe using CuO-water nanofluid. *Adv. Mater. Res.* **2011,** 160-162, 507-512.

196. Horton, M.; Hong, H.; Li, C.; Shi, B.; Peterson, G. P.; Jin, S., Magnetic alignment of Ni-coated single wall carbon nanotubes in heat transfer nanofluids. *J. Appl. Phys.* **2010,** 107, 104320

197. Shima, P. D.; Philip, J.; Raj, B., Magnetically controllable nanofluid with tunable thermal conductivity and viscosity. *Appl. Phys. Lett.* **2009,** 95, 133112.

198. Gowda, R.; Sun, H.; Wang, P.; Charmchi, M.; Gao, F.; Gu, Z.; Budhlall, B., Effects of Particle Surface Charge, Species, Concentration, and DispersionMethod on the Thermal Conductivity of Nanofluids. *Adv. Mech. Eng.* **2010,** 2010, 1-10.

199. Shima, P. D.; Philip, J., Role of Thermal Conductivity of Dispersed Nanoparticles on Heat Transfer Properties of Nanofluid. *Ind. Eng. Chem. Res.* **2014,** 53, 980−988.

200. Li, C. H.; Peterson, G. P., Experimental investigation of temperature and volume fraction variations on the effective thermal conductivity of nanoparticle suspensions (nanofluids). *J. Appl. Phys.* **2006,** 99, 084314.

201. Chopkar, M.; Sudarshan, S.; Das, P. K.; Manna, I., Effect of Particle Size on Thermal Conductivity of Nanofluid. *Mettal. Mater Trans. A* **2008,** 39, 1535-1542.

202. Sinha, K.; Kavlicoglu, B.; Liu, Y.; Gordaninejad, F.; Graeve, O. A., A comparative study of thermal behavior of iron and copper nanofluids. *J. Appl. Phys.* **2009,** 106, 064307.

203. Wang, X. J.; Zhu, D. S.; yang, S., Investigation of pH and SDBS on enhancement of thermal conductivity in nanofluids. *Chem. Phys. Lett.* **2009,** 470, 107-111.

204. Zhu, D.; Li, X.; Wang, N.; Wang, X.; Gao, J.; Li, H., Dispersion behavior and thermal conductivity characteristics of Al_2O_3–H_2O nanofluids. *Curr. Appl. Phys.* **2009,** 9, 131-139.

205. Angayarkanni, S. A.; Philip, J., Role of adsorbing moieties on thermal conductivity and associated properties of nanofluids. *J. Phys. Chem. C* **2013,** 117 9009-9019.

206. Das, S. K.; Putra, N.; Roetzel, W., Pool boiling characteristics of nanofluids. *Int. J. Heat Mass Transfer* **2003,** 46, 851-862.

207. Shima, P. D.; Philip, J.; Raj, B., Synthesis of aqueous and nonaqueous iron oxide nanofluids and study of temperature dependence on thermal conductivity and viscosity. *J. Phys. Chem. C* **2010,** 114 (44), 18825-18833.

208. Gao, J. W.; Zheng, R. T.; Ohtani, H.; Zhu, D. S.; Chen, G., Experimental Investigation of Heat Conduction Mechanisms in Nanofluids.Clue on Clustering. *Nano Lett.* **2009,** 9, 4128-4132.

209. Duangthongsuk, W.; Wongwises, S., Measurement of Temperature-Dependent Thermal Conductivity and Viscosity of TiO_2-Water Nanofluids. *Exp. Therm. Fluid Sci.* **2009,** 33, 706-714.

210. Zeng, Y.-X.; Zhong, X.-W.; Liu, Z.-Q.; Chen, S.; Li, N., Preparation and Enhancement of Thermal Conductivity of Heat Transfer Oil-Based MoS2 Nanofluids. *J Nanomater.* **2013,** 2013, 1-6.

211. Ghozatloo, A.; Rashidi, A. M.; Shariaty-Niasar, M., Effects of surface modification on the dispersion and thermal conductivity of CNT/water nanofluids. *Int. Commn. Heat Mass Transfer* **2014,** 54, 1-7.

212. Wamkam, C. T.; Opoku, M. K.; Hong, H.; Smith, P., Effects of pH on heat transfer nanofluids containing ZrO_2 and TiO_2 nanoparticles *J. Appl. Phys.* **2011,** 109, 024305.

213. Li, X. F.; Zhu, D. S.; Wang, X. J.; Wang, N.; Gao, J. W.; H.Li, Thermal conductivity enhancement dependent pH and chemical surfactant for Cu-H2O nanofluids. *Thermochim. Acta* **2008,** 469, 98-103.

214. Meibodi, M. E.; Sefti, M. V.; Rashidi, A. M.; Amrollahi, A.; Tabasi, M.; Kalal, H. S., The role of different parameters on the stability and thermal conductivity of carbon nanotube/water nanofluids. *Int. Commu. Heat Mass Transfer* **2010,** 37, 319-323.

215. Amrollahi, A.; Hamidi, A. A.; Rashidi, A. M., The effects of temperature, volume fraction and vibration time on the thermo-physical properties of a carbon nanotube suspension (carbon nanofluid). *Nanotechnology* **2008,** 19 315701.

216. Garg, P.; Alvarado, J. L.; Marsh, C.; Carlson, T. A.; Kessler, D. A.; Annamalai, K., An experimental study on the effect of ultrasonication on viscosity and heat transfer performance of multi-wall carbon nanotube-based aqueous nanofluids. *Int. J. Heat Mass Transfer* **2009,** 52, 5090–5101.

217. Xie, H.; Wang, J.; Xi, T.; Liu, Y.; Ai, F.; Wu, Q., Thermal conductivity enhancement of suspensions containing nanosized alumina particles. *J. Appl. Phys.* **2002,** 91, 4568-4570.

218. Higano, M.; Miyagawa, A.; Saigou, K.; Masuda, H.; Miyashita, H., Measuring the specific heat capacity of magnetic fluids using a differential scanning calorimeter. *Int. J. Thermophys.* **1999,** 20, (1).

219. Yang, Y.; Zhang, Z. G.; Grulke, E. A.; Anderson, W. B.; Wu, G., Heat transfer properties of nanoparticle-in-fluid dispersions (nanofluids) in laminar flow. *Int. J. Heat Mass Transfer* **2005,** 48, 1107.

220. Zhou, S. Q.; Ni, R., Measurement of the specific heat capacity of water-based Al_2O_3 nanofluid. *Appl. Phys. Lett.* **2008,** 92, 093123

221. Zhou, L.-P.; Bu-XuanWang; Peng, X.-F.; Du, X.-Z.; Yang, Y.-P., On the specific heat capacity of CuO nanofluid. *Advances in Mechanical Engineering* **2010,** 2010, (172085), 1-4.

222. Namburu, P. K.; Kulkarni, D. P.; Dandekar, A.; Das, D. K., Experimental investigation of viscosity and specific heat of silicon dioxide nanofluids. *Micro & Nano Letters* **2007,** 2, (3), 67–71.

223. Wang, B.-X.; Zhou, L.-P.; Peng, X.-F., Surface and size effects on the specific heat capacity of nanoparticles. *Int. J. Thermophys.* **2006,** 27(1), 139-151.

224. Shin, D.; Banerjee, D., Specific heat of nanofluids synthesized by dispersing alumina nanoparticles in alkali salt eutectic. *Int. J Heat Mass Transfer* **2014,** 74, 210-214.

225. Ho, M. X.; Pan, C., Optimal concentration of alumina nanoparticles in molten Hitec salt to maximize its specific heat capacity. *Int. J Heat Mass Transfer* **2014,** 70, 174-184.
226. Nelson, I. C.; Banerjee, D., Flow Loop Experiments Using Polyalphaolefin Nanofluids. *J. Thermophys. Heat Transfer* **2009,** 23, (4), 752-761.
227. Shin, D.; Banerjee, D., Enhanced Specific Heat Capacity of Nanomaterials Synthesized by Dispersing Silica Nanoparticles in Eutectic Mixtures. *J. Heat Transfer* **2013,** 135, 032801.
228. Vajjha, R. S.; Das, D. K., Specific heat measurement of three nanofluids and development of new correlations. *J Heat Transfer* **2009,** 131, 071601.
229. Xiong, S.; Qi, W.; Cheng, Y.; Huang, B.; Wang, M.; Li, a. Y., Universal relation for size dependent thermodynamic properties of metallic nanoparticles. *Phys. Chem. Chem. Phys.* **2011,** 13, 10652-10660.
230. Novotny, V.; Meincke, P. P. M.; Watson, J. H. P., Effect of Size and Surface on the Specific Heat of Small Lead Particles. *Phys. Rev. Lett.* **1972,** 28, (14), 901-903.
231. Sarı, A.; Karaipekli, A., Thermal conductivity and latent heat thermal energy storage characteristics of paraffin/expanded graphite composite as phase change material. *Appl. Therm. Eng.* **2007,** 27, 1271-1277.
232. Kuznik, F.; David, D.; Johannes, K.; Roux, J.-J., A review on phase change materials integrated in building walls. *Renew. Sust. Energ. Rev.* **2011,** 15, 379-391.
233. Shatikian, V.; Ziskind, G.; Letan, R., Numerical investigation of a PCM-based heat sink with internal fins: Constant heat flux. *Int. J. Heat Mass Transfer* **2008,** 51, 1488-1493.
234. Karaipekli, A.; Sarı, A., Capric–myristic acid/vermiculite composite as form-stable phase change material for thermal energy storage. *Solar Energy* **2009,** 83, 323-332.
235. Aia, D.; Sua, L.; Gaob, Z.; Denga, C.; Dai, X., Study of ZrO_2 nanopowders based stearic acid phase change materials. *Particuology* **2010,** 8, 394-397.
236. Sun, P. C.; Wu, Y. L.; Gao, J. W.; Cheng, G. A.; Chen, G.; Zheng, R. T., Room Temperature Electrical and Thermal Switching CNT/ Hexadecane Composites. *Adv. Mater.* **2013,** 25, 4938-4943.
237. Zheng, R.; Gao, J.; Wang, J.; Chen, G., Reversible Temperature Regulation of Electrical and Thermal Conductivity using Liquid–Solid Phase Transitions. *Nat. Commun.* **2011,** 2, (2889), 1-6.
238. Harish, S.; Ishikawa, K.; Chiashi, S.; Shiomi, J.; Maruyama, S., Anomalous Thermal Conduction Characteristics of Phase Change Composites with Single-Walled Carbon Nanotube Inclusions. *J. Phys. Chem. C* **2013,** 117, 15409-15413.
239. Sutherland, R.; Davis, R.; Seyer, W., Heat Transfer Effects - Molecular Orientation of Octadecane. *Ind. Eng. Chem.* **1959,** 51, (4), 585-588.
240. Powell, R. W.; Challoner, A. R.; Seyer, W. F., Correspondence. Measurement of Thermal Conductivity of n-Octadecane. *Ind. Eng. Chem.* **1961,** 53, (7), 581-582.
241. Lyeo, H.-K.; Cahill, D. G.; Lee, B.-S.; Abelson, J. R.; Kwon, M.-H.; Kim, K.-B.; Bishop, S. G.; Cheong, a. B.-k., Thermal conductivity of phase-change material $Ge_2Sb_2Te_5$. *Appl. Phys. Lett.* **2006,** 89, 151904.
242. Babaei, H.; Keblinski, P.; Khodadadi, J. M., Thermal conductivity enhancement of paraffins by increasing the alignment of molecules through adding CNT/graphene. *Int. J. Heat Mass Transfer* **2013,** 58, 209-216.

243. Schiffres, S.; Harish, S.; Maruyama, S.; Shiomi, J.; Malen, J. A., Tunable Electrical and Thermal transport in Ice-Templated Multilayer Graphene nanocomposites through freezing rate control. *ACS Nano* **2013,** 7, (12), 11183-11189.

244. Lee, D., Thermophysical Properties of Interfacial Layer in Nanofluids. *Langmuir* **2007,** 23, 6011-6018.

245. Chen, G., Thermal conductivity and ballistic-phonon transport in the cross-plane direction of superlattices. *Phys. Rev. B* **1998,** 57, (23), 14958-14973.

246. Eapen, J.; Li, J.; Yip, S., Beyond the Maxwell limit: Thermal conduction in nanofluids with percolating fluid structures. *Phys. Rev. E.* **2007,** 76, 062501.

247. Williams, W.; Buongiorno, J.; Hu, L. W., Experimental Investigation of Turbulent Convective Heat Transfer and Pressure Loss of Alumina/Water and Zirconia/Water Nanoparticle Colloids (Nanofluids) in Horizontal Tubes. *ASME J. Heat Transfer* **2008,** 130, 042412.

248. Buongiorno, J.; Hu, L. W.; Apostolakis, G.; Hannink, R.; Lucas, T.; Chupin, A., A feasibility assessment of the use of nanofluids to enhance the in-vessel retention capability in light-water reactors. *Nucl. Eng. Des.* **2009,** 239, 941-948.

249. Huxtable, S. T.; Cahill, D. G.; Shenogin, S.; Xue, L.; Ozisik, R.; Barone, P.; Usrey, M.; Strano, M. S.; Siddons, G.; Shim, M.; Keblinski, P., Interfacial heat flow in carbon nanotube suspensions. *Nat. Mater.* **2003,** 2, 731-734.

250. Yang, H. S.; Bai, G. R.; Thompson, L. J.; Eastman, J. A., Interfacial thermal resistance in nanocrystalline yttria stabilized zirconia. *Acta Mater.* **2002,** 50, 2309.

251. Nan, C. W.; Birringer, R.; Clarke, D. R.; Gleiter, H., Effective thermal conductivity of particulate composites with interfacial thermal resistance. *J. Appl. Phys.* **1997,** 81, 6692-6699.

252. Gnanaprakash, G.; Philip, J.; Jayakumar, T.; Raj, B., Effect of digestion time and alkali addition rate on physical properties of magnetite nanoparticles. *J. Phys. Chem. B* **2007,** 111, (28), 7978-7986.

253. Elmore, W. C., The magnetization of ferromagnetic colloids. *Phys. Rev.* **1938,** 54, 1092-1095.

254. Zhang, S.; Wu, J.-Y.; Tse, C.-T.; Niu, J., Effective dispersion of multi-wall carbon nano-tubes in hexadecane through physiochemical modification and decrease of supercooling. *Sol. Energ. Mat. Sol. Cells* **2012,** 96 124-130.

255. Horrocks, J. K.; McLaughlin, E., Non-steady state measurements of thermal conductivities of liquids polyphenyls. *Proc. R. Soc. Lond.* **1963,** 273, (1353), 259-274.

256. Zhu, D.; Li, X.; Wang, N.; Wang, X.; Gao, J.; Li, H., Dispersion behavior and thermal conductivity characteristics of Al2O3–H2O nanofluids. *Curr. Appl Phys.* **2009,** 9, (1), 131-139.

257. Hu, P.; Shan, W.-L.; Yu, F.; Chen, Z.-S., Thermal Conductivity of AlN–Ethanol Nanofluids. *Int. J. Thermophys.* **2008,** 29, 1968-1973.

258. Wang, F.; Han, L.; Zhang, Z.; Fang, X.; Shi, J.; Ma, W., Surfactant-free ionic liquid-based nanofluids with remarkable thermal conductivity enhancement at very low loading of graphene. *Nanoscale Res. Lett.* **2012,** 7, (314), 1-7.

259. AR, C.; RW, P., Thermal conductivity of liquids: new determinations for seven liquids and appraisal of existing values. . *Proc. R Soc. Lond. Ser. A* **1956,** 238, 90-106.

260. Cahill, D., Thermal conductivity measurement from 30 to 700 K: the 3v method. *Rev. Sci. Instrum.* **1990,** 61, 802-808.

261. Deshpande, A. P.; Krishnan, M. J.; Kumar, S., *Rheology of complex fluids*. Springer: 2010.

262. McHugh, J.; Fideu, P.; Herrmann, A.; Stark, W., Determination and review of specific heat capacity measurements during isothermal cure of an epoxy using TM-DSC and standard DSC techniques. *Polym. Test.* **2010,** 29 759–765.

263. ASTM *Standard test method for determining specific heat capacity by differential scanning calorimetry*; 2005.

264. Gilmour, I. W.; Hay, J. N., Determination of specific heat capacity of polystyrene by dsc. *Polymer* **1977,** 18, 281-285.

265. Ward, C. A.; Neumann, A. W., On the surface thermodynamics of a two-component liquid-vapor-ideal solid system. *J Colloid Interf Sci.* **1974,** 49, (2), 286-290.

266. Fang, J.; Kang, C. B.; Huang, Y.; Tolbert, S. H.; Pilon, L., Thermal conductivity of ordered mesoporous nanocrystalline silicon thin films made from magnesium reduction of polymer- templated silica. *J. Phys. Chem. C* **2012,** 116, (23), 12926−12933.

267. Alaghemandi, M.; Gharib-Zahedi, M. R.; Spohr, E.; Boohm, M. C., Thermal Conductivity of Polyamide-6,6 in the Vicinity of Charged and Uncharged Graphene Layers: A Molecular Dynamics Analysis. *J. Phys. Chem. C.* **2012,** 116, 14115−14122.

268. Gao, T.; Jelle, B. P., Thermal Conductivity of TiO_2 Nanotubes. *J. Phys. Chem. C* **2013,** 117, 1401−1408.

269. Huang, X.; Zhi, C.; Jiang, P., Toward Effective Synergetic Effects from Graphene Nanoplatelets and Carbon Nanotubes on Thermal Conductivity of Ultrahigh Volume Fraction Nanocarbon Epoxy Composites. *J. Phys. Chem. C* **2012,** 116, 23812−23820.

270. Nanda, J.; Maranville, C.; Bollin, S. C.; Sawall, D.; Ohtani, H.; Remillard, J. T.; Ginder, J. M., Thermal Conductivity of Single-Wall Carbon Nanotube Dispersions: Role of Interfacial Effects. *J. Phys. Chem. C* **2008,** 112, 654-658.

271. Zhu, H. T.; Zhang, C. Y.; Tang, Y. M.; Wang, J. X., Novel Synthesis and Thermal Conductivity of CuO Nanofluid. *J. Phys. Chem. C* **2007,** 111, 1646-1650.

272. Aravind, S. S. J.; Baskar, P.; Baby, T. T.; Sabareesh, R. K.; Das, S.; Ramaprabhu, S., Investigation of Structural Stability, Dispersion, Viscosity, and Conductive Heat Transfer Properties of Functionalized Carbon Nanotube Based Nanofluids. *J. Phys. Chem. C.* **2011,** 115, 16737-16744.

273. Murshed, S. M. S.; Castro, C. A. N. d.; Lourenco, M. J. V., Effect of Surfactant and Nanoparticle Clustering on Thermal Conductivity of Aqueous Nanofluids. *J. Nanofluids* **2012,** 1, (2), 175-179.

274. Hong, H.; Wensel, J.; Smith, P., Evidences of Aggregation Between Metal Oxide Nanoparticles and Carbon Nanotubes in Heat Transfer Nanofluids *J. Nanofluids* **2013,** 2, (1), 38-44.

275. Shalkevich, N.; Shalkevich, A.; Burgi, T., Thermal Conductivity of Concentrated Colloids in Different States. *J. Phys. Chem. C* **2010,** 114, 9568–9572.

276. Komati, S.; Suresh, A. K., Anomalous enhancement of interphase transport rates by nanoparticles: effect of magnetic iron oxide on gas-liquid mass transfer. *Ind. Eng. Chem. Res.* **2010,** 49, 390-405.

277. Prasher, R.; Evans, W.; Meakin, P.; Fish, J.; Phelan, P.; Keblinski, P., Effect of aggregation on thermal conduction in colloidal nanofluids. *Appl. Phys. Lett.* **2006,** 89, 143119

278. Murshed, S. M. S.; Castro, C. A. N. d., Predicting the Thermal Conductivity of Nanofluids-Effect of Brownian Motion of Nanoparticles. *J. Nanofluids* **2012,** 1, (2), 180-185.

279. Gorla, R. S. R.; Kumari, M., Mixed Convection Flow of a Non-Newtonian Nanofluid Over a Non-Linearly Stretching Sheet. *J. Nanofluids* **2012,** 1, (2), 186-195.

280. Huang, X.; Iizuka, T.; Jiang, P.; Ohki, Y.; Tanaka, T., Role of Interface on the Thermal Conductivity of Highly Filled Dielectric Epoxy/AlN Composites. *J. Phys. Chem. C* **2012,** 116, 13629-13639.

281. Wei, Z.; Ni, Z.; Bi, K.; Chen, M.; Chen, Y., Interfacial thermal resistance in multilayer graphene structures. *Phys. Lett. A* **2011,** 375, 1195-1199.

282. Sato, K.; Fujimoto, K.; Kawamura, K.; Dai, W.; Hunger, M., Rheological Mechanism of Long-Term Self-Assembly in Saponite Nanoparticles. *J. Phys. Chem. C* **2012**.

283. Duplatre, G.; Marques, M. F. F.; Miguel, M. d. G., Size of sodium dodecyl dulfate micelles in aqueous solutions as studied by positron annihilation lifetime spectroscopy. *J. Phys. Chem.* **1996,** 100, 16608-16612.

284. Wu, C.; Ma, R.; Zhou, B.; Shen, J.; Chan, K. K.; Woo, K. F., Laser light-scattering study of the dendritic-like polyelectrolytes and CTAB complex formation. *Macromolecules* **1996,** 29, 228-232.

285. Mata, J. P.; Aswal, V. K.; Hassan, P. A.; Bahadur, P., A phenol-induced structural transition in aqueous cetyltrimethylammonium bromide solution. *J. Colloid Interface Sci.* **2006,** 299, 910-915.

286. Bagwe, R. P.; Mishra, B. K.; Khilar, K. C., Effect of chain length of oxythylene group on particle size and absorption spectra of silver nanoparticles prepared in non-ionic water-in-oil micro emulsion. *J. Dispersion Sci. Technol.* **2012,** 20, (6), 1569-1579.

287. Bibette, J.; Calderon, F. L.; Poulin, P., Emulsions: Basic principles. *Rep. Prog. Phys.* **1999,** 62, 969-1033.

288. Os; N.M.Van; Haak.J.R; Rupert; L.A.M, *Physico-chemical properties of selected anionic, cationic and nonionic surfactants*. Elsevier Science Pub Co: 1993; p 608.

289. Ekwall, P.; Mandell, L.; Solyom, P., The aqueous cetyl trimethylammonium bromide solutions. *J. Colloid Interface Sci.* **1971,** 35, (4), 519-528.

290. Lindmann, B.; Olofsson, G.; Stenius, P., *Surfactants, adsorption, surface spectroscopy and disperse systems*. Springer: 1985.

291. Costa, T. M. H.; Gallas, M. R.; Benvenutti, E. V.; Jornada, J. A. H. d., Study of nanocrystalline g - Al_2O_3 produced by high-pressure compaction. *J. Phys. Chem.* **1999,** 103, 4278-4284.

292. Parida, K. M.; Pradhan, A. C.; Das, J.; Sahu, N., Synthesis and characterization of nano-sized porous gamma-alumina by control precipitation method. *Mater. Chem. Phys.* **2009,** 113, 244-248.

293. Tan, B. H.; Xue, J. M.; Shuter, B.; Li, X.; Wang, J., Synthesis of PEOlated Fe_3O_4@SiO_2 nanoparticles via bioinspired silification for magnetic resonance imaging. *Adv. Funct. Mater.* **2010,** 20, 722-731.

294. Anderson, D. R., Thermal conductivity of polymer. *Chem. Rev.* **1966,** 66, (6), 677-690.

295. F.H.Mueller; Houwink, R., *Chemie und technologie der kunststoffe*. Leipzig: 1942.

296. Vladkov, M.; Barrat, J. L., Modeling transient absorption and thermal conductivity in a simple nanofluid. *Nano Lett.* **2006,** 6, 1224-1228.

297. Zhao, H.; Freund, J. B., Phonon scattering at a rough interface between two fcc lattices. *J. Appl. Phys.* **2009,** 105, 013515.

298. Aubry, S.; Kimmer, C. J.; Skye, A.; Schelling, P. K., Comparison of theoretical and simulation-based predictions of grain-boundary Kapitza conductance in silicon. *Phys. Rev. B.* **2008,** 78, 064112.

299. Kimmer, C.; Aubry, S.; Skye, A.; Schelling, P. K., Scattering of phonons from a high-energy grain boundary in silicon: Dependence on angle of incidence. *Phys. Rev. B* **2007,** 75, 144105.

300. Schellinga, P. K.; Phillpot, S. R.; Keblinski, P., Kapitza conductance and phonon scattering at grain boundaries by simulation. *J. Appl. Phys.* **2004,** 95, (11), 6082-6091.

301. Zhao, H.; Pokharel, M.; Zhu, G.; Chen, S.; Lukas, K.; Jie, Q., Dramatic thermal conductivity reduction by nanostructures for large increase in thermoelectric figure-of-merit of FeSb2. *Appl. Phys. Lett.* **2011,** 99, 163101.

302. Wang, Z.; Alaniz, J. E.; Jang, W.; Garay, J. E.; Dames, C., Thermal conductivity of nanocrystalline silicon: importance of grain size and frequency-dependent mean free paths. *Nano Lett.* **2011,** 11, 2206-2213.

303. Yang, N.; Zhang, G.; Li, B., Ultralow thermal conductivity of isotope-doped silicon nanowires. *Nano Lett* **2007,** 8, (1), 276-280.

304. Zhang, G.; Li, B., Thermal conductivity of nanotubes revisited: Effects of chirality, isotope impurity, tube length, and temperature. *J. Chem. Phys.* **2005,** 123, 114714.

305. Chang, C. W.; Fennimore, A. M.; Afanasiev, A.; Okawa, D.; Ikuno, T.; Garcia, H.; Li, D.; Majumdar, A.; Zettl, A., Isotope effect on the thermal conductivity of boron nitride nanotubes. *Phys Rev lett.* **2006,** 97, 085901.

306. Tamura, S.-i.; Tanaka, Y.; Maris, H. J., Phonon group velocity and thermal conduction in superlattices. *Phys. Rev. B* **1999,** 60, (4), 2627-2630.

307. Berber, S.; Kwon, Y.-K.; Tománek, D., Unusually high thermal conductivity of carbon nanotubes. *Phys. Rev. Lett.* **2000,** 84, 4613-4616.

308. Rosen, M. J., *Surfactants and interfacial phenomenon*. 2nd ed.; Wiley: 1989.

309. Li, D.; W., N. A., A reformulation of the equation of state for interfacial tensions. *J Colloid Interf Sci.* **1990,** 137, (1), 304-307.

310. Li, D.; Neumann, A. W., Contact angles on hydrophobic solid surfaces and their Interpretation. *J. Colloid Interface Sci.* **1992,** 148, 190-200.

311. Spirk, S.; Ehmann, H. M.; Kargl, R.; Hurkes, N.; Reischl, M.; Novak, J.; Resel, R.; Wu, M.; Pietschnig, R.; Ribitsch, V., Surface Modifications Using a Water-Stable Silanetriol in Neutral Aqueous Media. *ACS Appl. Mater. Interfaces.* **2010,** 2, (10), 2956-2962.

312. Pashley, R. M.; Israelachvili, J. N., A comparison of surface forces and interfacial properties of Mica in purified surfactant solutions. *Colloids Surf.* **1981,** 2, 169-187.

313. Barrat, J.-L.; Chiaruttini, F., Kapitza resistance at the liquid solid interface. *Mol.Phys* **2003,** 101, (11), 1605-1610.

314. Musselman, S. W.; Chander, S., Wetting and adsorption of acetylenic diol based nonionic surfactants on heterogeneous surfaces. *Colloids and Surfaces A: Physicochem. Eng. Aspects* **2002,** 206 497-513.

315. Every, A. G.; Tzou, Y.; Hasselman, D. P. H.; Raj, R., The Effect of particle size on the Thermal Conductivity of ZnS/Diamond composites. *Acta metall.mater* **1992,** 40, 123-129.

316. Reiss-Husson, F.; Luzzati, V., The structure of the micellar solutions of some amphiphilic compounds in pure water as determined by absolute small-angle x-ray scattering techniques. *J. Phys. Chem.* **1964,** 68, (12), 3504-3511.

317. Aswal, V. K.; Goyal, P. S., Counterions in the growth of ionic micelles in aqueous electrolyte solutions: A small-angle neutron scattering study. *Phys. Rev. E* **2000,** 61, 2947-2953.

318. Hassan, P. A.; Yakhmi, J. V., Growth of Cationic Micelles in the Presence of Organic Additives. *Langmuir* **2000,** 16, (7187-7191), 7187.

319. Aswal, V. K.; Goyal, P. S.; Menon, S. V. G.; Dasannacharya, B. A., Role of inter-micellar interaction on micellar growth. *Physica B* **1995,** 213-214, 607-609.

320. Desai, A.; Varade, D.; Mataa, J.; Aswal, V.; Bahadur, P., Structural transitions of cetyltrimethylammonium bromide micelles in aqueous media: Effect of additives. *Colloids Surf., A* **2005,** 259, 111-115.

321. Einstein.A, *Investication on the theory of the Brownian motion*. Dover: New York, 1956.

322. Batchelor, G. K., The effect of brownian motion on the bulk stress in a suspension of spherical particles. *J.Flulid Mech.* **1977,** 83, 97-117.

323. Krieger, I. M.; Dougherty, T. J., A mechanism for non-newtonian flow in suspensions of rigid spheres. *Trans.Soc.Rheol.* **1959,** III, 137-152.

324. Shima, P. D.; Philip, J.; Raj, B., Role of microconvection induced by Brownian motion of nanoparticles in the enhanced thermal conductivity of stable nanofluids. *Appl. Phys. Lett.* **2009,** 94, (22), 223101-223101-3.

325. P.Keblinski; Phillpot, S. R.; Choi, S. U. S.; Eastman, J. A., Mechanism of heat flow in suspensions of nano-sized particles (nanofluids). *Int. J. Heat Mass Transfer* **2002,** 45, 855-863.

326. Angayarkanni, S. A.; Philip, J., Role of surface charge, morphology, and adsorbed moieties on thermal conductivity enhancement of nanofluids. *Appl. Phys. Lett.* **2012,** 101, 173113.

327. Arruebo, M.; Fernández-Pacheco, R.; Ibarra, M. R.; Santamaría, J., Magnetic nanoparticles for drug delivery. *Nano Today* **2007,** 2, 22.

328. Philip, J.; Rao, C. B.; Jayakumar, T.; Raj, B., A new optical technique for detection of defects in ferromagnetic materials and components. *NDT & E Int.* **2000,** 33, 289-295.

329. Mahendran, V.; Philip, J., Nanofluid based optical sensor for rapid visual inspection of defects in ferromagnetic materials. *Appl. Phys. Lett.* **2012,** 100 073104.

330. Mahendran, V.; Philip, J., Spectral response of magnetic nanofluid to toxic cations. *Appl. Phys. Lett.* **2013,** 102, 163109.

331. Philip, J.; Shima, P. D., Thermal properties of nanofluids. *Adv. Colloid Interface Sci.* **2012,** 183-184, 30-45.

332. S.Melle; Rubio, M. A.; Fuller, G. G., Time Scaling Regimes in Aggregation of Magnetic Dipolar Particles: Scattering Dichroism Results. *Phys. Rev. Lett.* **2001,** 87, 115501.

333. Minea, A. A.; Luciu, R. S., Investigations on electrical conductivity of stabilized water based Al2O3 nanofluids. *Microfluid Nanofluid* **2012,** 13, 977-985.

334. Sarojini, K. G. K.; Manoj, S. V.; Singh, P. K.; Pradeep, T.; Das, S. K., Electrical conductivity of ceramic and metallic nanofluids. *Colloids and Surfaces A: Physicochem. Eng. Aspects* **2013,** 417, 39-46.
335. Jiang, W., A general model for thermal conductivity and electric conductivity of nanofluids. *Adv. Mat. Res.* **2013,** 614-615, 529-535.
336. White, S. B.; Shih, A. J.-M.; Pipe, K. P., Investigation of the electrical conductivity of propylene glycol-based ZnO nanofluids. *Nanoscale Res. Lett.* **2011,** 6, (346), 1-5.
337. Baby, T. T.; Ramaprabhu, S., Investigation of thermal and electrical conductivity of graphene based nanofluids. *J. Appl. Phys.* **2010,** 108, 124308.
338. Tsenoglou, C., Scaling concepts in suspension rheology. *J. Rheol.* **1990,** 34, (1), 15-24.
339. Jones, D. A. R.; Leary, B.; Boger, D. V., The Rheology of a Concentrated Colloidal Suspension of Hard Spheres. *J. Colloid Interface Sci.* **1991,** 147, (2), 479-495.
340. Phuoc, T. X.; Massoudi, M., Experimental observations of the effects of shear rates and particle concentration on the viscosity of Fe_2O_3–deionized water nanofluids. *Int. J. Therm. Sci.* **2009,** 48, 1294–1301.
341. Veld, P. J. i. t.; Petersen, M. K.; Grest, G. S., Shear thinning of nanoparticle suspensions. *Phys. Rev. E* **2009,** 79, 021401.
342. Wilking, J. N.; Chang, C. B.; Fryd, M. M.; Porcar, L.; Mason, T. G., Shear-Induced Disruption of Dense Nanoemulsion Gels. *Langmuir* **2011,** 27, 5204-5210.
343. JR, J. V. C., Aggregate Refractive Indices and Unit Cell Parameters of Synthetic Serpentine in the System MgO-Al2O3-SiO2-H2O. *American Mineralogist* **1975,** 60, 200-208.
344. Evdokimov, I. N.; Losev, A. P., Effects of molecular de-aggregation on refractive indices of petroleum-based fluids. *Fuel* **2007,** 86, 2439-2445.
345. Prabhat, N.; Buongiorno, J.; Hu, L.-W., Convective Heat Transfer Enhancement in Nanofluids: Real Anomaly or Analysis Artifact? *J. Nanofluids* **2012,** 1, 55-62.
346. Patel, H. E.; Anoop, K. B.; Sundararajan, T.; Das, S. K., Model for thermal conductivity of CNT-nanofluids. *Bull. Mater. Sci.* **2008,** 31, 387.
347. Wright, B.; Thomas, D.; Hong, H.; Smith, P., Time dependent thermal conductivities of nanofluids containing carbon nanotubes and metal oxides. *J. Nanofluids* **2013,** 2, (1), 45-49.
348. Angayarkanni, S. A.; Philip, J., Effect of Nanoparticles Aggregation on Thermal and Electrical Conductivities of Nanofluids. *J. Nanofluids* **2014,** 3, 17-25.
349. Angayarkanni, S. A.; Philip, J., Role of adsorbing moieties on thermal conductivity and associated properties of nanofluids. *J. Phys. Chem. C* **2013,** 117, 9009-9019.
350. Shin, D.; Banerjee, D., Enhanced specific heat of silica nanofluid. *J Heat Transfer* **2011,** 133, 024501.
351. Ding, Y.; Alias, H.; Wen, D.; Williams, R. A., Heat transfer of aqueous suspensions of carbon nanotubes (CNT nanofluids). *Int. J. Heat Mass Transfer* **2006,** 49, 240-250.
352. Wang, L.; Tan, Z.; Meng, S.; Liang, D.; Li, G., Enhancement of molar heat capacity of nanostructured Al_2O_3. *J Nanopart Res* **2001,** 3, 483-487.
353. Hellstern, E.; Fecht, H. J.; Fu, Z.; Johnson, W. L., Structural and thermodynamic properties of heavily mechanically deformed Ru and AlRu. *J. Appl. Phys.* **1989,** 65, 305-310.

354. Yang, Y.; Zhang, Z. G.; Grulke, E. A.; Anderson, W. B.; Wu, G., Heat transfer properties of nanoparticle-in-fluid dispersions (nanofluids) in laminar flow. *Int. J. Heat Mass Transfer* **2005,** 48 1107–1116.

355. Yang, W.; Sokhansanj, S.; Tang, J.; Winter, P., Determination of Thermal Conductivity, Specific Heat and Thermal Diffusivity of Borage Seeds. **2002,** 82, (2), 169-176.

356. Cullity, B. D., *Elements of X-Ray Diffraction*. 3rd ed.; Addison- wesley publishing company. Inc.: Massachusetts, 2001.

357. Gosselin, L.; Silva, A. K. d., Combined “heat transfer and power dissipation” optimization of nanofluid flows. *Appl. Phys. Lett.* **2004,** 85, (18), 4160-4162.

358. Polidori, G.; Fohanno, S.; Nguyen, C. T., A note on heat transfer modelling of Newtonian nanofluids in laminar free convection. *Int. J. Thermal Sci.* **2007,** 46, 739-744.

359. Maıga, S. E. B.; Palm, S. J.; Nguyen, C. T.; Roy, G.; Galanis, N., Heat transfer enhancement by using nanofluids in forced convection flows. *Int. J. Heat Fluid Flow* **2005,** 26, 530-546.

360. Palm, S. J.; Roy, G.; Nguyen, C. T., Heat transfer enhancement with the use of nanofluids in radial flow cooling systems considering temperature-dependent properties. *Appl. Therm. Eng.* **2006,** 26 2209-2218.

361. Haynes, W. M., *CRC Handbook of Chemistry and Physics, 94th Edition*. 94th ed.; CRC Press: Florida, 2009.

362. Sinnott, R. K., *Chemical Engineering*. Second ed.; Butterworth-Heinemann: 1996; Vol. 6.

363. Zhang, X.; Gu, H.; Fujii, M., Effective thermal conductivity and thermal diffusivity of nanofluids containing spherical and cylindrical nanoparticles. *Exp. Therm Fluid Sci.* **2007,** 31 593–599.

364. Oh, S. H.; Kauffmann, Y.; Scheu, C.; Kaplan, W. D.; Ruhle, M., Ordered liquid aluminum at the interface with sapphire. *Science* **2005,** 310, 661-663.

365. Crosthwaite, J. M.; Muldoon, M. J.; Dixon, J. K.; Anderson, J. L.; Brennecke, J. F., Phase transition and decomposition temperatures, heat capacities and viscosities of pyridinium ionic liquids. *J. Chem. Thermodynamics* **2005,** 37, 559-568.

366. Likhachev, V. N.; Astakhova, T. Y.; Vinogradov, G. A.; Alymov, M. I., Anomalous heat capacity of nanoparticles. *Russ. J. Phys. Chem. B* **2007,** 26, (1), 89-93.

367. Novotny, V.; Meincke, P. P. M.; Watson, J. H. P., Effect of Size and Surface on the Specific Heat of Small Lead Particles. *Phys. Rev. Lett.* **1972,** 28, (14), 901-903.

368. Sun, C. Q.; Wang, Y.; Tay, B. K.; S. Li , H. H.; Zhang, Y. B., Correlation between the melting point of a nanosolid and the cohesive energy of a surface atom. *J. Phys. Chem. B* **2002,** 106, (41), 10701-10705.

369. Chu, K.; Li, W. S.; Jia, C. C.; Tang, F.-l., Thermal conductivity of composites with hybrid carbon nanotubes and graphene nanoplatelets. *Appl. Phys. Lett.* **2012,** 101, 211903.

370. Ashtiani, D.; Akhavan-Behabadi, M. A.; Pakdaman, M. F., An experimental investigation on heat transfer characteristics of multi-walled CNT-heat transfer oil nanofluid flow inside flattened tubes under uniform wall temperature condition. *Int. Commu. Heat Mass Transfer* **2012,** 39, 1404-1409.

371. Lamas, B. C.; Fonseca, M. A. L.; Gonçalves, F. A. M. M.; Ferreira, A. G. M.; I.M.A.Fonseca; Kanagaraj, S.; Martins, N.; Oliveira, M. S. A., EG/CNTs Nanofluids Engineering and Thermo-Rheological Characterization. *J. Nano Res.* **2011,** 13 69-74.

372. Aravind, S. S. J.; Ramaprabhu, S., Graphene–multiwalled carbon nanotube-based nanofluids for improved heat dissipation. *RSC Adv.* **2013,** 3, 4199-4206.

373. Zhang, H.-S.; Guo, Z.-X.; Gong, X.-G.; Cao, J.-X., Thermal conductivity of sawtooth-like graphene nanoribbons: A molecular dynamics study. *J. Appl. Phys.* **2012,** 112, 123508.

374. Faugeras, C.; Faugeras, B.; Orlita, M.; Potemski, M.; Nair, R. R.; Geim, A. K., Thermal Conductivity of Graphene in Corbino Membrane Geometry. *ACS Nano* **2010,** 4, (4), 1889–1892.

375. Kim, P.; Shi, L.; Majumdar, A.; Euen, P. L. M., Thermal Transport Measurements of Individual Multiwalled Nanotubes. *Phys. Rev. Lett.* **2001,** 87, 215502.

376. Christensen, G.; Younes, H.; Hong, H.; Peterson, G. P., Alignment of Carbon Nanotubes Comprising Magnetically Sensitive Metal Oxides by Nonionic Chemical Surfactants *J. Nanofluids* **2013,** 2, (1), 25-28.

377. Nika, D. L.; Askerov, A. S.; Balandin, A. A., Anomalous size dependence of the thermal conductivity of graphene ribbons. *Nano Lett.* **2012,** 12, 3238−3244.

378. Prasher, R., Graphene Spreads the Heat. *Science* **2010,** 328 185-186.

379. Pastoriza-Gallego, M. J.; Lugo, L.; Legido, J. L.; Pineiro, M. M., Enhancement of thermal conductivity and volumetric behavior of Fe_xO_y nanofluids. *J. Appl. Phys.* **2011,** 110, 014309.

380. Taha-Tijerina, J.; Narayanan, T. N.; Gao, G.; Rohde, M.; Tsentalovich, D. A.; Pasquali, M.; Ajayan, P. M., Electrically Insulating Thermal Nano-Oils Using 2D Fillers. *ACS Nano* **2012,** 2, 1214-1220.

381. Murakami, K.; Chan, S. Y.; Routtenberg, A., Protein Kinase C Activation by cis-Fatty Acid in the Absence of Ca^{2+} and Phospholipids. *J. Biol. Chem.* **1986,** 261, (33), 15424-15429.

382. Zulauf, M.; Eicke, H.-F., Inverted Micelles and Microemulsions in the Ternary System H,O/Aerosol-OT/Isooctane as Studied by Photon Correlation Spectroscopy. *J. Phys. Chem.* **1979,** 83, (4), 480-486.

383. Pileni, M.-P.; Zemb, T.; Petit, C., Solubilization by reverse micelles: Solute localization and structure perturbation. *Chem. Phys. Lett.* **1985,** 118, (4), 414-420.

384. Peltonen, L.; Hirvonen, J.; Yliruusi, J., The Behavior of Sorbitan Surfactants at the Water–Oil Interface: Straight-Chained Hydrocarbons from Pentane to Dodecane as an Oil Phase. *J. Colloid Interface Sci.* **2001,** 240, 272-276.

385. Shrestha, L. K.; Dulle, M.; Glatter, O.; Aramaki, K., Structure of Polyglycerol Oleic Acid Ester Nonionic Surfactant Reverse Micelles in Decane: Growth Control by Headgroup Size. *Langmuir* **2010,** 26, (10), 7015-7024.

386. Zulauf, M.; Eicke, H.-F., Inverted Micelles and Microemulsions in the Ternary System H,O/Aerosol-OT/Isooctane as Studied by Photon Correlation Spectroscopy. *J. Phys. Chem.* **1979,** 83, (4), 480-486.

387. Abou-Nemeh, I.; Bart, H. J., Microstructures in the System Water/D2EHPA/Span-80/n-Dodecane. *Langmuir* **1998,** 14, 4451-4459.

388. Tubbs, K. W.; Nguyen, V. T.; Adalsteinsson, T., Phase Transitions of n-Hexadecane in Nanoencapsulated Binary Solutions of n-Hexadecane and 1-Octanol. *J. Phys. Chem. B* **2012,** 116, 3954-3960.

389. Patel, H. A.; Garde, S.; Keblinski, P., Thermal Resistance of Nanoscopic Liquid-Liquid Interfaces: Dependence on Chemistry and Molecular Architecture. *Nano Lett* **2005,** 5, (11), 2225-2231.

390. Lei, Q.; Bain, C. D., Surfactant-Induced Surface Freezing at the Alkane-Water Interface. *Phys. Rev. Lett.* **2004,** 92, (17), 176103.

391. Esenturk, O.; Walker, R. A., Surface Structure at Hexadecane and Halo-hexadecane Liquid/Vapor Interfaces. *J. Phys. Chem. B* **2004,** 108, (30), 10631-10635.

392. Khadem, M. H.; Wemhoff, A. P., Thermal Conductivity Predictions of Herringbone Graphite Nanofibers Using Molecular Dynamics Simulations *J. Chem. Phys.* **2013,** 138, 084708.

393. Zheng, R.; Gao, J.; Wang, J.; Feng, S.-P.; Ohtani, H.; Wang, J.; Chen, G., Thermal Percolation in Stable Graphite Suspensions. *Nano Lett.* **2012,** 12, 188−192.

394. Wei, C., Structural phase transition of alkane molecules in nanotube composites. *Phys. Rev. B* **2007,** 76, 134104.

395. He, Y.; Men, Y.; Zhao, Y.; Lu, H.; Ding, Y., Numerical investigation into the convective heat transfer of TiO2 nanofluids flowing through a straight tube under the laminar flow conditions. *Appl. Therm. Eng.* **2009,** 29 1965.

396. Duan, F.; Kwek, D.; Crivoi, A., Viscosity affected by nanoparticle aggregation in Al2O3-water nanofluids. *Nanoscale Res. Lett.* **2011,** 6, 248.

397. Park, S. D.; Lee, S. W.; Kang, S.; Bang, I. C.; Kim, J. H.; Shin, H. S.; Lee, D. W.; Lee, D. W., Effects of nanofluids containing graphene/graphene-oxide nanosheets on critical heat flux. *Appl. Phys. Lett.* **2010,** 97, 023103.

398. Barrau, S.; Demont, P.; Peigney, A.; Laurent, C.; Lacabanne, C., DC and AC Conductivity of Carbon Nanotubes-Polyepoxy Composites. *Macromolecules* **2003,** 36, 5187-5194.

399. Bryning, M. B.; Milkie, D. E.; Islam, M. F.; Kikkawa, J. M.; Yodh, A. G., Thermal conductivity and interfacial resistance in single-wall carbon nanotube epoxy composites. *Appl. Phys. Lett.* **2005,** 87, 161909.

400. Cipriano, B. H.; Kota, A. K.; Gershon, A. L.; Laskowski, C. J.; Kashiwagi, T.; Bruck, H. A.; Raghavan, S. R., Conductivity enhancement of carbon nanotube and nanofiber-based polymer nanocomposites by melt annealing. *Polymer* **2008,** 49, 4846–4851.

401. Marconnet, A.; Yamamoto, N.; Panzer, M. A.; L.Wardle, B.; Goodson, K. E., Thermal Conduction in Aligned Carbon Nanotube Polymer Nanocomposites with High Packing Density. *ACS Nano* **2011,** 5, (6), 4818–4825.

402. ShuyingWu; Zhu, D.; Li, X.; Li, H.; Lei, J., Thermal energy storage behavior of Al2O3–H2O nanofluids. *Thermochim acta* **2009,** 483, 73-77.

403. Zeng, J. L.; Cao, Z.; Yang, D. W.; Sun, L. X.; Zhang, L., Thermal conductivity enhancement of Ag nanowires on an organic phase change material. *J. Therm. Anal. Calorim* **2010,** 101, 385-389.

404. Babu, K.; Kumar, T. S. P., Effect of CNT concentration and agitation on surface heat flux during quenching in CNT nanofluids. *Int. J. Heat Mass Transfer* **2011,** 54, 106-117.

405. Angayarkanni, S. A.; Philip, J., Tunable Thermal Transport in Phase Change Materials Using Inverse Micellar Templating and Nanofillers. *J. Phys. Chem. C* **2014,** 118, 13972−13980.
406. Wang, S.; Cheng, Y.; Wang, R.; Sun, J.; Gao, L., Highly Thermal Conductive Copper Nanowire Composites with Ultralow Loading: Toward Applications as Thermal Interface Materials. *ACS Appl. Mater. Interfaces* **2014,** 6, 6481−6486.
407. Cherkasova, A. S.; Shan, J. W., Particle Aspect-Ratio Effects on the Thermal Conductivity of Micro- and Nanoparticle Suspensions. *ASME J. Heat Transfer* **2008,** 130, 082406.
408. Evans, W.; Prasher, R.; Fish, J.; Meakin, P.; Phelan, P.; Keblinski, P., Effect of aggregation and interfacial thermal resistance on thermal conductivity of nanocomposites and colloidal nanofluids. *Int. J. Heat Mass Transfer* **2008,** 51, 1431-1438.
409. Shenogin, S.; Xue, L.; Ozisik, R.; Keblinski, P.; Cahill, D. G., Role of thermal boundary resistance on the heat flow in carbon-nanotube composites. *J. Appl. Phys.* **2004,** 95, (12), 8136-8144.